# Load and Response Estimation and Model Recalibration using Inverse Finite Element Methods

by

Celeste Barnardo

*Dissertation presented for the degree of Doctor of Civil Engineering at the University of Stellenbosch*


Department of Civil Engineering
University of Stellenbosch
Private Bag X1, 7602 Matieland, South Africa

Promoter: Dr P Mainçon
Prof P.E. Dunaiski

December 2006

# Declaration

I, the undersigned, hereby declare that the work contained in this dissertation is my own original work and that I have not previously in its entirety or in part submitted it at any university for a degree.

Signature:

C Barnardo

Date: 28:12:2006

# Abstract


## Load and Response Estimation and Model Recalibration using Inverse Finite Element Methods

C Barnardo

*Department of Civil Engineering*
*University of Stellenbosch*
*Private Bag X1, 7602 Matieland, South Africa*

Dissertation: PhD (Eng)

December 2006

The inverse finite element method (iFEM) allows estimating the loads and the complete response of a structure, given a finite element model of the structure and imperfect measurements of its response. The theoretical basis of iFEM is described in two publications by Philippe Mainçon [44,45].

Testing of the inverse Finite Element Method was initially [44,45] done under the assumption that the model used in the iFEM analysis behaves exactly as the structure on which the measurements are taken. In practice, however, the model (represented by a stiffness matrix, and where appropriate, damping and mass matrices) will not match the actual structure exactly. Sources of modelling error include errors due to discretisation, and uncertainty on the characteristics of the structure, including structural damage.

**Sensitivity to modelling errors** In the first part of this work, the influence of modelling errors on the performance of iFEM is discussed. The influence of modelling errors was investigated for localised and/or distributed model errors, using

data from numerically simulated experiments. This had the benefit of being much easier to carry out, less time consuming than the generation of real measurement data, and that the answer is known. In addition to the test cases with simulated measurement data, real measurement data was also obtained from dynamic experiments on a damaged beam.

The influence of modelling errors was investigated as follows: 'Measurement' data were simulated by creating a FEM model of the structure considered, computing response values and adding adequate noise. The FEM model was then modified to obtain the inaccurate iFEM model. This approach gave a great liberty to explore different structures and scenarios.

The investigation concludes that iFEM is stable in the presence of modelling errors: Distributed model error gives rise to distributed error in the assessed external loads. The output of iFEM in the presence of localised error (damage) is such that it can be used to detect discrepancies between the model and the actual structure.

**Model parameter estimation algorithms** In the second part of the work, two further iFEM algorithms are developed, for model parameter identification in static and dynamic systems respectively. The new algorithms allow model parameter identification in addition to force and response estimation, combining data from several experiments. A third algorithm allows to decrease their computing time considerably. These algorithms have applications in the field of damage identification, structural health monitoring, and material property estimation. The algorithms are implemented and integrated into the existing iFEM software SAFRAN. Initial testing of the algorithms using several simulated test cases are presented and gave very encouraging results. A literature review on the topic of damage identification places the new developments in perspective.

**Applications** In the third part of the work, actual experiments are used to evaluate the performance of iFEM algorithms in the face of real world challenges, including model uncertainty, measurement inaccuracy and the handling of large

amounts of data.

Vortex induced vibrations (VIV) are caused by oscillating hydrodynamic forces, which appear as a result of vortex shedding from fluid flow around slender structures. In the design of marine structures, the ability to accurately predict these vibrations would be of great value. While time histories of these forces would be invaluable in aiding understanding of VIV, they are difficult to measure. Using iFEM, the time histories of hydrodynamic forces acting along the length of a slender marine riser were estimated, based on measurements of its acceleration at several positions along the riser. These results were well received by experts in vortex induced vibrations. Data from a simpler, well understood VIV experiment allowed to validate the existing iFEM dynamic force identification theory as well as the newly developed dynamic parameter identification theory before moving on to the more difficult slender structure problem. A literature review briefly introduces the topic of vortex induced vibrations.

The iFEM dynamic parameter identification algorithm is applied to successfully locate damage in a simple vibrating beam. In addition, the parameter identification algorithm was tested against a benchmark structure. In experiments conducted on the steel frame scale model structure at the University of British Columbia, acceleration data was gathered of the response of the structure under three methods of excitation. Various damage configurations were investigated and it was proposed that this structure should be used as a benchmark for comparative studies of damage detection methods. The iFEM dynamic parameter identification is applied to locate and quantify the damage in the structure and this is compared to results obtained by other authors using different methods. Damage were identified and located for several of the damage scenarios, but for some scenarios difficulties were encountered in locating the damage. Uncertainties regarding the method and the experiment are discussed.

# Uittreksel

## Invers Eindige Element Metodes vir die Bepaling van Belasting, Vervorming en Model Herkalibrasie.

C Barnardo

*Departement Siviele Ingenieurswese*
*Universiteit van Stellenbosch*
*Privaatsak X1, 7602 Matieland, Suid Afrika*

Proefskrif: PhD (Ing)

Desember 2006

Die eksterne kragte wat op 'n struktuur aangewend word kan bereken word met behulp van die inverse eindige element metode (iEEM) indien 'n eindige element model van die struktuur beskikbaar is tesame met metings (al is dit onvolledig en onakkuraat) wat die reaksie van die struktuur beskryf. Die teoretiese grondslag vir die metode word beskryf in twee artikels deur Philippe Mainçon [44,45].

Die iEEM metode is aanvanklik [44,45] getoets onder die aanname dat die eindige element modelle van strukture volkome akkuraat is. Hierdie is 'n onrealistiese aanname, aangesien die model (bestaande uit 'n styfheidsmatriks, en indien dit van toepassing is, demping en massa matrikse) nie die fisiese struktuur perfek kan beskryf nie. Diskretisering, asook onsekerheid oor materiaal en struktuur eienskappe, insluitende strukturele skade, kan en sal aanleiding gee tot onakkurate modelle.

**Sensitiwiteit ten opsigte van model onakkuraathede** Die eerste paar hoofstukke bespreek die invloed van verspreide en/of lokale modeleringsfoute op die

resultate, in terme van die berekende eksterne kragte. Die invloed van modeleringsfoute is ondersoek met behulp van numeries gesimuleerde eksperimente. Hierdie benadering skep ruimte om 'n verskeidenheid verskillende scenarios te ondersoek, terwyl dit terselfdertyd baie makliker en goedkoper is as om ware metingsdata uit eksperimente te verkry. Addisioneel tot die gesimuleerde voorbeelde, is ware metingsdata verkry vanaf dinamiese eksperimente op 'n beskadigde balkstruktuur.

Die invloed van modeleringsfoute is soos volg ondersoek: 'n Eindige element model van die struktuur is gebruik om 'gemete' waardes te bereken wat die reaksie van die struktuur beskryf. Lukrake foutwaardes is by die berekende reaksiewaardes getel om die onakkuraatheid van metings te simuleer. Die onakkurate eindige element model is vervolgens verkry deur modeleringsfoute by die oorspronklike model te voeg.

Uit die resultate van die ondersoek kan die gevolgtrekking gemaak word dat iEEM wel stabiel is in die teenwoordigheid van modeleringsfoute. Verspreide modeleringsfoute gee aanleiding tot verspreide foute in die berekende eksterne kragte, terwyl die resultate in die teenwoordigheid van lokale modeleringsfoute, soos byvoorbeeld strukturele skade, gebruik kan word om verskille tussen die werklike struktuur en die model uit te wys.

**Ontwikkeling van model parameter identifikasie algoritmes** In die tweede deel van die proefskrif word nog twee iEEM algoritmes ontwikkel, vir model parameter identifikasie van onderskeidelik statiese en dinamiese probleme. Hierdie algoritmes laat die gebruiker toe om data vanuit verskeie eksperimente te kombineer ten einde onseker model eienskappe te bereken. Die volledige reaksie van die struktuur, tesame met kragte wat op die struktuur ingewerk het, word ook bepaal. Die berekeningstyd verbonde aan bogenoemde algoritmes word drasties verminder met die gebruik van 'n aanvullende algoritme wat ook ontwikkel is. Hierdie algoritmes kan gebruik word om strukturele skade te bepaal en het verskeie toepassings in die gebied van strukturele monitering. Die bestaande iEEM sagteware SAFRAN is aangepas en die algoritmes is daarin implementeer. Bemoedigende resultate is verkry van verskeie gesimuleerde eksperimente wat gebruik is om die nuwe algoritmes te toets. n Literatuurstudie oor die onderwerp van defek identifikasie plaas

die nuwe ontwikkelinge in perspektief.

**Toepassings** Die laaste deel van die proefskrif is toegewy om die iEEM algoritmes te evalueer deur ware eksperimente te gebruik, wat uitdagings soos onseker modeleienskappe, onakkurate metings en groot hoeveelhede data sal insluit.

Vorteks induseerde vibrasies (VIV) word veroorsaak deur ossilerende hidrodinamiese kragte wat verskyn wanneer vortekse vorm soos 'n vloeistof verby 'n slanke struktuur vloei. Indien hierdie vibrasies akkuraat voorspel kon word, sou dit van groot waarde wees vir die ontwerp van mariene strukture. Rekords oor tyd van die kragte wat hierdie vibrasies veroorsaak sal baie help om VIV beter te verstaan, maar is baie moeilik om te meet. iEEM kon daarin slaag om sulke tydrekords van kragte, wat oor die lengte van 'n lang dun pyp ingewerk het, te bereken uit versnellingsmetings by 'n paar posisies op die vibrerende pyp. Hierdie resultate het die entoesiasme van kenners in VIV navorsing uitgelok. Voordat bogenoemde, meer ingewikkelde probleem aangepak is, is 'n eenvoudige VIV eksperiment, wat goed verstaan word, eers gebruik om die geldigheid van resultate van die bestaande iEEM dinamiese krag berekeningsmetode asook die nuut ontwikkelde iEEM dinamiese parameter identifikasie metode te bevestig. 'n Literatuurstudie stel die onderwerp van vorteks induseerde vibrasies kortliks bekend.

Die iEEM dinamiese parameter identifikasie metode is verder aangewend om skade in 'n eenvoudige vibrerende balk te lokaliseer. Die iEEM dinamiese parameter identifikasie metode is ook getoets teen 'n sogenaamde 'benchmark' struktuur, 'n struktuur wat 'n vergelykbare basis daar stel, sodat verskillende defek indentifikasie metodes met mekaar vergelyk kan word. Sodanige stel struktuur eksperimente is by die Universiteit van British Columbia uitgevoer op 'n staalraam struktuur. Versnellingsmetings van die struktuur vibrasies vir verskeie kombinasies van skade en aangewende kragte is op hul webblad beskikbaar gestel. Die iEEM dinamiese parameter identifikasie metode is gebruik om die skade in verskeie scenarios te lokaliseer en kwantifiseer en resultate word vergelyk met die van ander metodes. In die meeste gevalle is die skade suksesvol gelokaliseer, maar daar was ook gevalle waar die skade onopgespoor gebly het. Onsekerhede ten opsigte van die eksperiment en die metode word bespreek.

# Acknowledgements

Above all, I wish to thank my heavenly Father for blessing me with ability, opportunity and success. May my every accomplishment be to the glory of the One worthy of all praise: Jesus Christ.

To Dr. Philippe Mainçon, my study leader: My sincere thanks and admiration go to this talented researcher, who never ceased to amaze me with more creative ideas on applying theory to solve engineering problems. Thank you for always being available and willing to help, for your enormous contributions to my understanding of FEM, dynamics and related issues and for many fruitful discussions while developing iFEM. Thanks also for introducing me to iFEM, for expertly giving direction in the development of this dissertation and for mercilessly demanding excellence.

The Centre for the Development of Steel Structures (CDSS) at the University of Stellenbosch and the Wilhelm Frank Trust are acknowledged for funding this research effort.

Special thanks to Prof. Carl Martin Larsen for inviting me to the Norwegian University of Science and Technology, and to the Department of Marine Technology for welcoming me as a guest there for the duration of 2005. Thank you, Prof. Larsen, for introducing me to vortex induced vibrations, for patiently explaining the basics and for many rewarding discussions later.

I am indebted to MARINTEK (Norwegian Marine Technology Research Institute) and the Department of Marine Technology of NTNU, Trondheim, Norway. They kindly made experimental data on vortex induced vibrations available to me,

including the Rotating Rig experiment and the experiments of Dr. Kyrre Vikestad. I wish to thank Dr. Kyrre Vikestad, a former PhD student of that Department, for answering my questions relating to his work, as well as Dr. Halvor Lie and Dr. Carl Eric Kaason, MARINTEK, for their contributions.

I am grateful to Prof. Karl Beucke for inviting me to the Bauhaus University of Weimar in 2002, making available a computer and office space, and for organising visits for myself and fellow student Jacques Maree, to civil engineering companies in Germany, to Prof. Christian Bucher for insight gained from his course in structural dynamics attended in Weimar, for pointing out the applicability of the damaged beam experiment in verifying iFEM and for valuable discussions on the theory, and to Dr. Volkmar Zabel for making available his data from previous experiments on the damaged beam, and for assisting me in conducting additional tests.

I admire Dr. Corne Coetzee for his abilities as an independent researcher. His encouragement and support were more valuable than he could ever imagine.

Thanks to my parents and family for always praying for me, providing encouragement, sympathy and praise, all at the appropriate times!

Thank you Johan Troskie for your solid friendship. It would be impossible to tell the value of this gift.

Annie van der Westhuizen: No one can ask for a better friend. During the eight years that we have studied together, you have been a tremendous inspiration.

Thanks to all the guys at NTNU for great coffee breaks and parties. You made me feel welcome.

# Contents

# List of Figures

# List of Tables

# Nomenclature

**Acronyms and Abbreviations**

| | |
|---|---|
| FEM | Finite Element Method |
| iFEM | Inverse finite element method |
| iFEM XU | Inverse finite element method for the estimation of forces and response |
| iFEM XUA | Inverse finite element method for the estimation of forces, response and model parameters |
| SAFRAN | The prototype iFEM software |
| PDF | Probability distribution function |
| VIV | Vortex Induced Vibrations |
| ISPI | Inverse Static Parameter Identification - An early computer implementation of the iFEM XUA theory |
| NExT | Natural Excitation Technique |
| ERA | Eigensystem Realization Algorithm |
| $nXper$ | Number of experiments |
| $nXdof$ | Number of $\overline{\mathbf{X}}$ degrees of freedom |
| $nUdof$ | Number of $\overline{\mathbf{U}}$ degrees of freedom |
| $n\alpha$ | Number of $\overline{\alpha}$ degrees of freedom |
| $nT$ | Number of time steps |
| $2D$ | Two dimensional |
| $3D$ | Three dimensional |

**Variables**

| | |
|---|---|
| $\overline{\overline{\mathbf{K}}}$ | Stiffness matrix |
| $\overline{\overline{\mathbf{C}}}$ | Damping matrix |
| $\overline{\overline{\mathbf{M}}}$ | Mass matrix |
| $\overline{\mathbf{X}}$ | Vector of nodal response coefficients |
| $\overline{\mathbf{U}}$ | Vector of nodal force coefficients |
| $\overline{\alpha}$ | Vector of nodal model parameter coefficients |
| $\overline{\mathbf{dX}}$, $\overline{\mathbf{dU}}$, $\overline{\mathbf{d}\alpha}$ | Vector of incremental nodal response, -force and -parameter coefficients respectively |
| $t$ | Time |
| $\overline{\mathbf{x}}(t)$, $\overline{\dot{\mathbf{x}}}(t)$, $\overline{\ddot{\mathbf{x}}}(t)$, and $\overline{\mathbf{u}}(t)$ | Vector of incremental nodal displacement, -velocity, -acceleration and -force respectively, for each time step. |
| $\overline{\mathbf{R}}$ | Vector of nodal consistent forces |
| $\overline{\xi}$ | Position in a finite element |
| $\overline{\mathbf{f}}_o(\overline{\xi})$ | Known force distribution over a finite element |
| $\overline{\mathbf{u}}(\overline{\xi})$ | Unknown force distribution over a finite element |
| $\overline{\overline{\mathbf{N}}}(\overline{\xi})$ | Matrix of shape functions used to describe a displacement or strain distribution |
| $\overline{\overline{\mathbf{L}}}(\overline{\xi})$ | Matrix of shape functions used to describe an external force distribution |
| $\overline{\overline{\mathbf{H}}}$ | A matrix that transforms the vector of nodal force coefficients into a vector of nodal consistent forces. |
| $\overline{\overline{\mathbf{G}}}$ | A matrix that transforms the vector of model parameter coefficients into a vector of nodal consistent forces. |
| $\overline{\lambda}$ | Vector of Lagrange multipliers |
| $J'$ | Augmented Lagrangian |
| $J$ | Cost function |
| $\overline{\overline{\mathbf{Q}}}$ and $\overline{\mathbf{Q}}$ | A cost matrix and a cost vector respectively. Used to encode a prior probability distribution. |

| | |
|---|---|
| $\overline{\overline{\overline{\mathbf{T}}}}_K$ | Third order tensor containing stiffness components |
| $\overline{\overline{\overline{\mathbf{T}}}}_C$ | Third order tensor containing damping components |
| $\overline{\overline{\overline{\mathbf{T}}}}_M$ | Third order tensor containing mass components |
| $\overline{\mathbf{f}}$ | Equilibrium relation |
| $U_x$, $U_y$ and $U_z$ | Three orthogonal components of a point load. |
| $U_{rx}$, $U_{ry}$ and $U_{rz}$ | Three orthogonal components of a moment. |

### Section Properties

| | |
|---|---|
| $E$ | Young's modulus |
| $I$ | Moment of inertia |
| $L$ | Length |
| $A$ | Section area |

### Greek Symbols

| | |
|---|---|
| $\lambda$ | Lagrange multiplier |
| $\nabla$ | Derivative |
| $\sigma$ | Standard deviation |
| $\rho$ | Density |
| $\Delta$ | Differential |
| $\sum$ | Sum |
| $\mu$ | mass ratio |
| $\omega$ | Pulsation |
| $\theta_v$, $\phi_v$ | Phase angles |
| $\nu$ | Kinematic viscosity |

### Superscripts

| | |
|---|---|
| $^T$ | Transpose |
| $^*$ | Complex conjugate |

**Subscripts**

| | |
|---|---|
| $_{m,\ meas}$ | Measurement or Measured |
| $_x$ | Displacement or Strain |
| $_{\dot{x}}$ | Velocity |
| $_{\ddot{x}}$ | Acceleration |
| $_u$ | Force |
| $_0$ | Approximation point |
| $_{opt}$ | Optimal |
| $_k$ | Iteration |
| $_i$ | Experiment |
| $_{osc}$ | oscillation |
| $_v$ | vortex |
| $_e$ | external |

**VIV related symbols (Chapters 9 to 12)**

| | |
|---|---|
| $D$ | Cylinder diameter |
| $U$ | Cross flow velocity |
| $Re$ | Reynolds number |
| $St$ | Strouhal number |
| $f_v$ | Vortex shedding frequency |
| $f_n$ | Natural frequency |
| $f_{osc}$ | Frequency of the response oscillation |
| $U_R$ | Reduced velocity |
| $\hat{f}$ | Dimensionless frequency |
| $x_0$ | Amplitude of dynamic motion $x(t)$ |
| $F_L(t)$ | Hydrodynamic lift force. The component of hydrodynamic force in the transverse direction of the flow. |
| $F_D(t)$ | Hydrodynamic lift force. The component of hydrodynamic force in the flow direction. |

| | |
|---|---|
| $\hat{F}_L$ | Amplitude of the oscillating vortex induced hydrodynamic lift force |
| $F_{D_{mean}}$ | Mean component of the drag force. |
| $\hat{F}_D$ | Amplitude of the oscillating component of the drag force. |
| $\hat{F}_{LV_0}$ | Amplitude of the vortex induced force (lift force) component in phase with the structure's velocity. |
| $M_{A_0}$ | Added mass |
| $C_{M_0}$ | Added mass coefficient (dimensionless) |
| $C_{LV_0}$ | Lift coefficient (dimensionless) |
| $F_e$ | External excitation force |
| $F_L$ | Hydrodynamic force |
| $m_{dry}$ | Dry mass |

**Tensor notation**

| | |
|---|---|
| $\overline{\mathbf{V}}$ | Vector. A single bar denotes a first order tensor, or vector. |
| $\overline{\overline{\mathbf{M}}}$ | Matrix. Double bars denote a second order tensor, or matrix. |
| $\overline{\overline{\overline{\mathbf{T}}}}$ | Third order tensor. The number of bars denotes the order of the tensor. |
| $\overline{\overline{\mathbf{M}}} = \overline{\overline{\overline{\mathbf{T}}}}.\overline{\mathbf{V}} \Leftrightarrow \overline{\overline{\mathbf{M}}}_{ij} = \sum_k \overline{\overline{\overline{\mathbf{T}}}}_{ijk}\overline{\mathbf{V}}_k$ | The dot product in the tensor notation corresponds to a sum over one index in the component notation. |
| $\overline{\overline{\mathbf{M}}}^T_{ij} = \overline{\overline{\mathbf{M}}}_{ji}$ | For a matrix (second order tensor), there is only one possible transposition, noted "T". |
| $\overline{\overline{\overline{\mathbf{T}}}}^{T132}_{ijk} = \overline{\overline{\overline{\mathbf{T}}}}_{ikj}$ | For a tensor of order n, there are n! ways of permuting the indexes, so it is important to state which permutation is meant. |

# Part I

# Introduction

# Chapter 1

# Introduction

## 1.1 Background

Given a finite element model of a structure, and imperfect measurements of the response of the structure, the inverse Finite Element Method (iFEM) allows assessment of the external loads acting on the structure. Once these loads are determined, the state of the structure is known, including stresses and strains everywhere in the structure. The theoretical basis of iFEM is described in Chapter 2 based on two papers by Philippe Mainçon [44, 45]. The quality of the results of iFEM are of course influence by the number, location, type and accuracy of sensors that are available on an instrumented structure. A useful algorithm, developed by Jacques Maree [46] allows to evaluate the adequacy of a given measurement setup or sensor configuration for static experiments.

## 1.2 Goals of the dissertation

**Investigating the influence of errors in the structural model on the output of iFEM** iFEM was initially tested assuming a perfect structural model. In practical cases however, the model (represented by a stiffness matrix, and where appropriate, damping and mass matrices) that is used in the iFEM analysis will not behave exactly as the actual structure on which the measurements were taken.

The first goal of the present work is to understand how local and distributed errors in

the model affect the quality of the load and response estimates. It was initially feared that iFEM might be unstable in the presence of modelling error, meaning that iFEM would be of no practical use. It is also to be investigated whether the output of iFEM in the presence of modelling error can be used to detect discrepancies between the model and the real structure.

**Development of iFEM algorithms for parameter estimation** Civil engineering structures may suffer damage from heavy excitation by a natural phenomenon such as earthquakes, or may display conditions such as corrosion or fatigue from regular daily use. Visual inspection is currently the preferred procedure to detect such damage. However, as technology provides researchers with faster computing tools and less expensive sensors, the need for techniques that improve the accuracy, reliability, and speed of damage detection has become clear.

The second goal of this work is to develop algorithms for model parameter estimation for both static and dynamic systems and to implement these algorithms in a computer software that would allow us to treat inspection problems numerically. Such algorithms would allow to estimate uncertain or unknown structural properties from structural response measurements, by explicitly defining unknown model parameters in the iFEM model. Important applications of such techniques would be the detection of defects in structures, structural damping estimation and material property estimation. While the output of iFEM load and response estimation algorithms might be used to detect discrepancies between the model and the real structure, by judging the credibility of the estimated forces, this is often difficult to discern. It would be of much greater value to be able to directly estimate uncertain model properties.

**Experimental validation** The iFEM algorithms can be divided into two groups: The first group of algorithms were developed by Philippe Mainçon and is classified as the iFEM load and response estimation algorithms. In this dissertation iFEM load and response estimation algorithms are often in short referred to as iFEM XU algorithms. The second

group of algorithms, developed by the author of this dissertation, can be classified as the iFEM load-, response- and model parameter estimation algorithms, in short referred to as iFEM XUA algorithms.

As the third goal, the iFEM algorithms are to be tested on real world problems. Real world problems brings with it the challenge of experimental uncertainties, changing environmental conditions, unknown model properties, unknown or uncertain excitations, large amounts of measurement data, a limited number of sensors, and sensor noise that is often difficult to quantify and cannot always be considered a white noise process. Any method that is to be of use in practice must be robust enough to face these challenges. For this purpose, the existing linear dynamic iFEM XU algorithm was tested against three experimental studies. These were the *Weimar Beam Experiment*, *Vikestad's experiment* and the *Rotating Rig experiment*, described shortly in the following section. The newly developed linear dynamic iFEM XUA algorithm was also tested against three experimental studies. These were the *Weimar Beam Experiment*, *Vikestad's experiment* and the *Benchmark experiment*.

## 1.3 Contents of the dissertation

**Introduction** Chapter 2 presents the existing iFEM theory as developed by Philippe Mainçon.

**Investigating the influence of errors in the structural model on the output of iFEM** Chapter 3 reports the results of an investigation into the effect of model error on static iFEM analyses. Three numerically simulated static experiments are designed to investigate the effect of distributed and localised model errors. In Chapter 4 an actual experiment on a damaged beam was used to investigate the effect of model errors for dynamic analyses. These chapters conclude that iFEM is stable in the presence of model error, and describes how errors affect the output of iFEM.

Although this is not directly relevant to model error sensitivity, an interesting observation that was made during the course of work is presented in Chapter 5. It was observed that even when continuity of the externally estimated load is not required, it is often achieved anyway.

**Development of iFEM algorithms for parameter estimation** The output of iFEM in the presence of localised model error (damage), as described in Chapters 3 and 4, hints at the possibility of damage detection. A literature study of existing methods used for parameter estimation is presented in Chapter 6.

A theory for iFEM parameter estimation using data from multiple static experiments is developed in Chapter 7. This algorithm can treat both linear and non-linear static parameter estimation problems. Quadratic "cost" functions are used to minimise the difference between measured and estimated response values and to encode prior knowledge (according to engineering judgment) of what the forces and model parameters could be. The cost is typically proportional to the square of the difference between measured and estimated response values, to the square of estimated external forces, and to the square of the difference between assumed and estimated model parameters. The cost is minimized under the constraint that external and internal forces and response are related by the equilibrium equations. For static systems this constrained optimisation problem is solved using Lagrange multipliers.

In Chapter 8 an algorithm for iFEM parameter estimation of linear dynamic systems is developed. This algorithm also allows data from several experiments to be combined to form a better basis for parameter estimation. The dynamic algorithm uses the Fourier transformation to solve the problem in the frequency domain. Dynamic equilibrium is enforced at each time step and the quadratic cost function (similar to the one used in the static problem), integrated over time, is minimised. Lagrange multipliers are again used to obtain a system of equations that can be solved, after transformation to the frequency domain, for each frequency. The time domain solution is found by superposition of the

different frequency components. This method allows to treat linear dynamic systems with a large number of degrees of freedom.

By avoiding the inversion of large matrices, the computing time of both the static and dynamic parameter estimation algorithms can be dramatically improved.

All the above algorithms are implemented in a computer software which is used to test their capabilities.

**Experimental validation** Four experiments were used in the iFEM validation process. The *Weimar Beam Experiments*, conducted by Dr. Volkmar Zabel at the Bauhaus University of Weimar, Germany, considered the vibrations of a damaged beam of which the mass properties could be altered. In Chapter 4 the dynamic iFEM XU algorithm is used to estimate, from acceleration measurements, the hammer impact applied to the damaged beam and also to estimate the inertia force that a lumped mass applied to the beam. In Chapter 8 the dynamic iFEM XUA algorithm uses the same acceleration measurements to detect the damage in the *Weimar Beam*.

The *Benchmark Experiments*, conducted by several researchers at the University of British Columbia, Canada, considered the vibrations of a three dimensional four-story truss structure, excited by one of three possible load configurations. Nine different damage configurations were investigated by removing bracing and loosening beam-column connections within the test structure. In Chapter 9 the dynamic iFEM XUA algorithm is used to locate damaged members in several damage scenarios from measurement data gathered in the *Benchmark Experiments*.

When a fluid flows around a cylinder, periodic vortices will often be shed as a result of the fluid separating from the cylinder. The alternating pressure field that is caused around the cylinder gives rise to oscilating hydrodynamic forces, which causes the cylinder to vibrate. This is known as Vortex Induced Vibrations (VIV). Chapter 10 summarises the

most important aspects of VIV in the context of marine risers. Two VIV related experiments are treated, conducted by MARINTEK and the Department of Marine Technology, NTNU, in Norway. The first experiment, conducted by *Vikestad* [72], investigated the vibration of a short cylinder in fluid flow. In Chapter 11 *Vikestad's Experiments* allowed to validate both the dynamic iFEM XU and XUA algorithms, since this experiment is well understood from existing VIV theories. The iFEM XU algorithm was used to calculate the hydrodynamic forces acting on the vibrating cylinder and these estimates could be compared to the known (measured) values. The iFEM XUA algorithm was used to calculate the "added mass", a hydrodynamic force constant that is often used to describe the hydrodynamic load process in VIV research. The estimated "added mass" values could be compared to the known values. In Chapter 12 the *Rotating Rig Experiment* is discussed. This experiment investigated the vibrations of a long slender pipe in constant or sheared current, a problem that is not yet well understood. In such experiments it is very unpractical to measure the hydrodynamic forces acting on the structure. The dynamic iFEM XU algorithm was applied to estimate the hydrodynamic loads from acceleration measurements. The estimated loads are then compared to existing VIV theory.

Most of the experiments used in the validation process were conducted by individuals and institutes other than the author. This approach allowed to treat a fairly large number of case studies, while keeping within the limitations of time and funding. The choice of experiments used to validate the algorithms were much influenced by the availability of data from previous experiments by other authors, which happen to be mostly dynamic applications.

Unfortunately, the static algorithms were validated using numerically simulated experiments only, since appropriate real experimental data for such systems were not forthcoming. Chapter 3 presents three numerical examples where the static iFEM XU algorithm is applied. In the second half of Chapter 7, the static iFEM XUA algorithm were used to locate and quantify damage in several numerical examples.

**Conclusions** Chapter 13 concludes the dissertation and includes useful suggestions for future work.

# Chapter 2

# iFEM load and response estimation and the prototype software Safran

## 2.1 Introduction

In this chapter the inverse finite element method, as developed by Philippe Mainçon[44, 45] is presented. This method allows to estimate the loads and complete response of a structure from limited measurements of its response. Potential uses of the inverse finite element method include monitoring of structures, where the stresses are known everywhere in the structure once the loads acting on the structure have been calculated. Solving the inverse problem would also allow to refine models for aerodynamic and hydrodynamic loads on structures in cases where measuring the fluid pressure on the surface of the structure becomes impractical.

## 2.2 An overview of the inverse finite element method

### 2.2.1 Background

The finite element method (FEM) allows to calculate the response of a structure once a model of the structure is available and either the displacement value or the corresponding nodal force is known for each degree of freedom. The equilibrium equation, $\overline{\overline{\mathbf{K}}}.\overline{\mathbf{X}} = \overline{\mathbf{R}}$, with $\overline{\overline{\mathbf{K}}}$ the stiffness matrix of the structure, $\overline{\mathbf{X}}$ the nodal response values and $\overline{\mathbf{R}}$ the

consistent nodal forces acting on the structure, is found by discretising the differential equation using energy methods or Galerkin's method. Solving the inverse problem, where the externally applied forces are to be calculated using measurements of the response when $\overline{\overline{\mathbf{K}}}$ is known, presents several problems. The inverse problem is said to be ill-posed, so that small errors in response measurements cause large errors in the force estimates. Also, the vector $\overline{\mathbf{X}}$ is not completely known, since measurements will not be taken at all degrees of freedom.

### 2.2.2 The inverse finite element method

The inverse finite element method, as presented by Mainçon [44, 45], addresses the above-mentioned difficulties and allows to estimate the external forces and the complete response of a structure, based on incomplete and imprecise measurements of forces and/or response.

To this effect quadratic "cost" functions are used to encode the measurement data and prior knowledge (according to engineering judgment) of what the forces could be. The cost is typically proportional to the square of the difference between measured and estimated response values, and to the square of estimated external forces. The cost is minimized under the constraint that forces and response are related by the equilibrium equations.

For static systems this constrained optimisation problem is solved using Lagrange multipliers, and a system of equations is obtained with displacements and external forces as unknowns.

For dynamic systems, two algorithms were developed. The first one, developed in 2001, (shortly after the static algorithm), had the severe drawback that it could not handle systems with a large number of degrees of freedom. It failed at approximately one hundred degrees of freedom. A second algorithm was invented in late 2003 to address this problem.

For dynamic systems, the cost function at each time step, integrated over time, is

minimised, while equilibrium is enforced at each time step. Inverse dynamic problems differ from direct or forward dynamic problems in the sense that they are no longer initial value problems. The first dynamic algorithm built strongly on principles from control theory. The state of the system is assumed known at the first time step, while values for the externally applied forces are only known at the last time step, where they are assumed to be zero. The constrained optimisation problem is solved time step by time step using the sweep method of Brian and Ho (1970). An expression of the state of the system at step $n+1$ is written as a function of the state of the system at step $n$, and of external forces. The sweep method is then used to iterate backwards from time step to time step to compute 'gains' that relate the unknown external forces to the state of the system at each step. Finally, the state of the system is computed by forward iteration from step to step. This algorithm was used in Chapter 4 to estimate the load that acted on a vibrating damaged beam.

The second dynamic algorithm uses the Fourier transformation to solve the problem in the frequency domain. Dynamic equilibrium is enforced at each time step and the cost function, integrated over time, is minimised. Lagrange multipliers are again used to obtain a system of equations that can be solved, after transformation to the frequency domain, for each frequency. The time domain solution is found by superposition of the different frequency components. This method allows to treat linear dynamic systems with a large number of degrees of freedom. Chapters 11 and 12 utilises this method in their investigation of vortex induced forces on marine structures, while in Chapter 9 it is applied to detect damage in a four story steel model structure.

In setting up the cost function, a compromise must be found between the cost of deviating from measured displacements, and the cost of having non-zero external forces. When the cost of forces is too high, the estimate is over-regularised ("sluggish") with too small external forces and the estimated response following the measured response very loosely. When the cost of deviation from the response measurement is too high, the estimate is under-regularised ("jittery") with large forces calculated to squeeze the estimated

response into reproducing the measurement noise.

The theory allows for many types of measurements to be treated, including force-, displacement-, velocity-, acceleration- and strain measurements. Measurements can be arbitrarily distributed over the structure, and need not be taken at the nodes.

### 2.2.3 Mathematical model for static iFEM force- and response estimation

#### Equilibrium equations

From classical FEM, the equilibrium equations that describe a structure can be written as

$$\overline{\overline{\mathbf{K}}}.\overline{\mathbf{X}} = \overline{\mathbf{R}} \tag{2.1}$$

In Equation 2.1, $\overline{\overline{\mathbf{K}}}$ is the stiffness matrix of the structure. $\overline{\mathbf{X}}$ is the vector of nodal response values that allows describing the displacement as a function of the position $\overline{\xi}$ in the element, using chosen shape functions $\overline{\overline{\mathbf{N}}}(\overline{\xi})$, by stating that $\overline{\mathbf{x}}(\overline{\xi}) = \overline{\overline{\mathbf{N}}}(\overline{\xi}).\overline{\mathbf{X}}$. The nodal consistent forces are calculated as

$$\overline{\mathbf{R}} = \int_{\xi} \overline{\overline{\mathbf{N}}}(\overline{\xi}).\overline{\mathbf{f}}(\overline{\xi}) d\xi \tag{2.2}$$

with $\overline{\mathbf{f}}(\overline{\xi})$ being the force distribution over the element.

Unknown external forces are introduced in the inverse problem. To allow this, $\overline{\mathbf{f}}(\xi)$ can be written as

$$\overline{\mathbf{f}}(\overline{\xi}) = \overline{\mathbf{f}}_o(\overline{\xi}) + \overline{\mathbf{u}}(\overline{\xi}) \tag{2.3}$$

where $\overline{\mathbf{f}}_o(\overline{\xi})$ is the known part of the force distribution and $\overline{\mathbf{u}}(\overline{\xi})$ is the unknown externally applied force distribution. As was the case with the displacement distribution, the unknown force distribution can be described by nodal force coefficients $\overline{\mathbf{U}}$, using chosen shape functions $\overline{\overline{\mathbf{L}}}(\overline{\xi})$.

$$\overline{\mathbf{u}}(\overline{\xi}) = \overline{\overline{\mathbf{L}}}(\overline{\xi}).\overline{\mathbf{U}} \tag{2.4}$$

The $\overline{\mathbf{U}}$ degrees of freedom are the nodal values used to interpolate the distributed external force $\overline{\mathbf{u}}(\overline{\xi})$ over the element, just as nodal response values, $\overline{\overline{\mathbf{X}}}$, are used to interpolate the displacements $\overline{\mathbf{x}}(\overline{\xi})$ over the element. Note that $\overline{\mathbf{U}}$ are not consistent forces. The unit of translational $\overline{\mathbf{U}}$ degrees of freedom is $N.m^{-1}$, while the corresponding unit for the consistent forces ($\overline{\mathbf{R}}$ and $\overline{\overline{\mathbf{H}}}.\overline{\mathbf{U}}$) is $N$.

Substituting 2.3 and 2.4 into 2.2 yields the equilibrium equation

$$\overline{\overline{\mathbf{K}}}.\overline{\mathbf{X}} = \overline{\mathbf{R}} + \overline{\overline{\mathbf{H}}}.\overline{\mathbf{U}} \tag{2.5}$$

with $\overline{\overline{\mathbf{H}}} = \int \overline{\overline{\mathbf{N}}}(\overline{\xi}).\overline{\overline{\mathbf{L}}}(\overline{\xi})d\xi$.

The nodal forces now consist of a known part $\overline{\mathbf{R}}$, and an unknown part $\overline{\overline{\mathbf{H}}}.\overline{\mathbf{U}}$, where $\overline{\mathbf{U}}$ are the unknown force coefficients, and $\overline{\overline{\mathbf{H}}}$ transforms these coefficients into consistent forces. Thus, the unknowns in an iFEM problem are not only the response values $\overline{\mathbf{X}}$, but also the unknown external force coefficients $\overline{\mathbf{U}}$.

### The cost function

Measurements describing the response of a structure will be of limited precision, therefore one should not require that the estimate of the response reproduce them exactly. Also, a reasonable estimate of the external forces is seeked, not too far from an expected value. Squeezing the response, $\overline{\mathbf{X}}$, into better agreement with the measurements comes at the expense of increasing the forces $\overline{\mathbf{U}}$. Mathematically, this is expressed as a cost function that is to be minimised. The function is a second degree polynomial in $\overline{\mathbf{X}}$ and $\overline{\mathbf{U}}$ and contains matrices of cost coefficients.

$$J = \frac{1}{2}\begin{bmatrix}\overline{\mathbf{X}}\\ \overline{\mathbf{U}}\end{bmatrix}^T \cdot \begin{bmatrix}\overline{\overline{\mathbf{Q}}}_{xx} & \overline{\overline{\mathbf{Q}}}_{xu}\\ \overline{\overline{\mathbf{Q}}}_{xu}^T & \overline{\overline{\mathbf{Q}}}_{uu}\end{bmatrix} \cdot \begin{bmatrix}\overline{\mathbf{X}}\\ \overline{\mathbf{U}}\end{bmatrix} + \begin{bmatrix}\overline{\mathbf{Q}}_x\\ \overline{\mathbf{Q}}_u\end{bmatrix}^T \cdot \begin{bmatrix}\overline{\mathbf{X}}\\ \overline{\mathbf{U}}\end{bmatrix} \tag{2.6}$$

The coefficients in Equation 2.6 are calculated such that the cost associated with a measurement is

$$j = \frac{1}{2}\frac{(m - m_x)^2}{\beta_m} \tag{2.7}$$

where $m$ is the estimated response value, $m_x$ the measured value, and $\beta_m$ a Tikhonov regularisation parameter.

Each measurable quantity can be written as a linear function of the nodal response values $\overline{\mathbf{X}}$

$$m = \overline{\mathbf{A}}^T.\overline{\mathbf{X}} + B \tag{2.8}$$

Replacing 2.8 in 2.7 yields

$$j = \frac{1}{2}\overline{\mathbf{X}}^T.\overline{\overline{\mathbf{Q}}}_{xx}.\overline{\mathbf{X}} + \overline{\mathbf{Q}}_x.\overline{\mathbf{X}} \tag{2.9}$$

with $\overline{\overline{\mathbf{Q}}}_{xx} = \frac{1}{\beta_m}\overline{\mathbf{A}}\overline{\mathbf{A}}^T$ and $\overline{\mathbf{Q}}_x = \frac{m_x - B}{\beta_m}\overline{\mathbf{A}}$.

The cost assigned to non-zero values of $\overline{\mathbf{u}}(\overline{\xi})$ can be taken as

$$j = \int \frac{1}{2}\overline{\mathbf{u}}(\overline{\xi})^T.\overline{\overline{\mathbf{q}}}_{uu}.\overline{\mathbf{u}}(\overline{\xi})d\xi \tag{2.10}$$

where $\overline{\overline{\mathbf{q}}}_{uu}$ is a symmetric matrix containing a Tikhonov parameter for each force field $\overline{\mathbf{u}}(\overline{\xi})$. Large values in $\overline{\overline{\mathbf{q}}}_{uu}$ would correspond to a low probability for non-zero forces, while small values would correspond to a high probability.

Inserting 2.4 into 2.10 yields

$$j = \frac{1}{2}\overline{\mathbf{U}}^T.\overline{\overline{\mathbf{Q}}}_{uu}.\overline{\mathbf{U}} + \overline{\mathbf{Q}}_u.\overline{\mathbf{U}} \tag{2.11}$$

with $\overline{\overline{\mathbf{Q}}}_{uu} = \int \overline{\overline{\mathbf{L}}}(\overline{\xi})^T.\overline{\overline{\mathbf{q}}}_{uu}.\overline{\overline{\mathbf{L}}}(\overline{\xi})d\xi$ and, assuming that the unknown force has a mean value of zero (assuming it equally probable that the unknown forces be positive or negative), $\overline{\mathbf{Q}}_u = \overline{0}$.

When the probability of externally applied force are independent of the response values, $\overline{\overline{\mathbf{Q}}}_{xu} = \overline{\overline{0}}$.

**Choice of Cost** As shown above, the calculation of the cost coefficients matrices $\overline{\overline{\mathbf{Q}}}_{xx}$ and $\overline{\overline{\mathbf{Q}}}_{uu}$ make use of user defined Tikhonov regularisation parameters. For a given problem, the choice of the relative magnitude of Tikhonov parameters affects the character of

the solution: If $\overline{\overline{\mathbf{Q}}}_{xx}$ is high, the iFEM solution will only have small differences between measured and estimated strain. There will correspondingly be large external loads to force the structure into the measured pattern (which contains measurement noise). Such an under-regularised ("jittery") solution is highly sensitive to the measurement errors, and would be referred to by statisticians as a *high variance estimator*. Alternatively, if $\overline{\overline{\mathbf{Q}}}_{uu}$ is high, the iFEM solution will only have small external loads, and the estimated strains will correspondingly only be weakly related to the measured ones. Such an over-regularised ("sluggish") solution tends to ignore the measured response, and is a *biased estimator*. Experience shows that, if the measurement data is adequate, a range of ratios for $\overline{\overline{\mathbf{Q}}}_{xx}$ and $\overline{\overline{\mathbf{Q}}}_{uu}$ exists, over which the iFEM solution does not change significantly and is of good quality. A direct transition from high variance to biased estimates is a sign that the measurement data is inadequate: There are too few sensors, the sensors are ill-placed, the sensors are not of the right type, or the measurement precision is too low.

When choosing Tikhonov parameters for a given analysis, the user is required to observe the character of the analysis output and adjust the Tikhonov parameters accordingly, so that a stable solution somewhere between under-regularised ("jittery") and over-regularised ("sluggish") behaviour is obtained. This way of choosing costs is subjective. Nevertheless, Tikhonov Regularisation have been applied successfully in heat transfer problems, where a similar kind of quadratic cost function is to be minimised.

A Bayesian theory was developed to aid the user in the choice of Tikhonov parameters based on prior knowledge of measurement precision and probable forces. Surprisingly, this theory did not work and was discarded. A theory that would allow the objective choice of cost parameters would be valuable.

### Constrained optimisation

Introducing an augmented Lagrangian allows for Equation 2.6 to be minimised while the set of conditions $\overline{\mathbf{F}}(\overline{\mathbf{X}}, \overline{\mathbf{U}}) = \overline{\mathbf{0}}$ (Equation 2.5) is respected. This is achieved by requiring that the derivatives of the augmented Lagrangian, $J' = J + \overline{\lambda}^T.(\overline{\overline{\mathbf{K}}}.\overline{\mathbf{X}} - \overline{\mathbf{R}} - \overline{\overline{\mathbf{H}}}.\overline{\mathbf{U}})$, equal

zero for gradients taken with respect to $\overline{\mathbf{X}}$, $\overline{\mathbf{U}}$ and $\overline{\lambda}$. Using the symmetry of $\overline{\overline{\mathbf{Q}}}_{xx}$ and $\overline{\overline{\mathbf{Q}}}_{uu}$, this yields Equations 2.5, 2.12 and 2.13 respectively:

$$\lambda.\nabla_{\mathbf{X}}\mathbf{F} + \nabla_{\mathbf{X}}\mathbf{J} = \overline{\overline{\mathbf{K}}}^{\mathbf{T}}.\overline{\lambda} + \overline{\overline{\mathbf{Q}}}_{\mathbf{xx}}.\overline{\mathbf{X}} + \overline{\overline{\mathbf{Q}}}_{\mathbf{xu}}.\overline{\mathbf{U}} + \overline{\mathbf{Q}}_{\mathbf{x}} = \overline{\mathbf{0}} \tag{2.12}$$

$$\lambda.\nabla_{\mathbf{U}}\mathbf{F} + \nabla_{\mathbf{U}}\mathbf{J} = \overline{\overline{\mathbf{H}}}^{\mathbf{T}}.\overline{\lambda} + \overline{\overline{\mathbf{Q}}}_{\mathbf{uu}}.\overline{\mathbf{U}} + \overline{\overline{\mathbf{Q}}}^{\mathbf{T}}_{\mathbf{xu}}.\overline{\mathbf{X}} + \overline{\mathbf{Q}}_{\mathbf{u}} = \overline{\mathbf{0}} \tag{2.13}$$

The above two equations, together with Equation 2.5, can be written in matrix form

$$\begin{bmatrix} \overline{\overline{\mathbf{0}}} & \overline{\overline{\mathbf{K}}} & -\overline{\overline{\mathbf{H}}} \\ \overline{\overline{\mathbf{K}}}^{T} & \overline{\overline{\mathbf{Q}}}_{xx} & \overline{\overline{\mathbf{Q}}}_{xu} \\ -\overline{\overline{\mathbf{H}}}^{T} & \overline{\overline{\mathbf{Q}}}^{T}_{xu} & \overline{\overline{\mathbf{Q}}}_{uu} \end{bmatrix} \cdot \begin{bmatrix} \overline{\lambda} \\ \overline{\mathbf{X}} \\ \overline{\mathbf{U}} \end{bmatrix} = \begin{bmatrix} \overline{\mathbf{R}} \\ -\overline{\mathbf{Q}}_{x} \\ -\overline{\mathbf{Q}}_{u} \end{bmatrix} \tag{2.14}$$

The matrices $\overline{\overline{\mathbf{K}}}$, $\overline{\overline{\mathbf{H}}}$, $\overline{\overline{\mathbf{Q}}}_{xx}$, etc. and vectors $\overline{\mathbf{R}}$, $\overline{\mathbf{Q}}_{x}$, etc. are found for each element and assembled in the usual way. Solving the system of equations 2.14 then allows obtaining estimates for $\overline{\mathbf{X}}$ and $\overline{\mathbf{U}}$.

### 2.2.4 Sources of error

#### Systematic biases

iFEM estimates exhibit some systematic biases: For the same total force, a distributed force has a lower associated cost than a point load. For this reason, forces tend to be spread unless necessary to match measurements. For similar reasons, force distributions will generally be continuous. An unknown force acting at a support will cause no response. This force does not influence estimated strains, and will therefor be estimated as zero, since this yields the lowest cost.

## 2.3 The prototype iFEM software Safran

SAFRAN is a MATLAB implementation of the iFEM algorithms in a relatively versatile demonstration software, written in order to test and develop iFEM algorithms. Static and dynamic iFEM algorithms are included, allowing linear or non-linear static analyses

as well as linear dynamic analyses to be carried out. The program also allows standard FEM analyses, including linear and non-linear static FEM algorithms and linear and non-linear dynamic FEM algorithms. At present only two-dimensional frame elements can be modelled, but new element types can be added to the element library of SAFRAN.

### 2.3.1 Input

As input the structural model must be given, including element types, support conditions as well as stiffness, damping and mass properties. By default, elements are rigidly connected; where a hinged connection is desired, this must be indicated.

The unknown load model must also be specified. The load model allows the user to describe the unknown external forces. For frame elements, the distributed external forces are interpolated, using the $\overline{\mathbf{U}}$ degrees of freedom, by the same shape functions that are used to interpolate the displacement within the element. Where no forces are expected, the $\overline{\mathbf{U}}$ degrees of freedom can be constrained away. At positions where an unknown point load needs to be estimated, a point load element can be used. A point load element has only one node, on which six $\overline{\mathbf{U}}$ degrees of freedom exist, referring to the three orthogonal components of the point load ($U_x$, $U_y$ and $U_z$) and moment ($U_{rx}$, $U_{ry}$ and $U_{rz}$) at that position.

Available response and force measurement values from the real structure are also given as input, including the time, position, type and precision of each measurement. Measurement types that can be handled by SAFRAN at present are displacement-, acceleration- and strain measurements.

The type of analysis required must also be indicated, specifying all relevant parameters, such as convergence criteria for non-linear analyses.

### 2.3.2 Output

The output of an iFEM analysis is external force estimates and a complete description of the response of the modelled system over time. The output is graphically represented, but results are also available in numerical form, if requested. The force estimation would comply with the user's load model in that forces will only be calculated where $\overline{\mathbf{U}}$ degrees of freedom were allowed.

SAFRAN's graphical output uses the following conventions: The structure, with its modelled elements and nodes, is plotted in black. The axis of graphs indicate vertical and horisontal position in meters. Point loads are represented as arrows, while curves describe distributed loads. Known loads are plotted in blue, and estimated external forces are plotted in red. In future developments, model parameters $\alpha$ are introduced and estimated model parameters are plotted in green. The calculated $\alpha$ value for each element is graphically represented by a green line, drawn next to the element at a distance proportional to the value of the $\alpha$. If an element is defined from left to right, a negative $\alpha$ will be drawn below the element and a positive $\alpha$ above the element.

# Part II

# Investigating the influence of errors in the structural model on the output of iFEM

# Chapter 3

# Influence of model error on static iFEM analysis

## 3.1 Introduction

In this chapter an empirical approach is followed to investigate the sensitivity of static iFEM to model errors. An analytical approach was attempted, resulting in complicated expressions that do not provide insight. The analytical developments are hence reported in Appendix A.

There can be various reasons for distributed model errors being present in an iFEM analysis. Besides gross errors, sources of uncertainties include for example the survey of the geometry of the structure, the stiffness of cracked concrete, the stiffness of steel connections, the mass of equipment carried by a structure, and the mechanical properties of foundations.

In this chapter three different frame structures are used as static test cases to study the behaviour of iFEM when errors are present in the model that describes the structure. Both distributed errors, such as incorrect section properties for some structural elements, and localised error, such as a loose connection, are considered.

The influence of modelling errors was investigated as follows: Measurement data was simulated by creating a FEM model of the structure considered, computing deflection values and adding adequate noise to them, in order to obtain the imperfect "measurements". The "measurement" accuracy could be manipulated by changing the amount of noise added. Errors were then added to the exact FEM model to obtain the inaccurate iFEM model. The FEM model would be the model of the actual structure, which might be damaged. In such a case, the iFEM model would be inaccurate if it does not account for the damaged state of the actual structure (FEM model).

In this chapter a few examples are discussed, with corresponding figures of the iFEM assessed external loads, that illustrate the behaviour of iFEM for frame structures, when modelling errors are present.

## 3.2 Description of test case frame structures and the base analysis concept

Three different frame structures used to study model sensitivity are described below.

The response of a structure is described by measurements at a finite number of points on the structure. Because it uses this limited data, iFEM does not reproduce FEM loads even if the model is perfect and no measurement error is present. An iFEM analysis with an accurate model will be referred to as the *base analysis*. In the following sections of this chapter, errors will be introduced into the iFEM model, causing the FEM and iFEM models not to be identical. The resulting assessed external loads of such cases are then compared to the assessed external loads of these base analyses to investigate the effect of the model error.

In all the analyses, a Gaussian distribution is assumed for the measurements (Refer to Chapter 2, Equations 2.7 to 2.11). The cost associated with a measurement was taken

to be proportional to $(\frac{1}{\sigma_x^2})$, where $\sigma_x$ is the standard deviation of the measurement. The more precise measurements are, the lower the standard deviation would be, and the higher the cost associated with deviating from the measurement. Likewise, the cost associated with external forces should be taken as proportional to $(\frac{1}{\sigma_u^2})$, where $\sigma_u$ is the standard deviation of the external force. Since the external forces are unknown, and a value for its standard deviation not always available, an engineering estimate of the standard deviation of the external forces is used. Under-regularised or over-regularised behaviour (cf. Chapter 2, Section 2.2.4) will indicate whether the cost associated with external forces is inappropriate, and the cost can be adjusted accordingly.

### 3.2.1 Frame structure

The first test case is a frame structure commonly found as part of industrial buildings. Figure 3.1 shows the FEM model and the applied load that was used to generate measurement data. Figure 3.2 and Figure 3.3 give graphical representations of the assessed external loads when a model identical to the FEM model is used in the iFEM analyses. The load model of Figure 3.2 allows distributed unknown forces only on the lower members of the roof, while the load model of Figure 3.3 allows distributed unknown forces on all roof element members. Vertical and horisontal displacement measurements were taken along the entire span at every third node of the lower roof elements. These measurements were used for all instances of test case 1, unless otherwise indicated.

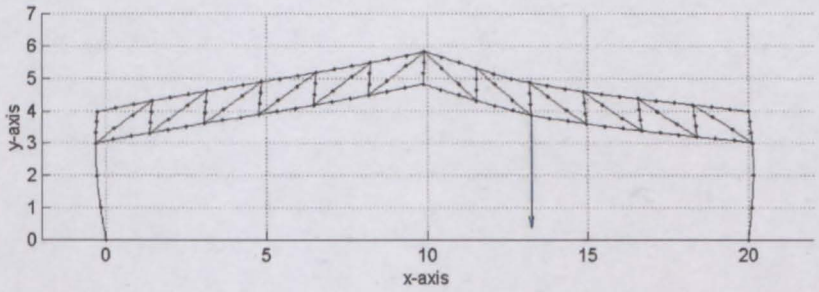


**Figure 3.1:** *FEM model for test case 1*

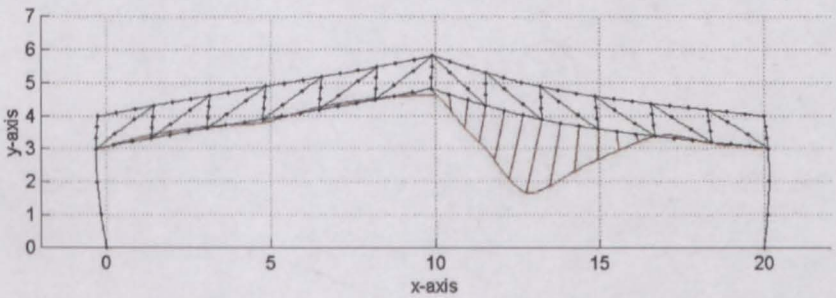


**Figure 3.2:** *Base iFEM analysis for test case 1, when forces are only allowed on the lower roof elements*

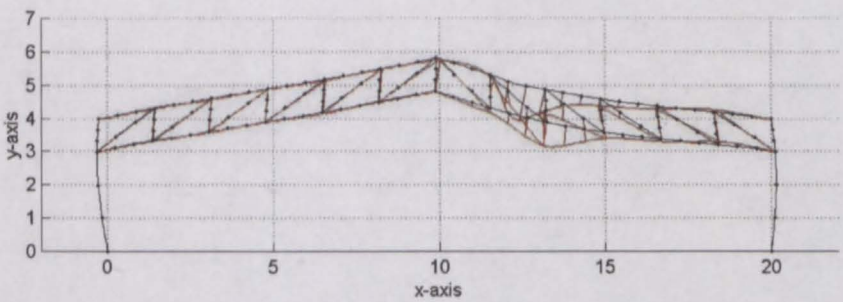


**Figure 3.3:** *Base iFEM analysis for test case 1, when forces are allowed on all roof elements*

### 3.2.2 Crane structure

The second test case is a simplified version of a crane structure. Figure 3.4 shows the FEM model and the applied load that was used to generate measurement data. Figure 3.5(a) and Figure 3.5(b) give graphical representations of the assessed external loads when a model identical to the FEM model is used in the iFEM analyses. The load model of Figure 3.5(a) allows distributed unknown forces only on the lower members of the crane-arm, while the load model of Figure 3.5(b) allows distributed unknown forces on all element members. Vertical and horisontal displacement measurements were taken at six points, one at every third node of the lower crane-arm elements. These measurements were used for all instances of test case 2, unless otherwise indicated.

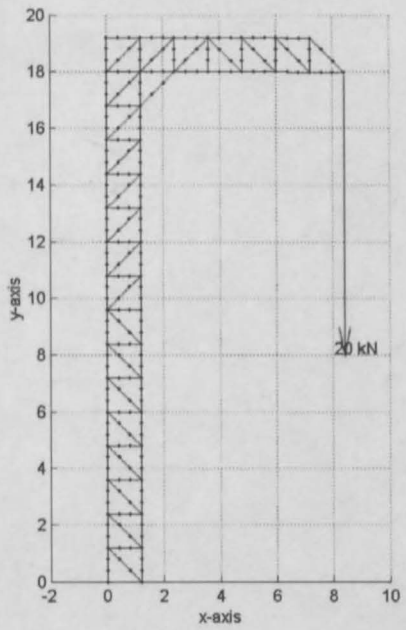


**Figure 3.4:** *FEM model for test case 2*

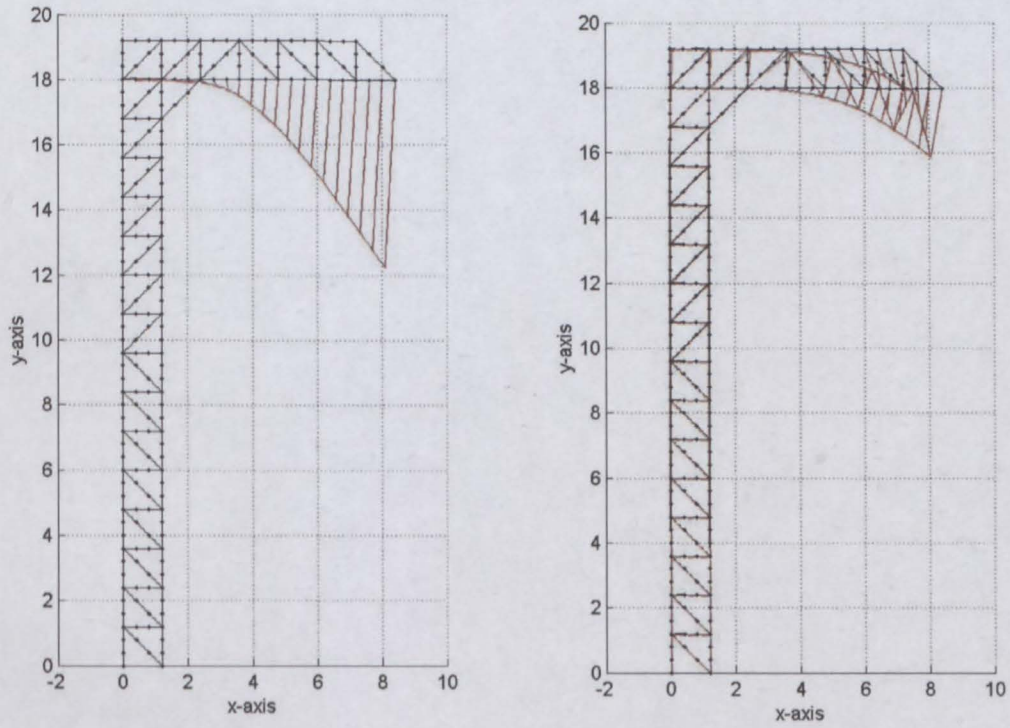


**Figure 3.5:** *Base iFEM analyses for test case 2*

### 3.2.3 Bridge structure

The third test case is a cantilever bridge structure. Figure 3.6 shows the FEM model and the applied load that was used to generate measurement data. Figure 3.7 gives a graphical representation of the assessed external loads when a model identical to the FEM model is used in the iFEM analyses. The load model allows distributed unknown forces only on the bridge deck members. Vertical displacement measurements were taken from all deck members, midway between nodes. These measurements were used for all instances of test case 3, unless otherwise indicated.

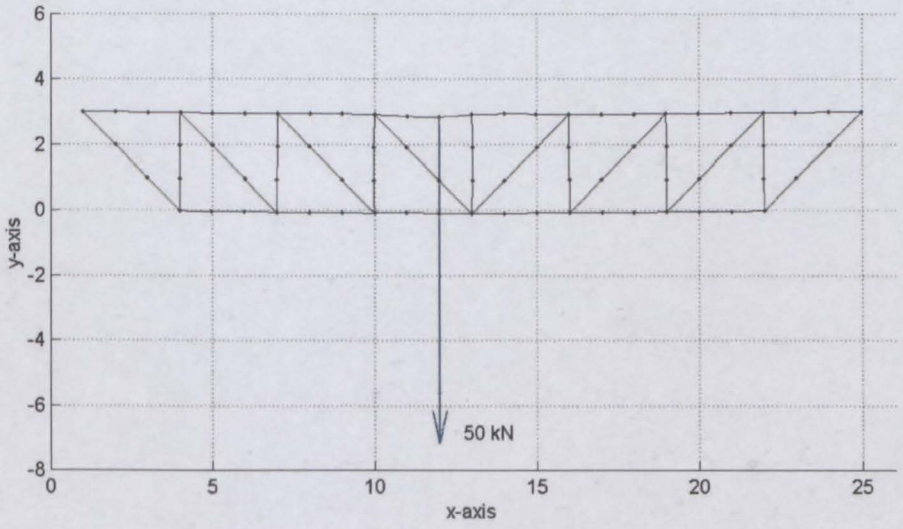


**Figure 3.6:** *FEM model for test case 3*

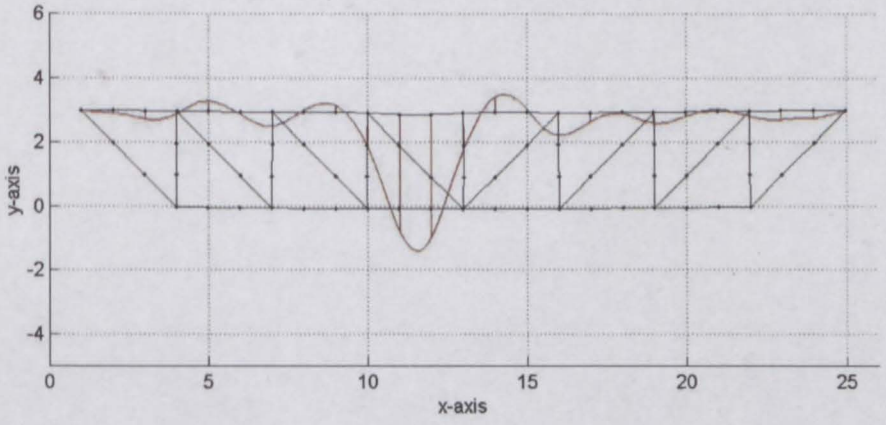


**Figure 3.7:** *Base iFEM analysis for test case 3*

## 3.3 Effect of distributed model error

Figure 3.9 shows the assessed external loads for test case 1, when the iFEM model underestimates the section properties of all the roof elements. The FEM model used to generate measurement data thus had "stiffer" roof elements. The "weaker" iFEM model now needs less externally applied load to deform into the measured shape, and the externally applied loads are under-estimated as can be clearly seen when Figure 3.9 is compared to Figure 3.2, reproduced for convenience as Figure 3.8.

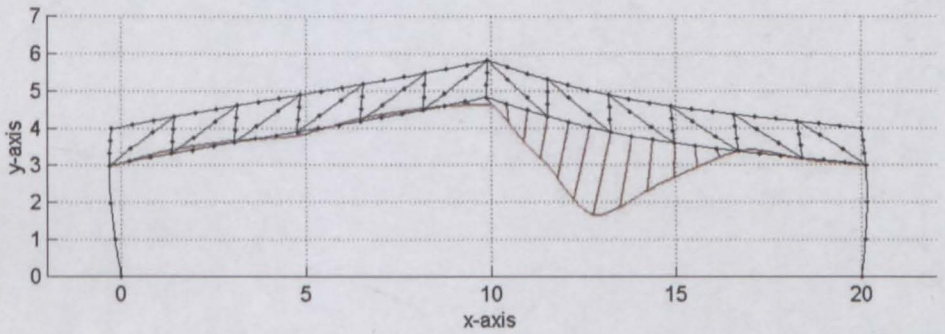


**Figure 3.8:** *Base iFEM analysis for test case 1*

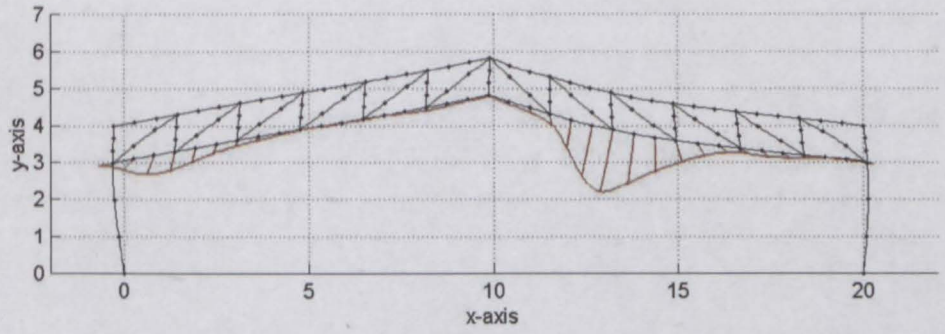


**Figure 3.9:** *iFEM analysis for test case 1, where the iFEM model underestimated the stiffness of all roof elements in the real (FEM) structure.*

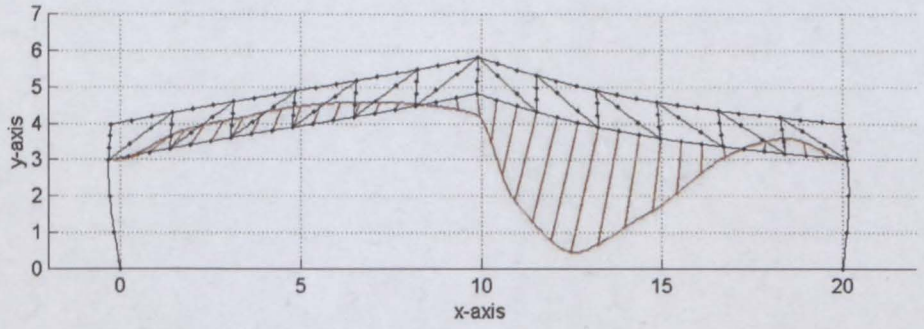


**Figure 3.10:** *iFEM analysis for test case 1, where the iFEM model overestimated the stiffness of all roof elements in the real (FEM) structure.*

Figure 3.10 shows the assessed external loads for test case 1 (The frame structure), where the iFEM model overestimates the section properties of all the roof elements. Accordingly, the externally applied loads are overestimated as can be clearly seen when Figure 3.10 is compared to Figure 3.8.

Test case 2 (The crane structure) and test case 3 (The bridge structure) show similar behaviours. When the iFEM model's stiffness for all the column members are lowered in test case 2, Figure 3.12(a) is the result. Again, the applied load is underestimated, when Figure 3.12(a) is compared to Figure 3.11. For test case 3, the stiffness of the deck elements were lowered, resulting in the applied load being underestimated, as can be seen in Figure 3.14, when compared to Figure 3.13. When the section properties for these two test cases are overestimated, the applied loads are also overestimated. This is obvious when Figure 3.12(b) is compared to Figure 3.11 and when Figure 3.15 is compared to Figure 3.13.

When comparing the figures from test case 1, it can be seen that, for the base analysis, the distributed forces estimated on the left side of the roof are small, whereas significant distributed forces do appear on this part of the roof when errors are introduced in the model. In the case where the iFEM model had overestimated section properties for the

roof elements, the distributed forces estimated on the left side of the roof tend to push that side of the roof upwards (Figure 3.10). This is so because the stiffer structure of the inaccurate iFEM model will tend to distribute the deflection, caused by the point load on the right side of the roof, more than the less stiff structure of the FEM model did. External forces are then calculated on the left side to push that part of the roof upwards to match the measured deflection values.

In the case where the iFEM model had underestimated section properties for the roof elements, the distributed forces estimated on the left side of the roof tend to pull that side of the roof downwards (Figure 3.9). This is so because the more flexible structure of the inaccurate iFEM model will tend to deflect locally, in the area of the point load on the right side of the roof, without causing much deflection on the left side of the roof. External forces are then calculated on the left side to pull that part of the roof down to match the measured deflection values from the stiffer FEM model. Thus, the forces that appear on the left side of the roof are an indication of an inaccurate model.

Test case 2 (The crane structure) shows similar behaviour. In the case where the iFEM model overestimated the section properties of the column members (Figure 3.12(b)), the predicted externally applied forces are not only larger, but also tend to pull the structure to the right, compared to the forces calculated for the base analysis (Figure 3.5(a), reproduced here as Figure 3.11). The inaccurate iFEM model is less flexible than the FEM model and the eccentric point load, which caused the FEM model to bend over to the right, will not cause the less flexible iFEM model to bend over as far. The external forces tend to pull the less flexible iFEM structure to the right to match the measured horisontal deflection values taken from the more flexible FEM structure.

In the case where the iFEM model underestimated the section properties of the column members (Figure 3.12(a)), the predicted externally applied forces tend to pull more to the left, compared to the case for the base analysis. The inaccurate iFEM model is more flexible than the FEM model and the eccentric point load, which caused the FEM

model to bend over to the right, will cause the more flexible iFEM model to bend over even further. The external forces tend to push the more flexible iFEM structure to the left, in order to ensure that the deflections match the measured values. The forces pushing to the left are not very pronounced, because the more flexible iFEM structure needs less vertically applied force to match the measured vertical deflection, and accordingly the moment caused by the eccentricity of the load is smaller, and the structure bends over less.

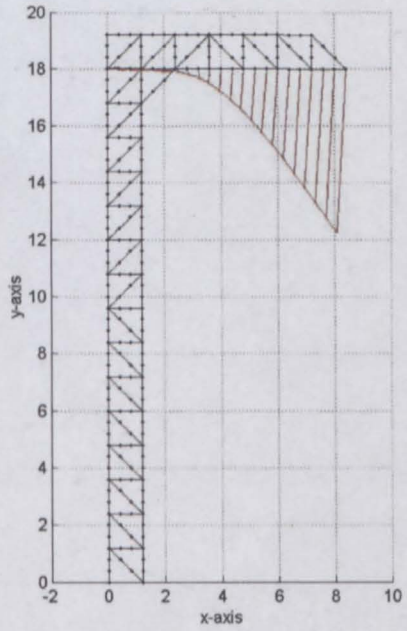


**Figure 3.11:** *Base iFEM analysis for test case 2*

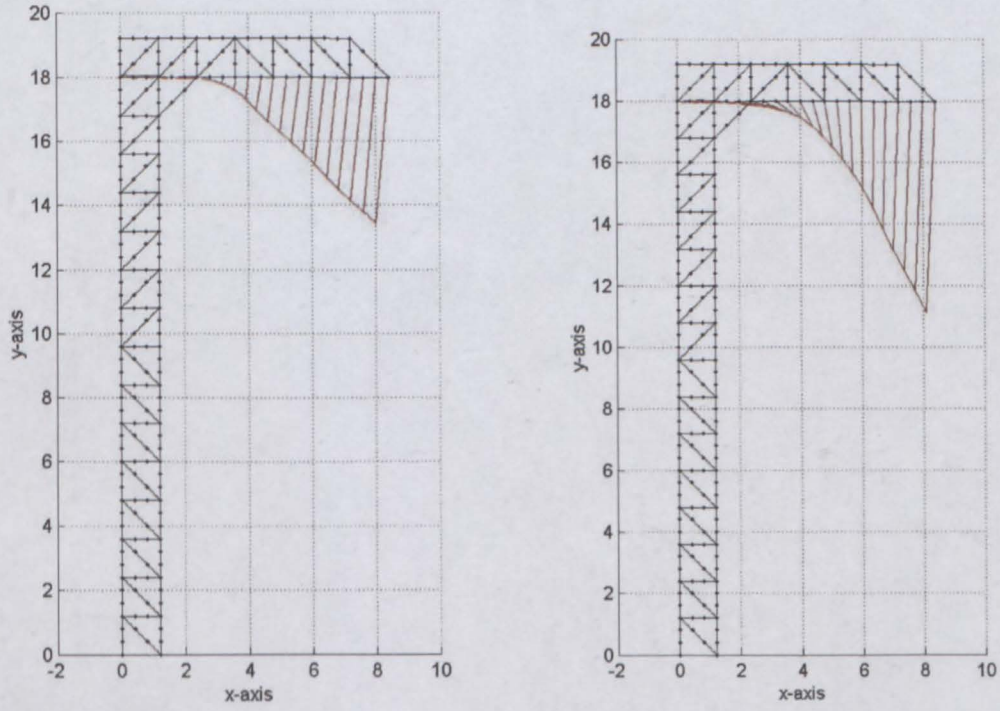


(a) *iFEM analysis for test case 2, where the iFEM model underestimated the stiffness of all column elements in the actual (FEM) structure.*

(b) *iFEM analysis for test case 2, where the iFEM model overestimated the stiffness of all column elements in the actual (FEM) structure.*

**Figure 3.12:** *iFEM analyses for test case 2*

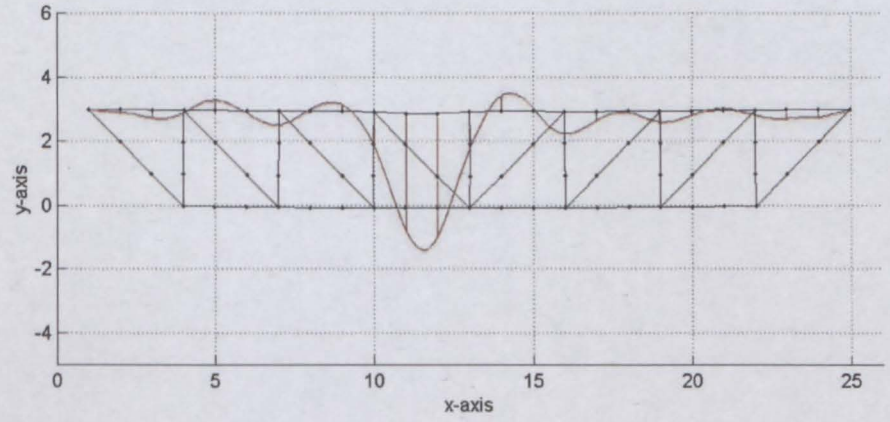


**Figure 3.13:** *Base iFEM analysis for test case 3*

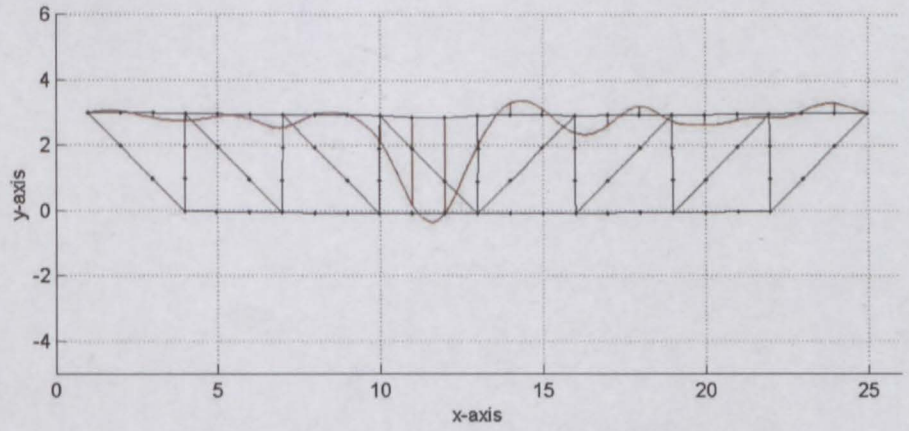


**Figure 3.14:** *iFEM analysis for test case 3, where the iFEM model underestimated the stiffness of all deck elements of the actual (FEM) structure.*

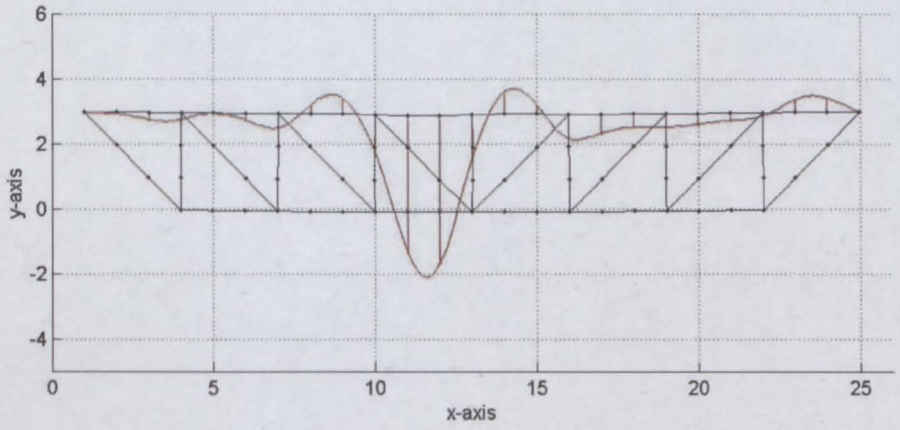


**Figure 3.15:** *iFEM analysis for test case 3, where the iFEM model overestimated the stiffness of all deck elements of the actual (FEM) structure.*

The above examples also show that iFEM gives credible results in the presence of a model with distributed error, and such an incorrect model can easily go undetected. The result will be that externally applied forces are under- or overestimated, depending on the nature of the modelling error. If the error tends to weaken the modelled structure, compared to the actual, measured one, iFEM will tend to underestimate applied forces, and the other way around.

### 3.3.1 Relation between model error and error in estimated force.

Investigation of the iFEM responses of the previous section showed that a linear correlation exists between model error and error in the estimated forces, so that a 10% error in the stiffness matrix $K$, will result in a 10% error in the total estimated force value. This correlation ceases to exist when the iFEM model error is reducing the stiffness of the structure by a large percentage, because buckling behaviour will then set in. Results from test case 1 are given in tabular form. The first column shows the percentage error that was introduced in the material stiffness, $E$, of the iFEM model. The second column gives the value of the total estimated force, as computed by integrating the distributed force estimation along the length of the elements. Five tests were conducted for each level of model error and the average estimated force is used. The third column gives the percentage over- or underestimation of the total estimated force, as compared to the estimated force from the base analysis (0% error).

| Model error in E (%) | Total estimated force ($kN$) | Force overestimation (%) |
|---|---|---|
| −20 | 612 | −19.7 |
| −10 | 686 | −9.9 |
| 0 | 762 | 0 |
| 10 | 837 | 9.8 |
| 20 | 916 | 20.2 |
| 30 | 983 | 29 |
| 40 | 1063 | 39.5 |
| 50 | 1141 | 49.7 |

**Table 3.1:** *Correlation of model error in E with error in estimated force.*

## 3.4 Effect of localised model error

Besides distributed errors in setting up the model, one important source of local modelling error would be the presence of hidden local defects in a structure. This can for example be a cracked weld, cracks in masonry, corrosion, a loose bolt, etc. Such a defect will influence the way in which a structure responds when loaded. If measurements taken on this structure, with its undetected defect, are used in an iFEM analysis to compute the forces that caused these deflections, the iFEM model will not account for the presence of the defect. How does this local model error influence output?

The frame structures of section 3.2 are used to demonstrate the effect of localised model errors in terms of the assessed external loads.

In each test case, a connection in the FEM model (the "actual structure"), was loosened. Each time, this loosened connection is indicated as Point A. The iFEM models do not account for loose connections, resulting in unphysical external forces in order to get the iFEM estimate to corroborate the measurement data. These are refered to as ghost forces[1]. Note that a correct model in this case is the model that accounts for the defect.

Figure 3.16 shows the assessed external loads for test case 1, with ghost forces in the area of the defect. The iFEM structure must deflect according to measurements that were taken on a structure where the diagonal element at point A was effectively missing. This element was not carrying any element forces, because of the loose connection, and the structure deflected accordingly with a visible kink in the area of the defect. The ghost forces allow the iFEM estimate to follow this strange kink in the presence of a now fully load bearing diagonal member. This is a non-linear analysis, allowing buckling behaviour

[1]When a structure is poorly represented by the chosen iFEM model, unphysical external forces are calculated in order to get the iFEM estimate to corroborate the measurement data. In the following, such forces are refered to as "ghost forces". In cases where no external forces can occur, the ghost forces are easily identified.

to be described, and it is interesting to note that some of the iFEM calculated ghost forces initiate the buckling of the member that is supposed to have a loose connection.

Figure 3.17 shows the estimated external loads for test case 2. Ghost forces again clearly indicate the presence of a defect. The same can be said for test case 3, where Figure 3.18 shows how large ghost forces coerce the bridge structure towards the measured deflection pattern.

The above three examples clearly indicate that, if measurements are adequate in precision, placement, type and number, to describe the effect of a defect on the response of the real structure, iFEM detects the presence and location of that defect by means of ghost forces.

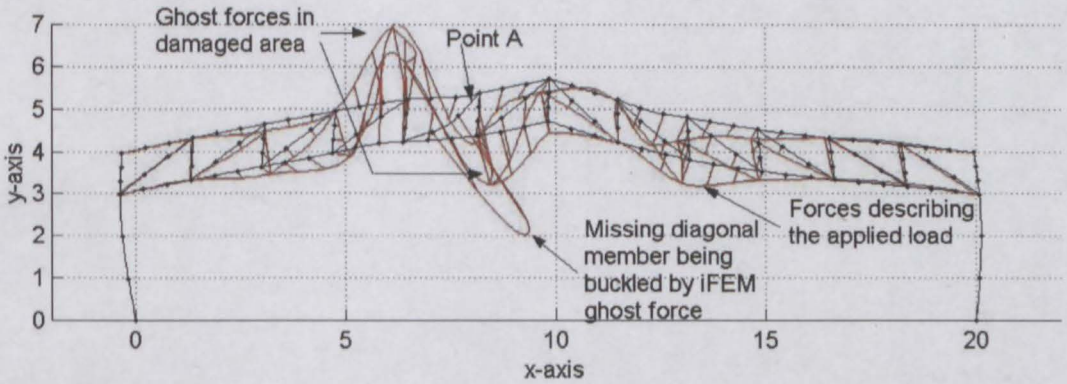


**Figure 3.16:** *iFEM analysis of test case 1, where the actual (FEM) structure has a loose connection at point A, which is not accounted for in the iFEM model.*

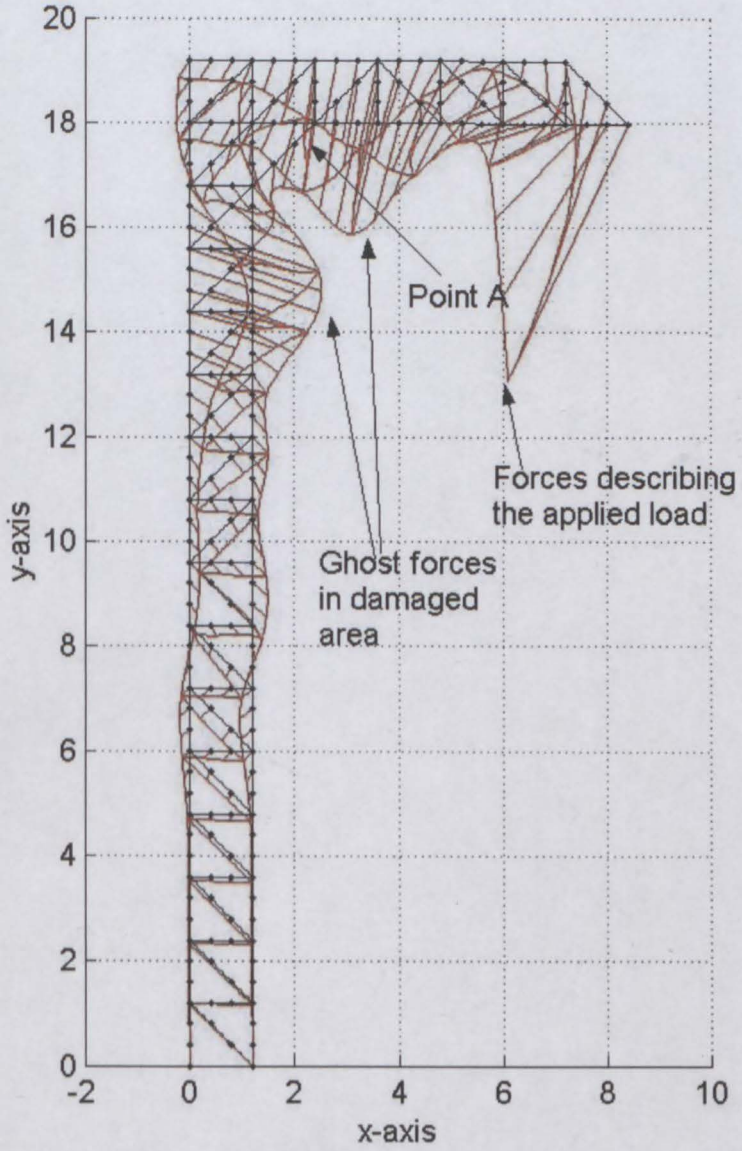


**Figure 3.17:** *iFEM analysis of test case 2, where the actual (FEM) structure has a loose connection at point A, which is not accounted for in the iFEM model.*

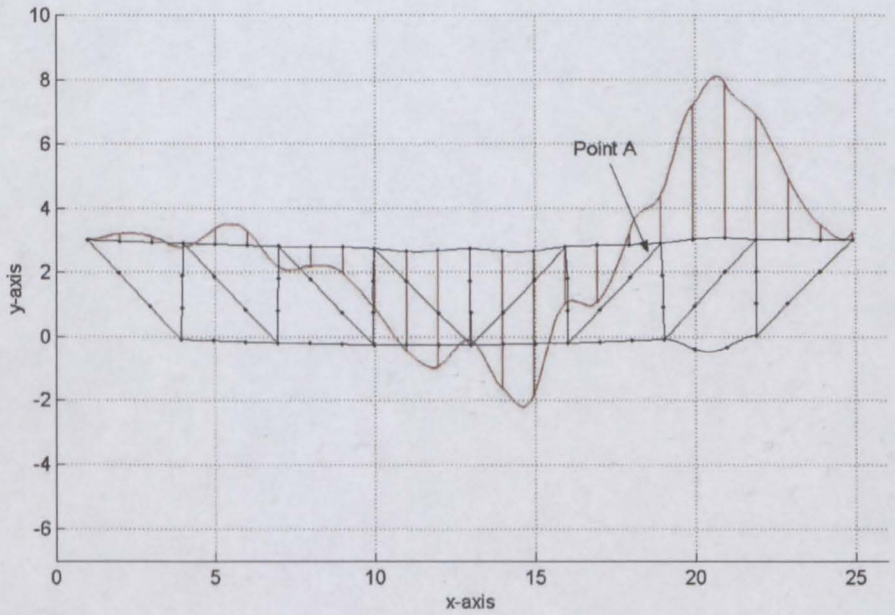


**Figure 3.18:** *iFEM analysis of test case 3, where the actual (FEM) structure has a loose connection at point A, which is not accounted for in the iFEM model.*

### 3.4.1 Influence of measurement precision and placement

The effect of measurement precision and placement is now investigated. The only way knowledge can be gained on the presence of defects in a structure, using iFEM, is indirectly by means of the measurements taken on the structure. If measurements are not adequate to describe the effect of the defect on the response of the real structure, iFEM will not indicate the presence of such a defect by means of ghost forces and the defect will go undetected. Two examples of such cases are discussed, the first being a case where the number of measurements, or their placement, was inadequate. In the second example the defect again goes undetected, this time because measurement precision was inadequate.

Figure 3.19 shows the iFEM output of test case 1 in the presence of a defect, but with measurements only taken on the right hand side of the roof. (Previously measurements were taken along the entire span of the roof.) These measurements are inadequate to describe the effect of the defect, which is mainly seen in the deflections of the left side of the roof. In the iFEM analysis, the structure does not deflect to match the kink in the area of the defect, since no measurement data indicated that there should be a kink, and accordingly no give-away ghost forces appear in the area of the defect.

Figure 3.20 shows a case where the measurement precision was inadequate to describe the effect of the defect. The lower measurement precision was simulated by adding more noise to the simulated deflection data to obtain more noisy "measurements". In such a case the ghost forces resulting from the presence of a defect can not be distinguished clearly from the forces resulting from poor measurement precision, or very few ghost forces appear, due to the poor description of the effect of the defect on the response of the structure.

The above two cases indicate that the number, placement and precision of measurement sensors can have a significant influence on the iFEM estimate. Questions that need further attention concern the effect of the number and position of measurements taken and the precision and type of the measurement sensors used. How many measurements

are enough and where must they be placed to ensure that damage is detected? What measurement precision is required to adequately describe the response of a structure? Such an investigation is not a goal of this work, but these questions should be addressed in future research.

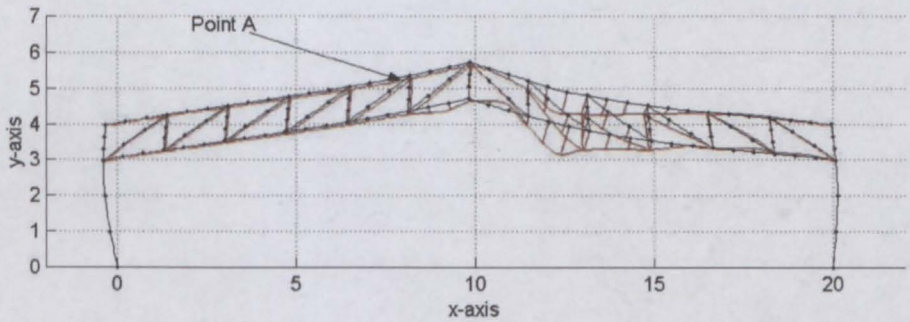


**Figure 3.19:** *iFEM analysis of test case 1, in the presence of a defect, with an inadequate number of measurements being taken when generating measurement data.*

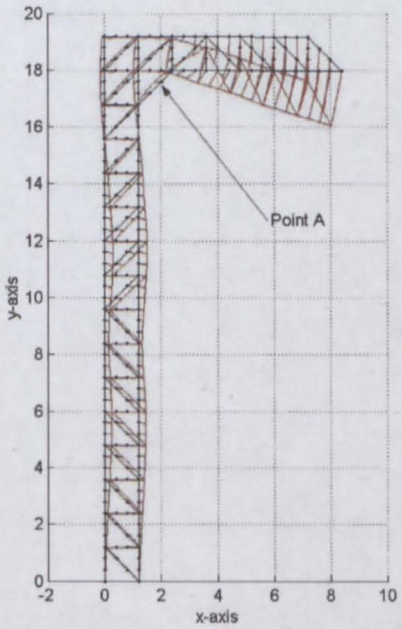


**Figure 3.20:** *iFEM analysis of test case 2, in the presence of a defect, with inadequate measurement precision being used when generating measurement data.*

## 3.5 Conclusions

Based on the limited empirical study of this chapter, it is postulated that

1. iFEM is stable with respect to model errors, meaning that an inaccurate structural model usually does not cause numerical difficulties (such as ill-conditioned matrices or diverging Newton-Raphson iterations), and iFEM gives useable results in spite of such inaccurate models. Thus, assuming that appropriate costs are associated to deviation from measurements and deviation from expected load values, iFEM can be used to process physical measurement data. The combination of inaccurate response measurement and inaccurate model description does not cause iFEM to become unstable. However, buckling behaviour can sometimes cause problems.

2. Model errors cause the appearance of unphysical forces, referred to as *ghost forces*.

3. Distributed modelling errors cause distributed ghost forces that can easily go undetected. The behaviour of the structure does not appear unphysical and the estimated external forces appear to be reasonable. The loads are under- or over-estimated depending on the type of error. If the error reduces the stiffness of the modeled structure, compared to the actual, measured one, iFEM will tend to under-estimate applied forces, and the other way around.

4. A linear relation exists between model error and the resulting error in the estimated force value.

5. Local damage causes localised ghost forces in the area of the defect if measurements are adequate in precision, position, type and number to describe the influence of the defect on the response of the structure.

6. An attempt was made to derive an analytical sensitivity formula, but this resulted in complicated expressions that do not provide insight. The mathematical development is reported in Appendix A.

7. Questions that need further attention concern the effect of the number and position of measurements taken and the precision of the measurements. How many measure-

ments are enough and where must they be placed to ensure that damage is detected? What measurement precision is required to adequately describe the response of a structure?

8. This chapter showed the potential of iFEM for damage detection. In this chapter, although only one load case is considered, the ghost forces identify the defects. This finding inspired the research reported in chapter 7, where a theory is described that allows using several experiments in order to accumulate information on the response, allowing a better basis for damage detection.

# Chapter 4

# Influence of model error on dynamic iFEM analysis

## 4.1 Introduction

Experiments on a damaged beam were conducted to study the behaviour of dynamic iFEM in the presence of modelling error. Acceleration measurements were gathered from the vibrating beam. The impact force that caused the beam to vibrate was also measured. Subsequently iFEM analyses were carried out, using the acceleration measurement data with various iFEM models. In this chapter, the predicted loads are compared to the measured ones. The performance of iFEM in the presence of modelling error is evaluated, by introducing models that do not account for the damage. Several conclusions on the behaviour of iFEM in the presence of modelling error are drawn and comment is made on the possibility of damage detection. At the time when these experiments were conducted the prototype software SAFRAN was not yet available and the author wrote a primitive implementation, suitable only for this specific case, to perform iFEM analyses on the damaged beam.

## 4.2 Experimental setup

Experiments were conducted at the Bauhaus University of Weimar in Germany on a damaged beam system [76]. The section properties of the beam are given in Table 4.1. Figure 4.2 shows the experimental setup, the total length of the simply supported beam being 4.4m. An external force was applied to the beam by hitting it with a hammer, causing the beam to vibrate. This externally applied force was also measured. Seven accelerometers, fixed at the positions indicated, supplied measured acceleration values of the vibrating beam during testing. The beam was damaged in two areas, each damaged area consisting of five cuts at intervals of one centimeter and each cut reaching from the bottom halfway through the cross section of the beam.

| $a$ $(m)$ | $b$ $(m)$ | $S$ $(m)$ | $A$ $(m^2)$ | $G$ $(kg/m)$ | $I_z$ $(m^4)$ | $E$ $(GPa)$ |
|---|---|---|---|---|---|---|
| 0.03 | 0.05 | 0.004 | $5.62 \cdot e^{-4}$ | 4.41 | $7.25 \cdot e^{-8}$ | 210 |

**Table 4.1:** *Section properties of Hohlprofil 50×30×4,0 DIN 59410*

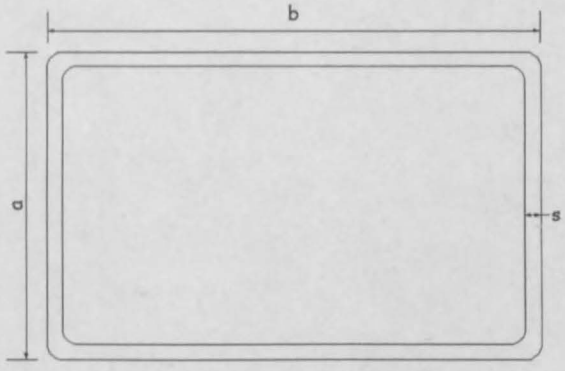


**Figure 4.1:** *Cross section of the beam*

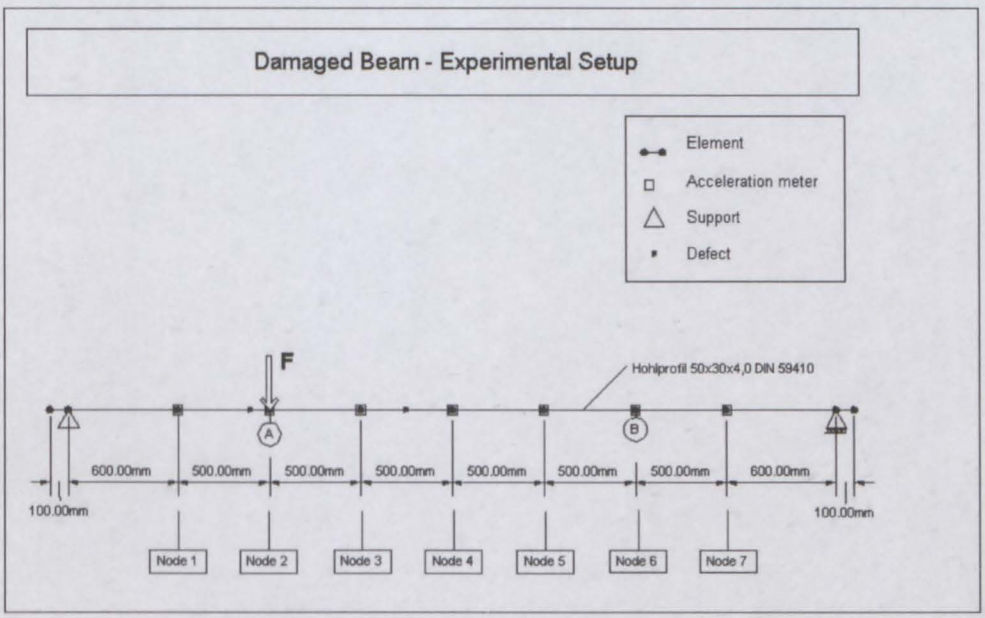


**Figure 4.2:** *Diagram of the experimental setup*

**Figure 4.3:** *Experimental setup*

**Figure 4.4:** *Hammer hit application point, with the force cell on top, attached accelerometer below and one of the defects to the left.*

**Figure 4.5:** *Damage: Five cuts on the left side of the picture, each cut reaching from the bottom halfway through the beam.*

## 4.3 Testing

The damaged beam was used to conduct several tests. They are described below.

### 4.3.1 Test 1 - Single impact on damaged beam

The damaged beam with the accelerometers where indicated in figure 4.2, was subjected to an impact force (hammer hit) at point A. This impact force, as well as the accelerations of the vibrating beam, were measured over time. Ten such tests were carried out, each with a duration of 1 second. Another ten tests, each with duration of 4 seconds, were also carried out.

### 4.3.2 Test 2 - Single impact on damaged beam with an additional point mass

The same damaged beam of figure 4.2, with the accelerometers as indicated, was tested, but with a mass added at point B. Two different tests were carried out, with masses of 270g and 540g respectively. The beam was subjected to an impact force at point A. This impact force was measured, as well as the acceleration time-series of the vibrating beam.

### 4.3.3 Test 3 - Multiple impacts on damaged beam

The damaged beam of figure 4.2, with the accelerometers as indicated, was subjected to three consecutive impact forces (hammer hits) at point A. These impact forces were measured, as well as the acceleration time series of the vibrating beam. No additional masses were present.

## 4.4 iFEM modelling

For all analyses, the measured acceleration data was given as input, but not the measured impact load. The measured impact load was used to compare with the iFEM estimate.

Three different iFEM models were created for use with the data collected from the tests. They are as follows:

### 4.4.1 Model 1 - Undamaged beam model

In this model the presence of defects is not taken into account. The beam structure is modelled without damage, using frame elements with the section properties of Table 4.1. Nodes are placed at the ends of the beam, at the supports, and at the accelerometers. The masses of the accelerometers are accounted for in the mass matrix of the model.

### 4.4.2 Model 2 - Damaged beam model

This model is similar to model 1, but it takes into account the presence of defects, by modelling them as weakened beam members. The damage consists out of five cuts, close to each other, and reaching halfway through the cross section of the beam. The damaged areas were modelled as short frame elements and their bending and axial stiffness were calculated by considering only the top half of the cross section, assuming that the bottom half makes no contribution to the stiffness.

### 4.4.3 Model 3 - Damaged beam, with additional mass

This model is designed with test 2 in mind. It is similar to model 2, taking the presence of defects into account. The relevant additional mass (270g or 540g) is also added to the mass matrix of the model.

### 4.4.4 The load model

The same load model was used for all analysis, independently of the structural model used. Unknown distributed forces are allowed on all the frame elements. This means that two $\overline{U}$ degrees of freedom (value and slope) are present at each node, and the load distribution is interpolated between nodes, using the $\overline{U}$ values and the same shape functions as are used to interpolate displacements for 2D frame elements. A "point load element" is added at the position where the impact force was applied during testing. The point load element

has a single $\overline{U}$ degree of freedom referring to the value of the point load at the position of the element, and allows iFEM to calculate point loads at this position, in addition to the distributed (isoparametric) forces that are calculated on the frame elements. The estimated point load can then be compared to the measured impact.

### 4.4.5 Choice of cost associated with response measurements and external forces

It is known that the output of iFEM is only influenced by the ratio between the cost associated with the response measurements and the cost associated with external forces, and not by the specific cost values. It is also known that the optimal solution should be somewhere between under-regularised and over-regularised behaviour. (Refer to Chapter 2, Section 2.2.4 for an explanation on the concepts of under-regularised or over-regularised). A unit cost was assigned to each of the acceleration measurements. The cost assigned to the unknown external forces was then adjusted, steering away as far as possible from an over-regularised ("sluggish") estimate, without moving into the under-regularised ("jittery") region. This involved a trial and error process, and it was found that the cost associated with the distributed unknown external forces had a much greater influence on the output than the cost associated with the single unknown point load. Therefore, the cost associated with the point load was only decided on after the cost associated with the distributed forces had been established as described above. Figure 4.6 shows how under-regularised behaviour, caused by an inappropriate choice in the cost associated with the unknown distributed external forces, influences the estimate of the point load. Appropriate choice of costing allows a good estimate of the applied point load to be made, as will be evident from the results obtained later in the chapter.

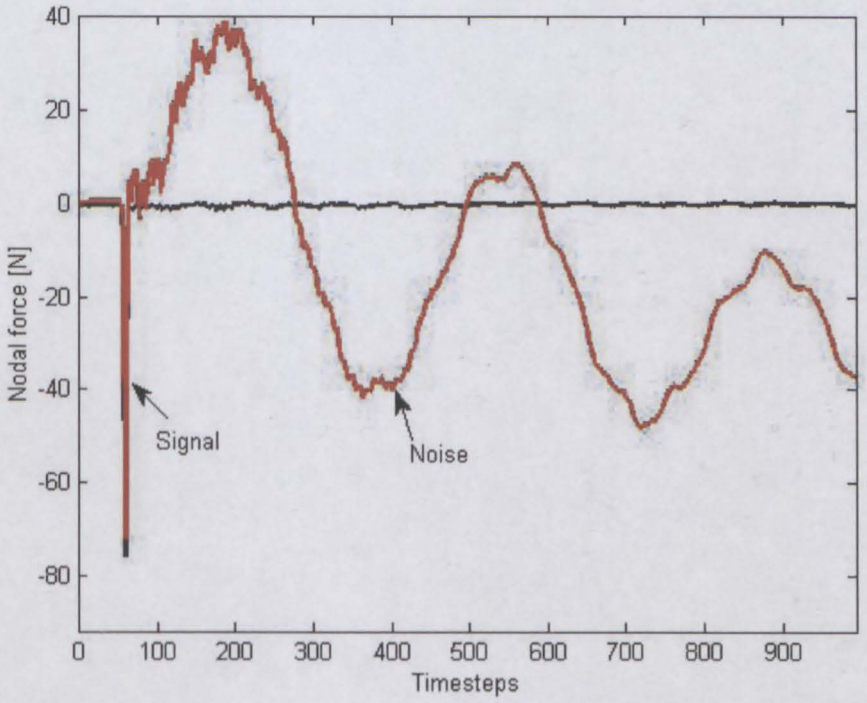


**Figure 4.6:** *Inappropriate costing results in high variance of the point load estimate*

## 4.5 Results

The acceleration data collected during the different tests was used in linear dynamic iFEM analyses with an appropriate choice from one of the models described above, according to the goal of each analysis. The results of every combination that was investigated are discussed below.

### 4.5.1 Test 1 - Model 1

In this analysis, acceleration measurements from the vibrating, damaged beam were used with an iFEM model that does not take the defects into account.

In spite of the incorrect modelling, the externally applied impact load was estimated

quite well. The hit's location in time was predicted accurately. The peak value of the externally applied force was calculated as 72N, compared to the measured peak value of 76N, showing an underestimation of 5% on the impact load. Figure 4.7 shows how the applied force was predicted, the alternating forces after impact are ghost forces due to the imperfect model.

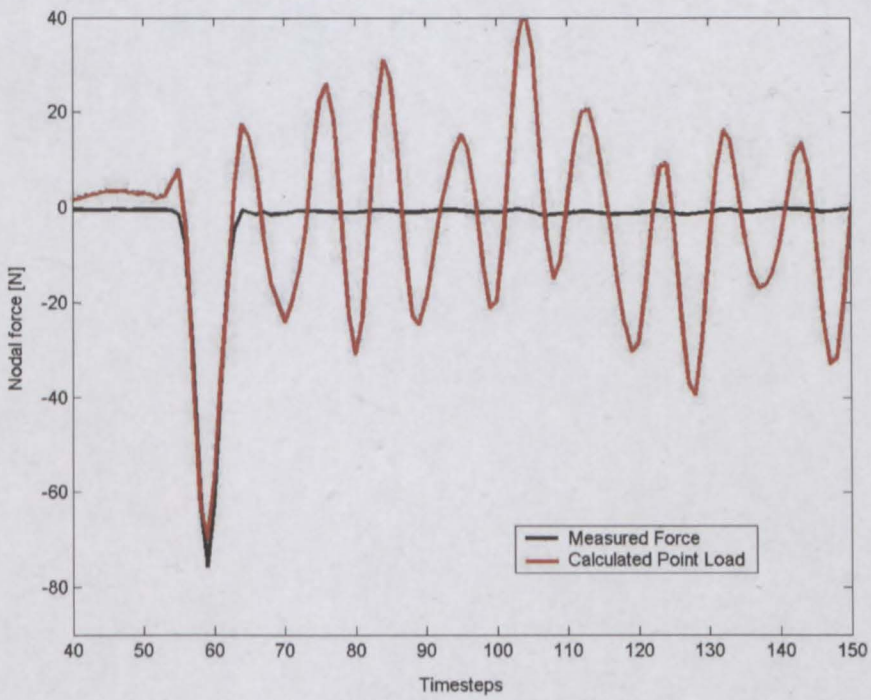


**Figure 4.7:** *Test 1 - Model 1: Comparison of measured and calculated impact load.*

Alternating distributed ghost forces appear in the area of the defects. The beam is bending more in the area of the defects, as detected indirectly by the accelerometers. The reason for the increased bending is, of course, the presence of the defects, but since the model does not account for the defects, ghost forces appear. The alternating forces appear in order to force the inaccurate model to respond as the real beam, according to measurements, did. The alternating forces are easily observed when the input file is run, so that the distributed forces are dynamically displayed at each time step. When the calculated values of the consistent distributed load in time are plotted for seven nodes of

the beam, the alternating nature of the ghost forces can be observed when the distributed load values of the nodes at 1.2m and 1.7m (nodes 2 and 3) are compared. Figure 4.8 shows an example.

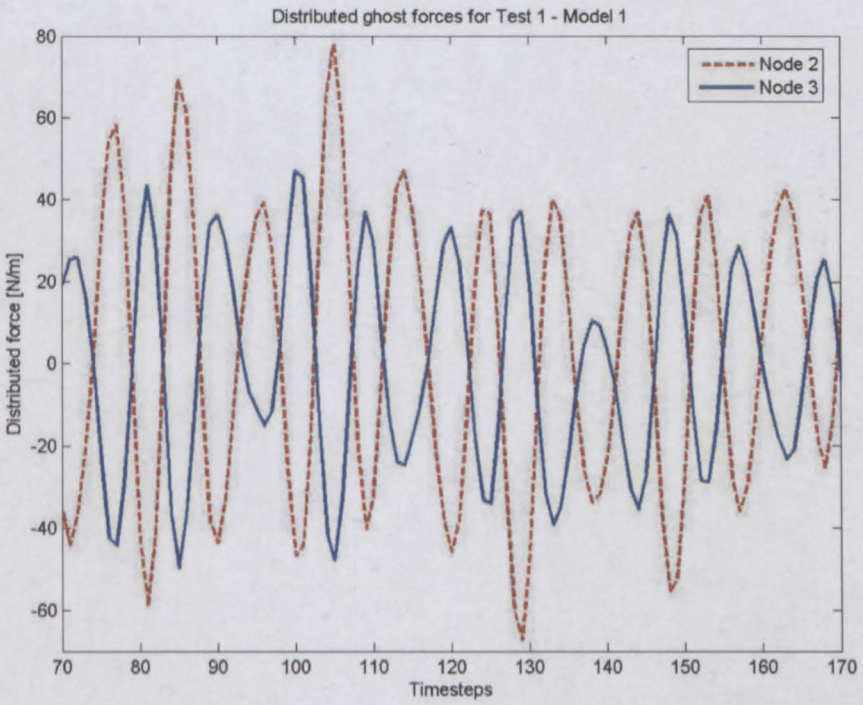


**Figure 4.8:** *Alternating ghost forces in the area of the defects*

Refining the mesh of the model did not help to better pin-point the location of the defects, probably because the defects are so close to each other that their effect on the measurements (taken by a limited number of sensors) cannot be distinguised from each other. Increasing the sensor density should improve the damage location detection.

### 4.5.2 Test 1 - Model 2

In this analysis, measurements from the vibrating, damaged beam were used with an iFEM model that does account for the presence of the defects.

Figure 4.9 shows how the calculated impact load compares to the measured impact load. The significant reduction in noise (compare Figure 4.9 to Figure 4.7) is ascribed to removal of incorrect modelling.

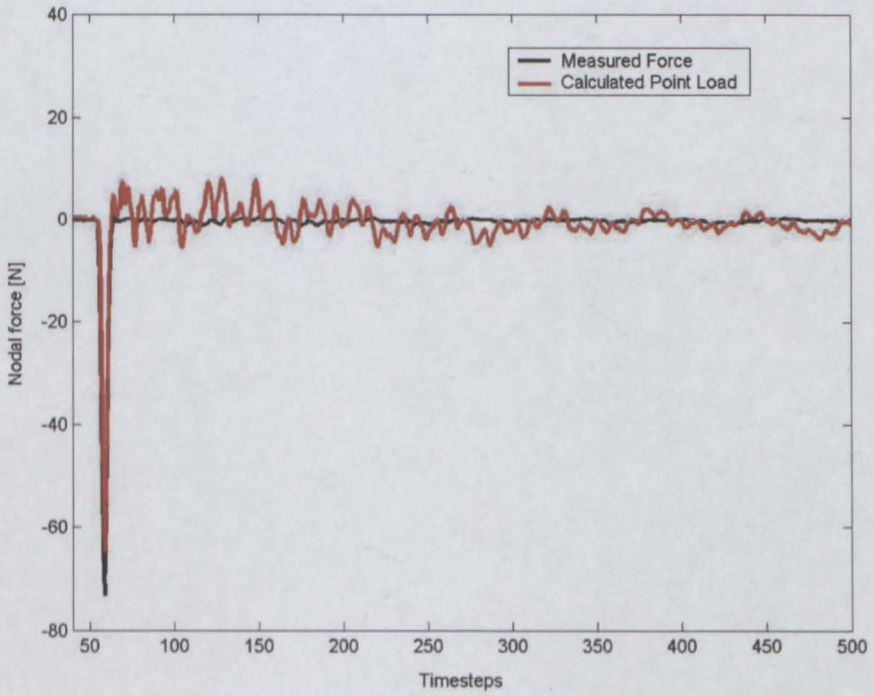


**Figure 4.9:** *Test1 - Model2: Comparison of measured and calculated impact load.*

The alternating distributed ghost forces are also significantly reduced. The distributed load values are around zero for the entire beam, with the maximum deviation from zero being 8N/m for small lengths of the beam.

### 4.5.3 Test 2 - Model 1

In this analysis, measurements from the vibrating, damaged beam with additional mass, were used with an iFEM model that takes neither the defects, nor the additional mass, into account. The position of the additional mass is indicated as point B in Figure 4.2.

In spite of the poor modelling, the externally applied impact load was predicted rea-

sonably. The hit's location in time was predicted accurately. The peak value of the externally applied force was calculated as 75.5N, compared to the measured peak value of 87N, showing an underestimation 15% on the impact load. Figure 4.10 shows how the applied force was predicted, the alternating forces (ghost forces) after impact being due to the imperfect model.

The alternating ghost forces are again present in the area of the defects, but now another ghost force appears at the position where the mass was attached. This force will be further investigated in the next section.

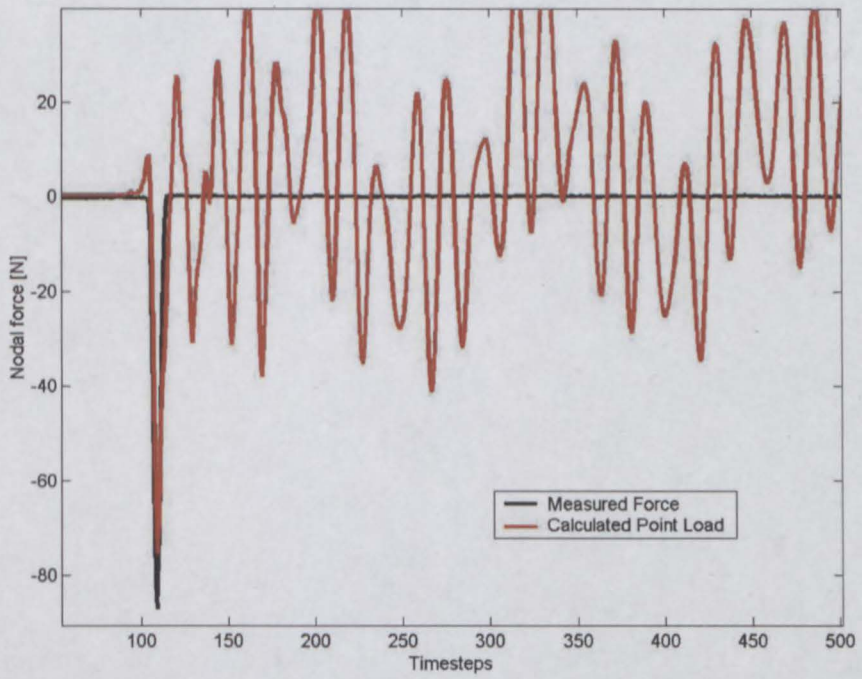


**Figure 4.10:** *Test 2 (mass 540g) - Model 1: Comparison of measured and calculated impact load.*

### 4.5.4 Test 2 - Model 2

In this analysis, measurements from the vibrating, damaged beam with additional mass, were used with an iFEM model that does take the defects into account, but not the additional mass.

Figure 4.11 shows how the calculated impact load compares to the measured impact load. Note that the influence of inaccurate modelling which is obvious in Figure 4.10, does not appear in the plot of the point load.

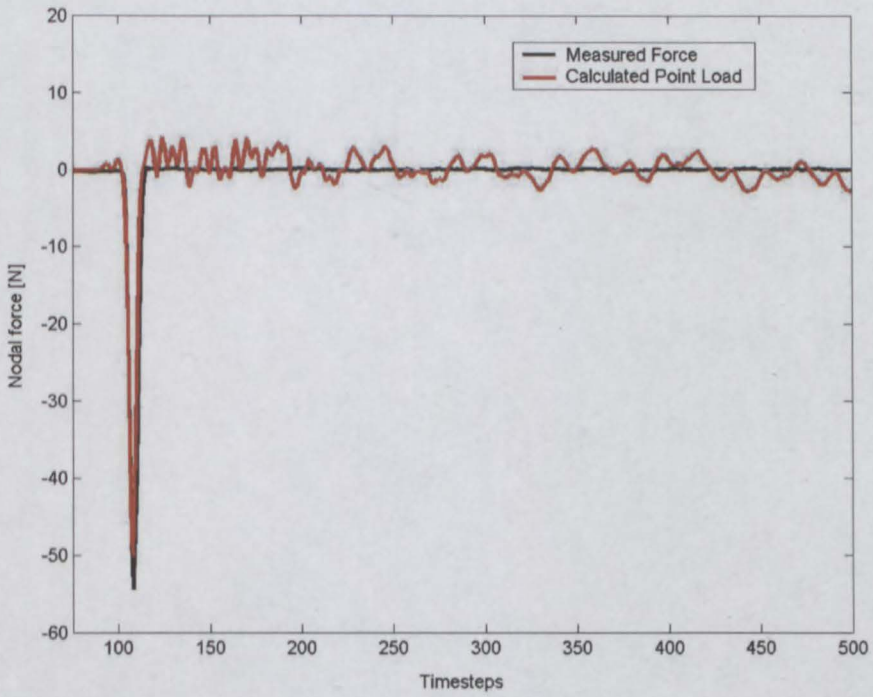


**Figure 4.11:** *Test2 (mass 270g) - Model2: Comparison of measured and calculated impact load.*

The alternating distributed ghost forces also disappeared, as was expected. The distributed load values are around zero for the entire beam, with the maximum deviation from zero being 5N/m for small lengths of the beam. The only exception is at point B,

where the extra mass was added.

The mass-related ghost force at point B can be explained as the inertia effect of the additional mass. The consistent force at point B was calculated from the distributed ghost forces, as no 'point load element' was present at point B. This consistent force shows a strong negative correlation to the measured acceleration at that point. In Figure 4.12 the consistent ghost force at point B is compared to the inertia force that the mass applies to the beam $((mass) \times (-measured\ acceleration))$.

The results strongly suggest that mass matrices can be adjusted by examining the correlation between accelerations and ghost forces. The presence of additional mass can be detected where a strong negative correlation exists between the calculated ghost force and the acceleration at a point. The correlation would be negative, because an unmodelled additional mass will always cause a ghost force that has opposite sign to the acceleration at that point. The value of the additional mass can be calculated as $Additional\ mass = \frac{CalculatedGhostForce}{Acceleration}$.

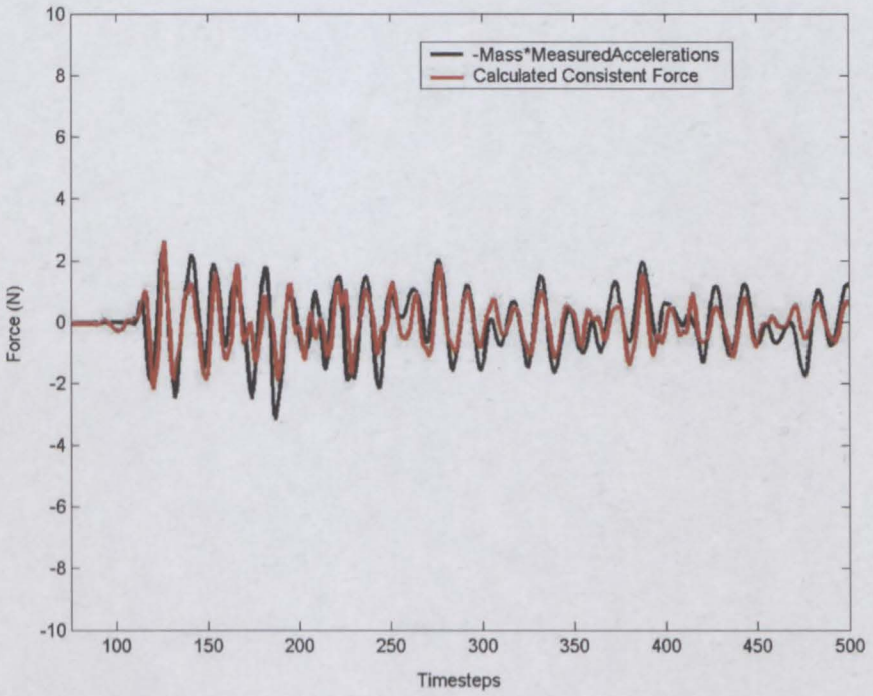


**Figure 4.12:** *Mass-related ghost force correlated with (mass) × (−measured acceleration) (mass 270g).*

### 4.5.5 Test 2 - Model 3

In this analysis, measurements from the vibrating, damaged beam with additional mass, were used with an iFEM model that takes into account both the defects and the additional mass.

Figure 4.13 shows how the calculated impact load compares to the measured impact load. Note that the improvement from Figure 4.11 to Figure 4.13 is barely noticeable. It can be seen that omitting the additional mass from the model was significantly less influential than omitting the defects from the model. This might be because the mass was added far from the impact point, and the ghost force resulting from the mass's presence is thus also far from the impact point. The mass-related ghost force could not be confused with the calculated impact load, whereas, in the case of defects not being accounted for,

the ghost forces are also in the area of the impact point, leading to some ghost forces being incorrectly plotted as impact force.

The mass-related ghost force at point B disappeared, as was expected.

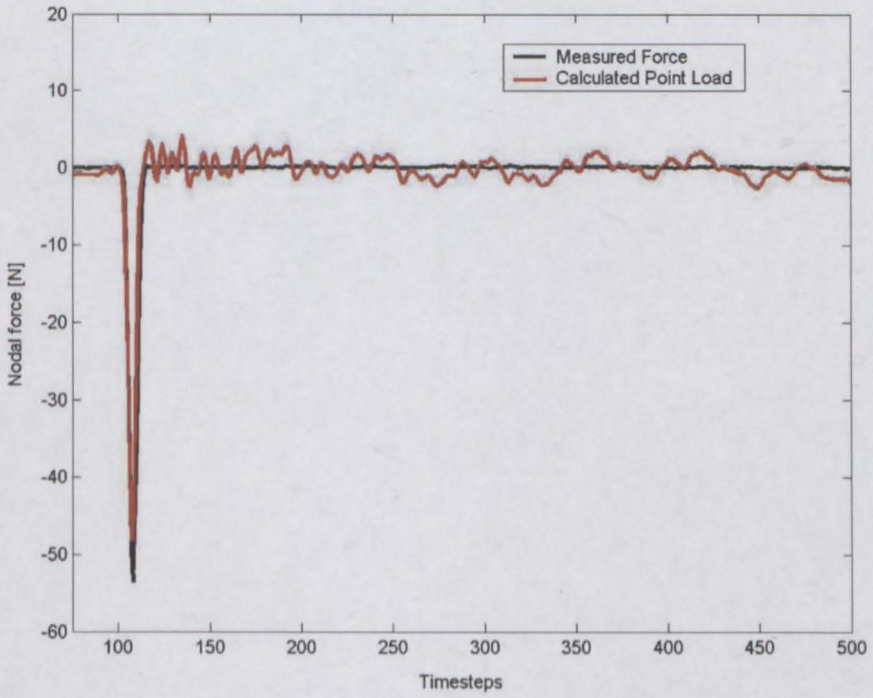


**Figure 4.13:** *Test2 (mass 270g) - Model3: Comparison of measured and calculated impact load.*

### 4.5.6 Test 3 - Model 1

In this analysis, measurements from the vibrating, damaged beam were used with an iFEM model that does not take the defects into account. The beam was hit with three consecutive hammer blows.

Using an inaccurate model results in the appearance of ghost forces, and it is hard to distinguish the predicted point loads from these ghost forces. Figure 4.14 shows how

the point loads were predicted. The alternating ghost forces are again present, and the alternation could be seen when comparing the distributed forces of the nodes at 1.2m and 1.7m (nodes 2 and 3), similar to what was shown in Figure 4.8.

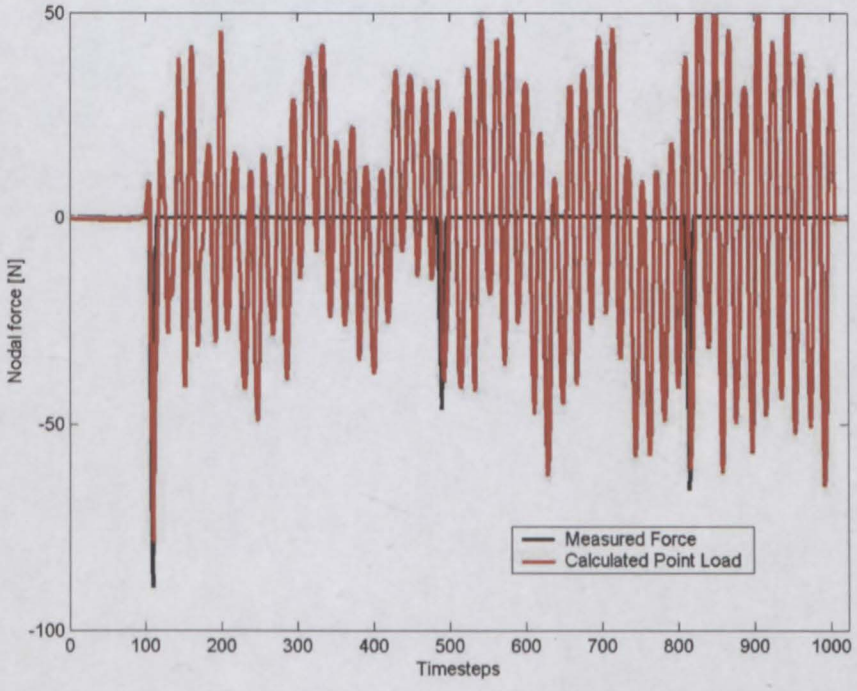


**Figure 4.14:** *Test3 - Model1: Comparison of measured and calculated impact loads.*

### 4.5.7 Test 3 - Model 2

In this analysis, measurements from the vibrating, damaged beam were used with an iFEM model that does take the defects into account.

The three hammer hits are very well defined in terms of magnitude and location in time. Figure 4.15 shows how the hammer hits are detected. The influence of the inaccurate model do not appear in the plot. The alternating ghost forces also do not appear, so that the distributed load values along the beam are small.

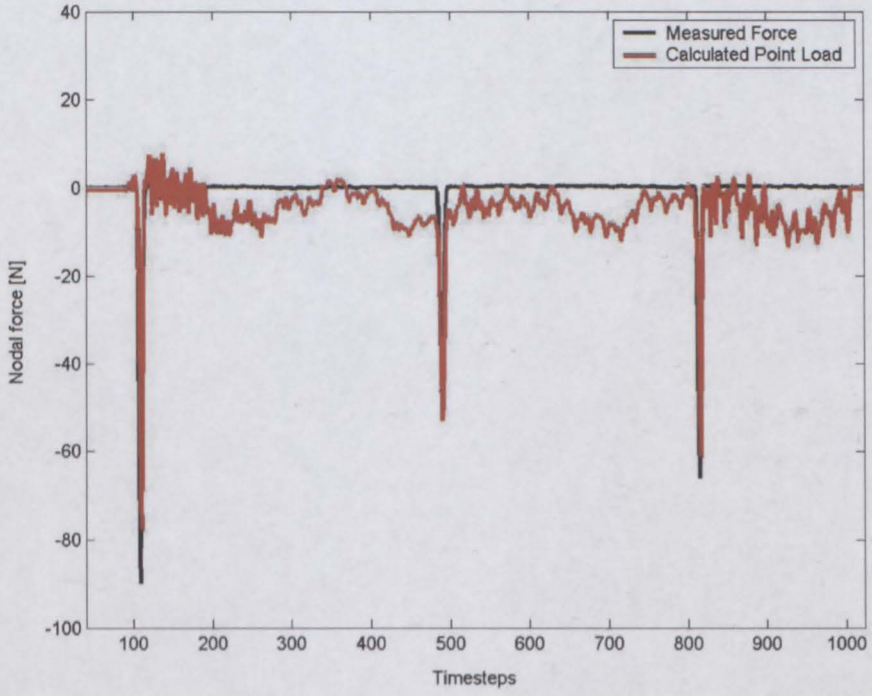


**Figure 4.15:** *Test3 - Model2: Comparison of measured and calculated impact loads.*

## 4.6 Conclusions

1. iFEM is stable with respect to model errors, meaning that an inaccurate structural model usually does not cause numerical difficulties and iFEM gives useable results in spite of such inaccurate models. Thus, assuming that appropriate costs are associated with deviation from measurements and deviation from expected load values, iFEM can be used to process physical measurement data. The combination of inaccurate response measurement and inaccurate model description does not cause iFEM to become unstable.

2. Inaccurate modelling has a significant influence on the output of iFEM. Specifically, it leads to the appearance of ghost forces.

3. In spite of inaccurate modelling, iFEM was able to make an assessment of the impact load that was applied to the beam. This assessment was relatively accurate and, in some cases, easily distinguishable from the ghost forces that appeared as a result of the incorrect model.

4. iFEM gives the possibility of defect detection, at least in the present case.

5. There is need for a post processing method to attribute ghost forces to stiffness-, damping-, or mass-related defects. In the present case, for example, inaccuracies related to the mass matrix of a system might be detected by correlating ghost forces and accelerations. A strong negative correlation showed the presence of additional mass.

6. The introduction of a point load-element allows a point load to be calculated, in addition to the distributed forces, at the position where the point load-element is placed in the model. If a high cost is placed on a point load, iFEM will cause some of the point load to be calculated as distributed forces, because this results in a lower cost, or vice versa. When using a point load element, the cost assigned to it must be correct, compared to the cost that is placed on distributed forces. This might involve a trial and error approach.

7. If the cost associated to the distributed forces is too low, compared to the cost placed on deviating from specified measurements, the estimate will be under-regularised (cf. Section 2.2.4), which will also worsen the point load estimate. Figure 4.6 shows an example of how inappropriate costs influenced the point load that was calculated for one of the beam experiments. A too low cost associated to the single point load does not have the same significant influence.

# Chapter 5

# Continuity of assessed external loads

## 5.1 Introduction

During the course of work, it was observed that when continuity of the externally assessed load is not required, it is often achieved anyway. Although this is not directly relevant to model error sensitivity, the circumstances under which this occurs are discussed.

## 5.2 When does SAFRAN enforce continuity of the externally assessed load?

In SAFRAN, continuity of all $\overline{\mathbf{X}}$ degrees of freedom is enforced at a node when elements share that node. Elements are added to the model by defining "element groups", where all elements of the same group are of the same type. When elements that are part of one element group in SAFRAN share a node, SAFRAN will automatically also enforce continuity in slope and value of the externally assessed load, $\overline{\mathbf{u}}(\overline{\xi})$, at that node. However, continuity of $\overline{\mathbf{u}}(\overline{\xi})$ is not enforced across boundaries of elements belonging to different element groups.

To achieve a hinged connection, it is necessary to define two nodes, with the same coordinates, at the position where a hinged connection is wanted. Constraints must then be introduced to ensure that the horizontal and vertical translation of the two nodes are set equal. In the case of a hinged connection, continuity of $\overline{\mathbf{u}}(\overline{\xi})$ are not enforced by

SAFRAN, even if the elements form part of the same element group, since the elements do not share nodes.

## 5.3 Other circumstances under which continuity of the externally assessed load is observed

It is observed that in most cases continuity of $\overline{\mathbf{u}}(\overline{\xi})$ is achieved for elements that are not of the same element group (even though, in such a case this is not enforced), if all their shared $\overline{\mathbf{X}}$ degrees of freedom are required to be continuous. Figure 5.1 shows an example. Each element group consists of three elements, and it can be seen that continuity is obtained over the boundaries of the element groups.

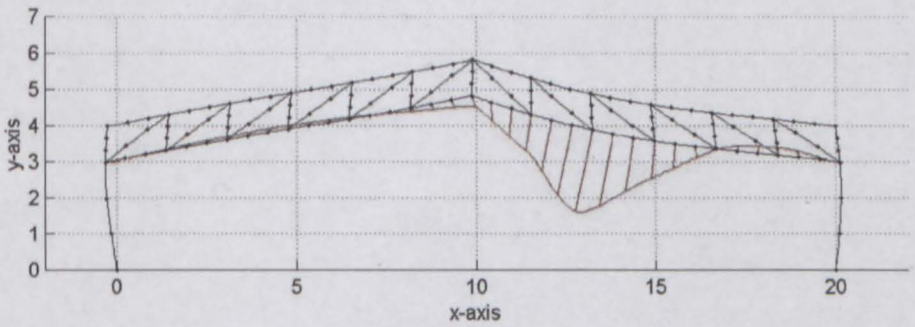


**Figure 5.1:** *Obtaining continuity in slope and value of* $\overline{\mathbf{u}}(\overline{\xi})$

If two elements are connected by a hinge, the values of $\overline{\mathbf{u}}(\overline{\xi})$ for the two elements are equal at the shared node. However the slopes of the $\overline{\mathbf{u}}(\overline{\xi})$ for the two elements are not equal at the shared node. Figure 5.2 shows an example.

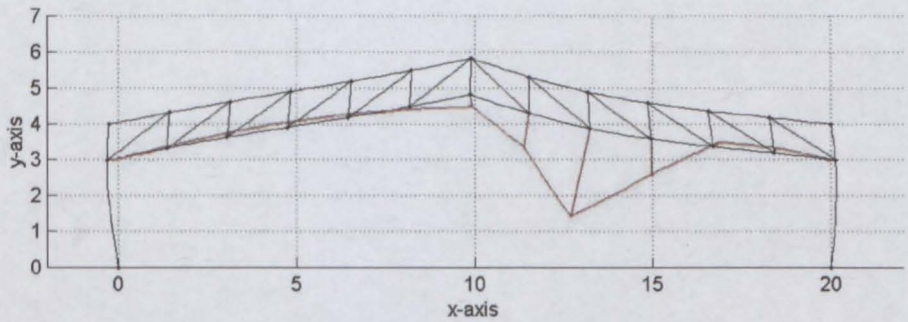


**Figure 5.2:** *Obtaining continuity in value of* $\overline{\mathbf{u}}(\overline{\xi})$

## 5.4 Circumstances under which continuity of the externally assessed load is not observed

Although continuity of externally applied load, $\overline{\mathbf{u}}(\overline{\xi})$, is generally observed, as explained above, there are exceptions. If the probabilities of externally applied load are not the same for connected elements, continuity of $\overline{\mathbf{u}}(\overline{\xi})$ is not observed between them. Figure 5.3 shows an example of such a case. It is observed that, if the cost placed on assessed externally applied load of one element is $b$ times as large as the cost placed on assessed externally applied load of the joining element, the value of $\overline{\mathbf{u}}(\overline{\xi})$ of that element at the connection will be $1/b$ times the value of $\overline{\mathbf{u}}(\overline{\xi})$ at the same point for the joining element.

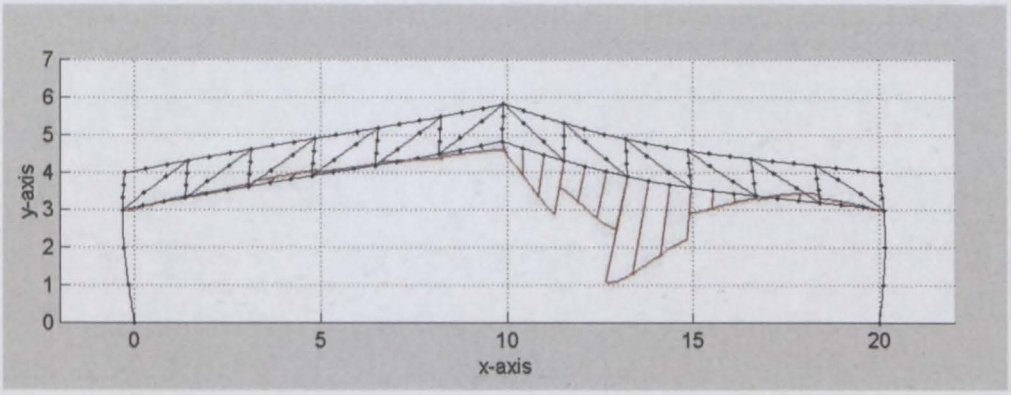


**Figure 5.3:** *Continuity of* $\overline{\mathbf{u}}(\overline{\xi})$ *is not obtained*

## 5.5 Conclusions

1. Experience indicates that, when continuity is not enforced, continuity of those $\overline{\mathbf{U}}$ degrees of freedom will be observed, of which the corresponding $\overline{\mathbf{X}}$ degrees of freedom have been required to be continuous.

2. One exception is that, if the probability of externally applied load is not the same for connected elements, continuity of $\overline{\mathbf{u}}(\overline{\xi})$ is not observed between them.

3. A general rule can thus be formulated, although this is only observed and not proven: Provided that the probability of externally applied load is the same for connected elements, continuity of those $\overline{\mathbf{U}}$ degrees of freedom will be observed, of which the corresponding $\overline{\mathbf{X}}$ degrees of freedom have been required to be continuous. If continuity for $\overline{\mathbf{X}}$ translations and slope is required, continuity of $\overline{\mathbf{u}}(\overline{\xi})$ will also be observed in value and slope (even though it is not enforced). If only continuity for $\overline{\mathbf{X}}$ translations, but not rotations, is required, only continuity for $\overline{\mathbf{u}}(\overline{\xi})$ values, but not slopes, are observed.

4. It is observed that continuity of $\overline{\mathbf{U}}$ need not be enforced in order to obtain continuity. This indicates that the $\overline{\mathbf{U}}$ degrees of freedom can be eliminated from the iFEM system, thus reducing the number of unknown variables and the size of the system

matrices that need to be inverted. However, we choose not to do this, since it will take away our ability to later suppress or constrain $\overline{\mathbf{U}}$ degrees of freedom.

# Part III

# Development of iFEM theories for static and dynamic model parameter estimation

# Chapter 6

# Model recalibration, parameter estimation and damage detection: a literature review

## 6.1 Introduction

The integrity of some structures are of utmost importance. This is the case for aircraft where failure takes human life or oil carrying pipelines where failure results in oil spillage, environmental hazard, equipment damage and down-time. Often, these structures are costly to maintain. Deep sea oil pipelines are inaccessible and tedious to inspect. The down-time cost associated with some mining equipment's maintenance and inspection is enormous. In these cases, much can be gained from on-line damage detection methods and structural monitoring.

Monitoring of structures has applications in civil, mining, mechanical, aerospace, off-shore, and other branches of engineering. The market is fast expanding thanks to improved measurement and data-logging possibilities.

In chapter 7 a parameter identification theory is developed that demonstrates the possibility of applying iFEM for damage detection. Suggestions to further develop this

potential are made in chapter 13. The literature study of the present chapter places the development of chapter 7 and the suggested future work into perspective, by giving a broad overview of existing methods for damage identification. Review articles by other authors [79, 50, 12] were of great help in choosing a framework within which to group the different methods. Both local and global damage identification methods have been developed. Local damage identification methods include methods such as radiography, x-rays, magnetic field methods, acoustic or ultrasonic methods, and thermal field methods [13]. All of these are experimental techniques that require the excitation and sensors to be close to the damaged area, therefore the part of the structure to be inspected must be accessible. Among these methods the acoustic emission method was used with great success to detect damage in metallic and composite aerospace structures [65]. The method also allows larger monitoring areas than most of the other local inspection methods. X-rays are useful to inspect welds for possible defects. The focus in this chapter falls on global identification methods that allow damage detection by examining changes in the vibration response of the structure. The development in chapter 7 and the suggested future iFEM parameter identification development can be classified as penalty function methods, described in section 6.2.6.

## 6.2 Global damage identification methods.

### 6.2.1 System identification

System identification [42] [63] is used for determining a model to describe a system based on observations of the input and output of the system, taking into account the presence of measurement noise and system disturbances. System identification, as derived from control theory, is used for control of systems, where a model is judged on its ability to predict the output of a system, given the input to that system. In this application field, the model itself need not be a physical description of the system in order serve its purpose. However, for the purpose of structural damage identification, the model parameters must describe actual structural properties.

### Direct system identification

Direct system identification allows the identification of the matrices that describe a structural system without the updating of a reference model. The spatial parameters may be identified using measured modal data if the available modal matrix is square and invertible [69]. Frequency response function data can also be used in a number of direct identification techniques to estimate spatial parameters [60]. However, these methods do not allow for the terms in the identified matrices to be directly related to material properties and the geometry of the structure. Berman [4] concluded that a physically meaningful model cannot be identified using a direct approach.

### Parameter estimation

Parameterised models can be used to describe a system, typically using continuous-time state-space models derived from basic laws of physics that describe the behaviour of the system. For model structures with physical parameters, the idea is to incorporate physical insight into the model set to bring the number of adjustable parameters down to what is actually unknown about the system. Identification methods can be applied to estimate the unknown parameters. An identification experiment is performed by exciting the system and observing its input and output over a time interval. A parametric model of the process is then fitted to the recorded input and output sequences. It is obvious that a poor choice of model parameters can never offer a good model, regardless of the amount and quality of available data.

Minimizing prediction errors is one approach to estimate the unknown parameters. For a chosen model structure, a predictor function can be written based on the system description $y(t) = G(q, \theta).u(t) + H(q, \theta).e(t)$, where $\theta$ are the unknown parameters, $u(t)$ is the input, $y(t)$ the output, and $e(t)$ the disturbance to the system. For example a one-step ahead predictor function allows prediction of the output at the next time step, based on measurements of the input and output at the previous time steps and a probability distribution function of the disturbance. The unknown parameters are then estimated

by minimising the error between the measured and predicted output. Different weighting functions allows frequency weighting and different weights can be attached to measurements that vary in reliability. The prediction error function to be minimised is usually taken as its quadratic norm. The prediction error method is sometimes called the *generalised least squares method* or an *output error method*. The *least squares method* is also a special case of the prediction error method.

The *maximum likelihood estimate* of $\theta$ is obtained by maximizing the probability distribution function of the observations conditioned on the parameter vector $\theta$.

Ideally, the prediction error $\epsilon(t, \theta)$ for a 'good' model should be independent of past data $Z^{t-1}$, because, if $\epsilon(t, \theta)$ is correlated with $Z^{t-1}$ then there was more information available in $Z^{t-1}$ than picked up by the predictor. For a system given by $y(t) = \phi^T(t).\theta_o + e(t)$, the parameter estimates under the condition that prediction errors should be independent of past data are given by $\theta = [\sum_t Z(t)\phi^T(t)]^{-1}[\sum_t Z(t)y(t)]$, where the matrix $Z(t)$ is most commonly obtained by various operations (filtering, delaying, etc.) on the input $u(t)$. This approach, known as the *instrumental variable method*, is useful when the disturbance is not a white noise function.

In solving for $\theta$, a numerical search method is generally used. Numerical minimization methods can be divided into three groups: methods using function values only, methods using values of the function as well as of its gradient and methods using values of the function, of its gradient and of its Hessian.

### 6.2.2 Error localisation

In this type of approach the most inaccurate model parameters are to be identified prior to updating. This would allow for updating to be performed economically and minimise the problems associated with processing noisy and incomplete measurement data. Eigenvector expansion methods [77, 25], a sensitivity based localization approach [41], and a

force balance method for error localization [17] are some of the methods that have been proposed.

In [77] the stiffness- and mass perturbation matrices, obtained by an eigenvector expansion method, are used for searching for the dominant sub-matrices that they contain. This allows the spatial identification of areas where the most important modelling errors have been made, so that only those parameters that are sensitive in poorly modelled areas can be selected for parametric adjustment.

### 6.2.3 Methods utilising frequency changes

Any crack or localized damage in a structure reduces the stiffness and increases the damping in the structure. Reduction in stiffness is associated with decreases in the natural frequencies and modification of the modes of vibration of the structure. A large amount of literature describes the use of frequency shifts to detect damage, and Salawu [56] presents a useful review on these methods. Frequency shifts are not sensitive indicators of damage and therefore require high measurement precision or severe levels of damage. Nevertheless, natural frequencies can be measured more accurately than other modal parameters, which suffer greater statistical variation from random error sources [15]. Frequency changes as a method for damage detection are applied mostly in controlled environments where the frequency shifts can be measured with great precision, for example in manufacturing.

#### Forward identification

In the forward identification approach, frequency shifts are analytically calculated for a number of likely damage scenarios, with the damage being modelled mathematically. The calculated frequencies and the measured frequencies are compared to determine the damage. In this way, damage has been detected in offshore oil platforms [43].

Assuming that the analytical model of a structure is perfect, frequency shifts were calculated in [19] for the first number of modes for several likely damaged states, and ratios of these frequency shifts were calculated by comparison with the undamaged model.

The same ratios were calculated for the structure. The probability of damage was judged according to the quality of the fit of these ratios to each pattern of assumed damage.

Contrast maximization [32] is a technique that allows locating damage by comparing the response of the damaged structure to a database of computed structural responses. The structure is harmonically excited with sensors and shakers assumed to be co-located. The actuator force amplitude vector, that would maximise the difference between the response of the undamaged (FEM) and the damaged (measured) structure, can be calculated for each structural model using their flexiblility matrices. This vector is compared to a database of such vectors from modeled damage scenarios, to give an indication of the presence and location of damage.

**The inverse methods**

Solving the inverse problem using frequency shift data allows detecting the location of damage in a structure and can give an indication of the severity of the damage.

The sensitivity of modal frequency changes to changes in the characteristics of the structure is used in a damage detection method by Osegueda and Stubbs [52]. The sensitivity is computed using a FEM model of the structure, making it reliant on the accuracy of this reference model. Assuming that only one member is damaged, an error function is calculated for each mode and member of the structure. The member that minimizes this error is the most probable damaged member.

For beams, the location of a crack can be determined [51] using measured bending- or axial frequencies. A solution for the crack position is given as a function of the frequency shifts from two modes for a simply supported beam in axial vibration or in longitudinal bending.

The problem of making vibration measurements in the field and the influence of the accuracy of reference models are discussed by Morassi [49].

### 6.2.4 Methods utilising changes in mode shape

One of the first approaches that systematically used mode shape information for damage detection without requiring a prior FEM model is described by West [73]. The modal assurance criterion (MAC) is used to determine the correlation between modes from the undamaged structure and modes from the damaged structure. The MAC indicates the correlation between two sets of mode shapes. It is used to study overall differences in the mode shapes. The structural damage is localized by observing the change in the MAC.

The MAC method is further developed by introducing 'Node line MAC', where MAC based on measurements taken close to a modal node point, proved to be a better indicator of damage [18]. When only mode shapes and resonant frequency data are available, damage is best located by graphically comparing the changes in mode shapes. A method is also presented that allows scaling of the relative mode shape changes to better locate damage. Correlating modal node points of modes that show little change in resonant frequencies, with the peak amplitude points of modes that show large changes in resonant frequencies, proved to locate the damage in a beam with a saw cut.

A method similar to the forward identification of frequency change methods, examines changes in mode shape and mode shape-slope parameters [75]. The damage was located by comparing the measured changes in these parameters to parameter changes that were obtained by simulating damage scenarios.

Methods for determining optimal sensor positions were developed based on an eigenvector sensitivity study and by using a substructure iterative technique based on changes in mode shapes and frequencies [61].

### 6.2.5 Methods utilising changes in curvature mode shape

Curvature and bending strain are directly related for beams, plates and shells. Therefore, the possibility of using changes in mode shape derivatives, such as curvature, has been

investigated. The mode shape curvature is also much more sensitive to small changes in the system than the mode shape itself. However, a relatively large statistical uncertainty is associated with estimates of mode shape curvature. The practical issues of measuring strain or computing it from displacement values or from mode shapes have been investigated in [7], which concluded that direct measurement of strains substantially improved results.

Stubbs, et al. [67] use the curvature of measured mode shapes to define the modal strain energy between structural degrees of freedom for frame structures. Based on the decrease in this strain energy from the undamaged to the damaged state, a damage index can be computed for each element as a function of the experimentally determined fractional strain energy, summed over all modes, between the endpoints of the element. Statistical methods are then used to examine the changes in the damage index and associate these changes with the possible damage locations. An estimate for the severity of damage for the probable damaged elements can also be computed. This approach does not require the computation of sensitivity matrices from a prior model.

Absolute curvature mode shape changes can be a good indicator of damage for beam structures modelled using FEM [54]. In this case the displacement mode shape was used to compute curvature values. The changes in the curvature mode shapes are shown to be localized in the region of damage. Changes in displacement mode shapes indicated the presence of damage, but did not provide an indication of its location.

The frequency response function (FRF) curvature method [57] were able to detect, localise and assess the damage extent of the Interstate 40 bridge in the U.S.A. The absolute difference between the FRF curvatures of the damaged and undamaged structure along the chosen frequency range, is calculated and summed for several force location cases, and used as a measure to evaluate possible damage at each structural location.

### 6.2.6 Methods based on updating structural model parameters

This group of methods solve for updated system matrices (stiffness, damping and mass matrices) such that the updated system follows the measured response data as closely as possible. This is achieved by solving a constrained optimization problem, based on the numerical model used to describe the system, the equations of motion, an objective function to be minimised and constraints placed on the problem. The methods differ in the choice of objective function, the choice of constraints placed on the problem and in the algorithm used to implement the optimization.

Some of the constraints used in these methods include the following: The equations of motion to be satisfied exactly; preserving the property matrix symmetry, preserving the property matrix sparsity and/or preserving the property matrix positivity. The *modal force error* can be used as a constraint or an objective function. The modal force error is defined as the harmonic force excitation that would cause the undamaged structure to respond with the damaged mode shape. Requiring this to be zero or minimum, allows one to update the undamaged model.

#### Optimal matrix updates

Baruch and Bar Itzhack [2] developed a matrix adjustment method for updating the structural stiffness using measured frequencies and mode shapes. Mode shapes determined experimentally are usually not orthogonal to the model mass matrix. The method first corrects the measured mode shapes to satisfy the orthogonality condition and are closest, in a weighted Euclidian sense, to the measured modes. The orthonormalized modes are then used to compute an optimally corrected stiffness matrix. Symmetry of the stiffness matrix is enforced and zero modal force error is implemented as a constraint, while an updated stiffness matrix as close as possible to a prior stiffness matrix estimate is sought.

Smith and Beattie [62] present a sparsity preserving optimal update technique. The

preservation of the sparsity pattern of the stiffness matrix is one way of preserving the allowable load paths of the real structure in the updated model, in this way helping to ensure that a physically meaningful model is obtained. The norms of the modal force error and of the perturbation matrix are minimized, while enforcing symmetry of the updated matrix.

It is observed that damage will tend to be concentrated in a few structural members, rather than distributed throughout a large number of structural members. This observation is the motivation for another approach to the optimal matrix update problem, where the rank of the perturbation matrix is minimised, rather than the norm of the perturbation matrix. In the *minimum rank perturbation theory (MRPT)* [33], a nonzero entry in the damage vector indicates the presence of damage. The method has been further developed to find the damage extent in any two of the three structural property matrices (stiffness, damping and mass matrices). The method can also be adapted to allow matrix updating directly from using measured FRFs. A limitation of this method is that the rank of the perturbation matrix is always equal to the number of modes used to compute the modal force error.

The effect of noise levels, the number of sensors used and the number of damaged elements, as well as various matrix update methods are evaluated with respect to their damage identification abilities [34]. Numerical simulation and experiments were used in the investigation, which concluded that the number of sensors used is the most critical parameter for damage detection.

### Sensitivity based methods

These methods are generally based on the use of a Taylor series of the modal data as a function (possibly non-linear) of the unknown parameters, where the object is to maximise the correlation between the measured and analytical modal model. For structure identification using sensitivity derivatives, a set of physical parameters are chosen to represent the structure. Elements of the dynamic model's property matrices (mass, stiffness, damp-

ing) are functions of the physical parameters. In turn, eigenvalues and eigenvectors of the response can be expressed as functions of the parameter set. Using local linearization, the functional relationship of the system modal response to each parameter is determined. An iterative approach is usually needed. Adjustments in the physical parameter set are identified using the measured modal response of the structure and the sensitivity derivatives. A main difference between the various sensitivity based update schemes is the method used to estimate the sensitivity matrix that relates the change in the structural parameters to changes in the vibration properties (natural frequencies and mode shapes). The sensitivity matrix can be estimated either from experimental data or analytically. These methods allow a wide choice of physical parameters, including material densities, moduli of elasticity, areas, lengths and masses, to update. The development in Appendix A was an attempt to derive an analytical sensitivity matrix.

Ricles and Kosmatka [55] established the location of damage based on differences in the system vibration properties of the damaged and undamaged structure. The residual force vector for the $i$th mode $(R_i)$ is deduced as $(K_a - \lambda_{di}.M_a)\phi_{di}$, where $\lambda_{di}$ and $\phi_{di}$ are the experimental measured eigenvalue and mode shape of the damaged structure, and $K_a$ and $M_a$ are the analytical stiffness and mass matrix of the structure. The damage severity is assessed based on establishing a relationship between the measured vibration characteristics and the structural parameters in the damaged region using a first order Taylor expansion, which allows updating system mass and stiffness parameters. A sensitivity matrix is used where the sensitivities of the natural frequency and mode shapes were obtained from experimental data, and the sensitivities of the structural parameters are computed from the analytical model. Statistical confidence factors for the measurement equipment and the initial values of structural parameters are taken into account.

Using a benchmark test structure, Goge and Link [22] compare two methods for model parameter updating. Both methods make use of the inverse sensitivity approach. The first method, which performed better, minimises the residue between measured and analytical mode shapes and eigenvalues. The second minimises the residue between mea-

sured and analytical (FEM) frequency response and eigenvalues. The residue is defined as $\overline{\epsilon} = \overline{\mathbf{v}}_t - \overline{\mathbf{v(p)}}$, where $\overline{\mathbf{v}}_t$ is a vector that contains the experimental data and $\overline{\mathbf{v(p)}}$ is a vector that contains the analytical data depending on the model parameters $p$. The model vector with regard to the parameters is linearised: $\overline{\mathbf{v(p)}} = \overline{\mathbf{v}}_0 + \overline{\overline{\mathbf{S}}}_0.\overline{\mathbf{\Delta p}}$, with $\overline{\mathbf{\Delta p}}$ being the parameter changes, $\overline{\overline{\mathbf{S}}}_0$ being the sensitivity matrix, and $\overline{\mathbf{v}}_0$ the model vector at linearization point 0. The sensitivity matrix is assembled (in the case of the first method) from the derivatives of the analytical eigenvalues and mode shapes with respect to the correction parameters. The objective function $J = \overline{\epsilon}^T.\overline{\overline{\mathbf{W}}}.\overline{\epsilon}$ is minimised in a weighted least squares sense to calculate the parameter changes. The second method allows updating modal damping parameters in addition to stiffness and mass properties. Both methods allow handling of incomplete test data vectors, meaning that all degrees of freedom need not be measured. This is a great advantage, making the methods able to cope with large order FEM models. In [21] Goge applies the first method to validate the FE model of a civil four-engine aircraft, using experimental data from ground vibration testing.

A method developed by Alvin [29] also allows the incorporation of statistical confidence factors for the measured data and the initial structural parameters. The sensitivities are formulated at element level, allowing better location of damage in specific members.

**Eigenstructure assignment**

For structure identification, the *eigenstructure assignment method* [39] is applied to determine the psuedo control which would be required to produce the measured modal properties with the initial structural model. Eigenstructure assignment theory is based on the design of a controller that would minimise the modal force error. The dynamic equations of motion for a structure are used and it is assumed that a FEM model of the structure exists. The pseudo control is then translated into adjustments to the initial FEM model, by interpreting the feedback gains as matrix perturbations to the undamaged structural model, providing an estimate of the severity of damage. If the modal force error is assumed to be zero, the best achievable eigenvectors can be found in terms of the measured eigenvectors. This relationship can be used as a measure of the damage location.

Cobb and Liebst [10] formulated a method using assigned partial eigenstructure, for identifying damaged structural elements from incomplete modal measurement data. A cost function is written that seeks to minimise the difference between the analytical and measured eigenvalues and eigenvectors. This is minimised subject to the eigenstructure constraint $(K - \lambda.M).\phi = 0$, and while ensuring that the change in stiffness matrix is consistent with the finite element formulation.

Similar to eigenstructure assignment are the *frequency response function assignment method* [59]. The problem is formulated as a linear solution for element stiffness and mass perturbation factors, and FRF measurements are used instead of mode shapes to solve the problem.

### 6.2.7 Statistical approaches

Bayesian estimation is based on Bayes' formula, which gives the probability density function of the updated parameters, knowing the measured information, in terms of the probability density function of the parameters before updating. The probability density functions are assumed to be Gaussian and are then given uniquely by their mean and variance. Both the measurements and the parameter estimates are assumed to have errors given in terms of their estimated variances. The updated parameters are calculated using Bayes' formula (for example, the mean of the calculated probability density function can be used as an estimate of the updated parameter), and the variance of the updated parameter is then also available.

Vanik et al. [70] use modal parameter data sets from the initially undamaged structure. These data sets are used to find the probability, using Bayesian updating, that the model parameters (from a later, possibly damaged state) are less than a specified fraction of the initial model stiffness parameters. A high likelihood is taken as an indication that damage is present.

Sohn et al. [64] pose the process of structural health monitoring in the context of statistical pattern recognition. A control chart provides a statistical framework for monitoring future measurements and identifying when new data are inconsistent with past data. Damage sensitive features are chosen by fitting an autoregressive model to the measured time-series from the undamaged model. When future measurements are evaluated according to these features, a statistically significant number of features outside of the control limits indicate a damaged state.

### 6.2.8 Methods based on dynamically measured flexibility

Changes in the static behaviour of structures can be predicted by using their dynamically measured flexibility matrices. In this group of identification methods, damage is typically detected by comparing the flexibility matrix from the damaged structure to the flexibility matrix from the undamaged structure. If a flexibility matrix is not available for the undamaged structure, it can be estimated using a FEM model. The mass-normalized measured mode shapes and frequencies can be used to estimate the measured flexibility matrix. These measured mode shapes and frequencies usually contain only the lower frequency modes, therefore the estimated flexibility matrix is not exact, and is sensitive to mode changes in the lower frequency range.

It was concluded [53], using experimental evidence and several numerical examples, that damage can be located and the severity of damage estimated based on measured flexibility changes. Only the first two measured modes of the structure were used. Zhang and Aktan [78], used the measured flexibility matrix to calculate the curvatures of a structure subject to uniform loading. They found that changes in these curvatures are a sensitive indicator of local damage.

The dynamically measured stiffness matrix of a structure can be computed as the pseudo-inverse of the dynamically measured flexibility matrix. Dynamically measured mass and damping matrices can also be estimated. Methods have been developed that

use changes in these matrices to identify damage location and severity.

The structural stiffness matrix $\overline{\overline{\mathbf{K}}}_a$ and the measured flexibility matrix $\overline{\overline{\mathbf{F}}}_e$ are used in the *unity check method* to define an error matrix as an indicator of the degree to which the inverse relationship between these two matrices is satisfied. The measured flexibility matrix is singular if all modes were not used to obtain it. Even if all modes are included, the matrix is still ill-conditioned, making the inversion very sensitive to experimental errors. The error matrix is therefor defined as $\overline{\overline{\mathbf{E}}} = \overline{\overline{\mathbf{F}}}_e.\overline{\overline{\mathbf{K}}}_a - \overline{\overline{\mathbf{I}}}$. Lim predicted the damage location by noting in each column of the error matrix, the entry with the largest magnitude. In later work [38] Lim defined a damage detection method to estimate stiffness changes in damaged elements in a least-squares way, based on the unity check error. He updates scaling factors for stiffness submatrices, with each submatrix corresponding to a structural element.

The *stiffness error matrix method* is based on calculating an error matrix by relating the flexibility change in the structure to the undamaged stiffness matrix of the structure, and was presented by He and Ewins [28]. This method is dependent on the number of modes used to estimate the flexibility matrix and on the type of matrix reduction used [26].

### 6.2.9 Non-linear methods

Many damage mechanisms are non-linear in their behaviour. A crack, that opens and closes as the structure vibrates, is a good example of such a mechanism. The identification of features that indicate non-linear response can be a very effective means of detecting the presence of damage in a structure that originally exhibited linear response. The damage location methods described thus far use linear techniques and models to detect damage. Lately, the need for developing methods to analyse and detect non-linear effects has been recognised and several authors published related work. Methods using wavelets and time-frequency domain transformation show promise.

Lin and Ewins [40] presented a technique for detecting a structural non-linearity, based on a model update technique. The measured eigenvectors and eigenvalues at two response levels are used with the original mass and stiffness matrix of the structure to calculate a matrix by considering the equations of motion. This matrix is used to find the stiffness non-linearity.

When an assumed linear system is subjected to a Gaussian load process, it is expected that the acceleration response amplitudes will also follow a Gaussian probability distribution function. Deviations of the acceleration response amplitudes from a Gaussian probability distribution function have been successfully used to identify that loose parts were present in such a system [30].

Morlet wavelet transformations were used to study damage in a FEM simulated cantilever beam [68]. When the crack was sufficiently large, the influence of the opening and closing behaviour of the crack could be observed in the amplitude of the wavelet transform.

### 6.2.10 Neural networks

Neural networks [5] are increasingly used to determine the location and severity of damage in complex structures. Neural networks are able to treat damage mechanisms implicitly, so that it is not necessary to model the structure in so much detail. The method can also deal with non-linear damage mechanisms. Models are still required to provide the training cases for the networks. There will always be systematic errors between the model used for training and the actual structure. For success, neural networks require that the essential features in the damaged structure are represented in the training data. Genetic algorithms and neural networks require a huge amount of computation for structures of practical complexity. The most commonly used neural network is the multilayer perceptron (MLP) trained by back-propagation. The back-propagation algorithm is a stochastic steepest descent learning rule. The back-propagation neural network consists of a system of functions. In each neuron of one layer the outputs of the underlying layer are multi-

plied by weights, summed, and then shifted by a bias. These values are then used as the inputs to the next layer. Once an architecture for the network is chosen, the actual back propagation learning algorithm is a way of adjusting the weights and biases by minimizing the error between the predicted and measured outputs.

## 6.3 Problems related to existing methods.

### 6.3.1 Systematic errors

Systematic errors arise from the fact that a prior finite element model is often used in damage identification. The use of this prior model of the undamaged structure is necessary, because it encodes our knowledge of the physical behaviour of the structure and the incomplete set of measurements requires extra information from the model for damage to be identified. However, the prior model will never be perfect and the damage identification methods discussed above have great difficulty in distinguishing between these *systematic errors* and the actual damage that is present in the structure. This is especially a problem for methods relying on frequency shifts, since the systematic model error will produce frequency changes that are normally far greater than the frequency shifts caused by the actual damage.

### 6.3.2 Effect of frequency range

The frequency range used in damage identification has a great influence on the application possibilities and the resolution of results. High frequency excitations can accurately pinpoint the location of damage, but the applications are limited to local identification methods, because the sensors and actuator must be close to the damage location. Low frequency excitation allows for fewer sensors to be used, since the sensors need not be so close to the damaged area, but the wavelengths of the low frequency modes are too large to precisely identify damage.

### 6.3.3 Environmental effects

Environmental effects, such as temperature changes or the absorption of moisture by concrete during damp weather, often have a significant influence on the stiffness or mass of a structure, thereby influencing the response of the structure under excitation. These effects are difficult to predict and also change from day to day.

### 6.3.4 Strength vs. stiffness

Most damage detection methods are based on the fact that damage will change the stiffness of the structure, thereby influencing its response to loading, and making it possible to detect this change in response using measurement data. However, in some cases this assumption does not hold true. For example, in a concrete bridge with tensioned steel reinforcement cables, the bridge derives its stiffness from the concrete deck, but this stiffness is dependent on the concrete remaining under compression. The steel cables keep the concrete deck under compression and should they fail the bridge is liable to collapse, since the concrete has very little stiffness under tension. Corrosion of the steel cables will therefore be difficult to detect using the methods described above, because the stiffness of the bridge will only change significantly after the steel cables have failed.

# Chapter 7

# Development of an algorithm for model parameter estimation in static systems using several experiments

## 7.1 Introduction

The inverse finite element formulation for static iFEM force and response estimation [44] is described in Chapter 2 and referred to as the static iFEM XU algorithm. In this chapter the iFEM XU algorithm is extended to create a new algorithm that allows for model parameter estimation in addition to force and response estimation, which is referred to as the static iFEM XUA algorithm.

**Static iFEM XU algorithm** In this formulation [44] the structure is modeled using the finite element method. This gives the linear system of equations $\overline{\overline{\mathbf{K}}}.\overline{\mathbf{X}} = \overline{\overline{\mathbf{H}}}.\overline{\mathbf{U}} + \overline{\mathbf{R}}$ where $\overline{\mathbf{X}}$ are the nodal displacements and $\overline{\overline{\mathbf{H}}}.\overline{\mathbf{U}} + \overline{\mathbf{R}}$ are the nodal forces. The forces are decomposed into a known part $\overline{\mathbf{R}}$, and an unknown part $\overline{\overline{\mathbf{H}}}.\overline{\mathbf{U}}$, where $\overline{\mathbf{U}}$ are unknown force coefficients. Chapter 2 presents a detailed explanation.

To obtain a stable estimate of $\overline{\mathbf{U}}$ and $\overline{\mathbf{X}}$ when measurement information on both is available, a cost function is introduced. The cost is a quadratic function of the difference

between estimated and measured displacements and of the external forces. The estimate is then found by minimizing the cost function under the constraint $\overline{\overline{\mathbf{K}}}.\overline{\mathbf{X}} = \overline{\overline{\mathbf{H}}}.\overline{\mathbf{U}} + \overline{\mathbf{R}}$.

Using Lagrange multipliers to solve this constrained optimisation problem leads to a system of equations with $\overline{\mathbf{X}}$, $\overline{\mathbf{U}}$ and the Lagrange multipliers as unknowns. Such a system can be seen as the matrix of a mixed finite element with displacements, external forces and Lagrange multipliers as nodal degrees of freedom. Such elements can then be assembled and boundary conditions applied using the classical procedures of finite element analysis.

**Static iFEM XUA algorithm for a single experiment** The static iFEM XU algorithm, described above, assumes the system matrices $\overline{\overline{\mathbf{K}}}$ and $\overline{\overline{\mathbf{H}}}$ to be known exactly. In reality, the stiffness matrix $\overline{\overline{\mathbf{K}}}$ of a structure will be subject to uncertainty. This is due to uncertainty on the characteristics of the structure, which can include structural damage. The matrix $\overline{\overline{\mathbf{H}}}$ transforms force coefficients into nodal consistent forces and is calculated according to Equation 2.5. The value of this matrix depends on the geometry of the modelled structure, which may also be subject to uncertainty. Explicitly introducing these uncertainties by defining a parameterised model will allow estimating the values and variance of the uncertain parameters.

It is shown here how the iFEM XU algorithm can be adapted to estimate model parameters in addition to forces and response, when measurement data from a single experiment is available. To this purpose model parameters must be introduced.

As an example of such parameterisation, uncertainty on the stiffness matrix, $\overline{\overline{\mathbf{K}}}$, is introduced by stating that $\overline{\overline{\mathbf{K}}} = \overline{\overline{\mathbf{K}}}_o + \sum_i \overline{\overline{\mathbf{K}}}_i.\alpha_i$, where $\overline{\overline{\mathbf{K}}}_o$ is the initial stiffness matrix, $\overline{\overline{\mathbf{K}}}_i$ partial stiffness matrices related to model parameters $\alpha_i$, and $\overline{\overline{\mathbf{K}}}$ is the updated system stiffness matrix. This can also be written as $\overline{\overline{\mathbf{K}}} = \overline{\overline{\mathbf{K_o}}} + \overline{\overline{\mathbf{T}}}_K.\overline{\alpha}$, where $\overline{\overline{\mathbf{T}}}_K$ is a third order tensor containing stiffness components (a stacked form of all the $\overline{\overline{\mathbf{K}}}_i$) and $\overline{\alpha}$ is a vector of model parameters.

This development has the severe limitation of only allowing a single experiment to be considered.

**Static iFEM XUA algorithm for multiple experiments** To allow for more than one experiment to be handled, the above development is modified so that the variance of the estimated $\overline{\alpha}$ is updated to reflect information from each experiment. This is done by solving the linear system of equations of the static iFEM XU algorithm to obtain an optimal solution of $\overline{\mathbf{X}}$ and $\overline{\mathbf{U}}$ as a function of the unknown model parameters $\overline{\alpha}$. Back substituting $\overline{\mathbf{X}}(\overline{\alpha})$ and $\overline{\mathbf{U}}(\overline{\alpha})$ into the cost function gives the cost for one experiment as a function of $\overline{\alpha}$. Summing the costs of all experiments and deriving with respect to $\overline{\alpha}$ gives an expression that can be solved to obtain the optimal value of $\overline{\alpha}$.

Initially, this approach required the inversion of large matrices when calculating the updated variance and estimating the model parameters. To reduce computing times it was considered to follow a steepest decent approach, an optimisation approach that requires only the gradient of the optimisation function with respect to the parameters, and not its jacobian. Instead, a solution was found that avoids the inversion of the large system matrices and computes the jacobian by solving linear systems of equations. This opened the way for a fast full jacobian solver, which was implemented.

Non-linear systems can also be handled: In an incremental non-linear analysis, a linearised system equilibrium equation is used as the approximate equilibrium equation over each increment.

An alternative approach for handling data from multiple experiments was also investigated, but complicated mathematical operations are required for this approach, rendering it impractical. This alternative approach is attached as Appendix B.

**Computer implementation** A computer implementation of the final development was created to test the theory. This computer implementation (ISPI) has certain limitations, which are discussed, and suggestions are made for future work.

## 7.2 Theory for static model parameter estimation using one experiment

### 7.2.1 Parameterized equilibrium equation

Given a model, the equilibrium relation between the internal and external forces are

$$\overline{\mathbf{f}}(\overline{\alpha}, \overline{\mathbf{X}}, \overline{\mathbf{U}}) = \overline{\mathbf{R}}_{external}(\overline{\mathbf{U}}) - \overline{\mathbf{R}}_{internal}(\overline{\alpha}, \overline{\mathbf{X}}) = \overline{\mathbf{0}} \tag{7.1}$$

where $\overline{\mathbf{X}}$ is the vector of nodal response values, $\overline{\mathbf{U}}$ are the unknown force coefficients, and $\overline{\alpha}$ contain model parameters.

A linear Taylor development of this at $[\overline{\mathbf{X}_0}, \overline{\mathbf{U}_0}, \overline{\alpha_0}]$ yields,

$$\begin{aligned} \overline{\mathbf{f}}(\overline{\mathbf{dX}}, \overline{\mathbf{dU}}, \overline{\mathbf{d}\alpha}) &= \underbrace{\overline{\mathbf{f}}(\overline{\alpha_0}, \overline{\mathbf{X}_0}, \overline{\mathbf{U}_0})}_{-\overline{\mathbf{R}}} + \underbrace{\overline{\nabla_X \mathbf{f}}}_{\overline{\overline{\mathbf{K}}}} . \overline{\mathbf{dX}} + \underbrace{\overline{\nabla_U \mathbf{f}}}_{-\overline{\overline{\mathbf{H}}}} . \overline{\mathbf{dU}} + \underbrace{\overline{\nabla_\alpha \mathbf{f}}}_{-\overline{\overline{\mathbf{G}}}} . \overline{\mathbf{d}\alpha} \\ &= \overline{\overline{\mathbf{K}}} . \overline{\mathbf{dX}} - \overline{\overline{\mathbf{H}}} . \overline{\mathbf{dU}} - \overline{\overline{\mathbf{G}}} . \overline{\mathbf{d}\alpha} - \overline{\mathbf{R}} \\ &= \overline{\mathbf{0}} \end{aligned} \tag{7.2}$$

where $\overline{\overline{\mathbf{K}}}$ is the stiffness matrix of the structure, $\overline{\mathbf{R}}$ being the externally applied consistent nodal forces. $\overline{\overline{\mathbf{H}}}$ transforms the unknown force coefficients $\overline{\mathbf{U}}$ (that describe an unknown force distribution) into consistent forces. Changes in model parameters $\overline{\alpha}$ will result in internal structural forces and $\overline{\overline{\mathbf{G}}}$ transforms these into consistent forces.

Equation 7.2 has no unique solution, since it contains more unknowns than equations. An approach is needed that allows finding the most probable values of $\overline{\mathbf{X}}$, $\overline{\mathbf{U}}$ and $\overline{\alpha}$ that verify the equilibrium equation 7.2.

### 7.2.2 The cost function

Based on measurement data and engineering judgment, the user will be able to choose a prior probability distribution of $\overline{\mathbf{X}}$, $\overline{\mathbf{U}}$ and $\overline{\alpha}$. Maximising a probability distribution function (PDF) is equivalent to minimising a cost function $J$ obtained as $J = -log(PDF)$. This cost function is locally approximated as a second order Taylor development at $[\overline{\mathbf{X_0}}, \overline{\mathbf{U_0}}, \overline{\alpha_0}]$.

$$\begin{aligned} J(\overline{\mathbf{dX}}, \overline{\mathbf{dU}}, \overline{\mathbf{d}\alpha}) \;=\; & \tfrac{1}{2}\overline{\mathbf{dX}}^T.\overline{\overline{\mathbf{Q}}}_{xx}.\overline{\mathbf{dX}} + \tfrac{1}{2}.\overline{\mathbf{dU}}^T.\overline{\overline{\mathbf{Q}}}_{uu}.\overline{\mathbf{dU}} + \tfrac{1}{2}.\overline{\mathbf{d}\alpha}^T.\overline{\overline{\mathbf{Q}}}_{\alpha\alpha}.\overline{\mathbf{d}\alpha} \\ & + \overline{\mathbf{dX}}^T.\overline{\overline{\mathbf{Q}}}_{xu}.\overline{\mathbf{dU}} + \overline{\mathbf{dX}}^T.\overline{\overline{\mathbf{Q}}}_{x\alpha}.\overline{\mathbf{d}\alpha} + \overline{\mathbf{dU}}^T.\overline{\overline{\mathbf{Q}}}_{u\alpha}.\overline{\mathbf{d}\alpha} \\ & + \overline{\mathbf{Q}}_x.\overline{\mathbf{dX}} + \overline{\mathbf{Q}}_u.\overline{\mathbf{dU}} + \overline{\mathbf{Q}}_\alpha.\overline{\mathbf{d}\alpha} \end{aligned} \tag{7.3}$$

If the probability distribution function is Gaussian, then the cost function is quadratic and the above approximation is exact.

### 7.2.3 Constrained optimisation

To minimise the cost (Equation 7.3), while verifying equilibrium (Equation 7.2), a constrained optimization problem is solved. Lagrange observed that, at a point $[\overline{\mathbf{dX}}, \overline{\mathbf{dU}}, \overline{\mathbf{d}\alpha}]$ where $J(\overline{\mathbf{dX}}, \overline{\mathbf{dU}}, \overline{\mathbf{d}\alpha})$ is minimum while the set of conditions $\overline{\mathbf{f}}(\overline{\mathbf{dX}}, \overline{\mathbf{dU}}, \overline{\mathbf{d}\alpha}) = 0$ is respected, the gradient of $J(\overline{\mathbf{dX}}, \overline{\mathbf{dU}}, \overline{\mathbf{d}\alpha})$ with respect to $[\overline{\mathbf{dX}}, \overline{\mathbf{dU}}, \overline{\mathbf{d}\alpha}]$ is in the subspace spanned by the gradients of $\overline{\mathbf{f}}$. There exist Lagrange multipliers $\overline{\lambda}$, such that $\nabla J' = 0$, for gradients taken with respect to $\overline{\mathbf{dX}}$, $\overline{\mathbf{dU}}$ and $\overline{\mathbf{d}\alpha}$, with $J'$ being the augmented Lagrangian given in Equation 7.4.

$$\begin{aligned} J' \;=\; & \overline{\lambda}^T.\overline{\mathbf{f}} + J \\ =\; & \overline{\lambda}^T.(\overline{\overline{\mathbf{K}}}.\overline{\mathbf{dX}} - \overline{\overline{\mathbf{H}}}.\overline{\mathbf{dU}} - \overline{\overline{\mathbf{G}}}.\overline{\mathbf{d}\alpha} - \overline{\mathbf{R}}) \\ & + \tfrac{1}{2}\overline{\mathbf{dX}}^T.\overline{\overline{\mathbf{Q}}}_{xx}.\overline{\mathbf{dX}} + \tfrac{1}{2}.\overline{\mathbf{dU}}^T.\overline{\overline{\mathbf{Q}}}_{uu}.\overline{\mathbf{dU}} + \tfrac{1}{2}.\overline{\mathbf{d}\alpha}^T.\overline{\overline{\mathbf{Q}}}_{\alpha\alpha}.\overline{\mathbf{d}\alpha} \\ & + \overline{\mathbf{dX}}^T.\overline{\overline{\mathbf{Q}}}_{xu}.\overline{\mathbf{dU}} + \overline{\mathbf{dX}}^T.\overline{\overline{\mathbf{Q}}}_{x\alpha}.\overline{\mathbf{d}\alpha} + \overline{\mathbf{dU}}^T.\overline{\overline{\mathbf{Q}}}_{u\alpha}.\overline{\mathbf{d}\alpha} \\ & + \overline{\mathbf{Q}}_x.\overline{\mathbf{dX}} + \overline{\mathbf{Q}}_u.\overline{\mathbf{dU}} + \overline{\mathbf{Q}}_\alpha.\overline{\mathbf{d}\alpha} \end{aligned} \tag{7.4}$$

Deriving this augmented Lagrangian with respect to $\overline{\mathbf{dX}}$, $\overline{\mathbf{dU}}$ and $\overline{\lambda}$ respectively, Equations 7.5, 7.6 and 7.7 are obtained.

$$\begin{aligned} \nabla_{\mathbf{dX}}\mathbf{J}' &= \overline{\overline{\mathbf{K}}}^T.\overline{\lambda} + \overline{\overline{\mathbf{Q}}}_{xx}.\overline{\mathbf{dX}} + \overline{\overline{\mathbf{Q}}}_{xu}.\overline{\mathbf{dU}} + \overline{\overline{\mathbf{Q}}}_{x\alpha}.\overline{\mathbf{d\alpha}} + \overline{\mathbf{Q}}_x \\ &= \overline{\mathbf{0}} \end{aligned} \tag{7.5}$$

$$\begin{aligned} \nabla_{\mathbf{dU}}\mathbf{J}' &= -\overline{\overline{\mathbf{H}}}^T.\overline{\lambda} + \overline{\overline{\mathbf{Q}}}_{uu}.\overline{\mathbf{dU}} + \overline{\overline{\mathbf{Q}}}_{xu}^T.\overline{\mathbf{dX}} + \overline{\overline{\mathbf{Q}}}_{u\alpha}.\overline{\mathbf{d\alpha}} + \overline{\mathbf{Q}}_u \\ &= \overline{\mathbf{0}} \end{aligned} \tag{7.6}$$

$$\begin{aligned} \nabla_{\mathbf{d\alpha}}\mathbf{J}' &= -\overline{\overline{\mathbf{G}}}^T.\overline{\lambda} + \overline{\overline{\mathbf{Q}}}_{\alpha\alpha}.\overline{\mathbf{d\alpha}} + \overline{\overline{\mathbf{Q}}}_{x\alpha}^T.\overline{\mathbf{dX}} + \overline{\overline{\mathbf{Q}}}_{u\alpha}^T.\overline{\mathbf{dU}} + \overline{\mathbf{Q}}_\alpha \\ &= \overline{\mathbf{0}} \end{aligned} \tag{7.7}$$

The above three equations, together with Equation 7.2, can be written in matrix form

$$\begin{bmatrix} \overline{\overline{\mathbf{0}}} & \overline{\overline{\mathbf{K}}} & -\overline{\overline{\mathbf{H}}} & -\overline{\overline{\mathbf{G}}} \\ \overline{\overline{\mathbf{K}}}^T & \overline{\overline{\mathbf{Q}}}_{xx} & \overline{\overline{\mathbf{Q}}}_{xu} & \overline{\overline{\mathbf{Q}}}_{x\alpha} \\ -\overline{\overline{\mathbf{H}}}^T & \overline{\overline{\mathbf{Q}}}_{xu}^T & \overline{\overline{\mathbf{Q}}}_{uu} & \overline{\overline{\mathbf{Q}}}_{u\alpha} \\ -\overline{\overline{\mathbf{G}}}^T & \overline{\overline{\mathbf{Q}}}_{x\alpha}^T & \overline{\overline{\mathbf{Q}}}_{u\alpha}^T & \overline{\overline{\mathbf{Q}}}_{\alpha\alpha} \end{bmatrix} \cdot \begin{bmatrix} \overline{\lambda} \\ \overline{\mathbf{dX}} \\ \overline{\mathbf{dU}} \\ \overline{\mathbf{d\alpha}} \end{bmatrix} = \begin{bmatrix} \overline{\mathbf{R}} \\ -\overline{\mathbf{Q}}_x \\ -\overline{\mathbf{Q}}_u \\ -\overline{\mathbf{Q}}_\alpha \end{bmatrix} \tag{7.8}$$

The above can be seen as the formulation of a type of mixed element. This element has incremental nodal displacements $\overline{\mathbf{dX}}$, nodal external force coefficients $\overline{\mathbf{dU}}$, Lagrange multipliers $\overline{\lambda}$ and nodal model parameter coefficients $\overline{\mathbf{d\alpha}}$ as unknowns, and can be assembled in the usual way. For degrees of freedom where it is known that $\mathrm{U}_i$ is zero, the U-degree of freedom is condensed, just as a displacement degree of freedom is condensed away when the boundary conditions specify that it is fixed. Similarly, one can specify $\overline{\mathbf{d\alpha}}$.

### 7.2.4 Obtaining the matrices

The theory for assembling the stiffness matrix $\overline{\overline{\mathbf{K}}}$ and force vector $\overline{\mathbf{R}}$ is well documented in familiar FEM theory. How to obtain $\overline{\overline{\mathbf{H}}}$, as well as the cost matrices $\overline{\overline{\mathbf{Q}}}$ is described in chapter 2. This section will focus on the matrix $\overline{\overline{\mathbf{G}}}$, its properties and how to compute it.

Equation 7.2 describes the equilibrium equation of an $\overline{\alpha}$ parameterised system as a first order Taylor expansion. According to this equation, the matrix $\overline{\overline{\mathbf{G}}}$ is the derivative

of the consistent force with respect to $\overline{\alpha}$. It is a sensitivity matrix that encodes how the internal force will change for given $\overline{\alpha}$ parameter changes.

**A simple example** Consider a simple static FEM system

$$\overline{\mathrm{f}} = \overline{\overline{\mathbf{K}}}.\overline{\mathbf{X}} - \overline{\mathbf{R}} = \overline{\mathbf{0}} \tag{7.9}$$

If stiffness parameters are introduced so that the stiffness matrix becomes a function of $\overline{\mathrm{d}\alpha}$, it follows from Equation 7.2 that

$$\begin{aligned} \overline{\overline{\mathbf{G}}} &= -\overline{\nabla}_{d\alpha}\overline{\mathrm{f}} \\ &= -\overline{\nabla}_{d\alpha}\left\{\overline{\overline{\mathbf{K}}}(\overline{\mathrm{d}\alpha}).\overline{\mathbf{X}}\right\} \end{aligned} \tag{7.10}$$

Thus, $\overline{\overline{\mathbf{G}}}$ encodes the change of internal force when $\overline{\mathrm{d}\alpha}$ changes for a given deformation. Uncertainty on the stiffness matrix, $\overline{\overline{\mathbf{K}}}$, can be introduced by stating that

$$\begin{aligned} \overline{\overline{\mathbf{K}}}(\overline{\mathrm{d}\alpha}) &= \overline{\overline{\mathbf{K}}}_o + \textstyle\sum_i \overline{\overline{\mathbf{K}}}_i.d\alpha_i \\ &= \overline{\overline{\mathbf{K}}}_o + \overline{\overline{\overline{\mathbf{T}}}}_K.\overline{\mathrm{d}\alpha} \end{aligned} \tag{7.11}$$

where $\overline{\overline{\mathbf{K}}}_o$ is the initial stiffness matrix, $\overline{\overline{\overline{\mathbf{T}}}}_K$ is a third order tensor (of size $nXdof \times nXdof \times n\alpha dof$) containing chosen system stiffness matrices, $\overline{\mathrm{d}\alpha}$ is a vector of incremental weighting coefficients, and $\overline{\overline{\mathbf{K}}}$ is the updated system stiffness matrix. Equation 7.10 then becomes

$$\begin{aligned} \overline{\overline{\mathbf{G}}} &= -\overline{\nabla}_{d\alpha}\left\{\left(\overline{\overline{\mathbf{K}}}_o + \overline{\overline{\overline{\mathbf{T}}}}_K.\overline{\mathrm{d}\alpha}\right).\overline{\mathbf{X}}\right\} \\ &= -\overline{\nabla}_{d\alpha}\left\{\overline{\overline{\mathbf{K}}}_o.\overline{\mathbf{X}} + \overline{\overline{\overline{\mathbf{T}}}}_K^{T132}.\overline{\mathbf{X}}.\overline{\mathrm{d}\alpha}\right\} \\ &= -\overline{\overline{\overline{\mathbf{T}}}}_K^{T132}.\overline{\mathbf{X}} \end{aligned} \tag{7.12}$$

**General theory** The displacement field $\overline{\mathbf{x}}(\overline{\xi})$ across an element can be described as a function of the position $\overline{\xi}$ in the element, with the total displacement being the sum of chosen shape functions $\overline{\overline{\mathbf{N}}}_x(\overline{\xi})$ multiplied by the vector of nodal response values $\overline{\mathbf{X}}$, so that $\overline{\mathbf{x}}(\overline{\xi}) = \overline{\overline{\mathbf{N}}}_x(\overline{\xi}).\overline{\mathbf{X}}$.

Under this assumption, the stiffness matrix of a beam element subject to bending can be computed as

$$\overline{\overline{\mathbf{K}}} = \int_{\xi} \overline{\overline{\mathbf{N}}}_x'^T(\bar{\xi}).\bar{\bar{\mathbf{c}}}.\overline{\overline{\mathbf{N}}}_x''(\bar{\xi})d\xi \tag{7.13}$$

where $\bar{\bar{\mathbf{c}}}$ is the constitutive matrix.

If stiffness parameters are introduced, so that the stiffness $\overline{\overline{\mathbf{K}}}$ becomes a function of $\overline{\mathbf{d}\alpha}$, it follows that

$$\begin{aligned} \overline{\overline{\mathbf{G}}} &= -\overline{\nabla}_{d\alpha}\left\{\overline{\overline{\mathbf{K}}}(\overline{\mathbf{d}\alpha}).\overline{\mathbf{X}}\right\} \\ &= -\int_{\xi} \overline{\overline{\mathbf{N}}}_x'^T(\bar{\xi}).\overline{\nabla}_{d\alpha}\left\{\bar{\bar{\mathbf{c}}}(\overline{\mathbf{d}\alpha})\right\}.\overline{\overline{\mathbf{N}}}_x''(\bar{\xi})d\xi.\overline{\mathbf{X}} \end{aligned} \tag{7.14}$$

The model parameter field $\overline{\mathbf{d}\alpha}(\bar{\xi})$ can also be described as the sum of shape functions $\overline{\overline{\mathbf{N}}}_{d\alpha}(\bar{\xi})$ multiplied by the vector of nodal model parameter values $\overline{\mathbf{d}\alpha}$, so that $\overline{\mathbf{d}\alpha}(\bar{\xi}) = \overline{\overline{\mathbf{N}}}_{d\alpha}(\bar{\xi}).\overline{\mathbf{d}\alpha}$.

If, for example, the constitutive matrix is parameterised such that $\bar{\bar{\mathbf{c}}}(\overline{\mathbf{d}\alpha}) = \bar{\bar{\mathbf{c}}}_0.\overline{\mathbf{d}\alpha}^T(\bar{\xi})$, Equation 7.14 becomes

$$\begin{aligned} \overline{\overline{\mathbf{G}}} &= -\int_{\xi} \overline{\overline{\mathbf{N}}}_x'^T(\bar{\xi}).\overline{\nabla}_{d\alpha}\left\{\bar{\bar{\mathbf{c}}}_0.\overline{\mathbf{d}\alpha}^T(\bar{\xi})\right\}.\overline{\overline{\mathbf{N}}}_x''(\bar{\xi})d\xi.\overline{\mathbf{X}} \\ &= -\int_{\xi} \overline{\overline{\mathbf{N}}}_x'^T(\bar{\xi}).\overline{\nabla}_{d\alpha}\left\{\bar{\bar{\mathbf{c}}}_0.(\overline{\overline{\mathbf{N}}}_{d\alpha}(\bar{\xi}).\overline{\mathbf{d}\alpha})^T\right\}.\overline{\overline{\mathbf{N}}}_x''(\bar{\xi})d\xi.\overline{\mathbf{X}} \\ &= -\underbrace{\int_{\xi} \overline{\overline{\mathbf{N}}}_x'^T(\bar{\xi}).\bar{\bar{\mathbf{c}}}_0.\overline{\overline{\mathbf{N}}}_{d\alpha}^T(\bar{\xi}).\overline{\overline{\mathbf{N}}}_x''(\bar{\xi})d\xi}_{\bar{\bar{\mathbf{T}}}_K^{T132}}.\overline{\mathbf{X}} \end{aligned} \tag{7.15}$$

## 7.3 Theory for static model parameter estimation using several experiments

The development of the Section 7.2 allows the estimation of model parameters, forces and the complete response of a structure based on a limited set of measurements of the response of the structure. However, only data from a single experiment can be included. In this section, the theory is adapted to allow data from several experiments to be included. While the forces acting on a structure and the structure's response will differ for

each experiment, model parameters (such as those used to estimate structural damage or material properties) can be assumed unchanged from one experiment to another. For this reason, the inclusion of data from several experiments, where different load configurations can activate different response patterns, will add valuable information for the estimation of constant model parameters.

### 7.3.1 An alternative constrained optimisation approach

Equations 7.2 and 7.3 could be used to do a constrained minimisation of $J$ with respect to $\overline{\mathbf{dU}}$, $\overline{\mathbf{dX}}$, $\overline{\lambda}$ and $\overline{\mathbf{d}\alpha}$. This approach was followed in the previous section, but does not allow the inclusion of data from more than one experiment. To include multiple experiments, one approach is to get an expression for $J_{opt}(\overline{\mathbf{d}\alpha})$ for each experiment. This is done by doing a constrained minimisation of $J$ with respect to $\overline{\mathbf{dU}}$, $\overline{\mathbf{dX}}$, and $\overline{\lambda}$ for each experiment as a function of $\overline{\mathbf{d}\alpha}$. The expression for the sum of $J_{opt}(\overline{\mathbf{d}\alpha})$ for all experiments is then computed. The most probable value of $\overline{\mathbf{d}\alpha}$ for the set of experiments is found by deriving this sum with respect to $\overline{\mathbf{d}\alpha}$.

For each experiment, for a given value of $\overline{\mathbf{d}\alpha}$, Equations 7.5, 7.6, 7.7 and 7.2 yield a system of the form:

$$\begin{bmatrix} \overline{\overline{\mathbf{0}}} & \overline{\overline{\mathbf{K}}} & -\overline{\overline{\mathbf{H}}} \\ \overline{\overline{\mathbf{K}}} & \overline{\overline{\mathbf{Q}}}_{xx} & \overline{\overline{\mathbf{Q}}}_{xu} \\ -\overline{\overline{\mathbf{H}}}^T & \overline{\overline{\mathbf{Q}}}_{xu}^T & \overline{\overline{\mathbf{Q}}}_{uu} \end{bmatrix} \cdot \begin{bmatrix} \overline{\lambda} \\ \overline{\mathbf{dX}} \\ \overline{\mathbf{dU}} \end{bmatrix} = \begin{bmatrix} \overline{\mathbf{dR}} + \overline{\overline{\mathbf{G}}}.\overline{\mathbf{d}\alpha} \\ -\overline{\mathbf{Q}}_x - \overline{\overline{\mathbf{Q}}}_{x\alpha}.\overline{\mathbf{d}\alpha} \\ -\overline{\mathbf{Q}}_u - \overline{\overline{\mathbf{Q}}}_{u\alpha}.\overline{\mathbf{d}\alpha} \end{bmatrix} \tag{7.16}$$

Inverting this system gives $\overline{\mathbf{dX}}$ and $\overline{\mathbf{dU}}$ as linear functions of $\overline{\mathbf{d}\alpha}$.

$$\begin{bmatrix} \overline{\mathbf{dX}} \\ \overline{\mathbf{dU}} \end{bmatrix} = \overline{\overline{\mathbf{L}}}.\overline{\mathbf{d}\alpha} + \overline{\mathbf{N}} \tag{7.17}$$

$\overline{\mathbf{dU}}(\overline{\mathbf{d}\alpha})$ and $\overline{\mathbf{dX}}(\overline{\mathbf{d}\alpha})$ can now be replaced into the cost function (Equation 7.3) to give the optimum value of the cost function for one experiment as a function of $\overline{\mathbf{d}\alpha}$.

Since we have several experiments $i$, the cost for each experiment $J_{opt}(\overline{\mathbf{d}\alpha})_i$ is computed as above for each experiment and summed to give the total cost $J_{total}(\overline{\mathbf{d}\alpha})$ in Equation

7.18. This total cost is of the form $J_{total}(\overline{\mathrm{d}\alpha}) = \overline{\mathrm{d}\alpha}^T.\overline{\overline{Q}_{\alpha\alpha_{updated}}}.\overline{\mathrm{d}\alpha} + \overline{Q}_{\alpha_{updated}}.\overline{\mathrm{d}\alpha}$, with $\overline{\overline{Q}_{\alpha\alpha_{updated}}}$ describing the updated variance of the parameter estimate.

$$\begin{aligned} J_{total}(\overline{\mathrm{d}\alpha}) &= \overline{\mathrm{d}\alpha}.\overline{\overline{Q}_{\alpha\alpha}}.\overline{\mathrm{d}\alpha} + \overline{Q}_{\alpha}.\overline{\mathrm{d}\alpha} + \textstyle\sum_i (J_{opt}(\overline{\mathrm{d}\alpha}))_i \\ &= \overline{\mathrm{d}\alpha}.\overline{\overline{Q}_{\alpha\alpha_{updated}}}.\overline{\mathrm{d}\alpha} + \overline{Q}_{\alpha_{updated}}.\overline{\mathrm{d}\alpha} \end{aligned} \tag{7.18}$$

with

$$\overline{\overline{Q}_{\alpha\alpha_{updated}}} = \overline{\overline{Q}_{\alpha\alpha}} + \textstyle\sum_i (\frac{1}{2}\overline{\overline{L}}_i^T.\overline{\overline{Q}_{vv_i}}.\overline{\overline{L}}_i + \overline{\overline{L}}_i^T.\overline{\overline{Q}_{v\alpha_i}}) \tag{7.19}$$

$$\overline{Q}_{\alpha_{updated}} = \overline{Q}_{\alpha} + \textstyle\sum_i (\overline{\overline{L}}_i^T.\overline{\overline{Q}_{vv_i}}.\overline{N}_i + \overline{N}_i^T.\overline{\overline{Q}_{v\alpha_i}}) \tag{7.20}$$

$$\overline{\overline{Q}}_{vv} = \begin{bmatrix} \overline{\overline{Q}}_{xx} & \overline{\overline{Q}}_{xu} \\ \overline{\overline{Q}}_{xu}^T & \overline{\overline{Q}}_{uu} \end{bmatrix} \tag{7.21}$$

$$\overline{\overline{Q}}_{v\alpha} = \begin{bmatrix} \overline{\overline{Q}}_{x\alpha} \\ \overline{\overline{Q}}_{u\alpha} \end{bmatrix} \tag{7.22}$$

The optimum value of $\overline{\mathrm{d}\alpha}$ for the set of experiments is found by requesting that $\overline{\nabla}_{d\alpha} J_{total} = 0$.

$$\overline{\mathrm{d}\alpha} = \overline{\overline{Q}_{\alpha\alpha_{updated}}}^{-1}.\overline{Q}_{\alpha_{updated}} \tag{7.23}$$

### 7.3.2 Computational sequence

The computational sequence for the algorithm described above is as follows, for each iteration $k$:

1. For each experiment $i$, at $[\overline{X}_k, \overline{U}_k, \overline{\alpha}_k]_i$: Approximate the equilibrium relation as a linear Taylor development to find $\overline{\overline{K}}$, $\overline{\overline{H}}$ and $\overline{\overline{G}}$. Approximate the cost function $J = -log(PDF_{prior})$ as a second order (quadratic) Taylor development to find $\overline{\overline{Q}}_{xx}$, $\overline{\overline{Q}}_{uu}$, $\overline{\overline{Q}}_{\alpha\alpha}$, $\overline{\overline{Q}}_{xu}$, $\overline{\overline{Q}}_{x\alpha}$, $\overline{\overline{Q}}_{u\alpha}$, $\overline{Q}_x$, $\overline{Q}_u$ and $\overline{Q}_{\alpha}$.

2. For each experiment, calculate $\overline{\overline{\mathbf{L}}}$, $\overline{\mathbf{N}}$, $\overline{\overline{\mathbf{Q}}}_{vv}$ and $\overline{\overline{\mathbf{Q}}}_{v\alpha}$ (Equations 7.16, 7.17, 7.21 and 7.22).

3. Calculate $\overline{\overline{\mathbf{Q}_{\mathbf{aa}}}}_{updated}$ and $\overline{\mathbf{Q}_{\mathbf{a}}}_{updated}$ from Equation 7.19 and 7.20.

4. Find $\overline{\mathbf{d}\alpha}$ from Equation 7.23.

5. For each experiment, calculate $\overline{\mathbf{dX}}$ and $\overline{\mathbf{dU}}$ from Equation 7.17.

6. For each experiment, update the position and force vectors: $\overline{\mathbf{X}}_{k+1} = \overline{\mathbf{X}}_k + \overline{\mathbf{dX}}$ and $\overline{\mathbf{U}}_{k+1} = \overline{\mathbf{U}}_k + \overline{\mathbf{dU}}$.

7. Update the parameter vector $\overline{\alpha}_{k+1} = \overline{\alpha}_k + \overline{\mathbf{d}\alpha}$.

8. Check for convergence. If convergence has not been reached, increment $k = k + 1$ and repeat from step 1.

### 7.3.3 Comments

$J$ and $\overline{\mathbf{f}}$ may be completely different for different experiments, including a change in number of degrees of freedom, as long as $\overline{\alpha}$ have the same interpretation in each experiment. This would for example allow for $\overline{\alpha}$ to be interpreted as material properties, with each experiment being done on a different structure with the same material.

In the current development, a linear equilibrium relation and a quadratic cost function is assumed. In practice this will often not be the case and iterative methods are used to handle non-linear equilibrium equations. In the computer implementation the Newton-Raphson technique was implemented. If the equilibrium relation is linear and the cost function is quadratic (a Gaussian probability density function will result in a quadratic cost function [45]), then the first iteration will be an exact solution.

Note that $\overline{\mathbf{dX}}$ and $\overline{\mathbf{dU}}$ are linear functions of $\overline{\mathbf{d}\alpha}$, because the system equilibrium equation (Equation 7.2) has been linearised. If Equation 7.2 were not linearised, $\overline{\mathbf{dX}}$ and $\overline{\mathbf{dU}}$ (Equation 7.17) would have additional quadratic terms, making further contributions

to the cost function. The second order approximation of $\overline{\overline{\mathbf{Q}}}_{\alpha\alpha_{updated}}$ given in Equation 7.8 is therefor inaccurate and the inaccuracy would be significant if $\overline{\overline{\mathbf{Q}}}_{\alpha\alpha_{prior}}$ is small and $\overline{\mathbf{dX}}(\overline{\mathbf{d}\alpha})$ or $\overline{\mathbf{dU}}(\overline{\mathbf{d}\alpha})$ is strongly non-linear. Should this be the case the iteration process will become a pseudo Newton-Raphson iteration, which will result in a lower rate of convergence.

The computation of $\overline{\overline{\mathbf{L}}}$ in Equation 7.17 requires, for each experiment, the inversion of the left hand side matrix of Equation 7.16. This matrix inversion is a costly operation in terms of computing time. The computing time associated with this algorithm is proportional to $nXper.(2 \times nXdof + nUdof)^3$, with $nXper$ the number of experiments, $nXdof$ the number of displacement degrees of freedom, and $nUdof$ the number of unknown force degrees of freedom. For large systems, a significant amount of computing time is required and it was therefore necessary to find a way to decrease computing time. An algorithm was developed that allows to dramatically reduce computing time. This improvement is discussed in the next section.

## 7.4 Improving computing time

The algorithm developed in the previous section allows the inclusion of data from many experiments to accumulate information for model parameter estimation. This algorithm, however, requires the inversion of large matrices and resulting long computing times for large systems. It became increasingly clear that a faster solution was needed.

To address this problem, it was considered to follow a steepest decent approach, an optimisation approach that requires only the gradient $\overline{\mathbf{Q}}_{\alpha}$ of the optimisation function with respect to the parameters, and not its variance $\overline{\overline{\mathbf{Q}}}_{\alpha\alpha}$. This approach was abandoned when the author found a solution that avoids the inversion of the large system matrices and instead, computes the variance by solving linear systems of equations. While it is the same constrained optimisation problem of Section 7.3 that is solved, the improved way of solving it allows to significantly reduce computing time:

The order of complexity of this algorithm is $nXper.(2 \times nXdof + nUdof)^2.n\alpha$, with $nXper$ being the number of experiments, $nXdof$ the number of displacement degrees of freedom, $nUdof$ the number of unknown force degrees of freedom, and $n\alpha$ the number of model parameters. Compared to the previous order of complexity of $nXper.(2 \times nXdof + nUdof)^3$ this algorithm significantly reduces the computer time required to solve large systems, because, in general $n\alpha << 2 \times nXdof + nUdof$. This fast full variance solver was implemented in a prototype software, discussed in the next section.

The new solution is protected by a confidentiality agreement and will not be discussed in detail. It is fully explained in a confidential report [1] owned by Safran Engineering Algorithms cc.

## 7.5 Computer Implementation

The iFEM prototype software SAFRAN was used as a framework within which a computer implementation based on the theory above was created. The implementation of the above theory will be referred to as ISPI, short for Inverse Static Parameter Identification. This early implementation, which was used to generate the examples studied at the end of this chapter, has several limitations. An extensive rebuild of the code was later undertaken to address these limitations (Refer to Section 8.4).

In SAFRAN a structure consists of several element groups, and for each element group it must be specified whether or not the element group allows $U$ degrees of freedom. ISPI now also requires that it is specified whether or not the element group allows $\alpha$ degrees of freedom. In this early implementation, when $\alpha$ degrees of freedom are allowed, each element of the group is defined with one $\alpha$ degree of freedom that corresponds to the Young's modulus $E$ of that element, so that $E_{updated} = E_{original} \cdot (1 + \alpha)$. A more flexible implementation followed later (Refer to Chapter 8, Section 8.4).

In ISPI, each experiment can be specified with a different load and correspondingly

different measurements, each with their own measurement precision. Equilibrium is computed for the entire group of experiments. This is necessary, because the vector $\overline{\alpha}$ is a global variable of the set of experiments, it does not differ for each individual experiment.

The calculated $\alpha$ value for each element is graphically represented by a green line, drawn next to the element at a distance proportional to the value of the $\alpha$. If an element is defined from left to right, a negative $\alpha$ will be drawn below the element and a positive $\alpha$ above the element.

### 7.5.1 Limitations of ISPI

While it can handle several load cases, ISPI can handle only one structural model in an analysis. Consider a situation where experimental data from several different structures, all made from the same material, are to be used to update prior knowledge on a property of the material. There is no theoretical reason that keeps $\alpha$ from referring to such a material property, but since a different model would be needed for each different structure, the present implementation will not be able to handle such a case.

Another limitation is that $\alpha$ degrees of freedom in ISPI are hard-coded to refer to changes in the element's stiffness modulus. This is not ideal. Instead, the user should be able to specify for each element to which element property its $\alpha$ degree of freedom refers.

In the present implementation, each element has only one $\alpha$ degree of freedom, corresponding to a constant changed stiffness along the element. An idea that needs further development is to have more than one $\alpha$ degree of freedom per element, interpolating a field of $\alpha$ along the element. This can correspond to, for example, a beam that is tapered, or a plate-element that does not have uniform thickness.

The algorithm computes equilibrium for an entire given group of experiments at each iteration. For a large number of experiments, this might make convergence difficult and time-consuming. It would be advantageous to run an analysis for a group of experiments

and obtain the calculated $\alpha$ values and the variance of this estimate, an updated $\overline{\overline{\mathbf{Q}}}_{\alpha\alpha}$. These values could then be used in a new analysis, together with a second group of experiments, to further update these values by the information gained from the second group of experiments. (In such a case the $\alpha$ values are adjusted according to the information gained from the second group of experiments. The computed $\overline{\mathbf{X}}$ and $\overline{\mathbf{U}}$ vectors of the first group of experiments do not obey equilibrium anymore, since they were computed using previous $\overline{\alpha}$ values. They must be recomputed.)

$\overline{\alpha}$ and its variance, an updated $\overline{\overline{\mathbf{Q}}}_{\alpha\alpha}$, are computed by ISPI, but they are not handed back to the model, because this would require changes in the basic structure of the SAFRAN software. This implies that another set of experiments cannot be added to a completed ISPI analysis.

## 7.6 Examples

ISPI was used to generate a few examples that demonstrate the possibility of damage detection using the theory described.

Measurement data was again simulated by creating a FEM model of the damaged structure considered, computing deflection values and adding adequate noise to them, in order to obtain the imperfect "measurements". The damage was then removed from the FEM model to obtain the iFEM model to be used by ISPI for damage detection.

### 7.6.1 Example - Industrial Frame Structure

In chapter 3 an industrial frame structure was introduced (repeated for convenience as Figure 7.1). In section 3.4 this structure was locally damaged by disconnecting the diagonal member fifth from the left. Figure 7.2 shows how the damage was detected by the

appearance of ghost forces[1] in the area of the damage.

The same structure, similarly damaged, was analysed with ISPI. $\alpha$ degrees of freedom were allowed on all diagonal members. It can be seen in Figure 7.3 that ISPI identifies the relevant member by assigning a negative alpha value (approximately $-0.99$) to the member. ISPI also succeeded in distinguishing between ghost forces and forces that were actually applied to the structure, keeping the distributed force that describes the point load that was applied. This is an important result, since it indicates that in an inspection situation, we could measure the response of a structure, but need not register the forces applied to the structure, allowing so called 'model recalibration under ambient loads'.

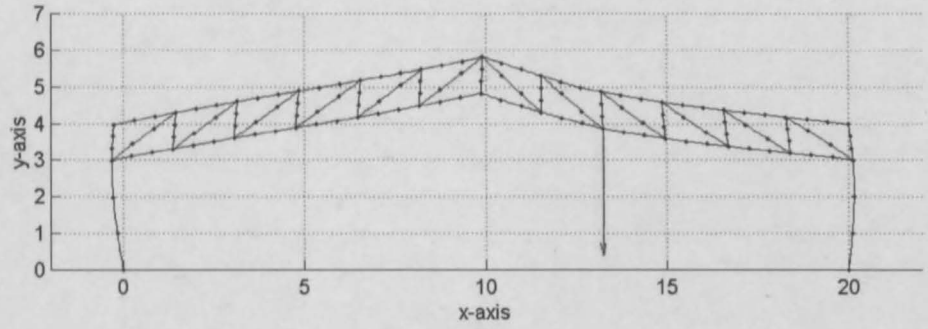


**Figure 7.1:** *FEM model for industrial frame structure*

[1]The term ghost force is explained on page 35

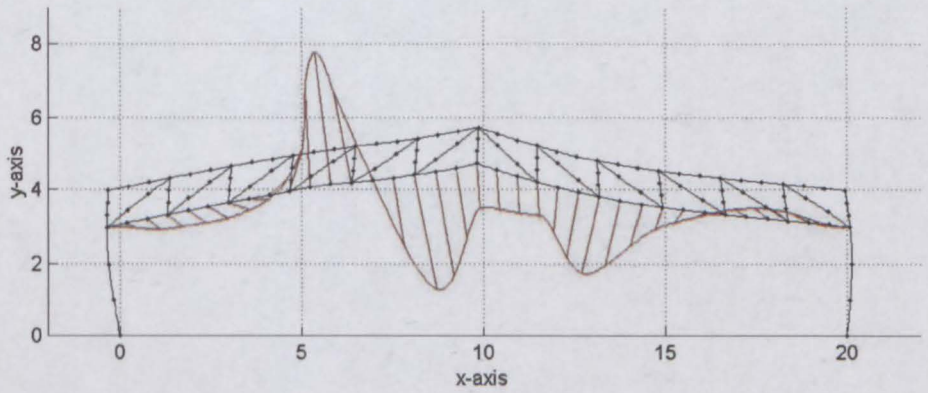


**Figure 7.2:** *Local damage resulting in ghost forces being calculated by iFEM*

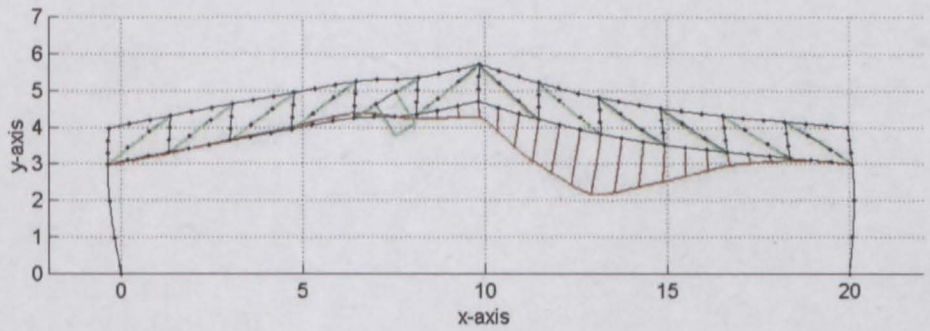


**Figure 7.3:** *Local damage detected by parameter identification technique*

### 7.6.2 Example - Cantilever Bridge

The behaviour of ISPI further investigated, using a cantilever bridge example. This is the cantilever bridge from chapter 3, but with additional diagonal members.

Figure 7.4 is the result of an ISPI analysis on the bridge model. Four different load levels and their corresponding measurements were used as experimental data. Deflection measurements were taken at 1 meter intervals along the deck of the bridge, using a

measurement precision with a standard deviation of 1mm. The damage to the diagonal member is detected. In this case the damage to the member was severe, with its element stiffness being 20% of the undamaged value.

The same ISPI analysis was repeated, but with the damage being less severe. This time the damaged member's element stiffness was 40% of the undamaged value. Figure 7.5 and Figure 7.6 are both results of this analysis, using two similar measurement sets generated from the same load cases: Although the measurements are sometimes adequate to describe the damage, measurement noise can cause the damage to go undetected. When damage is less severe so that the measurements do not always describe its influence adequately, more experiments must be done, measurement precision must be increased or more measurements must be taken to ensure that the damage is detected. When more experiments are added to this example, the damage is consistently detected. Eight different loads and their corresponding measurements were needed to ensure that the damage is consistently detected.

In Figure 7.7, ISPI is detecting distributed damage. Using a measurement precision with a standard deviation of 1mm, four different loads and their corresponding measurements were adequate to detect the damage.

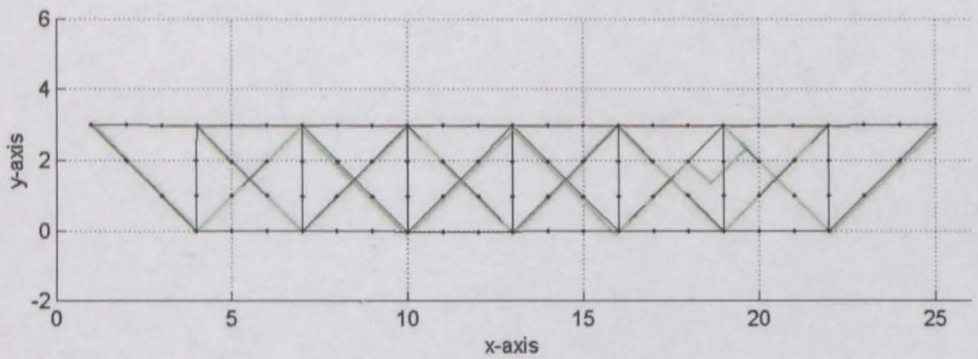


**Figure 7.4:** *Severe damage to diagonal brace detected by ISPI*

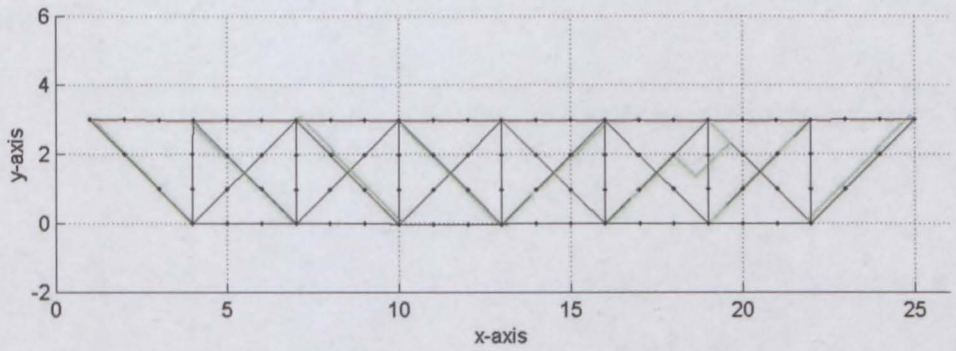


**Figure 7.5:** *Moderate damage to diagonal brace detected by ISPI*

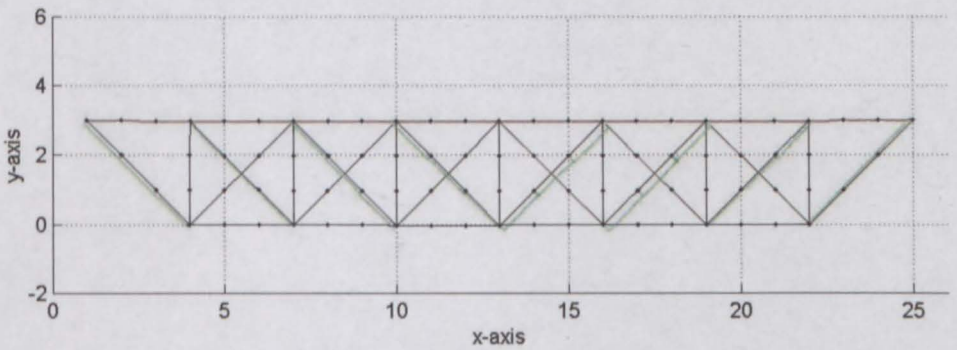


**Figure 7.6:** *Moderate damage to diagonal brace not detected by ISPI*

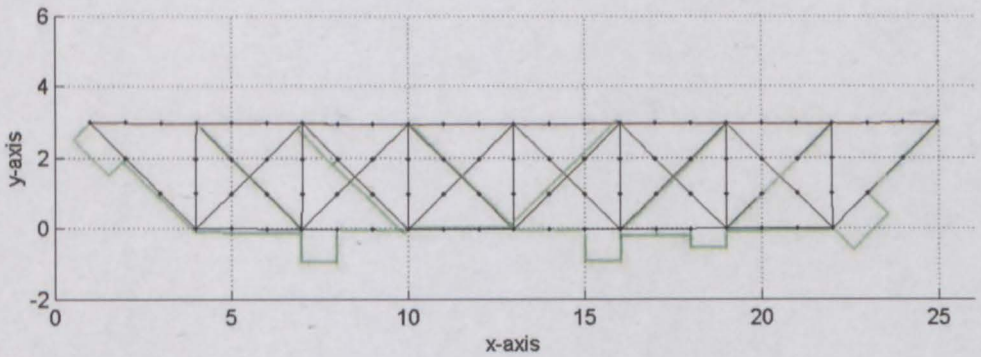


**Figure 7.7:** *Distributed damage detected*

### 7.6.3 Example - Powerline structure

Here a complex structure was treated, with many redundant diagonal members, four of which were damaged by reducing their stiffness by 70%. In practice the diagonal members would be designed to function as tension elements. SAFRAN does not yet allow for tension-only elements, and the diagonals had to be pre-tensioned to prevent instability of the analysis when buckling sets in in compressed braces. Forty different loads and their corresponding measurements, using a measurement precision with a standerd deviation of 1mm, were needed to ensure that the damage is consistently detected. Measurements were taken at 33 different nodes, randomly distributed accross the structure. Figure 7.8 shows how damage is detected for this structure. Thick black lines indicate the damaged members in each figure. In the bottom right part of the structure damage is detected that was not present in the real structure. Such "false alarms" will disappear if enough experiments are included in the analysis.

In strongly non-linear cases, buckling behaviour becomes a problem. When a member is weakened, it may reach a stage where it starts to buckle. Once a buckled shape is achieved, the element can be strengthened again during the following iterations, without affecting the displacement pattern. This leads to the damage not being detected and convergence not achieved. This problem can be avoided by ensuring that the behaviour of systems remains linear during experiments, or at least does not come close to buckling behaviour. If it is known that no buckling occurs in the real structure, the geometric stiffness contributions can be suppressed by requesting a linear analyses.

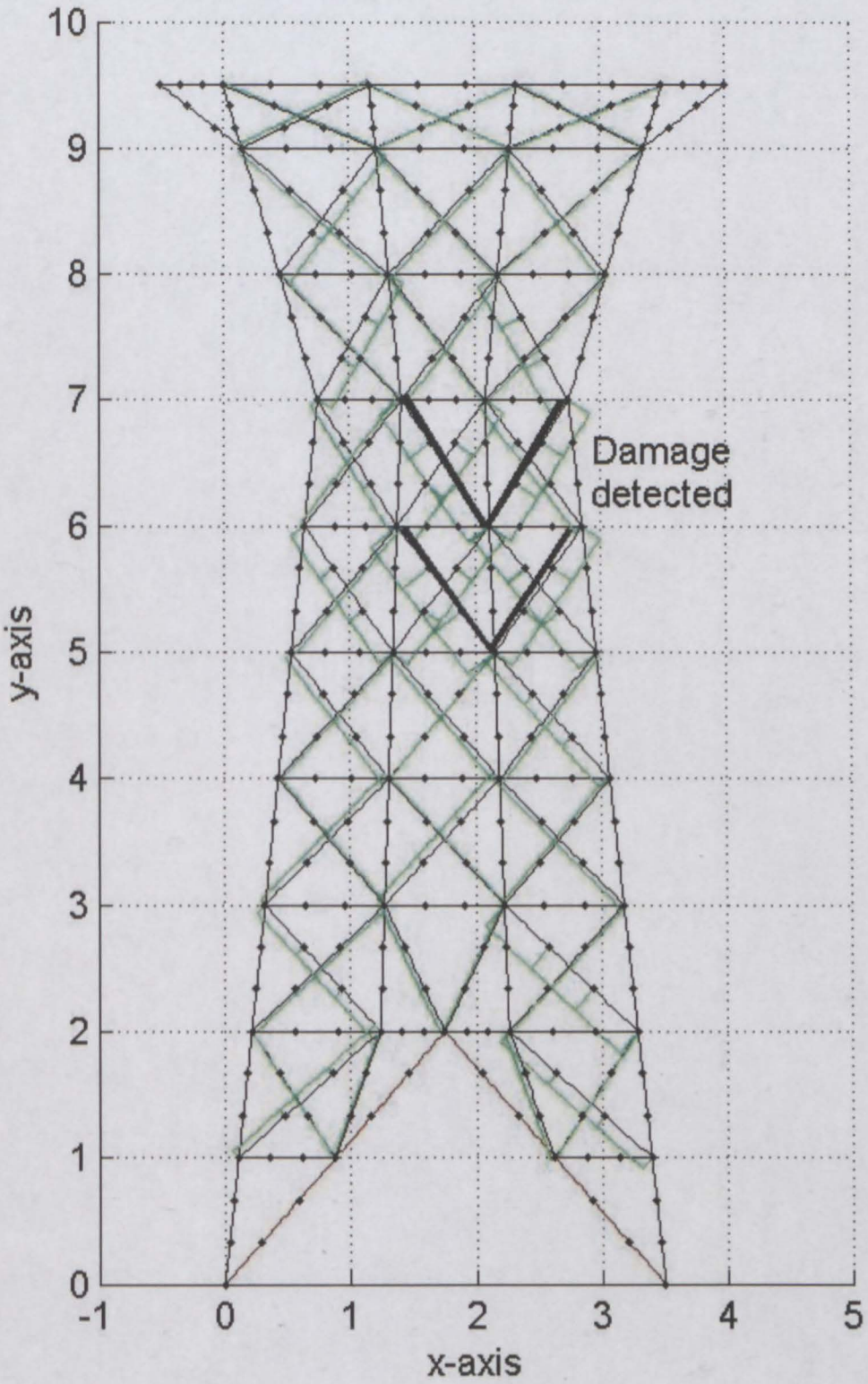


**Figure 7.8:** *Damage detected in upper diagonals of a complex powerline type of structure*

## 7.7 Conclusions

1. In this chapter an iFEM algorithm for the identification of model parameters in static systems is derived. The results obtained are very encouraging and indicate that the algorithm can be used to detect damage in structures, using response measurements.

2. The developed method allows data from several experiments to be combined and in this way accumulate information for the identification purpose. In complicated structures many experiments are needed to accurately point out the location of damage. Small damage is also hard to detect, especially locating its position, and again a great number of experiments must be done to ensure that the damage is adequately described.

3. Analysing structures with a high stiffness and resulting small displacements can prove difficult, because deflection measurement inaccuracies have a larger influence in these cases. The iFEM theory allows us to handle many kinds of measurement, including strains [46]. Using strain measurements might be a way to improve the estimate, since the second derivative of the strain is proportional to the force, introducing less error than the fourth order derivative that displacement data supply.

# Chapter 8

# An algorithm for model parameter estimation in linear dynamic systems using multiple experiments

## 8.1 Introduction

**Dynamic iFEM algorithms** In the present chapter an algorithm (The dynamic iFEM XUA algorithm) for model parameter estimation (or model calibration) of linear dynamic systems is developed. The theory builds on a solution to the linear dynamic force and response estimation problem (The dynamic iFEM XU algorithm) found by Dr. Philippe Mainçon combined with a solution to the static model parameter estimation problem (The static iFEM XUA algorithm) developed in Chapter 7. The dynamic iFEM XUA algorithm allows the use of data from several different dynamic experiments and the variance of the estimated parameters $\overline{\alpha}$ are updated by each experiment.

The computing times associated to linear dynamic iFEM algorithms (both the dynamic iFEM XU and the dynamic iFEM XUA algorithms) are reasonable, making them practical monitoring tools for large dynamic systems.

**Confidentiality** Both dynamic algorithms are protected by a confidentiality agreement. In this chapter the fundamentals of the problem that is solved by the dynamic iFEM XUA algorithm will be explained such that the behaviour of the solution can be fully understood. The details of how the solver for the algorithm is built in order to obtain a reasonable computing time (making it a competitive tool in the market for solving large systems) will be omitted. All aspects of the dynamic iFEM XUA algorithm are fully explained in a confidential report [1] owned by Safran Engineering Algorithms cc.

**Computer implementation** The prototype iFEM software SAFRAN was modified and further developed to include the algorithm presented here, and now allows treating a wide variety of static and dynamic parameter identification problems.

**Applications** The theory was tested with numerical examples and by experimental validation (refer to Chapter 9 to 12).

## 8.2 The dynamic iFEM XU algorithm

In this formulation by Dr. Philippe Mainçon [personal communication] the structure is modeled using the finite element method. This gives the linear system of equations $\overline{\overline{\mathbf{M}}}.\ddot{\overline{\mathbf{x}}}(t) + \overline{\overline{\mathbf{C}}}.\dot{\overline{\mathbf{x}}}(t) + \overline{\overline{\mathbf{K}}}.\overline{\mathbf{x}}(t) = \overline{\overline{\mathbf{H}}}.\overline{\mathbf{u}}(t) + \overline{\mathbf{R}}(t)$ where $\overline{\mathbf{x}}(t)$ are the nodal displacements and $\overline{\overline{\mathbf{H}}}.\overline{\mathbf{u}}(t) + \overline{\mathbf{R}}(t)$ are the nodal forces at each time step. The forces are decomposed into a known part $\overline{\mathbf{R}}(t)$, and an unknown part $\overline{\overline{\mathbf{H}}}.\overline{\mathbf{u}}(t)$, where $\overline{\mathbf{u}}(t)$ are unknown force coefficients.

To obtain a stable estimate of $\overline{\mathbf{u}}(t)$ and $\overline{\mathbf{x}}(t)$ when measurement information on both are available, a cost function is introduced. The cost is the integral over time of a quadratic function of the difference between estimated and measured displacements and of the external forces at all instants in time. The estimate is then found by minimizing the cost function under the constraint $\overline{\overline{\mathbf{M}}}.\ddot{\overline{\mathbf{x}}}(t) + \overline{\overline{\mathbf{C}}}.\dot{\overline{\mathbf{x}}}(t) + \overline{\overline{\mathbf{K}}}.\overline{\mathbf{x}}(t) = \overline{\overline{\mathbf{H}}}.\overline{\mathbf{u}}(t) + \overline{\mathbf{R}}(t)$.

To solve this constrained optimisation problem, Lagrange multipliers $\overline{\lambda}(t)$ are introduced, and similar to what was done in the solution of the static iFEM XU algorithm,

an augmented Lagrangian is obtained. Deriving the augmented Lagrangian with respect to $\overline{\mathbf{x}}$, $\overline{\mathbf{u}}$ and $\overline{\lambda}$ leads to three differential equations that must be solved simultaneously to obtain an optimal solution for $\overline{\mathbf{x}}(t)$, $\overline{\mathbf{u}}(t)$ and $\overline{\lambda}(t)$.

The dynamic iFEM XU algorithm allows the estimation of external forces over time and a complete description of the response (acceleration, deflection and strain) of dynamically excited structures, based on inaccurate measurements of the structure's response taken at a limited number of positions and time instants.

**Algorithms and authors of ideas** The dynamic iFEM XUA formulation presented in this chapter, builds strongly on ideas that were first developed by Dr. Mainçon in his dynamic iFEM XU formulation, described above. The first steps in the dynamic iFEM XUA algorithm were obtained by extending his theory to include model parameters $\overline{\alpha}$, a matrix $\overline{\overline{\mathbf{G}}}(t)$ that describes how these are transformed into consistent forces, and several cost matrices concerned with cost on $\overline{\alpha}$ parameters.

If all $\overline{\alpha}$ related matrices and vectors in the dynamic iFEM XUA algorithm ($\overline{\mathbf{d}\alpha}$, $\overline{\overline{\mathbf{G}}}(t)$, $\overline{\overline{\mathbf{Q}}}_{u\alpha}(t)$, $\overline{\overline{\mathbf{Q}}}_{x\alpha}(t)$, $\overline{\overline{\mathbf{Q}}}_{\dot{x}\alpha}(t)$, $\overline{\overline{\mathbf{Q}}}_{\ddot{x}\alpha}(t)$, $\overline{\overline{\mathbf{Q}}}_{\alpha\alpha}$, and $\overline{\mathbf{Q}}_{\alpha}$) are set equal to zero, the system of equations obtained will be exactly the system of equations arrived to at the end of the dynamic iFEM XU formulation.

Original ideas developed in this work includes: A way to accumulate information from multiple experiments into one XUA analysis, a solution that allows solving the large system of equations resulting from this multiple experiment formulation within reasonable computing time, and how to obtain the matrix $\overline{\overline{\mathbf{G}}}(t)$ (Section 8.3.4).

## 8.3 The dynamic iFEM XUA algorithm

### 8.3.1 Introduction

The dynamic iFEM XU algorithm, presented above, assumes the system matrices $\overline{\overline{\mathbf{K}}}$, $\overline{\overline{\mathbf{C}}}$, $\overline{\overline{\mathbf{M}}}$ and $\overline{\overline{\mathbf{H}}}$ to be known exactly. In reality, the stiffness matrix $\overline{\overline{\mathbf{K}}}$, damping matrix $\overline{\overline{\mathbf{C}}}$, and mass matrix $\overline{\overline{\mathbf{M}}}$ of a structure will be subject to uncertainty. This is due to uncertainty on the characteristics of the structure, which can include structural damage. The matrix $\overline{\overline{\mathbf{H}}}$ transforms force coefficients into nodal consistent forces. The value of this matrix depends on the geometry of the modelled structure, which may also be subject to uncertainty. Explicitly introducing these uncertainties by defining a parameterised model will allow estimating the values and variance of the uncertain parameters.

The dynamic iFEM XU algorithm is adapted by introducing model parameters, so that the dynamic equilibrium equation becomes $\overline{\overline{\mathbf{M}}}.\overline{\ddot{\mathbf{x}}}(t) + \overline{\overline{\mathbf{C}}}.\overline{\dot{\mathbf{x}}}(t) + \overline{\overline{\mathbf{K}}}.\overline{\mathbf{x}}(t) = \overline{\overline{\mathbf{H}}}.\overline{\mathbf{u}}(t) + \overline{\mathbf{R}}(t) + \overline{\overline{\mathbf{G}}}(t).\overline{\mathrm{d}\alpha}$, where $\overline{\alpha}$ are the uncertain model parameters. The matrix $\overline{\overline{\mathbf{G}}}(t)$ will transform the changes in model parameters $\overline{\mathrm{d}\alpha}$ into consistent forces. In this formulation, it was an important step to recognise that $\overline{\overline{\mathbf{G}}}(t)$ will be time-dependent, unlike the constant matrices $\overline{\overline{\mathbf{K}}}$, $\overline{\overline{\mathbf{C}}}$, $\overline{\overline{\mathbf{M}}}$, and $\overline{\overline{\mathbf{H}}}$.

To allow for more than one experiment to be handled, the algorithm is adapted so that the variance of the estimated $\overline{\alpha}$ are updated by each experiment. This is done in a way that closely resembles the formulation of the static XUA algorithm of Chapter 7.

A second order Taylor development of the equilibrium equation is used to demonstrate how various components contribute to the matrix $\overline{\overline{\mathbf{G}}}(t)$ and allows to understand the meaning of each component. Computation of the matrix $\overline{\overline{\mathbf{G}}}(t)$ at each time step requires repeated function calls and consequently a significant amount of computing time. To avoid these repeated function calls, a solution is developed that allows $\overline{\overline{\mathbf{G}}}(t)$ to be calculated faster.

The dynamic iFEM XUA algorithm allows the estimation of model parameters (or possible structural damage) in addition to external forces and a complete description of the response (acceleration, deflection and strain) over time of dynamically excited structures. The algorithm combines measurement information obtained from several experiments (the experiments may be different load conditions on the same structure, or different structures altogether) to obtain an estimate of the model parameters.

### 8.3.2 Equilibrium equation and Cost function

Given a model, and assuming dynamic behaviour, a linear Taylor development of the equilibrium relation between the internal and external forces at $[\overline{\mathbf{X}}_0, \dot{\overline{\mathbf{X}}}_0, \ddot{\overline{\mathbf{X}}}_0, \overline{\mathbf{U}}_0, \overline{\alpha}_0]$ yields,

$$\begin{aligned}
\overline{\mathbf{f}}(\overline{\mathbf{dX}}, \overline{\mathbf{dU}}, \overline{\mathbf{d}\alpha}, t) &= \underbrace{\overline{\mathbf{f}}(\overline{\alpha}_0, \overline{\mathbf{X}}_0(t), \overline{\mathbf{U}}_0(t))}_{-\overline{\mathbf{R}}(t)} + \underbrace{\overline{\nabla}_{\ddot{X}}\overline{\mathbf{f}}}_{\overline{\overline{\mathbf{M}}}}.\overline{\mathbf{d}\ddot{\mathbf{X}}}(t) + \underbrace{\overline{\nabla}_{\dot{X}}\overline{\mathbf{f}}}_{\overline{\overline{\mathbf{C}}}}.\overline{\mathbf{d}\dot{\mathbf{X}}}(t) + \underbrace{\overline{\nabla}_{X}\overline{\mathbf{f}}}_{\overline{\overline{\mathbf{K}}}}.\overline{\mathbf{dX}}(t) \\
&\quad + \underbrace{\overline{\nabla}_{U}\overline{\mathbf{f}}}_{-\overline{\overline{\mathbf{H}}}}.\overline{\mathbf{dU}}(t) + \underbrace{\overline{\nabla}_{\alpha}\overline{\mathbf{f}}}_{-\overline{\overline{\mathbf{G}}}(t)}.\overline{\mathbf{d}\alpha} \\
&= \overline{\overline{\mathbf{M}}}.\overline{\mathbf{d}\ddot{\mathbf{X}}}(t) + \overline{\overline{\mathbf{C}}}.\overline{\mathbf{d}\dot{\mathbf{X}}}(t) + \overline{\overline{\mathbf{K}}}.\overline{\mathbf{dX}}(t) - \overline{\mathbf{R}}(t) - \overline{\overline{\mathbf{H}}}.\overline{\mathbf{dU}}(t) - \overline{\overline{\mathbf{G}}}(t).\overline{\mathbf{d}\alpha} \\
&= \overline{\mathbf{0}}
\end{aligned} \tag{8.1}$$

Assuming a linear dynamic system, the dynamic response of the system can be described as small vibrations $\overline{\mathbf{x}}(t)$ around an average static configuration $\overline{\mathbf{X}}_0$, so that $\overline{\mathbf{X}}(t) = \overline{\mathbf{X}}_0 + \overline{\mathbf{x}}(t)$. The external forces can similarly be described by $\overline{\mathbf{U}}(t) = \overline{\mathbf{U}}_0 + \overline{\mathbf{u}}(t)$, and the model parameters by $\overline{\alpha} = \overline{\alpha}_0 + \overline{\mathbf{d}\alpha}$.

From this the equilibrium equation for this linear dynamic system is obtained, in incremental form

$$\overline{\overline{\mathbf{M}}}.\ddot{\overline{\mathbf{x}}}(t) + \overline{\overline{\mathbf{C}}}.\dot{\overline{\mathbf{x}}}(t) + \overline{\overline{\mathbf{K}}}.\overline{\mathbf{x}}(t) = \overline{\mathbf{R}}(t) + \overline{\overline{\mathbf{H}}}.\overline{\mathbf{u}}(t) + \overline{\overline{\mathbf{G}}}(t).\overline{\mathbf{d}\alpha} \tag{8.2}$$

where $\overline{\mathbf{u}}(t)$ is an unknown incremental force distribution to be estimated, as before, $\overline{\overline{\mathbf{H}}}$ transforms this distributed load into consistent forces and $\overline{\overline{\mathbf{G}}}(t).\overline{\mathbf{d}\alpha}$ is the internal consistent force caused by changes in model parameters $\overline{\mathbf{d}\alpha}$, which must also be estimated.

Minimising a cost function $J$ that is calculated from the prior probability density function of the variables $PDF_{prior}$ as $J = -log(PDF_{prior})$ is equivalent to maximising the probability function. This cost function is approximated by a second order Taylor development at $[\overline{\mathbf{X}}_0, \overline{\dot{\mathbf{X}}}_0, \overline{\ddot{\mathbf{X}}}_0, \overline{\mathbf{U}}_0, \overline{\alpha}_0]$. The total cost is integrated over all time steps.

$$
\begin{aligned}
J(\overline{\mathbf{x}}, \overline{\mathbf{u}}, \overline{\mathrm{d}\alpha}) \;=\; & \int_t (\frac{1}{2}.\overline{\mathbf{x}}(t).\overline{\overline{\mathbf{Q}}}_{xx}.\overline{\mathbf{x}}(t) + \overline{\dot{\mathbf{x}}}(t).\overline{\overline{\mathbf{Q}}}_{\dot{x}x}.\overline{\mathbf{x}}(t) + \overline{\ddot{\mathbf{x}}}(t).\overline{\overline{\mathbf{Q}}}_{\ddot{x}x}.\overline{\mathbf{x}}(t) \\
& + \frac{1}{2}.\overline{\dot{\mathbf{x}}}(t).\overline{\overline{\mathbf{Q}}}_{\dot{x}\dot{x}}.\overline{\dot{\mathbf{x}}}(t) + \overline{\dot{\mathbf{x}}}(t).\overline{\overline{\mathbf{Q}}}_{\dot{x}\ddot{x}}.\overline{\ddot{\mathbf{x}}}(t) + \frac{1}{2}\overline{\ddot{\mathbf{x}}}(t).\overline{\overline{\mathbf{Q}}}_{\ddot{x}\ddot{x}}.\overline{\ddot{\mathbf{x}}}(t) + \overline{\mathbf{Q}}_x(t).\overline{\mathbf{x}}(t) \\
& + \overline{\mathbf{Q}}_{\dot{x}}(t).\overline{\dot{\mathbf{x}}}(t) + \overline{\mathbf{Q}}_{\ddot{x}}(t).\overline{\ddot{\mathbf{x}}}(t) + \frac{1}{2}.\overline{\mathbf{u}}(t).\overline{\overline{\mathbf{Q}}}_{uu}.\overline{\mathbf{u}}(t) + \overline{\mathbf{u}}(t).\overline{\mathbf{Q}}_{ux}.\overline{\mathbf{x}}(t) + \overline{\mathbf{Q}}_u(t).\overline{\mathbf{u}}(t) \\
& + \overline{\mathbf{u}}(t).\overline{\overline{\mathbf{Q}}}_{u\dot{x}}.\overline{\dot{\mathbf{x}}}(t) + \overline{\mathbf{u}}(t).\overline{\overline{\mathbf{Q}}}_{u\ddot{x}}.\overline{\ddot{\mathbf{x}}}(t) + \overline{\mathbf{x}}(t).\overline{\overline{\mathbf{Q}}}_{x\alpha}(t).\overline{\mathrm{d}\alpha} + \overline{\dot{\mathbf{x}}}(t).\overline{\overline{\mathbf{Q}}}_{\dot{x}\alpha}(t).\overline{\mathrm{d}\alpha} \\
& + \overline{\ddot{\mathbf{x}}}(t).\overline{\overline{\mathbf{Q}}}_{\ddot{x}\alpha}(t).\overline{\mathrm{d}\alpha} + \overline{\mathbf{u}}(t).\overline{\overline{\mathbf{Q}}}_{u\alpha}(t).\overline{\mathrm{d}\alpha})dt + \frac{1}{2}.\overline{\mathrm{d}\alpha}.\overline{\overline{\mathbf{Q}}}_{\alpha\alpha}.\overline{\mathrm{d}\alpha} + \overline{\mathbf{Q}}_{\alpha}.\overline{\mathrm{d}\alpha}
\end{aligned}
\tag{8.3}
$$

where the vectors $\overline{\mathbf{Q}}_x$, $\overline{\mathbf{Q}}_u$, etc. and the matrices $\overline{\overline{\mathbf{Q}}}_{xx}$, $\overline{\overline{\mathbf{Q}}}_{uu}$, $\overline{\overline{\mathbf{Q}}}_{xu}$, etc. are found from the measured values and their standard deviations. The computation of these vectors and matrices were previously explained in Chapter 2. Non-zero values of the coefficients $\overline{\overline{\mathbf{Q}}}_{\ddot{x}\ddot{x}}$ and $\overline{\mathbf{Q}}_{\ddot{x}}$ appear if acceleration measurements are used. Speed measurements can be treated in a similar fashion.

In order to solve the system in a computationally efficient way [1], the following terms have to be constant:
$\overline{\overline{\mathbf{K}}}$, $\overline{\overline{\mathbf{C}}}$, $\overline{\overline{\mathbf{M}}}$, $\overline{\overline{\mathbf{H}}}$, $\overline{\overline{\mathbf{Q}}}_{xx}$, $\overline{\overline{\mathbf{Q}}}_{\dot{x}\dot{x}}$, $\overline{\overline{\mathbf{Q}}}_{\ddot{x}\ddot{x}}$, $\overline{\overline{\mathbf{Q}}}_{uu}$, $\overline{\overline{\mathbf{Q}}}_{xu}$, $\overline{\overline{\mathbf{Q}}}_{\dot{x}u}$, $\overline{\overline{\mathbf{Q}}}_{\ddot{x}u}$, $\overline{\overline{\mathbf{Q}}}_{\alpha\alpha}$, $\overline{\mathbf{Q}}_{\alpha}$ and $\overline{\mathrm{d}\alpha}$.

The time dependent terms are:
$\overline{\mathbf{x}}(t)$, $\overline{\mathbf{u}}(t)$, $\overline{\mathbf{R}}(t)$, $\overline{\mathbf{Q}}_x(t)$, $\overline{\mathbf{Q}}_{\dot{x}}(t)$, $\overline{\mathbf{Q}}_{\ddot{x}}(t)$, $\overline{\mathbf{Q}}_u(t)$, $\overline{\overline{\mathbf{G}}}(t)$, $\overline{\overline{\mathbf{Q}}}_{x\alpha}(t)$, $\overline{\overline{\mathbf{Q}}}_{\dot{x}\alpha}(t)$, $\overline{\overline{\mathbf{Q}}}_{\ddot{x}\alpha}(t)$ and $\overline{\overline{\mathbf{Q}}}_{u\alpha}(t)$.

Assuming system matrices $\overline{\overline{\mathbf{K}}}$, $\overline{\overline{\mathbf{C}}}$, $\overline{\overline{\mathbf{M}}}$, and $\overline{\overline{\mathbf{H}}}$ to be constant implies a linear dynamic analysis, while assuming cost matrices $\overline{\overline{\mathbf{Q}}}$ to be constant means that measurement precision is assumed not to vary with time.

### 8.3.3 Constrained optimisation

The cost function (Equation 8.3) is to be minimised, while verifying equilibrium (Equation 8.2) at each time-step. In the previous chapter Lagrange multipliers $\overline{\lambda}$ were used and an augmented Lagrangian obtained to solve such a constrained optimization problem for a static system. For dynamic systems the constrained minimization problem must be solved for all time-steps.

**Constrained optimisation with a single experiment** Using finite differences, one can transform the equilibrium equations (Equation 8.2) into $nXdof \times nT$ equations involving only $\overline{\mathbf{x}}(t)$ and $\overline{\mathbf{u}}(t)$, and not $\dot{\overline{\mathbf{x}}}(t)$ or $\ddot{\overline{\mathbf{x}}}(t)$. Similarly, the cost function (Equation 8.3) can be re-expressed as a quadratic function of $\overline{\mathbf{x}}(t)$ and $\overline{\mathbf{u}}(t)$ only. Requesting that equilibrium be verified at each time-step, means that a total of $nXdof \times nT$ constraints are applied. The unknowns that must be solved for are the displacement $\overline{\mathbf{x}}(t)$ and load $\overline{\mathbf{u}}(t)$ at each timestep and the unknown model parameters $\overline{\mathbf{d}\alpha}$. This is a constrained optimisation problem with $n\alpha + (nXdof + nUdof) \times nT$ unknowns and $nXdof \times nT$ constraints, where $nXdof$ is the number of displacement degrees of freedom, $nUdof$ the number of force degrees of freedom, $n\alpha$ the number of model parameters, and $nT$ the number of time steps.

This can in theory be solved like the static iFEM XUA problem, by introducing a total of $nXdof \times nT$ Lagrange multipliers $\overline{\lambda}(t)$, to obtain a linear system with $n\alpha + (2 \times nXdof + nUdof).nT$ equations and unknowns.

**Constrained optimisation with multiple experiments** When multiple experiments are used to contribute information, an equilibrium equation can be written for each experiment. The total cost function will then be the sum of the cost functions of the individual experiments. This leads to a constrained optimisation problem with $n\alpha + \sum_{i=1}^{nXper}((nXdof_i + nUdof_i) \times nT_i)$ unknowns and $\sum_{i=1}^{nXper}(nXdof_i \times nT_i)$ constraints, where $nXdof_i$ is the number of displacement degrees of freedom of experiment $i$, $nUdof_i$ the number of force degrees of freedom of experiment $i$, $n\alpha$ the number of model parame-

ters, $nXper$ the number of experiments, and $nT_i$ the number of time steps of experiment $i$. The unknowns are the displacement $\overline{\mathbf{x}}(t)$ and load $\overline{\mathbf{u}}(t)$ for each experiment for each time-step and the unknown model parameters $\overline{\mathbf{d\alpha}}$.

This can in theory be solved like the static iFEM XUA problem, by introducing a total of $\sum_{i=1}^{nXper}(nXdof_i \times nT_i)$ Lagrange multipliers ($\overline{\lambda}(t)_i$ for each experiment $i$), to obtain a linear system with $n\alpha + \sum_{i=1}^{nXper}((2 \times nXdof_i + nUdof_i) \times nT_i)$ equations and unknowns. The CPU time required to solve this system of equations is proportional to $(n\alpha + \sum_{i=1}^{nXper}((2 \times nXdof_i + nUdof_i) \times nT_i)^2$. For systems with many degrees of freedom or a large number of time-steps the CPU time required to solve this system of equations will become impractical.

For linear structures, and measurements with a precision that does not vary with time, a faster algorithm is available (dynamic iFEM XUA [1]), which solves the same constrained optimisation problem, even though the above-mentioned large system of equations is never built inside the computer. This implies that the dynamic iFEM XUA solver yields the same solution as solving the large system of equations. This is an important observation, because it allows to fully understand the behaviour of the dynamic iFEM XUA solution.

The dynamic iFEM XUA algorithm has an order of complexity of $\sum_{i=1}^{nXper}((2 \times nXdof_i + nUdof_i)^2 \times (n\alpha + 1) \times nT_i) + n\alpha^2$, where $nXper$ is the number of experiments, $nT$ being the number of time steps per experiment, $nXdof$ the number of displacement degrees of freedom, $nUdof$ the number of force degrees of freedom, and $n\alpha$ the number of model parameters.

### 8.3.4 Obtaining the matrices

For the solution to be fast, $\overline{\overline{\mathbf{K}}}$, $\overline{\overline{\mathbf{C}}}$, $\overline{\overline{\mathbf{M}}}$ and $\overline{\overline{\mathbf{H}}}$ must be constant over time. However, since $\overline{\mathbf{d\alpha}}$ is constant, $\overline{\overline{\mathbf{G}}}(t)$ may vary over time and so may $\overline{\mathbf{R}}(t)$.

The theory for assembling the stiffness, damping and mass matrices $\overline{\overline{\mathbf{K}}}$, $\overline{\overline{\mathbf{C}}}$, $\overline{\overline{\mathbf{M}}}$ and

force vector $\overline{\mathbf{R}}(t)$ is well documented in familiar FEM theory. How to obtain $\overline{\overline{\mathbf{H}}}$, as well as the cost matrices, is described in chapter 2.

The intuitive way of solving the system would be to compute the constant matrices once and the time-dependent matrices and vectors for each time-step. Obtaining $\overline{\overline{\mathbf{G}}}(t)$ for each time step is a computationally expensive operation, since it requires that at each time step, a function call must be made with the values of the state of the system at that time step, so that the value of $\overline{\overline{\mathbf{G}}}(t)$ can be computed and returned to the solver. Repeated function calls to obtain $\overline{\mathbf{R}}(t)$ can not be avoided, but a solution for obtaining $\overline{\overline{\mathbf{G}}}(t)$ faster was developed.

This section will focus on the matrix $\overline{\overline{\mathbf{G}}}(t)$, its properties and how to compute it. The repeated function calls needed to obtain this matrix can be avoided, so that a fast and effective solver can be realised.

**Obtaining the matrix $\overline{\overline{\mathbf{G}}}(t)$** Equation 8.1 describes the equilibrium equation of an $\overline{\alpha}$ parameterised system as a first order Taylor expansion. According to this equation, the matrix $\overline{\overline{\mathbf{G}}}(t)$ is the derivative of the consistent force with respect to the $\overline{\alpha}$ parameters. It is a sensitivity matrix that encodes how the internal and external forces will change for given $\overline{\mathbf{d}\alpha}$ parameter changes.

Consider a second order Taylor development at $(\overline{\alpha}_0, \overline{\mathbf{X}}_0, \overline{\mathbf{U}}_0)$ of the equilibrium equa-

tion

$$
\begin{aligned}
\overline{\mathbf{f}}(\overline{\alpha}, \overline{\mathbf{X}}, \overline{\dot{\mathbf{X}}}, \overline{\ddot{\mathbf{X}}}, \overline{\mathbf{U}}) &= \underbrace{\overline{\mathbf{f}}(\overline{\alpha}_0, \overline{\mathbf{X}}_0, \overline{\mathbf{U}}_0)}_{-\overline{\mathbf{R}}} + \underbrace{\frac{\partial \overline{\mathbf{f}}}{\partial \overline{\mathbf{X}}}}_{\overline{\overline{\mathbf{K}}}} . \overline{\mathrm{d}\mathbf{X}} + \underbrace{\frac{\partial \overline{\mathbf{f}}}{\partial \overline{\dot{\mathbf{X}}}}}_{\overline{\overline{\mathbf{C}}}} . \overline{\mathrm{d}\dot{\mathbf{X}}} \\
&\quad + \underbrace{\frac{\partial \overline{\mathbf{f}}}{\partial \overline{\ddot{\mathbf{X}}}}}_{\overline{\overline{\mathbf{M}}}} . \overline{\mathrm{d}\ddot{\mathbf{X}}} + \underbrace{\frac{\partial \overline{\mathbf{f}}}{\partial \overline{\mathbf{U}}}}_{-\overline{\overline{\mathbf{H}}}} . \overline{\mathrm{d}\mathbf{U}} + \underbrace{\frac{\partial \overline{\mathbf{f}}}{\partial \overline{\alpha}}}_{-\overline{\overline{\mathbf{G}}}_0} . \overline{\mathrm{d}\alpha} \\
&\quad + \frac{\partial^2 \overline{\mathbf{f}}}{\partial \overline{\mathbf{X}}^2} . \overline{\mathrm{d}\mathbf{X}} . \overline{\mathrm{d}\mathbf{X}} + \frac{\partial^2 \overline{\mathbf{f}}}{\partial \overline{\dot{\mathbf{X}}}^2} . \overline{\mathrm{d}\dot{\mathbf{X}}} . \overline{\mathrm{d}\dot{\mathbf{X}}} + \frac{\partial^2 \overline{\mathbf{f}}}{\partial \overline{\ddot{\mathbf{X}}}^2} . \overline{\mathrm{d}\ddot{\mathbf{X}}} . \overline{\mathrm{d}\ddot{\mathbf{X}}} \\
&\quad + \frac{\partial^2 \overline{\mathbf{f}}}{\partial \overline{\mathbf{X}} \partial \overline{\dot{\mathbf{X}}}} . \overline{\mathrm{d}\mathbf{X}} . \overline{\mathrm{d}\dot{\mathbf{X}}} + \frac{\partial^2 \overline{\mathbf{f}}}{\partial \overline{\mathbf{X}} \partial \overline{\ddot{\mathbf{X}}}} . \overline{\mathrm{d}\mathbf{X}} . \overline{\mathrm{d}\ddot{\mathbf{X}}} + \frac{\partial^2 \overline{\mathbf{f}}}{\partial \overline{\dot{\mathbf{X}}} \partial \overline{\ddot{\mathbf{X}}}} . \overline{\mathrm{d}\dot{\mathbf{X}}} . \overline{\mathrm{d}\ddot{\mathbf{X}}} \\
&\quad + \frac{\partial^2 \overline{\mathbf{f}}}{\partial \overline{\mathbf{U}}^2} . \overline{\mathrm{d}\mathbf{U}} . \overline{\mathrm{d}\mathbf{U}} + \frac{\partial^2 \overline{\mathbf{f}}}{\partial \overline{\mathbf{X}} \partial \overline{\mathbf{U}}} . \overline{\mathrm{d}\mathbf{X}} . \overline{\mathrm{d}\mathbf{U}} + \frac{\partial^2 \overline{\mathbf{f}}}{\partial \overline{\dot{\mathbf{X}}} \partial \overline{\mathbf{U}}} . \overline{\mathrm{d}\dot{\mathbf{X}}} . \overline{\mathrm{d}\mathbf{U}} \\
&\quad + \frac{\partial^2 \overline{\mathbf{f}}}{\partial \overline{\ddot{\mathbf{X}}} \partial \overline{\mathbf{U}}} . \overline{\mathrm{d}\ddot{\mathbf{X}}} . \overline{\mathrm{d}\mathbf{U}} + \underbrace{\frac{\partial^2 \overline{\mathbf{f}}}{\partial \overline{\alpha}^2}}_{\overline{\overline{\mathbf{T}}}_G} . \overline{\mathrm{d}\alpha} . \overline{\mathrm{d}\alpha} + \underbrace{\frac{\partial^2 \overline{\mathbf{f}}}{\partial \overline{\mathbf{X}} \partial \overline{\alpha}}}_{\overline{\overline{\mathbf{T}}}_K} . \overline{\mathrm{d}\mathbf{X}} . \mathrm{d}\alpha \\
&\quad + \underbrace{\frac{\partial^2 \overline{\mathbf{f}}}{\partial \overline{\dot{\mathbf{X}}} \partial \overline{\alpha}}}_{\overline{\overline{\mathbf{T}}}_C} . \overline{\mathrm{d}\dot{\mathbf{X}}} . \overline{\mathrm{d}\alpha} + \underbrace{\frac{\partial^2 \overline{\mathbf{f}}}{\partial \overline{\ddot{\mathbf{X}}} \partial \overline{\alpha}}}_{\overline{\overline{\mathbf{T}}}_M} . \overline{\mathrm{d}\ddot{\mathbf{X}}} . \overline{\mathrm{d}\alpha} + \underbrace{\frac{\partial^2 \overline{\mathbf{f}}}{\partial \overline{\mathbf{U}} \partial \overline{\alpha}}}_{\overline{\overline{\mathbf{T}}}_H} . \overline{\mathrm{d}\mathbf{U}} . \overline{\mathrm{d}\alpha} \\
&= \overline{\mathbf{F}}_{external} - \overline{\mathbf{F}}_{internal} \\
&= \overline{\mathbf{0}}
\end{aligned}
\tag{8.4}
$$

$\overline{\overline{\mathbf{K}}}$, $\overline{\overline{\mathbf{C}}}$, $\overline{\overline{\mathbf{M}}}$ and $\overline{\overline{\mathbf{H}}}$ must be constant over time in order to ensure that the constrained optimisation problem can be solved in a time-efficient way [1]. In assuming a linear dynamic situation, it is required that $\overline{\mathbf{x}(\mathbf{t})}$ and $\overline{\mathbf{u}(\mathbf{t})}$ must be small variations around the static configuration in order for the computations to be valid. For a linear dynamic

system, the following terms in Equation 8.4 will be negligible:

$$\frac{\partial^2 \overline{\mathbf{f}}}{\partial \overline{\mathbf{X}}^2}\overline{\mathrm{d}\mathbf{X}} = \frac{\partial \overline{\overline{\mathbf{K}}}}{\partial \overline{\mathbf{X}}}\overline{\mathrm{d}\mathbf{X}} = \overline{0},\ \frac{\partial^2 \overline{\mathbf{f}}}{\partial \dot{\overline{\mathbf{X}}}^2}\overline{\mathrm{d}\dot{\mathbf{X}}} = \frac{\partial \overline{\overline{\mathbf{C}}}}{\partial \dot{\overline{\mathbf{X}}}}\overline{\mathrm{d}\dot{\mathbf{X}}} = \overline{0},\ \frac{\partial^2 \overline{\mathbf{f}}}{\partial \ddot{\overline{\mathbf{X}}}^2}\overline{\mathrm{d}\ddot{\mathbf{X}}} = \frac{\partial \overline{\overline{\mathbf{M}}}}{\partial \ddot{\overline{\mathbf{X}}}}\overline{\mathrm{d}\ddot{\mathbf{X}}} = \overline{0},$$

$$\frac{\partial^2 \overline{\mathbf{f}}}{\partial \overline{\mathbf{U}}^2}\overline{\mathrm{d}\mathbf{U}} = \frac{\partial \overline{\overline{\mathbf{H}}}}{\partial \overline{\mathbf{U}}}\overline{\mathrm{d}\mathbf{U}} = \overline{0},\ \frac{\partial^2 \overline{\mathbf{f}}}{\partial \overline{\mathbf{X}}\partial \overline{\mathbf{U}}}\overline{\mathrm{d}\mathbf{U}} = \frac{\partial \overline{\overline{\mathbf{K}}}}{\partial \overline{\mathbf{U}}}\overline{\mathrm{d}\mathbf{U}} = \overline{0},\ \frac{\partial^2 \overline{\mathbf{f}}}{\partial \dot{\overline{\mathbf{X}}}\partial \overline{\mathbf{U}}}\overline{\mathrm{d}\mathbf{U}} = \frac{\partial \overline{\overline{\mathbf{C}}}}{\partial \overline{\mathbf{U}}}\overline{\mathrm{d}\mathbf{U}} = \overline{0},$$

$$\frac{\partial^2 \overline{\mathbf{f}}}{\partial \ddot{\overline{\mathbf{X}}}\partial \overline{\mathbf{U}}}\overline{\mathrm{d}\mathbf{U}} = \frac{\partial \overline{\overline{\mathbf{M}}}}{\partial \overline{\mathbf{U}}}\overline{\mathrm{d}\mathbf{U}} = \overline{0},\ \frac{\partial^2 \overline{\mathbf{f}}}{\partial \overline{\mathbf{X}}\partial \dot{\overline{\mathbf{X}}}}\overline{\mathrm{d}\dot{\mathbf{X}}} = \frac{\partial \overline{\overline{\mathbf{K}}}}{\partial \dot{\overline{\mathbf{X}}}}\overline{\mathrm{d}\dot{\mathbf{X}}} = \overline{0},\ \frac{\partial^2 \overline{\mathbf{f}}}{\partial \overline{\mathbf{X}}\partial \ddot{\overline{\mathbf{X}}}}\overline{\mathrm{d}\ddot{\mathbf{X}}} = \frac{\partial \overline{\overline{\mathbf{K}}}}{\partial \ddot{\overline{\mathbf{X}}}}\overline{\mathrm{d}\ddot{\mathbf{X}}} = \overline{0},$$

$$\frac{\partial^2 \overline{\mathbf{f}}}{\partial \dot{\overline{\mathbf{X}}}\partial \ddot{\overline{\mathbf{X}}}}\overline{\mathrm{d}\ddot{\mathbf{X}}} = \frac{\partial \overline{\overline{\mathbf{C}}}}{\partial \ddot{\overline{\mathbf{X}}}}\overline{\mathrm{d}\ddot{\mathbf{X}}} = \overline{0}$$

In non-linear problems some of the above terms, (for example $\frac{\partial^2 \overline{\mathbf{f}}}{\partial \overline{\mathbf{X}}\partial \overline{\mathbf{U}}}$ and $\frac{\partial^2 \overline{\mathbf{f}}}{\partial \overline{\mathbf{X}}^2}$) would have contributed to the geometric stiffness.

$\overline{\overline{\mathbf{G}}}_0$ is the change in internal force due to a change in $\overline{\alpha}$ parameters and can be computed at a given (static) configuration (for $\overline{\mathbf{X}}_0$). $\overline{\overline{\mathbf{G}}}_0$, however is constant over time. There will also be time-dependent changes in the internal force due to $\overline{\alpha}$ parameter changes, because of dynamic movement ($\overline{\mathbf{x}}(t)$ and $\overline{\mathbf{u}}(t)$) around the average static equilibrium configuration. These changes in internal force is encoded by $\overline{\overline{\mathbf{T}}}_K.\overline{\mathbf{x}}(t).\overline{\mathrm{d}\alpha}$, $\overline{\overline{\mathbf{T}}}_C.\dot{\overline{\mathbf{x}}}(t).\overline{\mathrm{d}\alpha}$, $\overline{\overline{\mathbf{T}}}_M.\ddot{\overline{\mathbf{x}}}(t).\overline{\mathrm{d}\alpha}$ and $\overline{\overline{\mathbf{T}}}_H.\overline{\mathbf{u}}(t).\overline{\mathrm{d}\alpha}$, which are time-dependent terms, since $\overline{\mathbf{x}}(t)$ and $\overline{\mathbf{u}}(t)$ vary with time. For example, $\overline{\overline{\mathbf{T}}}_K$ will be non-zero when $\overline{\alpha}$ parameters encode changes in stiffness properties. $\overline{\overline{\mathbf{T}}}_C$ will be non-zero when $\overline{\alpha}$ parameters encode changes in damping properties. $\overline{\overline{\mathbf{T}}}_M$ will be non-zero when $\overline{\alpha}$ parameters encodes changes in mass properties. $\overline{\overline{\mathbf{T}}}_H$ will be non-zero when $\overline{\alpha}$ parameters encodes geometry changes (since the consistent forces obtained from $\overline{\mathbf{U}}$ depends on geometry, such as element length), or when $\overline{\overline{\mathbf{H}}}$ is parameterised. $\overline{\overline{\mathbf{T}}}_H$ will be zero when the unknown forces can be assumed to be independent from the $\overline{\alpha}$ parameters. If the internal force varies linearly with the chosen $\overline{\alpha}$ parameters, $\overline{\overline{\mathbf{T}}}_G$ will be zero.

Considering Equation 8.4, $\overline{\overline{\mathbf{G}}}(t)$ from equation 8.2 becomes

$$\overline{\overline{\mathbf{G}}}(t) = \overline{\overline{\mathbf{G}}}_0 + \overline{\overline{\mathbf{T}}}_K.\overline{\mathbf{x}}(t) + \overline{\overline{\mathbf{T}}}_C.\dot{\overline{\mathbf{x}}}(t) + \overline{\overline{\mathbf{T}}}_M.\ddot{\overline{\mathbf{x}}}(t) + \overline{\overline{\mathbf{T}}}_H.\overline{\mathbf{u}}(t) + \overline{\overline{\mathbf{T}}}_G.\overline{\mathrm{d}\alpha} \tag{8.5}$$

Handling the calculation of $\overline{\overline{\mathbf{G}}}(t)$ in this way is very convenient from the programming perspective, since it eliminates the need for repeated function calls from the solver to the

model to obtain the value of $\overline{\overline{\mathbf{G}}}(t)$ at each timestep: $\overline{\overline{\mathbf{T}}}_K$, $\overline{\overline{\mathbf{T}}}_C$, $\overline{\overline{\mathbf{T}}}_M$ and $\overline{\overline{\mathbf{T}}}_H$ are constant over time and need to be returned only once. Thereafter it can be used to calculate $\overline{\overline{\mathbf{G}}}(t)$, for each time-step, from $\overline{\mathbf{x}}(t)$ and $\overline{\mathbf{u}}(t)$, which are available within the solver at each iteration. This approach constitutes a large improvement in the computing time needed to solve dynamic XUA systems. The time needed to generate matrices is, except for $\overline{\mathbf{R}}(t)$, now independent of the number of time steps. This yields an algorithm in which the time spent on computing matrices is small compared to the time spent on solving the system of equations.

### 8.3.5 Systematic biases

iFEM estimates exhibit some systematic biases, or "artifacts": It was noted for static problems that estimated loads tend to be spread over the structure, because a distributed force has a lower associated cost.

For dynamic problems, where displacement measurements are used, loads tend to distribute over time, because high frequency load fluctuations have limited effect on the displacements and only add to force costs.

Just as displacement measurements tend to filter out high frequency forces, acceleration measurements have a complicated relation with low frequency forces. This is discussed in detail in Chapter 12, where this phenomenon was first observed. A low frequency force, even if it causes displacement response, will cause only a small acceleration response, giving rise to low measurement-error costs. As a consequence, the measurement errors will be accepted in order to minimise the costs associated with external forces. This will often mean that low frequency load components are zeroed out.

Similarly, damage estimates would also be spread over the structure, because for the same total damage, distributed damage has a lower associated cost. For this reason, damage tends to be spread unless necessary to match measurements. For similar reasons,

damage distributions will generally be continuous.

## 8.4 Computer implementation

ISPI, the previous computer implementation for static parameter identification is discussed in Chapter 7. That implementation had several limitations and it was decided to invest significant programming effort to produce an implementation that has less limitations and is properly integrated into the existing SAFRAN software. SAFRAN was not originally written with parameter identification in mind, requiring extensive changes in the basic software structure to accommodate the new theory. The work included: The use of multiple models, one each for different experiments; Flexible $\alpha$ parameterisation for elements; The introduction of parameter constraints within a model, or between different models within a group of experiments; And the calculation and assembly of numerous new matrices and tensors, such as $\overline{\overline{\mathbf{G}}}$, $\overline{\overline{\mathbf{T}}}_K$ and $\overline{\overline{\mathbf{Q}}}_{\alpha\alpha}$.

In this implementation, the user can define multiple structural models and associate each of these to one or several experiments, which can be added to an analysis. Consider as an example a situation where we have several different structures, all made from the same material, and we want to use experimental data from these structures to update our prior knowledge on a property of the material. Allowing multiple structural models to be defined opens the door to treat such cases, which was impossible with the previous implementation.

In ISPI, the implementation of chapter 7, each element could have only one $\alpha$ degree of freedom. In addition it was hard-coded that this single $\alpha$ degree of freedom refers to a constant changed stiffness modulus along the element. This was a severe limitation, since treating dynamic systems requires damping- and mass related parameters. In the present implementation the user can specify, as input, the types of $\alpha$ degrees of freedom wanted for each element, ranging from stiffness related parameters such as $E$, $I$ or $A$, Rayleigh

damping parameters and mass parameters, such as $A$ or $\rho$, the material density. Also, the $\alpha$ parameter field is no longer assumed constant over each element, but is interpolated by linear shape functions and associated $\alpha$ degrees of freedom. This can correspond to, for example, a beam that is tapered, or a plate-element that does not have uniform thickness.

The parameter fields can be constrained within a single model and also across different models within a group of experiments. This is needed, for example, when parameters from different models or elements refer to the same material property. In addition, parameter measurements or expected values of parameters can be introduced, the most probable value of $\alpha$ is no longer simply assumed to be zero.

## 8.5 Numerical Example: Cantilever Bridge

A numerical example is used to demonstrate the possibility of damage detection using the theory described. The structure considered in this example is the cantilever bridge of chapter 7 with 50% loss of stiffness in one of the braces.

Measurement data was again simulated by creating a FEM model of the damaged structure, dynamically exciting this model by an impact load, computing deflection values over time and adding adequate noise to them in order to obtain the imperfect "measurements". In this example white noise with a chosen standard deviation was added to the calculated measurement values. The damage was removed from the FEM model to obtain the iFEM model to be used for damage detection.

Two experiments were conducted and the data from both was combined to update the model. In the first experiment the bridge was dynamically excited by applying an impulse load $11m$ from the left side of the bridge and in the second experiment the impulse load was applied at $14m$. In each experiment, deflection measurements with a standard deviation of noise of $1mm$ and a sampling frequency of $100Hz$ were taken in the middle of each of the eight tension braces for a duration of 2.56 seconds. Figure 8.1 shows the structure

with the damage in the tension brace detected and correctly quantified. For the same example damages of as little as 2% in the tension brace were correctly detected. In this study the model was perfect apart from the damage introduced. Of course, in practice it would be difficult to detect such small damage, because real world models would contain much more uncertainties. When model uncertainties exist in the absence of damage, parameter changes can be used to recalibrate the model. When damage is present, both structural damage and model recalibration will contribute to parameter changes and it might be difficult to distinguish the two from each other.

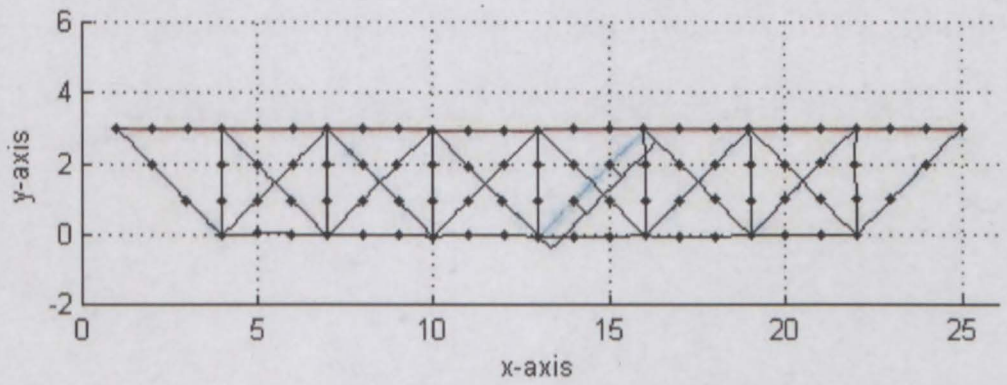


**Figure 8.1:** *Damaged brace identified in a cantilever bridge example.*

Increasing the measurement noise resulted in the damage being underestimated. When lower measurement precision was used, taking measurements at more positions improved the result.

For a bridge, displacement measurement might be impractical. The damage could also be detected using acceleration measurements. Acceleration sensors are easier to install and less expensive and therefore used more often in practice. Acceleration measurements with a standard deviation of noise of $5cm/s^2$ taken in the middle of each of the eight tension braces at a sampling frequency of $100Hz$ for a duration of 2.50 seconds, were adequate to detect damages between 2% and 50% in the tension brace.

In some cases, taking measurements in the close vicinity of the damage can hold an advantage, as will be shown in the next section. However, in this case the damage could also be detected from measurements taken not on the braces, but on the deck members of the bridge.

## 8.6 Experimental Example: 'Weimar Beam'

In this section, the damaged beam of Chapter 4 will be analysed using the dynamic parameter identification algorithm developed in this chapter.

**The experiment** This $4.4m$ long damaged beam was excited by an impact load at one point and the vibrations of the simply supported beam were measured by seven accelerometers along the length of the beam. The impact load was also measured. This data was gathered after impact for 1 second at a sampling frequency of $1000Hz$. The beam was damaged in two areas, each damaged area consisting of five cuts at intervals of one centimeter and each cut reaching from the bottom halfway through the cross section of the beam. Figure 4.2 in Chapter 4 shows a schematic drawing of the beam and measurement setup.

**iFEM analysis** The iFEM model for the parameter identification analysis consisted of 44 beam elements (2-node Euler beam), each of length $0.1m$, with section properties as given in Table 4.1 and assumed to be undamaged. A point load element was added at the position of load application, to input the measured impact load. Measurement data from the seven accelerometers and the single load cell were given as input to the analysis. Using the algorithm described in this chapter, the location of the damage could be found. Several repetitions of the same experiment were done and combining data from all of these improved the results only slightly. The reason for this is probably that the impact loads were each time applied at the same position, so that the additional experiments brought very little new information into the analyses.

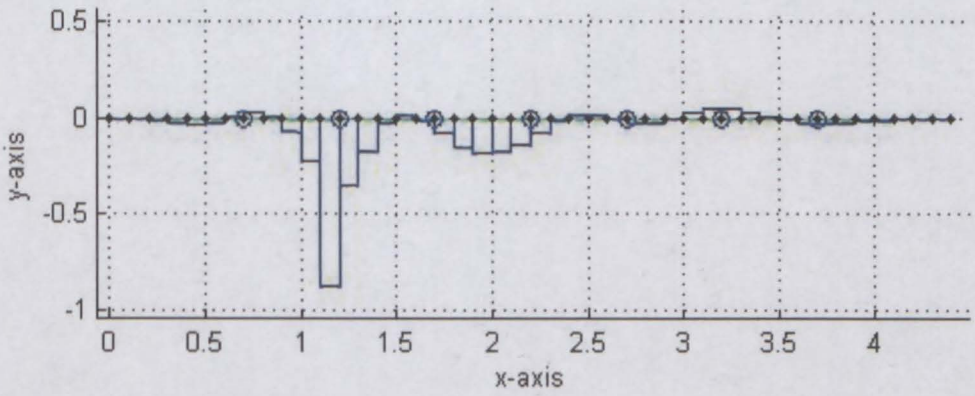


**Figure 8.2:** *Two damaged areas on a simply supported beam are identified from vibration data.*

**Influence of the cost on the quality of the damage estimate** The cost $Q_{xx}$ assigned to deviating from the measured acceleration values proved to play an important role. Measurements were taken for about fifty time steps before the impact load was applied. During that time, the beam was in a still position and environmental influences were kept to a minimum. The standard deviation of accelerations measured during this time was $0.017m/s^2$. This is assumed to be the standard deviation of a white noise process superposed on the response. The standard deviation of the measured load during this time was $0.07N$. Using these value to determine the cost on measured data (according to the theory described in Chapter 2, Equations 2.7 to 2.9), good estimates of the damage location were found, as shown in Figure 8.2.

If the measurements were assumed to be less precise, resulting in a higher standard deviation and thus lower $Q_{xx}$ cost, the damage zones were still detected, but in addition the algorithm lowered the stiffness of an undamaged area. The too low cost resulted in a false alarm, i.e. damage was detected where there was none. Figure 8.3 shows the actual damage being detected as well as the false alarm. This is a form of over-regularisation ("sluggishness") where the damage is spread, because it is a 'cheaper' solution. It was

noted before that over-regularised ("sluggish") force estimates[1] are usually the result when forces are priced too high. Here the under-regularised parameter estimate arrives from the cost on measurements being too low. An explanation can be found in the fact that the solution is not influenced by the actual costs, but only by the ratios between costs on forces, measurements and parameters. Thus, higher cost on measurements could have the same effect on the cost ratio as lower cost on parameters and produce less sluggish estimates. A low cost on deviating from measurements means that the measurements are judged to be inaccurate, therefore damage would not be concentrated (at high cost) to explain these measurements. A less probable explanation, since other experiments were conducted using the same beam, is that the beam was plastified in that area during those experiments. However, the fact that the false alarm disappears when correct costing is used, indicates that this is not the case.

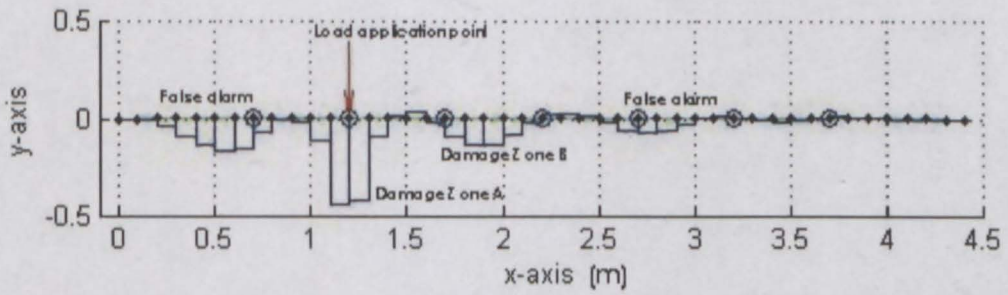


**Figure 8.3:** *A false alarm appears when measurement costing is incorrect.*

**Influence of damage and excitation on estimate quality** A numerical model of the damaged beam was created, from which numerical vibration data could be generated.

[1]See Chapter 2, Section 2.2.4. Under-regularised ("jittery") forces are unphysically large forces that appear as a result of a poor iFEM modeling choice. Usually, when the user defines measurement precision to be higher than it actually was, unphysically large forces will be estimated to squeeze the estimated response into reproducing the measurement noise. If on the other hand, the cost of forces is too high, the estimate is over-regularised ("sluggish") with too small external forces and the estimated response following the measured response very loosely. Localised loads would also tend to be spread out over a larger area than was actually the case.

Unless otherwise stated, acceleration data with added white noise of standard deviation $0.017m/s^2$ was generated at positions coinciding with the sensor position in the real experiment and the model was excited with the measured impact load from the real experiment. The model resembled the experiment closely, including the damaged zones. The analytical model allowed to investigate some other scenarios:

With measurements generated as described above and using an iFEM model that does not account for the damage, the same false alarm appeared when the cost was incorrect. This confirms that wrong cost was indeed the culprit and the beam was undamaged in the area of the false alarm, as visual inspection suggested.

In a second scenario one damaged zone at a time was removed from the FEM model and measurements generated with the impact load at the original position. Using iFEM on an undamaged model to detect the damage showed that a single damage zone, in combination with the impact at the original position, does not produce a false alarm even when the costing is incorrect. If damage zone B is removed, the iFEM analysis detects the damage (damage A) and no false alarms are present. The same is true when damage zone A is removed. Then damage B is detected and no false alarms are present. It is the combination of the two damages, with the load applied at that position and with wrong costing that results in a false alarm to the left. No single damage A or B in combination with the impact load and wrong costing resulted in a false alarm.

A third investigation showed that if the impact was applied $1.8m$ from the left, just above damaged zone B, damage B was detected more clearly. In the experiment the impact was applied $1.2m$ from the left along the beam, next to damage zone A, and Figure 8.2 shows how damage A is more clearly detected. Applying the impact to the right hand side of the beam resulted in both damaged zones being equally well detected. Clearly, the position of the excitation influences the detectability of damage and in this case, the closer the load was applied to a damaged area, the better that damage was detected.

Combining data from several repetitions of the same experiment did not result in a much improved damage description, probably because the impact loads were applied at the same position each time, so that the additional experiments brought very little new information into the analyses. A fourth investigation was to test if better damage identification is possible if the load is applied at a different position each time. Combining data from three experiments with different load application points improved the damage estimate, compared to the damage estimate obtained from three experiments where the load application point were the same each time.

**Information content of high frequency response components** A comparison of the measured accelerations with the estimated accelerations yields interesting results. The solid blue line in Figure 8.4 and Figure 8.5 shows the accelerations measured on the damaged beam, the dotted green line (hidden behind the blue line) shows the estimated accelerations if the damage is accounted for, while the dashed red line shows the estimated accelerations if the damage is not accounted for. From these figures it can be seen that the presence of damage in the beam has a significant influence on the high frequency response components, specifically, these frequencies are shifted. Many damage identification techniques make use of modal analysis and use only a limited number of modes. It is important not to discard the significant amount of information contained in the high frequency response components associated to higher modes.

Measurement noise may overrule the high frequency response components if care is not taken to adequately excite the structure in the range of frequencies of interest. Excitation forces that contain high frequency components will cause response at those same frequencies. The frequency content of measurement noise will depend on the process, but may also contain significant high frequency components. If the response signal can not be distinguished from measurement noise, the information contained therein will be lost. The range of high frequencies that are of interest will vary depending on the type of inspection that is considered. For example, if the application is the inspection of a weld using ultra-sound excitation, very high frequencies will be of interest, because the

damage that need to be detected is small and need to be accurately located. The high frequencies considered at the inspection of a bridge structure will not be nearly as high as those excited in the weld inspection. The excitation must contain an adequate level of forces at the high frequencies of interest to ensure that a measurable response is obtained at those frequencies.

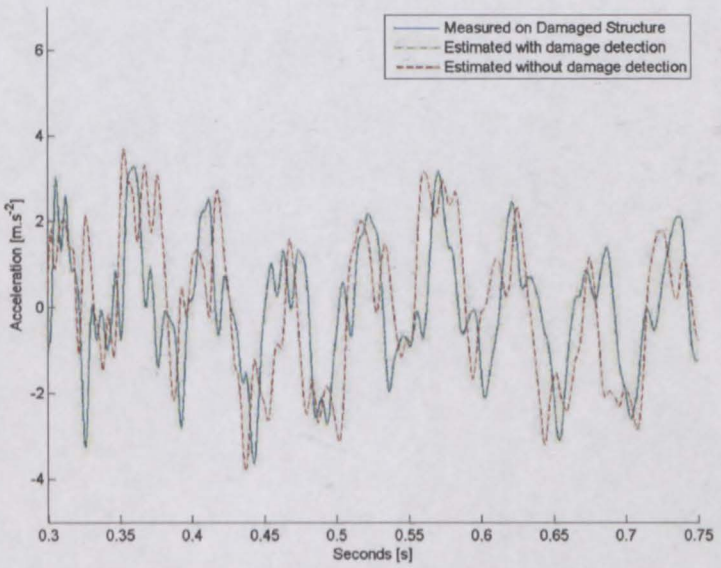


**Figure 8.4:** *Measured and estimated accelerations*

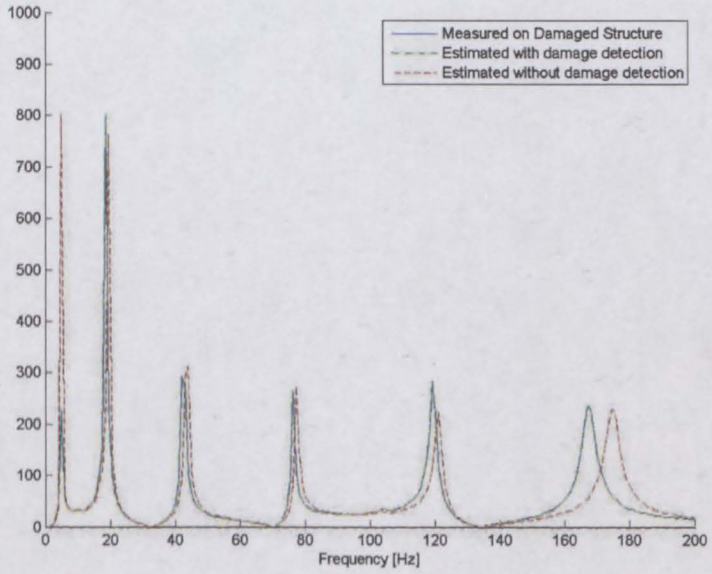


**Figure 8.5:** *Frequency components of measured and estimated accelerations*

## 8.7 Conclusions

1. In this chapter an iFEM algorithm for the identification of model parameters in dynamic systems is derived. The developed method allows data from several experiments to be combined and in this way accumulate information for the identification purpose.

2. The newly developed algorithm was implemented into the existing software SAFRAN. The software was also restructured and improved to allow both the static and dynamic parameter identification algorithms to be properly utilised.

3. The algorithm was tested using a numerically simulated experiment of a cantilever bridge and also using data from a real experiment conducted on a damaged beam. Results obtained are encouraging and indicate that the algorithm can be used to detect damage in structures, using measurements of its response.

4. In the cantilever bridge example iFEM was able to locate and quantify small dam-

ages. Compared to static experiments, it is believed that the dynamic algorithm's ability to detect small defects is related to both the larger volume of measurement data accumulated in one experiment and the ability of higher frequency response to localise small defects that only affect response in a small area.

5. The algorithm succeeded to detect damage from real measurements on a vibrating damaged beam. In this case damage located close to a load application point was better identified. If repeated experiments are carried out, it is more beneficial to change the point of excitation for each experiment, each time exciting the structure in a different way. In this way, the repetition of experiments brings more information into the identification process.

6. With regard to long-term health monitoring of large structures such as bridges and offshore platforms, the need to reduce the dependence upon measurable excitation forces is noted by many researchers. While a measured excitation force is an advantage, the algorithm developed in this chapter does not require the excitation force to be measured. The algorithm can use vibrations induced by ambient environmental or operating loads for the assessment of structural integrity.

# Part IV

# Experimental validation of the iFEM theories

# Chapter 9

# Experimental benchmark

## 9.1 Introduction

In August 2002, experiments were conducted on a small scale model of a steel frame structure, built at the Earthquake Engineering Research Laboratory of the University of British Columbia, Canada. High quality data was gathered of the response of the structure under various modes of excitation [14]. Different damage configurations were investigated by removing bracing and loosening beam-column connections within the test structure. It was proposed that this structure should be used as a benchmark for comparative studies of damage detection methods. In this chapter iFEM dynamic parameter identification is applied to locate and quantify the damage in the structure. Uncertainties regarding the method and the experiment are discussed. Where damage failed to be detected, reasons are discussed.

## 9.2 Experimental setup

This section provides a brief description of the benchmark experiment. A detailed description of the benchmark problem can be found in [14]. Three different methods of excitation were used to explore the response of the structure in nine damage scenarios. Acceleration measurement data for each combination was collected using 15 accelerometers.

Data records for this experiment were downloaded from the web page

*http://wusceel.cive.wustl.edu/asce.shm/*, where previous work, papers by other authors and more related information were also available.

### 9.2.1 The structure

The benchmark structure is a 4-storey, 2-bay by 2-bay steel frame scale model structure (shown in Figure 9.1), with a footprint of 2.5m by 2.5m and a height of 3.6m. The sections used for the different structural beam elements are given in Table 9.1.

Four steel plates were attached to each floor to represent the mass of a building. Each plate on the first three floors has a nominal mass of 454 kg (1000 lb), and the masses on the fourth floor have a mass of 340 kg (750 lb). The plates are identically placed at each floor, with masses being distributed asymmetrically so that torsional motions are also activated.

**Figure 9.1:** *The benchmark structure*

| Element | Section |
|---|---|
| Columns | B100×9 |
| Floor Beams | S75×11 |
| Sides Bracing | 2 solid rods, 12.7mm diameter |
| Floor Bracing | 50×50×3 mm Rectangular hollow profile |
| Floor Masses, floor 1-3 | 1.5×0.65×0.06 mm solid steel |
| Floor Masses, floor 4 | 1.5×0.65×0.045 mm solid steel |

**Table 9.1:** *Sections used for Benchmark's structural elements*

### 9.2.2 Excitation methods

Three loading conditions were applied for each of nine damage configurations: ambient vibration, broadband forced vibration produced by an electro-dynamical shaker and hammer impacts (impulse tests).

The structure was placed outdoors, so that *ambient vibration* was induced by several factors such as wind, and ground excitation produced by people walking near the structure, traffic, and working machinery. The duration of the recorded data was 300 seconds for each configuration, sampled at 200Hz.

A random input was introduced with an *electrodynamic shaker* placed on the roof of the structure, roughly at the center of north-east bay, applying a shaker force alternating direction from South-East to North-West. The shaker force input excited the benchmark structure for 120 seconds for each damage configuration, sampled at 200Hz. Two types of shaker force, random and sinusoidal sweep input, were used. This chapter considers only the random excitation.

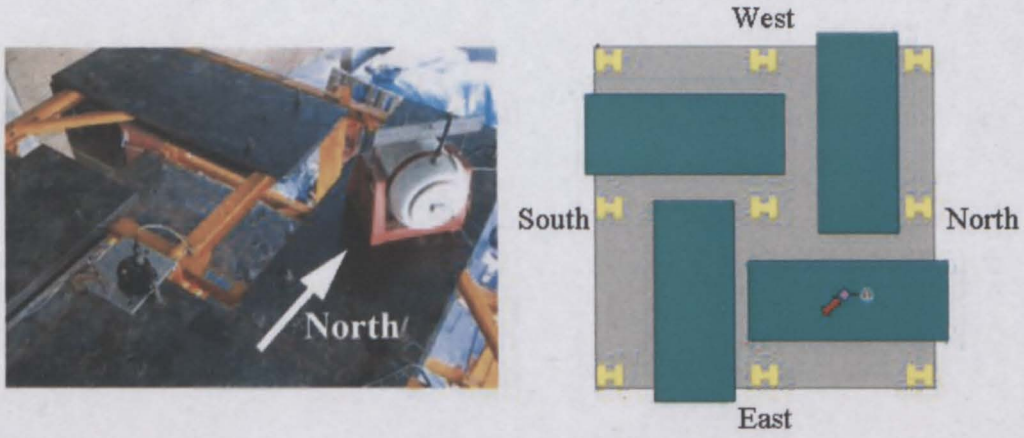


**Figure 9.2:** *Electrodynamic shaker setup*

*Hammer impacts* were all located on the South-West corner at the first floor (between first and second stories) and responses were recorded for each of the two impacts directed in the North-South and West-East directions respectively. For each configuration, the structure was hit three times in a single direction, recording data at 1000 Hz for as long as it took for the response to die out after each hit, typically around 30 seconds.

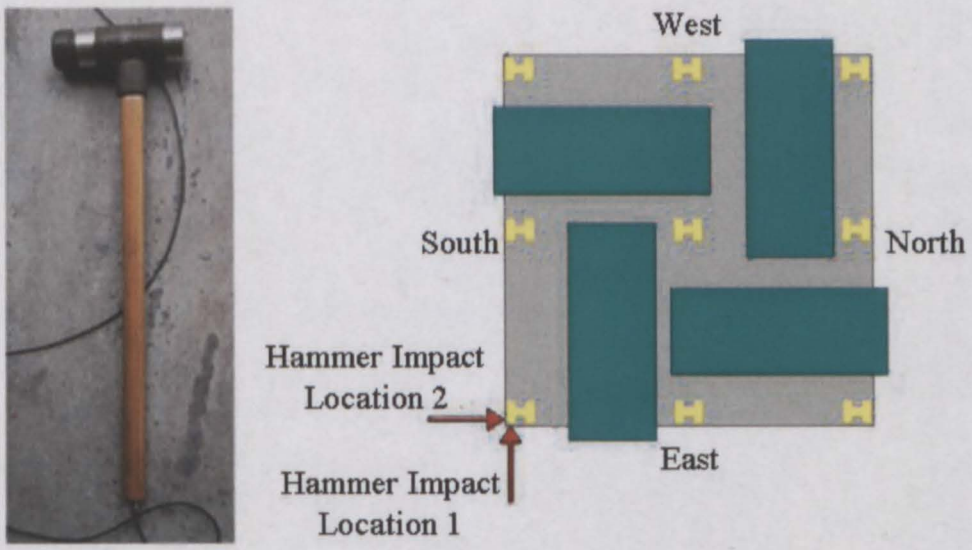


**Figure 9.3:** *Impact hammer setup*

### 9.2.3 Measurements

A total of 16 uni-axial accelerometers was placed on the structure to record its response. Each floor (including the base) was equipped with three sensors, two of which measured accelerations in the North-South direction at opposite sides of the structure, and the third measured West-East accelerations. Figure 9.4 shows the measurement setup for one floor, the setup being similar for all floors. The sixteenth accelerometer measured the accelerations of the electrodynamic shaker and can be used to calculate the force applied by the shaker. The impact force was measured by a load cell in the hammer tip.

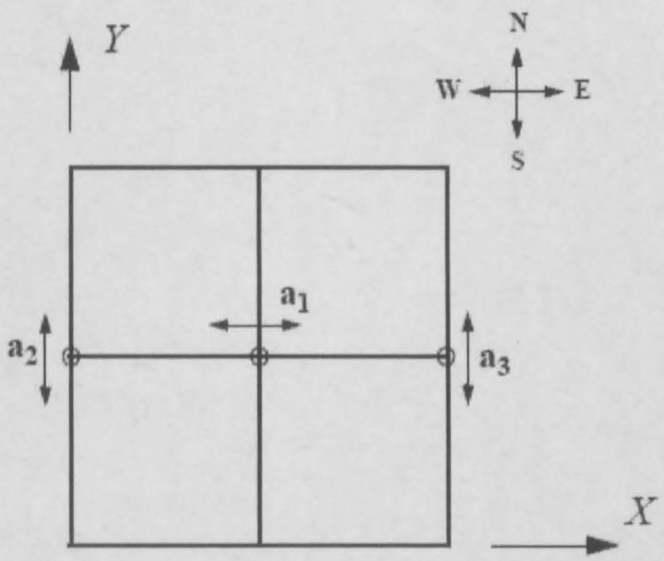


**Figure 9.4:** *Placement of the acceleration sensors*

### 9.2.4 Damage scenarios

Table 9.2 and Figure 9.5 describe the different damage scenarios. In this chapter, only damage configurations 1 to 7 are investigated.

| Configuration | Damage |
|---|---|
| Configuration 1 | Undamaged structure. All braces present. |
| Configuration 2 | All braces on the east side are removed. |
| Configuration 3 | Braces on the south half of the east side are removed. |
| Configuration 4 | Braces on the first and fourth floor of the south half of the east side are removed. |
| Configuration 5 | Braces on first floor of south half of east side are removed. |
| Configuration 6 | Braces on the second floor of the north side are removed. |
| Configuration 7 | All braces on all sides are removed. |
| Configuration 8 | All braces and floor beams of north half of east side are removed. |
| Configuration 9 | All braces and 2nd and 3rd floor floor beams of the north half of the east side are removed. |

**Table 9.2:** *Description of the damage configurations*

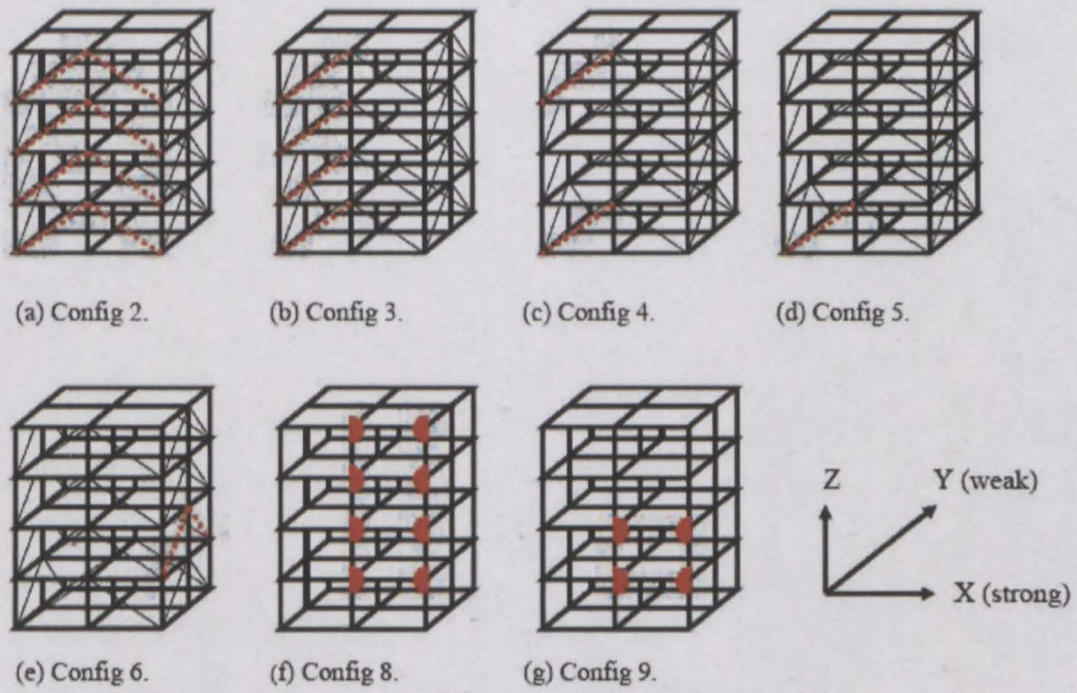


**Figure 9.5:** *Damage Configurations (J.Ching, J.L. Beck, 2003)*

### 9.2.5 Uncertainties

A major source of uncertainty lies in the stiffness of connections between the different structural elements. During one of the meetings held by the researchers conducting the benchmark experiments, the following concerns were raised regarding this uncertainty:

1. The way the braces are connected to the structure causes the brace stiffness to degrade significantly. The two 12.7mm threaded rods are connected to a flat plate that is then connected, at the center, to the column. According to preliminary calculations by one of the researchers, this flat plate is flexible enough to cause the axial brace stiffness to be half of the combined stiffness of the two rods.

2. The beam-column connections are bolted, but probably cannot be considered fully rigid connections. They can, perhaps, be modeled as torsional springs instead.

Other concerns identified by the author includes uncertain damping properties, inconsistent mass information, and confusion regarding the measurement units of recorded data:

No formal decay tests were done to determine the damping. However, a stiffness proportional damping coefficient was chosen such that the response obtained from the FEM model gives the same rate of decay of the measured response after a hammer impact. Mass proportional damping on such structures are known to be small and was assumed to be zero.

The masses on the first to third floor was claimed to be 1000 kg each, with the fourth floor masses 750 kg. This weight, however, did not correspond to the weight computed for the steel plates from their respective dimensions and the density of steel. This led to the conclusion that the unit (kg) given for the steel plate masses was falsely given as kilograms (kg), instead of pounds (lb). This was confirmed as a possibility by the researchers who conducted the experiment.

Given the measured hammer impact as input, the FEM model predicts accelerations of significantly higher order of magnitude (approximately 200 times too big) than what

was recorded. The reason for this is unclear. The same FEM model predicted an order of magnitude of accelerations comparable to what was recorded, when the shaker force (computed from the measured acceleration of the moving shaker mass) was applied. Uncertainty regarding the units of impact force measurements were suspected to be the cause. Possibly the hammer impact data is in Volts, from the voltmeter, and have never been converted to Newtons. Inquiries were made to the researchers who conducted the experiments, but they claim that they converted all American units and voltage data to the metric units shown in Table 9.3, so that the data files on their web page are given in these metric units. Because of this uncertainty, the measured impact force were omitted from the analyses, instead allowing an unknown point load to be identified at the position where the impact was applied. Assuming a linear dynamic response allows for the measured accelerations to be used as a basis for damage detection without using the measured force.

| Measurement | Unit |
|---|---|
| Acceleration | g |
| Displacement | cm |
| Force | N |

**Table 9.3:** *Metric measurement units used by Benchmark experimentalists*

### 9.2.6 Other considerations

The Fourier spectrum of the shaker input force (proportional to the measured acceleration of the moving mass) has resonant peaks at the natural frequencies of the benchmark structure [8], indicating substantial shaker-structure interaction. This shows that the force data was influenced by the structural response.

## 9.3 The iFEM model

Three dimensional beam elements are used to model the structural elements, defining 6 degrees of freedom per node. Element connections are assumed rigid and the footings of the structure are modeled to be pinned to the ground. The floor masses are also modeled as beam elements, with the correct mass per length, and pinned to the floor beams. Figure 9.6 shows the model. Acceleration magnitudes are defined on each floor (but not on the base) at the three positions where measurement sensors were located, allowing for the input of measurement data.

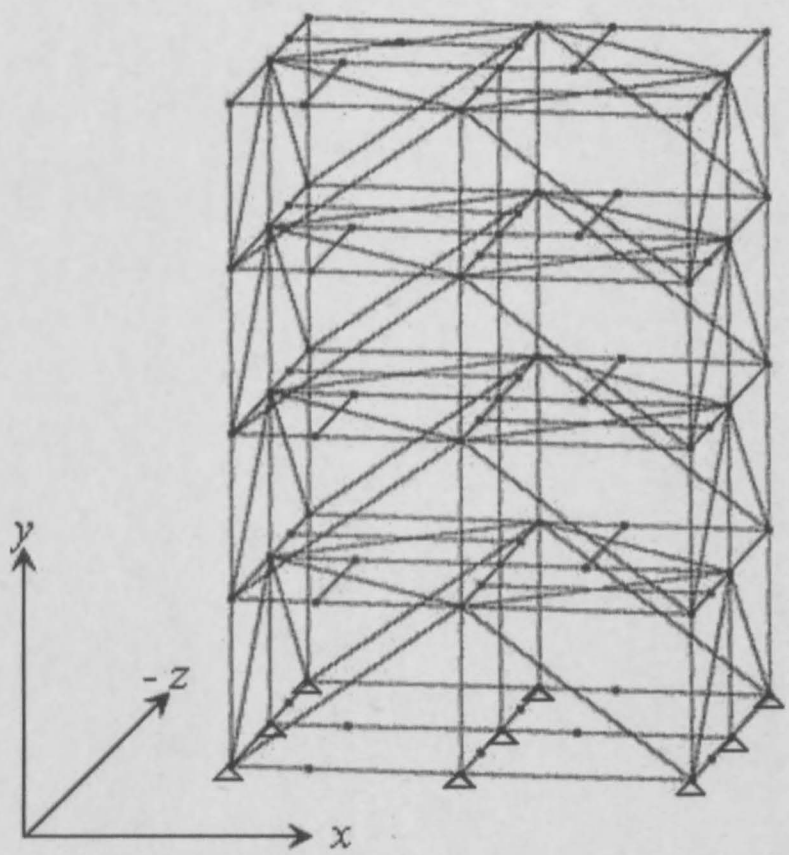


**Figure 9.6:** *The benchmark FEM model*

Since ambient excitation will always be present, distributed forces are allowed on all members, also for the shaker and hammer impact tests. Allowing these force degrees

of freedom improved our ability to locate and identify damage, as discussed in Section 9.5.

In the shaker tests, the iFEM model allowed for an additional point load to be identified at the position where the shaker was placed. The measured shaker force was given as input at this point.

In the hammer tests, the iFEM model allowed for an additional point load to be identified at the position where the hammer impact was applied. The impact measurement was not given as input, because of uncertainty regarding the unit of measurement and thus the magnitude of the force, as commented on in Section 9.2.5.

Unknown stiffness parameters, that allow for changes in section areas, were introduced on side brace elements only. This choice encodes a prior knowledge that damage is located somewhere in brace members. If it was to be assumed that the user had no prior knowledge of the location of damage, such parameters should have been allowed on all structural members.

Mainly because of memory problems[1], but also to avoid long computation times, only about 500 time steps of data were used for each configuration, for each type of excitation.

## 9.4 Results

Table 9.4 shows, for each damage configuration, the changes in section area of the different side brace members, as predicted by iFEM from hammer impact vibration data. Tables 9.5 and 9.6 show similar results for the shaker tests and the ambient vibration tests respectively. For each damage configuration, the elements that should be damaged are printed in bold font. As these braces were totally removed, the change in section area for these elements should be -100%. A star (∗) indicates that damage was not identified

[1]The memory problem is discussed in Section 9.5

(false negative), while a hash (#) indicates a false positive (damage being identified where there is none). A brace is considered to be damaged if its section area is reduced by more than 10%.

**Damage estimates** While the damage is located for most of the damage configurations, many false alarms[2] appeared. Probable reasons for this are discussed in Sections 9.5 and 9.6.

For the undamaged scenario (Configuration 1), for all methods of excitation, the estimated damage parameters are mostly negative and indicate a reduction in the section area of all the side brace members. This confirms the observation in Section 9.2.5 that the way the braces are connected to the structure causes the actual brace stiffness to be less than what the section properties alone would let one believe. If this was indeed the case, then many of the reduced brace stiffnesses (in all damage scenarios), that were classified as false positives, are actually indicating this lowered stiffness.

When only one brace in a floor is damaged, iFEM spreads the damage to also damage the neighbouring brace in the same face. This phenomenon can be seen in the results for Configurations 3, 4 and 5. In the tables, this is indicated by a dollar sign ($).

Configuration 5 is the scenario with the smallest damage, with only one brace member being damaged. This damage was located from both the hammer impact data and the shaker excitation data, with the missing brace member being significantly more damaged than any other brace. The damage was also located from ambient vibration data, but here false positives as large as the identified damage appeared in the top floor.

Damage configuration 6 was not identified from any of the three different load configuration data sets. The damage location for this configuration is on the south face of

[2]A false alarm can be either a false positive or a false negative.

| Brace location | | | Predicted percentage change in section area of side brace members | | | | | | |
|---|---|---|---|---|---|---|---|---|---|
| Floor | Face | Side | Config1 | Config2 | Config3 | Config4 | Config5 | Config6 | Config7 |
| 1 | E | S | -17.52 # | **-95.79** | **-52.93** | **-21.27** | **-20.95** | -18.44 # | **-61.57** |
| | E | N | -18.04 # | **-87.61** | -55.96 $ | -22.34 $ | -22.54 $ | -18.75 # | **-44.74** |
| | N | E | -5.94 | -10.20 # | -17.52 # | -10.49 # | -9.00 | -4.16 | **-13.78** |
| | N | W | -6.35 | -12.41# | -19.90 # | -10.50 # | -9.70 | -4.14 | **-8.31*** |
| | W | N | -8.68 | -16.81# | -10.97 # | -8.69 | -9.28 | -6.96 | **-12.48** |
| | W | S | -7.86 | -15.20 # | -10.05 # | -8.14 | -8.76 | -6.63 | **-10.27** |
| | S | W | -2.41 | 8.77 | 3.42 | -2.08 | -3.31 | -3.64 | **-10.03** |
| | S | E | -2.34 | 7.89 | 0.33 | -1.50 | -2.90 | -2.84 | **-8.29*** |
| 2 | E | S | -8.04 | **-57.23** | **-27.39** | -8.93 | -9.59 | -10.85 # | **-79.06** |
| | E | N | -8.26 | **-60.14** | -21.32 $ | -7.01 | -8.61 | -9.65 | **-81.98** |
| | N | E | 0.23 | -2.65 | -13.38 # | -1.96 | -0.20 | **-1.25 *** | **-14.87** |
| | N | W | 0.30 | -2.32 | -9.88 | -2.40 | 0.49 | **-0.60 *** | **-20.36** |
| | W | N | -4.97 | -1.24 | -4.30 | -4.63 | -5.95 | -4.97 | **-24.66** |
| | W | S | -4.65 | -10.49 # | -9.59 | -4.65 | -5.36 | -5.30 | **-21.77** |
| | S | W | 4.09 | 10.58 # | -8.13 | 0.22 | 3.96 | 3.98 | **-3.68*** |
| | S | E | 1.95 | 5.92 | -5.57 | -1.59 | 1.24 | 0.00 | **-2.55*** |
| 3 | E | S | -5.24 | **-69.21** | **-33.61** | -2.82 | -4.82 | -5.84 | **-57.95** |
| | E | N | -7.50 | **-67.99** | -33.91 $ | -4.85 | -6.2 | -8.08 | **-63.25** |
| | N | E | 2.06 | -2.89 | -5.61 | -1.49 | 1.27 | 2.35 | **-6.38*** |
| | N | W | -1.13 | -0.51 | -4.68 | -1.44 | -1.51 | -2.08 | **-4.23*** |
| | W | N | -5.88 | -10.75 # | -8.15 | -2.48 | -6.21 | -4.70 | **-49.06** |
| | W | S | -5.31 | -8.86 | -3.56 | -2.11 | -5.11 | -2.39 | **-58.80** |
| | S | W | -0.34 | 7.32 | -0.64 | -0.70 | -0.01 | -2.74 | **-11.47** |
| | S | E | 0.05 | 5.76 | -1.82 | -0.89 | 1.13 | -0.78 | **-14.79** |
| 4 | E | S | -8.08 | **-102.91** | **-36.60** | **-18.80** | -7.52 | -11.39 # | **-60.55** |
| | E | N | -1.81 | **-85.57** | -30.29 $ | -13.55 $ | -2.91 | -5.34 | **-39.56** |
| | N | E | 1.10 | -16.44 # | -6.21 | -1.81 | 1.74 | 1.79 | **-8.82*** |
| | N | W | 6.10 | -16.10 # | -3.11 | -1.6 | 4.13 | 5.04 | **-16.63** |
| | W | N | -3.1 | -17.08 # | -13.64 # | -5.63 | -5.33 | -1.84 | **-56.64** |
| | W | S | -3.26 | -7.33 | -6.97 | -2.91 | -4.19 | -3.09 | **-38.85** |
| | S | W | 2.62 | -5.53 | -6.19 | -2.42 | 3.67 | 3.49 | **-3.65*** |
| | S | E | 2.63 | -8.18 | -6.33 | -2.39 | 2.23 | 2.32 | **-7.96*** |

# False positive (damage detected when not present)

* False negative (stiffness reduction not detected)

$ Damage spread to neighbouring brace

**Table 9.4:** *Damage parameters from hammer impact analyses*

| Brace location | | | Predicted percentage change in section area of side brace members | | | | | | |
|---|---|---|---|---|---|---|---|---|---|
| Floor | Face | Side | Config1 | Config2 | Config3 | Config4 | Config5 | Config6 | Config7 |
| 1 | E | S | -8.94 | **-75.02** | **-16.04** | **-40.43** | **-28.14** | -6.11 | **-2.08*** |
| | E | N | -9.12 | **-74.17** | -16.27 $ | -41.40 $ | -33.42 $ | -5.51 | **-2.07*** |
| | N | E | -3.36 | -23.08 # | -10.35 # | -19.17 # | -14.29 # | -5.52 | **-0.84*** |
| | N | W | -3.30 | -22.54 # | -10.18 # | -18.93 # | -13.74 # | -5.40 | **-0.78*** |
| | W | N | -5.50 | -22.45 # | -12.79 # | -16.62 # | -15.66 # | -11.44 # | **-2.59*** |
| | W | S | -5.32 | -22.15 # | -13.18 # | -16.28 # | -14.64 # | -11.47 # | **-2.55*** |
| | S | W | -1.18 | -6.08 | -5.94 | -9.85 | -9.55 | -3.72 | **-0.65*** |
| | S | E | -1.01 | -6.18 | -6.28 | -10.37 # | -9.21 | -3.74 | **-0.59*** |
| 2 | E | S | -5.73 | **-68.25** | **-20.88** | -2.30 | -13.98 # | -3.27 | **-2.42*** |
| | E | N | -7.04 | **-64.69** | -18.76 $ | -1.61 | -0.40 | -7.54 | **-2.35*** |
| | N | E | -0.86 | -8.59 | -4.74 | -2.65 | -3.48 | **-3.35** * | **-0.16*** |
| | N | W | -0.36 | -7.47 | -4.19 | -2.62 | -1.01 | **-3.72** * | **-0.16*** |
| | W | N | -7.91 | -9.20 | -6.95 | -10.72 # | -9.83 | -5.62 | **-0.46*** |
| | W | S | -8.39 | -9.37 | -6.98 | -10.78 # | -9.95 | -5.94 | **-0.44*** |
| | S | W | -2.43 | -0.75 | -3.99 | -2.92 | -2.70 | -1.47 | **-0.18*** |
| | S | E | -2.22 | -1.05 | -3.85 | -2.69 | -1.61 | -1.57 | **-0.22*** |
| 3 | E | S | -16.35 # | **-65.54** | **-21.93** | -4.59 | -9.06 | -21.23 # | **-0.80*** |
| | E | N | -2.73 | **-59.86** | -17.78$ | -1.78 | -3.93 | -5.44 | **-0.86*** |
| | N | E | -3.03 | -12.64 # | -2.60 | 0.67 | -2.17 | -4.94 | **-0.64*** |
| | N | W | 0.13 | -10.61 # | -1.33 | 1.25 | 0.35 | -1.37 | **-0.59*** |
| | W | N | -10.52 # | -18.78 # | -4.48 | -2.20 | -8.21 | -6.07 | **-0.66*** |
| | W | S | -9.89 | -17.70 # | -2.51 | -1.57 | -6.66 | -4.90 | **-0.69*** |
| | S | W | -1.75 | -8.91 | -1.60 | -0.12 | -1.40 | -2.58 | **-0.42*** |
| | S | E | -0.74 | -8.91 | -1.09 | 0.54 | -0.24 | -1.66 | **-0.33*** |
| 4 | E | S | 4.76 | **-76.39** | **-31.17** | **-34.64** | 6.59 | 5.02 | **0.22*** |
| | E | N | -11.01 # | **-75.03** | -33.72 $ | -35.40 $ | -14.83 # | -9.05 | **0.09*** |
| | N | E | -3.10 | -15.92 # | -13.57 # | -10.74 # | -3.84 | -4.72 | **-0.97*** |
| | N | W | -11.83 # | -16.58 # | -17.23 # | -13.02 # | -18.33 # | -10.36 # | **-0.99*** |
| | W | N | -15.03 # | -8.37 | -21.59 # | -8.78 | -14.99 # | -8.28 | **-1.02*** |
| | W | S | -12.01 # | -8.24 | -22.50 # | -8.45 | -9.53 | -7.41 | **-0.98*** |
| | S | W | -1.74 | -4.25 | -4.72 | -3.09 | -1.25 | -4.46 | **-0.47*** |
| | S | E | -2.85 | -6.47 | -6.49 | -4.57 | -3.20 | -5.41 | **-0.33*** |

# False positive (damage detected when not present)

* False negative (stiffness reduction not detected)

$ Damage spread to neighbouring brace

**Table 9.5:** *Damage parameters from shaker vibration analyses*

| Brace location | | | Predicted percentage change in section area of side brace members | | | | | | |
|---|---|---|---|---|---|---|---|---|---|
| Floor | Face | Side | Config1 | Config2 | Config3 | Config4 | Config5 | Config6 | Config7 |
| 1 | E | S | -23.64 # | **-17.30** | **-46.15** | **-67.92** | **-13.69** | -10.01 # | **-71.80** |
| | E | N | -23.42# | **-17.46** | -47.40 $ | -62.98$ | -14.34 $ | -10.18 # | **-68.94** |
| | N | E | -7.59 | -9.23 | -8.26 | -26.26 # | -1.79 | -2.46 | **-35.32** |
| | N | W | -7.73 | -8.55 | -6.85 | -26.88 # | -1.94 | -2.51 | **-35.20** |
| | W | N | -27.92 # | -15.8 # | -46.25 # | -35.06 # | -7.61 | -15.41 # | **-51.95** |
| | W | S | -28.35 # | -15.91 # | -47.91 # | -31.97 # | -8.18 | -16.2 # | **-51.17** |
| | S | W | -12.02 # | -1.48 | -14.17 # | -11.23 # | -4.01 | -3.19 | **-40.79** |
| | S | E | -11.76 # | -1.60 | -12.37 # | -11.87 # | -4.12 | -3.28 | **-38.96** |
| 2 | E | S | -20.85 # | **-37.83** | **-64.77** | -16.33 | -6.39 | -8.81 | **-104.32** |
| | E | N | -20.48 # | **-39.84** | -62.99 $ | -17.21# | -6.85 | -8.95 | **-92.52** |
| | N | E | -6.18 | -6.47 | -2.27 | -21.23 # | -0.58 | **-3.12** * | **-39.79** |
| | N | W | -6.01 | -6.90 | -3.01 | -19.69 # | -0.60 | **-3.03** * | **-41.87** |
| | W | N | -33.87 # | -22.54 # | -15.89 # | -22.50 # | -8.20 | -10.84 # | **-29.47** |
| | W | S | -36.71 # | -23.62 # | -15.28 # | -25.98 # | -9.10 | -11.91 # | **-28.49** |
| | S | W | -11.77 # | -7.44 | -11.69 # | -31.98 # | -2.10 | -3.24 | **-81.41** |
| | S | E | -11.95 # | -7.21 | -12.90 # | -30.35 # | -2.15 | -3.27 | **-85.44** |
| 3 | E | S | -7.07 | **-51.23** | **4.08** * | -6.57 | 7.74 | -0.53 | **-39.83** |
| | E | N | -8.38 | **-55.77** | 1.53 | -10.54 # | 7.72 | -0.51 | **-76.38** |
| | N | E | -9.45 | -8.09 | -7.16 | -13.69 # | -7.35 | -4.53 | **-86.24** |
| | N | W | -9.80 | -8.19 | -9.88 | -12.73 # | -8.14 | -5.56 | **-84.5** |
| | W | N | -25.14 # | -14.10 # | -20.89 # | -7.59 | 4.84 | 3.04 | **-36.57** |
| | W | S | -24.31 # | -14.19 # | -19.11 # | -9.59 | 7.41 | 5.36 | **-38.34** |
| | S | W | -5.31 | -5.23 | 1.56 | -19.96 # | -5.99 | -7.81 | **-2.50*** |
| | S | E | -5.17 | -4.81 | 1.56 | -17.90 # | -6.14 | -8.35 | **0.58** * |
| 4 | E | S | -6.75 | **-24.63** | **-25.74** | **-17.19** | 1.07 | -2.03 | **-54.76** |
| | E | N | -5.47 | **-26.37** | -23.58 $ | -11.12 $ | 2.80 | 2.17 | **-51.85** |
| | N | E | -8.71 | -6.21 | -4.10 | -2.84 | -5.54 | -6.10 | **-37.23** |
| | N | W | -9.47 | -6.55 | -6.47 | -3.07 | -5.77 | -7.39 | **-35.60** |
| | W | N | -26.35 # | -18.90 # | -25.78 # | -9.97 | -9.86 | -22.27 # | **-46.17** |
| | W | S | -29.16 # | -18.58 # | -23.80 # | -11.02 # | -13.47 # | -25.99 # | **-35.71** |
| | S | W | -22.18 # | -3.26 | -3.14 | -13.55 # | -19.01 # | -28.02 # | **-14.20** |
| | S | E | -21.74 # | -2.82 | -4.63 | -12.81 # | -17.89 # | -27.22 # | **-14.07** |

# False positive (damage detected when not present)
* False negative (stiffness reduction not detected)
$ Damage spread to neighbouring brace

**Table 9.6:** *Damage parameters from ambient vibration analyses*

the structure, while measurements were taken in the middle of the west and east faces. The damage location being far from measurement locations might have contributed to difficulties in identifying the damage: In Chapter 8, it was mentioned that high frequency response components carry a large portion of the information needed to locate damage. On the other hand, in a system such as the benchmark structure, where stiffness proportional damping is high, the high frequency response components will be damped out fast. The influence of damage on the response originates at the damage location, but it might be that the high frequency components are damped out to a large extent before reaching the sensor locations. In Chapter 8 it was observed that applying the load close to the damage location improved iFEM's ability to identify the damage in the damaged beam example. This might be due to the response amplitude of the damage influence being larger and thus reaching more sensors before being damped out.

An interesting observation is that the damage is much better located from the hammer data than from either the shaker or ambient data. The hammer data was sampled at a sampling frequency of 1000Hz, allowing it to capture more high frequency components than the shaker data or ambient data, which were both sampled at 200Hz. This confirms the observation made in Chapter 8, Figures 8.4 and 8.5, that high frequency response components carry important information for damage location.

**Response and force estimates** In all analyses, the iFEM estimated response corresponds well with the measured data. For the ambient vibration tests, the iFEM estimated ambient excitation forces were realistically small. For the analysis of damage configurations 1-6 of the shaker excitation tests, the magnitude of the iFEM estimated shaker excitation force was of similar magnitude to the measured shaker excitation force. For the shaker excitation test of damage configuration 7, iFEM severely over-estimated the magnitude of the shaker force, compared to the measured force. This indicates an inappropriate choice of costing for this analyses, which is further discussed in Section 9.6, and which is the reason why damage was not detected in this case. When the costing is adjusted in order to obtain a better force estimate, the damage is also detected.

Even when damage is identified from hammer impact test data, the load is not well identified. The identified load often shows a clear impact, but the magnitude of this identified impact is much underestimated, compared to what was measured. Possible reasons could be

1. The unit of measurement for the impact force measurement is under suspicion (Refer to Section 9.2.5). This could confirm the assumed measurement unit to be incorrect.

2. The costs were tuned to give the best results in terms of damage identification. This might favour a costing setup in which the cost on forces is rather too high than too low. Too low cost on forces could contribute to damage going unidentified, because the effect of damage might then be explained by ghost forces.

3. iFEM will always tend to spread forces (and damage, for that matter) in time and space, because this yields a 'cheaper' solution in terms of the quadratic cost function.

**Results from an alternative modelling choice** If the footings, instead of being hinged, are modeled as spring connected, the acceleration measurements taken at the base of the structure can also be added to the analysis. Following this approach gave some interesting results: The analyses of damage configuration 1 showed several large false positives in its estimation of the section area changes. For damage configuration 2, the damage is identified, but in addition the same false positives that were seen in the analyses of damage configuration 1 are again present. If the parameters identified for configuration 2 are adjusted by subtracting the values found for configuration 1, the damage is well located. Table 9.7 shows an example of this phenomenon.

## 9.5 Discussion

**Memory problems** During the course of the analysis, computer memory related problems appeared in the prototype software. This was mostly due to some parts of the code having been written in a memory inefficient way. This will be corrected in the near future.

| Brace location | | | Predicted percentage change in section area of side brace members | | |
|---|---|---|---|---|---|
| Floor | Face | Side | Config1 | Config2 | Config2 – Config1 |
| 1 | E | S | -32.00 # | **-109.09** | **-77.08** |
| | E | N | -59.77 # | **-124.08** | **-64.32** |
| | N | E | -0.13 | 2.06 | 2.18 |
| | N | W | 2.81 | 4.90 | 2.09 |
| | W | N | -11.04 # | -14.62 # | -3.58 |
| | W | S | -13.94 # | -17.12 # | -3.17 |
| | S | W | 7.00 | 11.21 | 4.21 |
| | S | E | 24.50 | 28.09 | 3.59 |
| 2 | E | S | 195.50 | **160.81** * | **-34.69** |
| | E | N | -40.25 # | **-115.32** | **-75.07** |
| | N | E | -29.53 # | -35.15 # | -5.63 |
| | N | W | -27.01 # | -30.58 # | -3.57 |
| | W | N | -2.89 | 2.94 | 5.83 |
| | W | S | -7.67 | -11.73 # | -4.06 |
| | S | W | -23.35 # | -27.87 # | -4.52 |
| | S | E | -24.99 # | -29.39 # | -4.40 |
| 3 | E | S | 1.07 | **-80.72** | **-81.80** |
| | E | N | -6.90 | **-86.78** | **-79.88** |
| | N | E | -0.20 | -4.15 | -3.96 |
| | N | W | 0.03 | 1.25 | 1.22 |
| | W | N | -6.66 | 1.16 | 7.83 |
| | W | S | -5.45 | 7.13 | 12.58 |
| | S | W | -10.47 # | -1.00 | 9.46 |
| | S | E | -7.98 | -8.37 | -0.39 |
| 4 | E | S | -6.57 | **-107.91** | **-101.35** |
| | E | N | -6.30 | **-107.59** | **-101.29** |
| | N | E | 4.21 | -8.86 | -13.06 # |
| | N | W | 1.65 | -9.71 | -11.35 # |
| | W | N | -3.01 | 1.93 | 4.94 |
| | W | S | -1.95 | 7.48 | 9.43 |
| | S | W | -6.55 | -11.12 # | -4.56 |
| | S | E | -2.79 | -10.20 # | -7.41 |

# False positive (damage detected when not present)
* False negative (stiffness reduction not detected)
$ Damage spread to neighbouring brace

**Table 9.7:** *Damage parameters from shaker vibration analyses using a model with spring supported footings*

The benchmark is the example with the largest number of degrees of freedom treated by the prototype software up to date. The memory problems hampered the author's ability to use the iFEM theory to its full capacity:

1. The full length of measurement data could not be used. Only about 500 time steps of data were used for each analyses, while 24000 time steps or more were usually available.

2. The iFEM theory allows for information from different experiments to be combined to improve model parameter estimates. In the present case, we would have been able to combine information from ambient-, shaker- and hammer excitation tests. This, however, required that three times the number of degrees of freedom be introduced (each of the three different models making a contribution), and resulted in memory failure.

3. The memory problem can be solved by writing an "out of core" solver, which avoids the use of limited Random Access Memory (RAM) to store large amounts of data. The solver will be able to store measurement data and calculated matrices on hard disk in an intelligent way, such that reading and writing to disk takes little time compared to the Central Processing Unit's (CPU) time spent on solving the linear system of equations. This is possible because the dynamic iFEM XUA problem can be decomposed into independent blocks of data that can be solved separately. These blocks of data are not so small and many that the time spent in reading and writing them to and from disk will overshadow the CPU time spent on solving the subsystem. They are also not so large that one such independently solvable block cannot fit into RAM: The size of one such independent block is $(2 \times nXdof + nUdof) \times (2 \times nXdof + nUdof) + (2 \times nXdof + nUdof) \times (n\alpha)$, where $nXdof$ is the number of displacement degrees of freedom, $nUdof$ the number of force degrees of freedom and $n\alpha$ the number of model parameters. The order of complexity associated to solving this subsystem is $(2 \times nXdof + nUdof)^2 \times (n\alpha)$, so that the CPU time spent on solving a linear system of this size will become impractical before the RAM is exceeded. This means that the CPU computing time reported in

Chapter 8, Section 8.3.3 will dictate the practical feasibility of the dynamic iFEM XUA algorithm.

In addition to these problems, measured force data could not be used as input to any of the analyses, because of questionable force measurements.

**Influence of modelling choices** Allowing unknown forces on all structural elements was primarily done to simulate the presence of ambient excitation. It was, however, noticed that allowing these forces greatly increased iFEM's success in locating damage. This can be explained as follows: Model uncertainty has a significant influence on the ability of iFEM to identify damage. When model uncertainties introduces errors into the iFEM model, iFEM can explain measurements either by adjusting model parameters to describe the model uncertainties or by estimating external forces that would have a similar effect on the measured response than the modeling error. When the types of model parameters that have been introduced in the iFEM model do not correspond to the types of model errors that are present, it is very likely that iFEM will estimate external ghost forces to explain the effect of the model errors on the response of the structure. Alternatively, the model parameters that were allowed will be adjusted in a way that has little physical meaning, because the type of parameter that was allowed cannot adequately describe the model error that is present. Allowing distributed forces to be identified allowed iFEM to explain the discrepancies between the model and the real problem by estimating ghost forces, without polluting the damage estimate.

In the present case, damage parameters that allow for changes in section area were introduced on all side brace members. In addition to damage, there is uncertainty regarding the stiffness of beam-column connections and footing conditions. No model parameters were introduced to explicitly allow for these uncertainties. Disregarding these uncertainties would have introduced some error in the iFEM model. The effect of these errors on the structure's response, which is supposed to follow the measured response closely, might be suppressed by applying some distributed external force to the structure. Alter-

natively, the side brace section area parameters might be changed in an unphysical way to try to undo the effect of wrong beam-column connection modeling and wrong footing conditions. The best way to avoid this problem is to explicitly allow for as many model uncertainties as possible, by defining appropriate model parameters in the iFEM model. The lack of enough model parameters in the present iFEM model in combination with significant model uncertainty is probably the cause of many of the false alarms that were present in the results. Specifically, the beam connections, that were modeled as clamped, would be better modeled by rotational springs, with parameterised rotational stiffness. To this purpose it would be necessary to introduce a rotational spring element in the element library of the SAFRAN software.

Changing the footing conditions had a significant influence on the identified parameters, so that numerous large false alarms appeared. This raises the concern that the results seem to be fairly sensitive to poor modeling. Model uncertainties should therefor be explicitly allowed for by defining unknown model parameters. In this way, model uncertainty can be assigned where it is most probable. If this is not done, model uncertainties and consequent wrong modelling will cause ghost forces and ghost parameters[3] to appear.

## 9.6 Costing

Assigning the correct cost to each measurement or estimate proved to be very tricky. A costing theory exists and was presented in Chapter 2 Section 2.2.3, that allows the user to define a cost based on probability theory, using the standard deviation of the measure-

[3]When a structure is poorly represented by the chosen iFEM model, unphysical external forces are calculated in order to get the iFEM estimate to corroborate the measurement data. In cases where no external forces can occur, the unphysical external forces are easily identified. Such forces are referred to as "ghost forces". For similar reasons unphysical model parameters can be calculated and these are referred to as "ghost parameters".

ment noise. This theory allowed to successfully define the cost assigned to acceleration and force measurements used in the Weimar Beam example of the previous Chapter. Unfortunately, in practice, this theory seldom yields good results. In the current application, the author had to run a large number of analyses, each time tuning the cost matrices assigned to forces, measured accelerations and section parameters respectively, until useful results were obtained. Whether the results that were obtained are the best possible solutions to the problem is doubtful. It is urgently needed to revise the theory for costing in order to present a useful tool for experimentalists. Tuning the costs in a manual way, as was done in the present case, is time consuming and leaves the user questioning the quality of his result.

The cost was tuned for each load configuration, to give the best results in terms of damage identification for damage configuration 2. The 'optimal' cost was the combination of $Q_{xx}$, $Q_{uu}$ and $Q_{aa}$ for which iFEM gave the best damage identification result while following the measured data, estimating small ambient forces and estimating point loads (when they were present) of reasonable magnitude. Once this 'optimal cost' was decided on, the remaining six damage configurations were solved for using the same costs.

The probabilities associated to different levels of ambient excitation, and the standard deviation of point loads around zero, are independent from the damage configuration. Also, sensor noise is not expected to differ for the different damage configurations. Therefor, for each load configuration, the cost was kept identical for all damage configurations.

It is sometimes clear from the results that the costing should be tuned to get better damage identification and realistic force magnitudes. A good example of this is the results from the shaker test data for damage configuration 7: In this configuration, all braces were removed, and fairly large negative section area changes are therefor expected for all braces. This is not realised, with small damage parameters being identified. However, the predicted shaker force is about 4 times too large in magnitude compared to the measured shaker force, which indicates that a too small cost was assigned to the unknown point

load. Starting from the FEM model (which is inaccurate, since it doesn't account for the damage), iFEM can explain the difference between the measured and expected response by lowering the stiffness or by applying larger forces. The cost assigned to changes in section parameters were too large or the cost assigned to forces too low. Because of this, while lower stiffness was the reason for the difference between the measured and expected response, it is explained by larger forces instead of the damage being identified. The same costing gave good results (both in terms of damage detection and force magnitudes) for damage configuration 2.

## 9.7 Comparison with other methods

The experimental study of the benchmark structure is the second phase of a study that started out with numerically simulated experiments on the benchmark structure (known as phase I of the benchmark problem). Phase two of the study was carried out in August 2002, at the University of British Columbia, Canada. While numerous publications that address phase I of the benchmark problem were found, the author could find only two publications that treated damage identification in the Benchmark structure using real experimental data (known as phase II of the benchmark problem). Their methods and results are discussed below.

### 9.7.1 A damage detection approach using eigenfrequencies and mode shapes found from NExT and ERA

**Methodology** The damage detection technique used in this approach [20] consists of four steps:

First, the natural frequencies and mode shapes of the structure are identified. To this purpose, the Natural Excitation Technique (NExT) and the Eigensystem Realization Algorithm (ERA) are applied: NExT is a technique developed by James et al. [31], who showed that when forced vibration data is available from tests conducted with an

unknown excitation, cross-correlation functions between the response measurements and a single reference measurement can be treated as free responses. ERA is a method used to extract the structural eigen-frequencies and mode shapes from measured free response data. In the case of the hammer impact tests, ERA could be used directly to find the eigenfrequencies and mode shapes from the response data, while NExT had to be applied to the data from ambient vibration tests, before ERA could be applied. Shaker test data was not treated.

In the second step, an identification model of the structure must be chosen. The capabilities of this approach to detect damage are strongly linked to the selection of an appropriate identification model. The identification model has only as many model parameters as there are measurement sensors. The form of the identification model will determine and limit the range of potential structural behaviors that the model can represent. Modeling errors (errors in representing the dynamics of the physical structure with the simplified, discrete-parameter model) play a significant role in the accuracy of this technique [6]. The model used to treat the benchmark problem is shown in Figure 9.7.

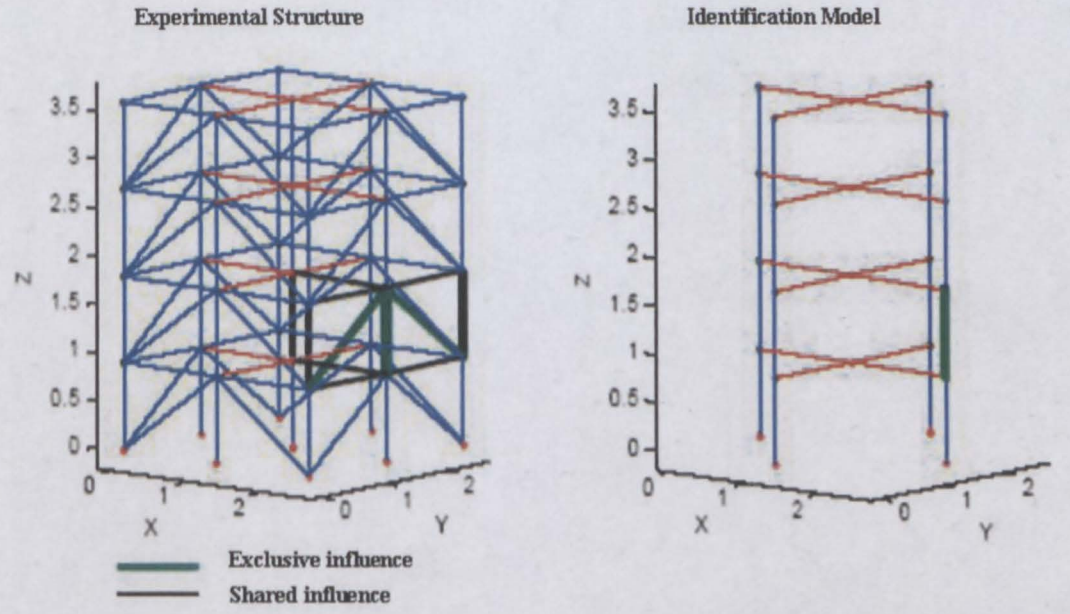


**Figure 9.7:** *Association between members of the physical structure and elements of the identification model.*

In the third step, the natural frequencies and mode shapes (obtained in the first step) are used to estimate the stiffnesses of the identification model, based on a least squares approximation of the unknown parameters (stiffnesses) in the characteristic free response equation:

$$(K - M\lambda_i)\phi_i = 0 \tag{9.1}$$

where $K$ is the parameterised stiffness matrix and the mass matrix $M$ of the structure is assumed known. $\lambda_i$ is the i-th eigenvalue (square of the i-th natural pulsation of the structure), and $\phi_i$ is the i-th eigenvector (corresponding to the i-th mode shape). Equation 9.1 can be rewritten as

$$\delta_i k = M\lambda_i\phi_i \tag{9.2}$$

where $k$ is a vector containing the $p$ unknown stiffness values corresponding to specific elements in the identification model, and the mode shapes are written in matrix form as $\delta$. The number of unknown stiffness values that the identification model may contain

is limited to the number of eigen-frequencies and mode shape pairs identified from the measurement data, which is in turn limited to the number of measurement sensors on the real structure.

The final step consists of an iterative process to refine the results obtained with the previous steps. The main assumption is that elements can neither gain stiffness after damage is introduced to the structure, nor have a negative value of stiffness. Several iterations may be needed in order to obtain a damaged model in which all stiffnesses lie between 0 and 100% of the stiffnesses in the undamaged case. Then, by examining changes in the identified stiffnesses between the undamaged and damaged models, faulty element groups are located and quantified.

**Results** The method described in this section produced good results in terms of damage detection and location of damaged element groups for the benchmark problem. Table 9.8 contains the stiffness reduction for each element group as obtained from ambient vibration data. Table 9.9 gives the same results as obtained from hammer vibration data. Vibration data from shaker excitation was not treated. Damage configurations 1 to 6 were analysed, and for configurations 1 to 5 the damage was successfully detected from both the ambient vibration data as well as the hammer impact data. Some problems were encountered with damage configuration 6, where the method failed to detect the damage from ambient vibration data. Damage configuration 6 were detected using hammer impact data, although some false alarms were present.

It is difficult to compare the results from this method with those obtained by iFEM because of the simplified lumped model that was used. In this model, several structural elements contributes to a single damage parameter. For this reason, the accuracy of damage location is limited to the element group contributing to the parameter. When only one brace in an element group was damaged, the damaged and undamaged braces could not be distinguished. From iFEM results it is easy to distinguish individual element damage and to flag false alarms on elements other than the damaged ones.

| Group location | | Predicted percentage change in stiffness of element group | | | | | |
|---|---|---|---|---|---|---|---|
| Floor | Face | Config 1 | Config 2 | Config 3 | Config 4 | Config 5 | Config 6 |
| 1 | E | 0 | **-66** | **-23** | **-32** | **-33** | 0 |
| | N | 0 | 0 | 0 | 0 | 0 | 0 |
| | W | 0 | 0 | 0 | 0 | 0 | 0 |
| | S | 0 | 0 | 0 | 0 | 0 | 0 |
| 2 | E | 0 | **-36** | **-32** | -10 # | -1 | -5 |
| | N | 0 | 0 | 0 | 0 | 0 | **0** * |
| | W | 0 | 0 | -2 | -22 # | -7 | -2 |
| | S | 0 | 0 | 0 | 0 | 0 | 0 |
| 3 | E | 0 | **-77** | **-42** | 0 | 0 | 0 |
| | N | 0 | -4 | -4 | -1 | 0 | 0 |
| | W | 0 | 0 | 0 | -20 # | -2 | 0 |
| | S | 0 | 0 | -12 # | -2 | -4 | 0 |
| 4 | E | 0 | **-88** | **-38** | **-41** | 0 | -4 |
| | N | 0 | -4 | 0 | 0 | 0 | -5 |
| | W | 0 | 0 | 0 | 0 | 0 | 0 |
| | S | 0 | 0 | -4 | 0 | 0 | 0 |

# False positive (damage detected when not present)
* False negative (stiffness reduction not detected)

**Table 9.8:** *Stiffness reduction from Ambient vibration using NeXT and ERA analyses*

| Group location | | Predicted percentage change in stiffness of element group | | | | | |
|---|---|---|---|---|---|---|---|
| Floor | Face | Config 1 | Config 2 | Config 3 | Config 4 | Config 5 | Config 6 |
| 1 | E | 0 | **-83** | **-38** | **-39** | **-42** | -5 |
| | N | 0 | 0 | 0 | 0 | 0 | 0 |
| | W | 0 | 0 | 0 | 0 | 0 | -3 |
| | S | 0 | 0 | 0 | 0 | 0 | 0 |
| 2 | E | 0 | **-79** | **-37** | -2 | -2 | 0 |
| | N | 0 | 0 | 0 | 0 | 0 | **-41** |
| | W | 0 | 0 | 0 | 0 | 0 | 0 |
| | S | 0 | 0 | 0 | 0 | 0 | -100 # |
| 3 | E | 0 | **-71** | **-37** | 0 | 0 | 0 |
| | N | 0 | 0 | 0 | 0 | 0 | 0 |
| | W | 0 | 0 | 0 | -10 # | -2 | 0 |
| | S | 0 | -23 # | 0 | -8 | 0 | -8 |
| 4 | E | 0 | **-79** | **-32** | **-35** | 0 | 0 |
| | N | 0 | 0 | 0 | 0 | 0 | 0 |
| | W | 0 | 0 | 0 | 0 | 0 | 0 |
| | S | 0 | -16 # | 0 | 0 | 0 | 0 |

# False positive (damage detected when not present)
* False negative (stiffness reduction not detected)

**Table 9.9:** *Stiffness reduction from Hammer vibration using NeXT and ERA analyses*

### 9.7.2 BAYES

**Methodology** The structural health monitoring technique used in this approach [8] and [9] propose an Expectation-Maximization algorithm to find the most probable values of substructure stiffnesses and then a local Gaussian approximation at the most probable values is used to compute the damage probabilities.

In the first step of the damage detection procedure, experimental modes shapes $\hat{\psi}$ and modal frequencies $\hat{\omega}$ are extracted from the measured data using a modal identification procedure called MODE-ID [3]. The identified modal parameters are modal frequencies, damping ratios, participation factors, and mode shape components at the measured degrees of freedom for $N_m$ dominant modes of vibration.

In the second stage a Bayesian probabilistic framework is used to update both stiffness and mass matrices, based on the identified modal parameters from the first step. A general Bayesian statistical approach is employed to construct an updated probability density function (PDF) for the stiffness and mass parameters using the prior PDF and the experimental modal parameters.

Prior probability density functions are specified for stiffness parameters, mass parameters, modal frequencies and mode shapes. Each of these prior probability density functions are assumed to be a normal distribution with a chosen mean and variance that reflect the relative plausibilities of their values in the absence of any measurement data.

It is assumed that the system mode shapes $\phi$ and eigenfrequencies $\omega/2\pi$ are related to the stiffness and mass matrix through the free response equilibrium equation:

$$\left[K(\theta) - \omega_r^2 M(\rho)\right] \phi_r = 0 \tag{9.3}$$

where $K(\theta)$ and $M(\rho)$ are the parameterised stiffness and mass matrices, with $\theta$ and $\rho$ being the stiffness parameters and mass parameters respectively.

The incomplete measured mode shape $\hat{\psi}$ is related to the full system mode shapes through a function

$$\hat{\psi}_r = a_r \Gamma \phi_r + e_r \tag{9.4}$$

where $\hat{\psi}_r$ is the experimental mode shape of the r-th mode, $\phi_r$ is the system mode shape of the r-th mode, $\Gamma$ is a matrix that picks the measured degree of freedom from the system mode shape, $a_r$ is a scaling parameter and $e_r$ is the error between the estimated and measured mode shape.

Given the above constraints, the measurement data, and the prior probability distributions, an updated probability density function $p(\theta, \rho|\hat{\psi}, \hat{\omega})$ can be obtained using Bayesian probabilistic theories. The most probable values of the parameters are given by maximizing this updated PDF and the variances of the updated parameters are then also known.

**Results** The current application used a simplified shear model with lumped masses, 12 degrees of freedom and 16 stiffness parameters. In this model, several structural elements contribute to a single damage parameter. For this reason, the accuracy of damage location is limited to the element group contributing to the parameter. Damage can not be located to a single brace. Apart from this limitation, results were fairly good: Damaged element groups could be successfully detected from both the hammer and ambient vibration data for damage configurations 1 to 6. The hammer data gave the most reliable results, while several false alarms appeared in the results from ambient data. For the shaker cases, reliable damage detection could not be achieved. Table 9.10 contains the stiffness reduction for each element group as obtained from ambient vibration data. Table 9.11 and Table 9.12 give similar results as obtained from shaker vibration data and hammer vibration data respectively.

An attempt was also made to detect damage from damage configurations 8 and 9, assuming the unbraced structure (damage configuration 7) to be the undamaged scenario.

Results from this study showed that connection damage is much more difficult to reliably detect and assess because the identified modal parameters are less sensitive to connection damage, allowing the modeling errors to have more influence on the results.

| Group location | | Predicted percentage change in stiffness of element group | | | | | |
|---|---|---|---|---|---|---|---|
| Floor | Face | Config 1 | Config 2 | Config 3 | Config 4 | Config 5 | Config 6 |
| 1 | E | 0 | **-70** | **-35** | **-34** | **-45** | 7 |
| | N | 0 | 5 | 5 | 5 | 3 | 5 |
| | W | 0 | 28 | 28 | 28 | -3 | 6 |
| | S | 0 | 5 | 5 | 5 | 5 | 5 |
| 2 | E | 0 | **-48** | **-50** | 13 | -22 # | -6 |
| | N | 0 | -11 # | -17 # | -12 # | 10 | **-24** |
| | W | 0 | 6 | 13 | 8 | -22 # | -19 # |
| | S | 0 | -18 # | -44 # | -44 # | -6 | -31 # |
| 3 | E | 0 | **-65** | **-53** | -7 | 17 | 17 |
| | N | 0 | -2 | -5 | -4 | -10 # | -4 |
| | W | 0 | 14 | 14 | -3 | -26 # | -11 # |
| | S | 0 | -3 | -3 | -3 | 3 | -1 |
| 4 | E | 0 | **-81** | **-49** | **-44** | 13 | -13 # |
| | N | 0 | -2 | -6 | -3 | -6 | -4 |
| | W | 0 | 18 | 18 | 18 | -24 # | -16 # |
| | S | 0 | -6 | -6 | -10 # | 4 | -3 |

# False positive (damage detected when not present)
* False negative (stiffness reduction not detected)

**Table 9.10:** *Stiffness reduction from Ambient vibration using Bayesian analyses*

| Group location | | Predicted percentage change in stiffness of element group | | | | | |
|---|---|---|---|---|---|---|---|
| Floor | Face | Config 1 | Config 2 | Config 3 | Config 4 | Config 5 | Config 6 |
| 1 | E | 0 | **-50** | **-33** | **-34** | **-41** | -4 |
| | N | 0 | -57 # | -25 # | -25 # | -10 # | -3 |
| | W | 0 | 16 | 16 | -3 | 0 | -11 # |
| | S | 0 | -73 # | -22 # | -11 # | 1 | 5 |
| 2 | E | 0 | **-3** | **-27** | 27 | 16 | 19 |
| | N | 0 | -18 # | -30 # | -39 # | -46 # | **-62** |
| | W | 0 | -2 | 20 | 8 | 15 | 7 |
| | S | 0 | -64 # | -36 # | -25 # | -6 | -26 # |
| 3 | E | 0 | **-65** | **-35** | 11 | 11 | 8 |
| | N | 0 | -68 # | -32 # | -27 # | -1 | 5 |
| | W | 0 | 9 | 9 | -17 # | -4 | 3 |
| | S | 0 | -47 # | -27 # | -4 | -1 | -4 |
| 4 | E | 0 | **-56** | **-15** | **-34** | 3 | -5 |
| | N | 0 | -90 # | -63 # | -77 # | -2 | 2 |
| | W | 0 | -24 # | -14 # | -17 # | -3 | -14 # |
| | S | 0 | -85 # | -93 # | -86 # | -3 | -3 |

# False positive (damage detected when not present)
* False negative (stiffness reduction not detected)

**Table 9.11:** *Stiffness reduction from Shaker vibration using Bayesian analyses*

| Floor | Face | Config 1 | Config 2 | Config 3 | Config 4 | Config 5 | Config 6 |
|---|---|---|---|---|---|---|---|
| 1 | E | 0 | **-84** | **-45** | **-43** | **-41** | 3 |
| | N | 0 | 3 | 6 | 6 | 1 | 6 |
| | W | 0 | 19 | 19 | 19 | 19 | -3 |
| | S | 0 | 6 | 6 | 5 | 2 | 6 |
| 2 | E | 0 | **-74** | **-29** | 20 | -4 | -11 # |
| | N | 0 | -12 # | -6 | 12 | -8 | **-37** |
| | W | 0 | -5 | -5 | 10 # | -7 | -15 # |
| | S | 0 | -10 # | 7 | 8 | 2 | 15 |
| 3 | E | 0 | **-75** | **-51** | -2 | -3 | -4 |
| | N | 0 | -4 | -5 | 1 | -4 | -5 |
| | W | 0 | 3 | 14 | 3 | 0 | -6 |
| | S | 0 | -4 | -5 | 1 | -4 | -8 |
| 4 | E | 0 | **-88** | **-47** | **-39** | -3 | -1 |
| | N | 0 | 3 | -6 | 1 | 1 | -1 |
| | W | 0 | 1 | 3 | 8 | 1 | -8 |
| | S | 0 | -2 | -8 | -6 | -2 | -7 |

# False positive (damage detected when not present)
* False negative (stiffness reduction not detected)

**Table 9.12:** *Stiffness reduction from Hammer vibration using Bayesian analyses*

### 9.7.3 Discussion

A drawback of the first method (NExT and ERA) is that the number of degrees of freedom of the identification model is limited to the number of measurement sensors available. This limits the resolution of damage location that can be obtained. In addition, the accuracy of results obtained are sensitive to the choice of identification model, which will determine and limit the range of potential structural behaviors that can be represented. The second method (BAYES) also used a model with very few degrees of freedom. Although the reason for this is not explicitly stated in that publication, the same limitation probably applies.

Both the above methods rely on a limited set of dominant modes, identified from measured data. There may, however, be other participating modes in addition to the dominant ones. Higher modes associated to high frequency response are particularly informative, but are discarded. The difference between the measured data and identified dominant modes will be a combination of measurement noise and participation of higher frequency modes, but it will be impossible to distinguish between these. iFEM does not discard this information, instead allowing a large number of degrees of freedom, and thus, many modes, to participate in the response.

The second method (BAYES) had trouble identifying damage from the shaker data, while the first method (NExT and ERA) was not used to treat shaker data at all. iFEM obtained fairly good damage identification results from the shaker data. In Bayes' analysis of the shaker data, the highest mode used has an eigenfrequency of 20.9 Hz, but several higher frequency components can be seen in the measured response. Disregarding higher modes might have been the reason why Bayes failed.

A weakness of iFEM is that, when unknown force fields are allowed, parameter changes can also be disguised in the form of ghost forces. Because of this, the appropriate choice of cost matrices plays an important role. This is a weakness that the NExT and ERA

method is not prone to, since loads are not identified in addition to damage.

Compared to the results from iFEM analyses, each of the two methods discussed above obtained better damage detection results from hammer vibration data and from ambient vibration data. Both managed to detect the damage in damage configuration 6, while iFEM failed to do so. Percentage wise, the number of false alarms for the above methods were also fewer. This might be due to the lumped nature of the models used in these methods, that do not allow for individual brace damage to be identified, with several structural elements contributing to a single damage parameter. In that respect, it might be argued that iFEM succeeded better in locating the damage for the different configurations. iFEM succeeded in locating damage configurations 1 to 5 from the shaker vibration data, where neither of the other two methods succeeded. It is believed that the results obtained by iFEM will improve once the problems that were discussed in Sections 9.5 and 9.6 have been addressed.

## 9.8 Conclusion

1. iFEM succeeded in locating the Benchmark damage for most of the damage scenarios and load configurations.

2. The presence of numerous false alarms could be explained by model uncertainty which were not properly accounted for due to a limited element library in the prototype software SAFRAN.

3. iFEM models should explicitly allow for model uncertainties by including appropriate model parameters.

4. Uncertainty related to the proper assignment of cost matrices in the iFEM theory also hampered performance. The existing iFEM theory for assigning costs yields unsatisfactory results. It is urgently needed that this theory be revised.

5. The full capacity of the iFEM theory could not be exploited due to computer memory problems, which were due to some parts of the computer code having been written in a memory inefficient way. This will be corrected in the near future.

6. Two other methods have successfully identified many of the Benchmark damage scenarios and proved to be useful tools for structural health monitoring. However, both of these methods have the drawback of being able to handle only a very limited number of degrees of freedom in the identification model. This limits the resolution of damage location that can be obtained. The accuracy of results obtained are also sensitive to the choice of identification model, which will determine and limit the range of potential structural behaviors that can be represented.

7. iFEM's main advantage is its flexibility in terms of modelling, allowing to avoid over-simplified FEM models.

# Chapter 10

# Fundamentals of Vortex Induced Vibrations

## 10.1 Introduction

When a fluid flows around a cylinder, periodic vortices will often be shed as a result of the fluid separating from the cylinder. The alternating pressure field that is caused around the cylinder gives rise to oscillating hydrodynamic forces, which cause the cylinder to vibrate. This process is known as Vortex Induced Vibrations (VIV).

Marine risers are slender vertical pipelines, used to carry oil or gas from the sea-floor to a platform. These structures are often subject to vortex induced vibrations and have to be designed against probable fatigue damage. Secondary effects of VIV, that needs to be considered during the design process, includes increased average drag and clashes between risers in riser groups.

In this chapter a basic summary of VIV is given in the context of marine risers. Attention is given to the parameters that govern the process, the problem of predicting the response of marine risers subject to VIV, experiments conducted to investigate this interaction and how results are usually presented. This is by no means a complete literature review on the subject, but gives an overview of the most important issues. It is intended

to give the reader enough background on VIV to follow discussions in subsequent chapters, where iFEM is applied to analyse VIV of marine risers.

## 10.2 Classification of flow regimes

The Reynolds number denotes the relation between inertia forces and viscous forces in a boundary layer of fluid. This is a dimensionless property of a flow that can be used when comparing fluid flow systems. Flows with an identical Reynolds number usually have related properties. In particular, the Reynolds number allows to predict turbulence. For a circular cylinder of diameter $D$ in a steady cross flow with flow velocity $U$, the Reynolds number is given by

$$Re = \frac{U.D}{\nu} \tag{10.1}$$

where $\nu$ is the kinematic viscosity of the fluid. Figure 10.1 shows the different flow regimes as classified by Lienhard (1966), based on flow visualisation experiments.

The different flow regimes are found to have an important influence on the vortex induced force acting on the cylinder and on the vortex shedding frequency.

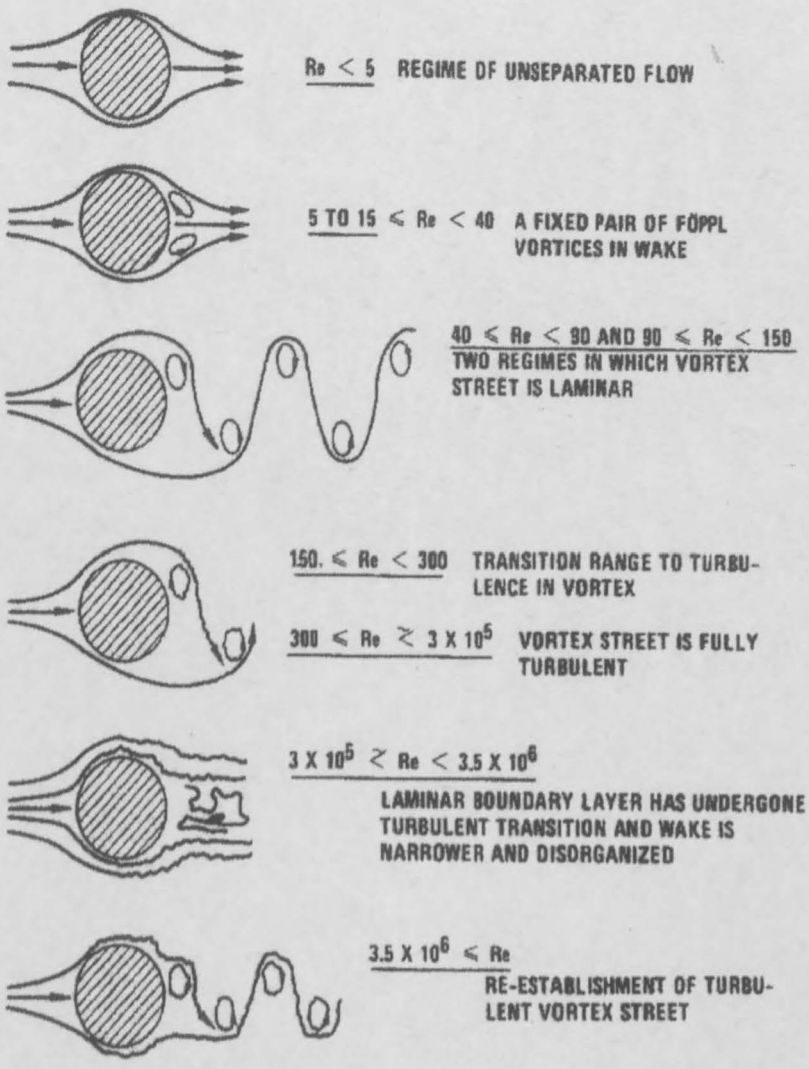


**Figure 10.1:** *Flow regimes for smooth circular cylinders (Lienhard, 1966)*

The Reynolds number range $300 < Re < 1.5e5$ is known as the sub-critical range. In this range, strong periodic vortex shedding takes place. The critical regime $1.5e5 < Re < 4.5e5$ denotes a transition where the boundary layer becomes unstable, but has not yet reached a state of turbulence. In the supercritical regime $4.5e5 < Re < 3.5e6$, the boundary layer becomes turbulent and the wake is disorganised. Periodic vortex shedding is re-established in the trans-critical regime $Re > 3.5e6$.

## 10.3 The vortex shedding frequency

The vortex shedding frequency $f_v$ from a fixed cylinder with diameter $D$ in a current with velocity $U$ is

$$f_v = St.\frac{U}{D} \tag{10.2}$$

where $St$ is known as the Strouhal number. The Strouhal number is the ratio between the vortex shedding frequency $f_v$ and the time taken by a water particle to pass the cylinder $t = \frac{D}{U}$. Experiments show that the Strouhal number is dependent on the flow condition and is thus a function of the Reynolds number. Figure 10.2 shows the relation. If the Reynolds number is known, the Strouhal number can be found and the vortex shedding frequency calculated. The surface roughness of the cylinder also has a significant influence on the Strouhal number, particularly in the critical and supercritical flow regimes.

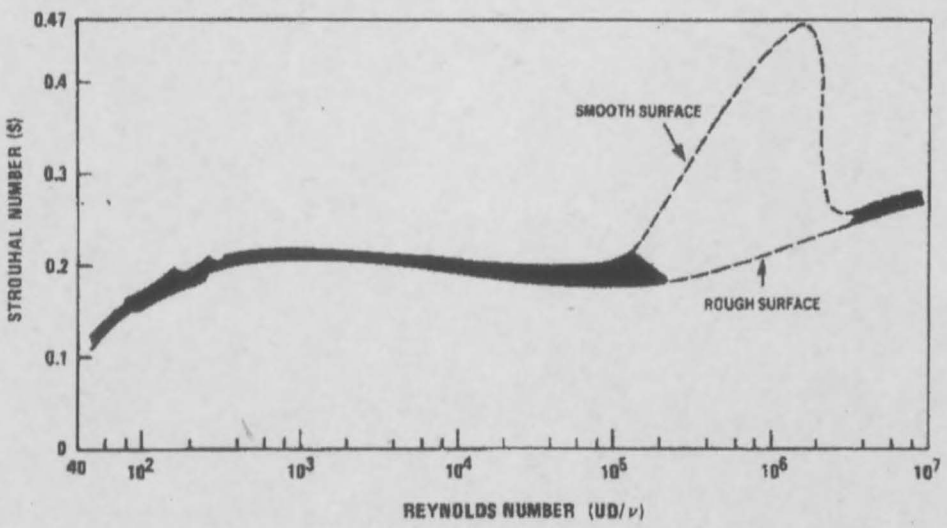


**Figure 10.2:** *St-Re relationship for a fixed cylinder (Blevins, 1990)*

**Comment on dimensionless numbers** Dimensionless numbers are often used in hydrodynamics, because it allows to extend the knowledge that was gained by observing one geometry and flow condition to describe the process expected at other geometries and flows. Dimensionless numbers have been invented to be able to take knowledge gained

from experimenting with one system to learning about another system with different dimensions. In a way, we are trying to get rid of dimensions in order to extend our knowledge beyond its source of acquisition.

## 10.4 Steady flow around a fixed cylinder

When a fluid is flowing around a fixed cylinder, the boundary layers of flow will separate from each side of the cylinder surface and form two shear layers that trail aft in the flow. The inner part of the shear layer is in contact with the cylinder and will move slower than the outer part of the shear layer, which is in contact with the free flow. A flat, detached shear layer is unstable and as a result it will fold onto itself and form discrete vortices.

Due to the periodic shedding of vortices, alternating pressures cause oscillating forces acting on the cylinder both in-line and transverse to the incoming flow direction. The component of force in the transverse direction of the flow is called the lift force $F_L$, while the component in the flow direction is the drag force $F_D$. The lift force oscillates at the frequency of vortex shedding around a mean value of zero. The drag force has a mean component $F_{D_{mean}}$ and an oscillating component with an amplitude $\hat{F}_D$ at a frequency typically twice that of the vortex shedding. For vortex shedding at a single frequency, these force components can be approximated by

$$F_L = \hat{F}_L cos(2\pi f_v t + \theta_v)) \tag{10.3}$$

$$F_D = F_{D_{mean}} + \hat{F}_D cos(4\pi f_v t + \phi_v)) \tag{10.4}$$

where $f_v$ is the frequency at which vortex shedding is taking place and $\hat{F}_L$ is the amplitude of the oscillating vortex induced lift force. $\theta_v$ and $\phi_v$ are phase angles for the oscillating forces relative to the vortex shedding.

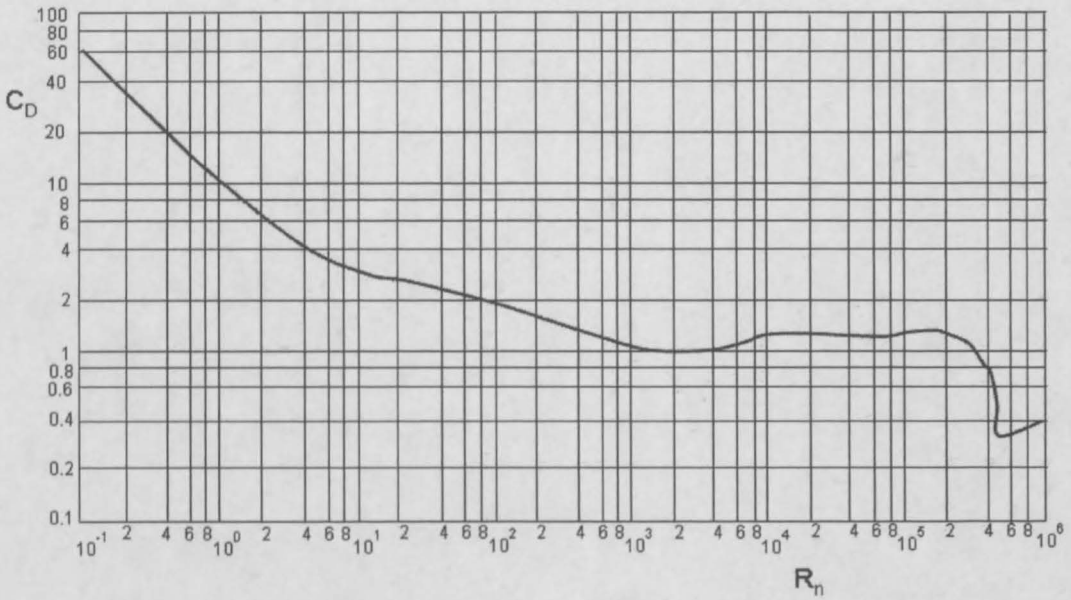


**Figure 10.3:** *In-line drag coefficient for a fixed cylinder (Schlichting, 1987)*

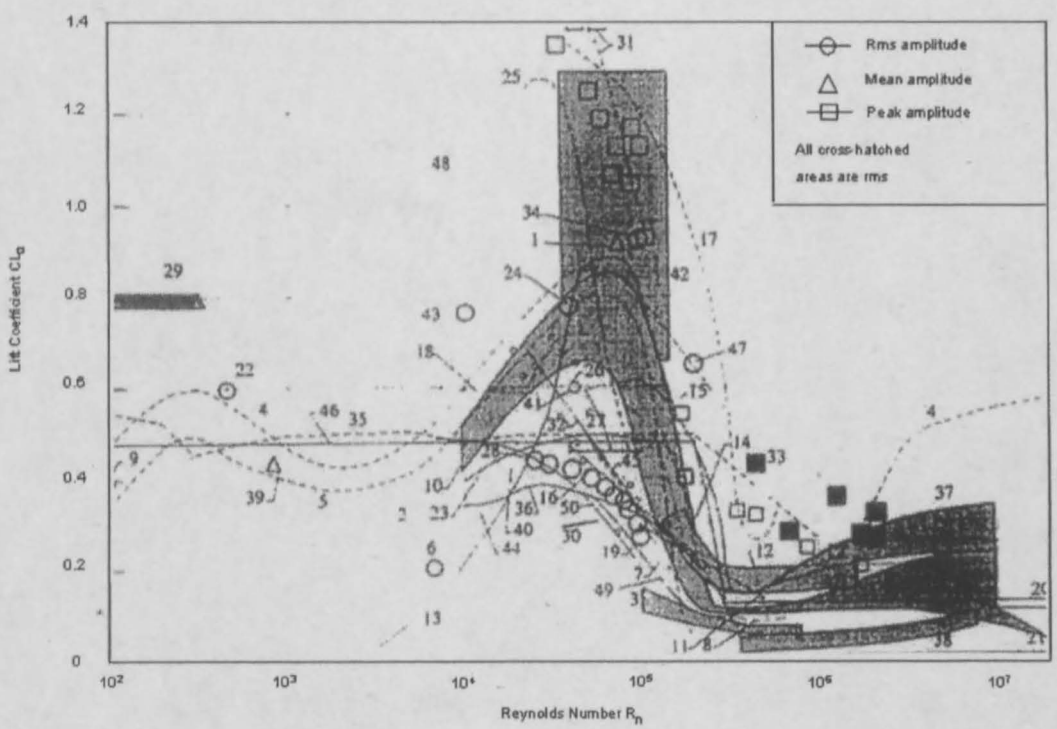


**Figure 10.4:** *Cross-flow lift coefficient for a fixed cylinder (Pantazopoulos, 1994)*

Drag and lift force depend on the Reynolds number, as shown in figures 10.3 and 10.4. In this context, the lift force shows much more variation than the drag force. The data for figure 10.4 is a collection from 48 different studies and different test conditions of fixed cylinders in steady flow.

## 10.5 Steady flow around a vibrating cylinder

When a cylinder is not fixed, vortex induced vibrations are caused by the dynamic variation of $F_L$ and $F_D$. This fluid-structure interaction can be very complicated and difficult to predict, because the motion of the cylinder influences the vortex shedding. Most models for VIV prediction will neglect the oscillating drag component $\hat{F}_D$, which is typically in the order of 15% of $F_{D_{mean}}$. (This is not necessarily a safe assumption, because even if the amplitudes of in-line oscilations are much smaller than the cross-flow oscilations, the in-line vibration takes place at higher frequency and involves higher modes, which might actually cause higher stresses and fatigue damage than the cross-flow vibration.)

In this fluid-structure interaction, the dynamic equilibrium equation is given by (given only for the cross-flow direction),

$$K.x(t) + C.\dot{x}(t) + M.\ddot{x}(t) = F_L(t) \tag{10.5}$$

At the same time the response $x(t)$ of the structure will influence the vortex shedding process and thus influence $F_L(t)$. The lock-in condition discussed below in Section 10.5.1 is an excellent example of this.

Consider the response at a single pulsation $\omega_s = 2\pi f_s$ and assume $F_L(t) = \hat{F}_L.sin(\omega_s t + \phi)$, where $\phi$ is the phase angle between the lift force and the body motion $x(t) = x_0 sin(\omega_s t)$. Equation 10.5 now becomes

$$\begin{aligned} K.x_0 sin(\omega_s t) + \omega_s.C.x_0 cos(\omega_s t) - \omega_s^2.M.x_0 sin(\omega_s t) &= \hat{F}_L.sin(\omega_s t + \phi) \\ &= \hat{F}_L.cos(\phi).sin(\omega_s t) + \hat{F}_L.sin(\phi).cos(\omega_s t) \end{aligned} \tag{10.6}$$

This can be re-written:

$$\begin{aligned} K.x_0 sin(\omega_s t) + \omega_s.C.x_0 cos(\omega_s t) - \omega_s^2.x_0(M + \frac{\hat{F}_L.cos(\phi)}{\omega_s^2.x_0}).sin(\omega_s t) &= \hat{F}_L.sin(\phi).cos(\omega_s t) \\ K.x_0 sin(\omega_s t) + \omega_s.C.x_0 cos(\omega_s t) - \omega_s^2.x_0(M + M_{A_0}).sin(\omega_s t) &= \hat{F}_{LV_0}.cos(\omega_s t) \end{aligned} \tag{10.7}$$

Equation 10.6 shows that the lift force $F_L(t)$ can be split into two components: One component is in phase with cylinder velocity $\dot{x}(t)$ and the other component is in phase with cylinder acceleration $\ddot{x}(t)$. (This is always possible, because $\dot{x}(t)$ and $\ddot{x}(t)$ have a $\frac{\pi}{2}$ phase difference.) The first component is known as added mass and the second is either excitation of the system or damping (Equation 10.7).

The excitation, $\hat{F}_{LV_0} = \hat{F}_L.sin(\phi)$, can be non-dimensionalised by the dynamic pressure factor $\frac{1}{2}\rho DU^2$, where $\rho$ is the fluid density, $U$ the free flow velocity and $D$ the cylinder diameter. This gives the lift coefficient in phase with cylinder velocity as

$$C_{LV_0} = \frac{\hat{F}_{LV_0}}{\frac{1}{2}\rho DU^2} \tag{10.8}$$

A positive value of $C_{LV_0}$ means that excitation is taking place, while a negative value signifies hydrodynamic damping.

The added mass $M_{A_0} = \frac{\hat{F}_L.cos(\phi)}{\omega_s^2.x_0}$ is often expressed using a dimensionless added mass coefficient $C_{M_0}$ comparing the added mass with the mass of the displaced fluid. For circular cylinders this gives

$$C_{M_0} = \frac{M_{A_0}}{\rho\pi\frac{D^2}{4}} \tag{10.9}$$

### 10.5.1 Lock-in

A linear dynamic system responds at the same frequency as that of the load. However, the VIV process often exhibits non-linear dynamic behaviour when the response of the structure influences the vortex shedding and thus the dynamic load. If the vortex shedding frequency $f_v$ (valid for a fixed cylinder) is close to the natural frequency of the cylinder (as defined by $f_n = 2\pi\sqrt{\frac{k}{m}}$), the natural vibration mode of the cylinder might take control

over the vortex shedding process, forcing the shedding of vortices to occur close to the cylinder's natural frequency. This is possible because added mass varies in such a way that the eigenfrequency $f_n$ is adjusted in the direction of the vortex shedding frequency $f_v$. The resulting response frequency $f_{osc} = 2\pi\sqrt{\frac{k}{m+m_{added}}}$ will become a compromise between the original eigenfrequency (valid for still water) and the original vortex shedding frequency (valid for a fixed cylinder). This condition is known as "lock-in".

The reduced velocity $U_R$ (Equation 10.10) is a non-dimensional number defined as the ratio between the distance traveled by a particle in the flow during one cycle of vibration $U/f_n$ and the diameter of the vibrating cylinder $D$. Lock-in can occur when the shedding frequency (Equation 10.2) is between 0.9 - 1.3 times the natural frequency, or when $U_R$ is between 4.8 - 8. The limits are dependent on the mass ratio of the cross section, as illustrated by Figure 10.5. Excitation near a natural frequency will usually cause large vibrations for low damped systems. But vibrations much larger than one diameter will destroy the harmonic vortex shedding process and the system will not receive additional energy from the fluid.

$$U_R = \frac{U}{f_n D} \tag{10.10}$$

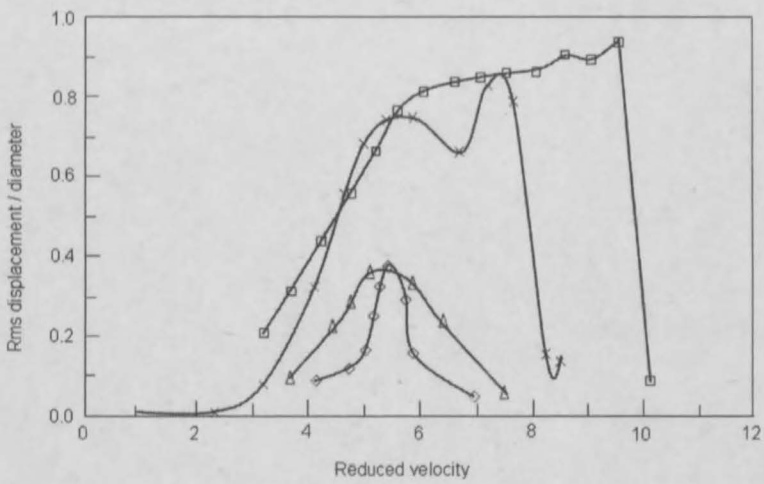


**Figure 10.5:** *Displacement vs. Reduced velocity of cylinders with different mass ratios:* $\diamond, \mu = 34$ ; $\Delta, \mu = 3.8$ ; $\times, \mu = 1.77$ ; $\circ, \mu = 0.78$. *(Chung, 1987)*

For long cylinders in sheared current (the flow speed varies with depth) it is difficult to predict whether or not lock-in is likely to occur, because these structures may be excited by vortex shedding forces at several natural frequencies.

### 10.5.2 Multi-moded response of flexible cylinders

A long riser will have several natural frequencies, which are likely to participate in its response. The reduced velocity parameter is used to predict whether excitation will take place. The reduced velocity is a function of the cylinder diameter, the flow speed at that position and a natural frequency of the riser in still water. A reduced velocity profile can be calculated for each natural frequency. The reduced velocity will vary along the length of the riser if the current flow is sheared (the flow speed varies with depth) or if the riser diameter is not constant over its length. When the reduced velocity calculated in this way is between 5 and 6.5, excitation will probably take place at that position. In this way different possible excitation zones, each with a corresponding probable response frequency, could be defined. This creates a problem, because excitation zones thus defined could overlap (Figure 10.6) and it is not clear which excitation zone or frequency is the correct choice for the VIV prediction. Overlap of excitation zones should not be allowed in prediction models, because the vortex shedding at one position along the riser cannot consist of more than one independent shedding process with different frequencies.

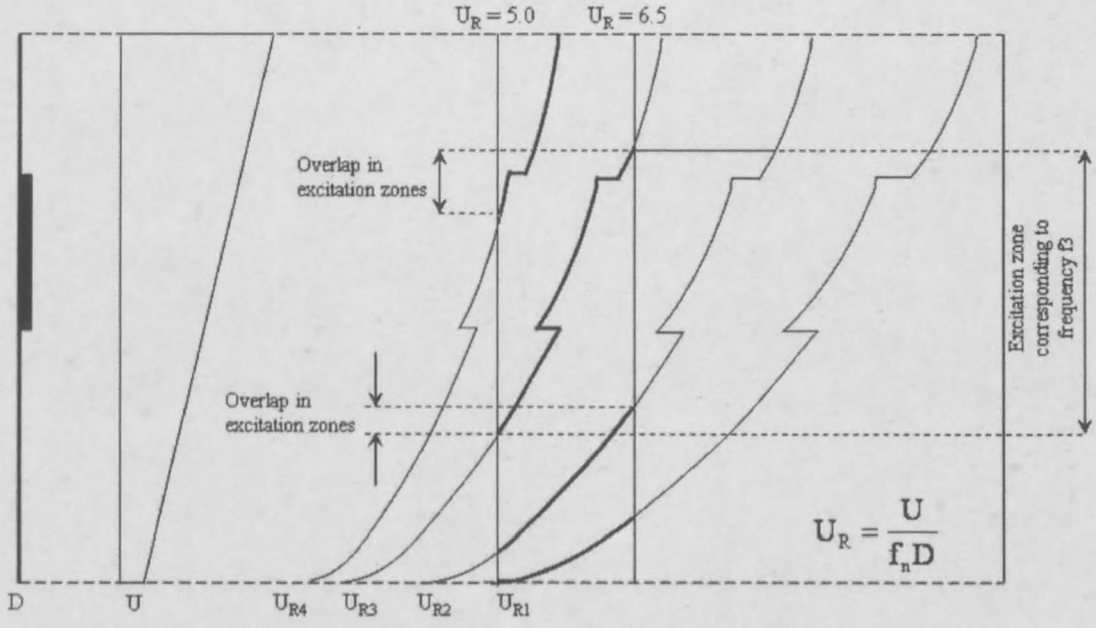


**Figure 10.6:** *Overlapping excitation zones*

Considering a single frequency, it is assumed that excitation will take place in its corresponding excitation zone, while hydrodynamic damping will take place outside of the excitation zone. When excitation is taking place at several zones and at several frequencies, it is difficult to predict the interaction that will take place between these frequencies. For example, if excitation is taking place at a certain frequency in one zone along the riser, the response will influence the vortex shedding process adjacent to that zone. Excitation at different frequencies can take place at several zones along the riser and the response from one zone will be damped out in other zones. Therefore, while excitation might be taking place at one frequency in a certain zone, response at a different frequency might be damped in that same zone. However, the multi-frequency interaction problem is not yet fully understood.

It is also not known how to predict whether the response will be multi-modal with several frequencies, or multi-moded at a dominant frequency [27], or maybe a lock-in response. And if it is lock-in, at which of the possible modes will it take place?

Several different methods exist for predicting the response of long risers. Shear7, a widely used software for prediction of vortex induced vibration, had problems in predicting the response that was observed in the Rotating Rig experiment [27] analysed in chapter 11. A comparison of different methods were done by Larsen and Halse [35]. It must be concluded that there is a wide variance in the response predicted by the different methods and the problem is not yet fully understood.

## 10.6 Experimental work

Experimental observation of VIV on long elastic cylinders or full scale risers are at present limited, but with the understanding of VIV in the simpler cases growing, more scientists are interested to forward this more challenging investigation. Experiments conducted to investigate VIV on short cylinders can be divided into three categories

1. Free vibrations of an elastically mounted cylinder in cross-flow. [24, 74, 16]
2. Driven cylinders in fluid flow, where the cylinder is forced to follow a displacement pattern of a given amplitude and frequency. [71, 23, 66, 58, 48]
3. The forced excitation method: Elastically mounted cylinder with additional energy input from external (non-fluid) forces. Prior to the test the oscillation amplitude and the frequency is unknown. [72]

In the case of elastically mounted cylinders, the reduced velocity (Equation 10.10) is often used to present results. For driven cylinders, a similar parameter is defined, known as the dimensionless frequency

$$\hat{f} = \frac{f_{osc} D}{U} \tag{10.11}$$

where the frequency $f_{osc}$ used is that of the forced oscillation. If the natural frequency is used $\hat{f}$ is equivalent to the inverse of $U_R$.

The results of Gopalkrishnan's work [23] is often used in empirical models for VIV prediction to predict the vortex induced forces that will act on a structure. His experiments falls in category 2 (above) and Figures 10.7 and 10.8 show the force coefficients $C_{LV_0}$ and $C_{M_0}$ respectively, as a function of the amplitude ratio and non-dimensional frequency. For systems with very low structural damping the contour $C_{LV_0} = 0$ represents the ideal steady oscillation lock-in situation. This is so because if a cylinder is oscillating harmonically with a constant amplitude, the total energy input to the system is zero. (If this was not so, the amplitude would either increase or decrease.) It follows that when an excitation force is present, the energy supplied in this way must be balanced by the energy absorption from structural damping, for the vibration amplitude to stay constant.

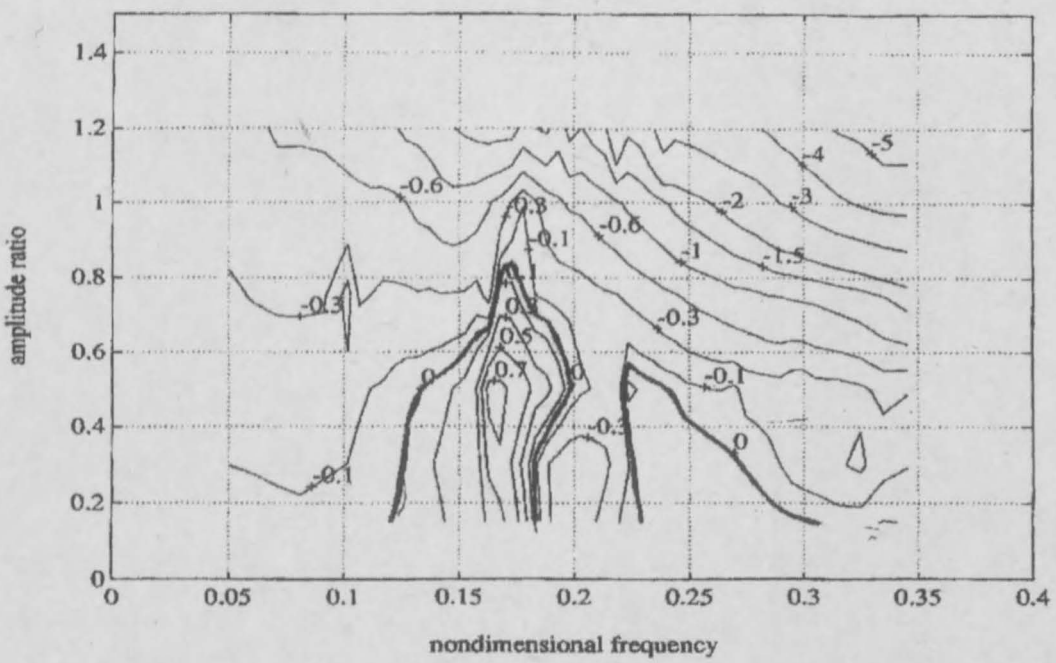


**Figure 10.7:** *Lift coefficient in phase with cylinder velocity (Gopalkrishnan, 1994)*

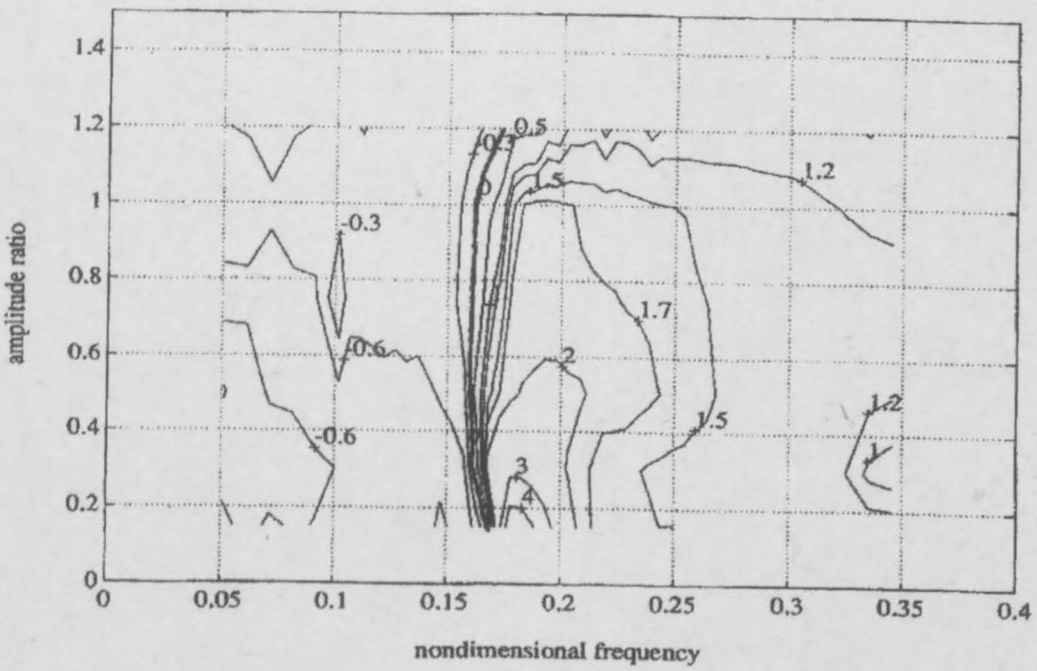


**Figure 10.8:** *Added mass coefficient (Gopalkrishnan, 1994)*

## 10.7 Other parameters that influences the VIV mechanism

There are many other factors that influence and complicate the VIV process and the analysis of the fluid-structure interaction. In addition there are several different parameters used by different authors to classify, predict and describe the process. Very few of these are discussed in this chapter, but some of them are shortly mentioned below.

*Surface roughness* will cause an increase in the friction force in the boundary layer, compared to a smooth cylinder, and is important for the definition of the different flow regimes (Section 10.2). Increased roughness could reduce the Reynolds number limits for the flow regimes.

The amount of shear in a non-uniform current profile can be described by the *shear*

*fraction*, $\frac{U_{max}-U_{min}}{U_{max}}$, where $U_{max}$ is the maximum flow velocity along the length of the cylinder.

The *excitation bandwidth*, $\Delta f = \frac{\Delta U}{U_R D}$, is used to calculate the number of possibly excited frequencies and is used to judge the probability of lock-in occurring. If many different frequencies are likely to be excited, the probability of lock-in behaviour is small.

The *response parameter*, $S_G$, describes the energy balance between the fluid excitation force and structural damping and is often used to predict the lock-in vibration amplitude.

The *wave propagation parameter*, $n\zeta_n$, is used to predict the response type when lock-in is not likely to occur. The parameter is defined as the product of the mode number $n$ and the total damping ratio $\zeta_n$ of that mode ($\zeta_n$ includes both structural and hydrodynamic damping). The response type will be a "short cylinder" or "standing wave" type of response when $n\zeta_n$ is less than 0.2. "Infinitely long cylinder" or "traveling wave" type of behaviour is expected when $n\zeta_n$ is above 2.0. Mixed behaviour can be expected for values between these limits.

# Chapter 11

# Vortex Induced Vibration of a cylinder in cross-flow

## 11.1 Introduction

The previous chapter showed that the nature of Vortex Induced Vibrations (VIV) can be very complicated. Therefore it was decided to first test the iFEM algorithms against a VIV problem that is well understood. Kyrre Vikestad conducted experiments for his Dr.Ing, some of which are used here to compare the output of the iFEM algorithms to existing data.

## 11.2 Description of the experiments

Kyrre Vikestad's experiments [72] included types 3 and 1 from the list mentioned in the previous chapter (section 10.6), namely free vibrations of a towed pipe section with, and without, forced excitation.

**Experimental setup** A two meter long pipe section of $0.1m$ diameter was elastically supported at both ends and placed horisontal in a $25m$ long towing tank. The pipe was only free to vibrate in the vertical (cross-flow) direction, while in-line vibrations were prevented. End plates were fixed to the ends of the pipe section to prevent three-dimensional end-effects from influencing the data. In the middle of the length of pipe a spring was

attached with an oscillating motor at the other end, which was used (in the type 3 tests) to apply a forced harmonic excitation to the pipe section at different chosen amplitudes and frequencies. Figure 11.1 from Vikestad's dissertation shows a schematic drawing of the apparatus. The spring $k_2$ denotes this middle spring and $k_1$ is the stiffness of the end supports. The structural damping ratio of the apparatus in water was low, in the order of 1.8%. The towing speed for different tests varied between $0.1m/s$ and $0.7m/s$, corresponding to a subcritical flow with Reynolds numbers of between $10^3$ and $10^5$.

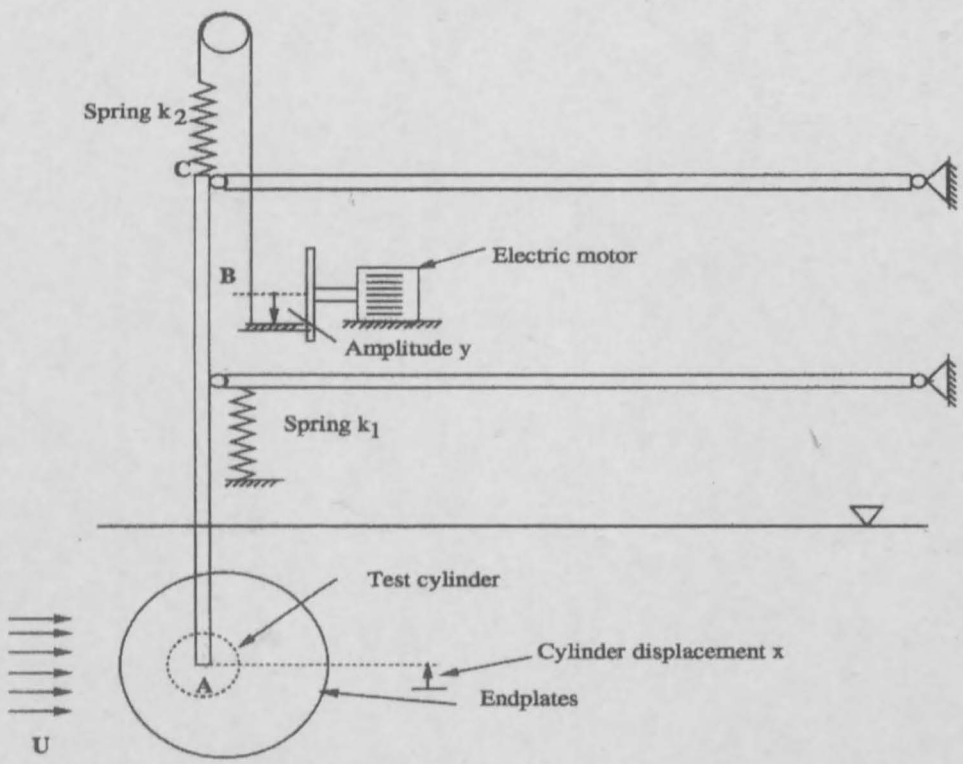


**Figure 11.1:** *Schematic drawing of the apparatus (Vikestad, 1996)*

**Measurements** Several types of measurements were taken during tests: At each end of the cylinder the displacement $x$, acceleration $\ddot{x}$ and in-line drag force were measured as well as the vertical lift force. In addition to these, the external excitation force ($F_e = k_2.(y-x)$), was measured. Note that even in the cases where no forced excitation were applied ($y = 0$), this force would not be zero, because of the spring stiffness and the vertical displacement

$x$ of the pipe section. The towing velocity was also measured.

**The equilibrium equation** Since the pipe section is rigid, a single degree of freedom is used to model the system. The structural stiffness used in the model is $k_1 = 149N/m$ and mass $m_{dry} = 26.12kg$. Damping is obtained from decay test data [72], using the damping in still water of the structure without the pipe section. Any damping force acting on the pipe section when moving through the water is thus assumed to be part of the hydrodynamic force $F_L$.

The equilibrium equation is

$$k_1.x + c.\dot{x} + m_{dry}.\ddot{x} = F_L + F_e \tag{11.1}$$

with $F_L$ being the hydrodynamic force and $F_e$ the external excitation force.

## 11.3 Force identification

In this section, the dynamic iFEM force and response algorithm (iFEM XU algorithm) is used to estimate the total external force acting on the vibrating pipe section, based on measurements of its response.

### 11.3.1 The iFEM model

For the iFEM force and response estimation, the only measurements used were that of the displacement and acceleration at cylinder ends. The structural stiffness, damping and mass that were used are the values described in Section 11.2 above. Thus the relevant equilibrium equation is $k_1.x(t) + c.\dot{x}(t) + m_{dry}.\ddot{x}(t) = u(t)$, where $u(t)$ is the external force to be estimated. Even though the displacement- and acceleration measurements are given, these may contain measurement error and the estimated displacement $x$ and acceleration $\ddot{x}$ are allowed to deviate from their measured values. The iFEM force and response algorithm will find an equilibrium solution with the response estimates following the measured displacement and acceleration values as close as possible (not necessarily

exactly, accounting for possible measurement noise). The most probable[1] force history that satisfies these conditions are calculated by minimising the cost function for this system, given in Equation 11.2, subject to equilibrium.

$$J = \int_t (\frac{1}{2}(x(t) - x(t)_{meas}).Q_{xx}.(x(t) - x(t)_{meas}) + \frac{1}{2}(\ddot{x}(t) - \ddot{x}(t)_{meas}).Q_{\ddot{x}\ddot{x}}.(\ddot{x}(t) - \ddot{x}(t)_{meas}) + \frac{1}{2}u(t).Q_{uu}.u(t))dt \quad (11.2)$$

The estimated force $u(t)$ is compared to the total measured external force. The total external force $F_{total} = F_L + F_e$ is derived from the vertical lift force measured at cylinder ends, taking into account the inertia component from the dynamic movement $(m_{dry}.\ddot{x})$.

### 11.3.2 Results and discussion

In all the pure towing test cases (no forced excitation), iFEM's force estimates compare reasonably with the actual measured forces. This is also the case for the forced excitation tests. Figures 11.2(a) to 11.2(c) show a typical example of the measured versus estimated values of the hydrodynamic force, displacement and acceleration respectively, for a test with forced excitation.

In the case of the forced excitation tests, results were generally good, with one exception: For an excitation frequency of $0.356Hz$, for all three different amplitudes of forced excitation and all 23 different towing velocities, the force estimate does not agree very well with the measured force. The iFEM solution is the most probable[1] of several possible equilibrium solutions in the vicinity of the measured values. It might be that in this case the most probable solution differed from the actual process. It might be that the measurements taken for that specific set of tests were somehow corrupted, but this could not be proved. The reason for the poor comparison is not established with certainty.

[1]Probable, in terms of the cost function (Equation 11.2). This cost function encodes that a probable solution is one in which the response follows the measured values and in which the externally applied forces are of reasonable magnitude, assumed to vary around a mean value of zero (cf. chapter 2).

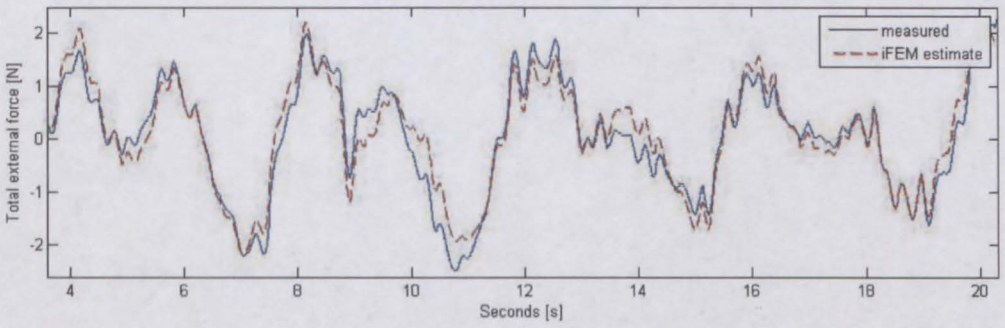


(a) iFEM estimated force compared to measured force

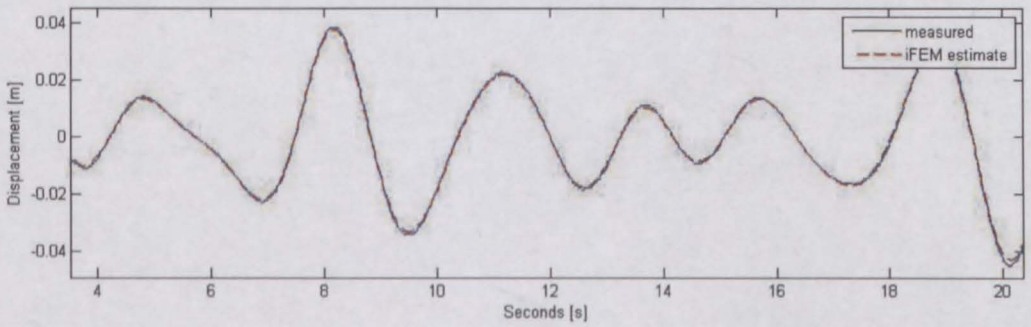


(b) iFEM estimated displacement compared to measured displacement

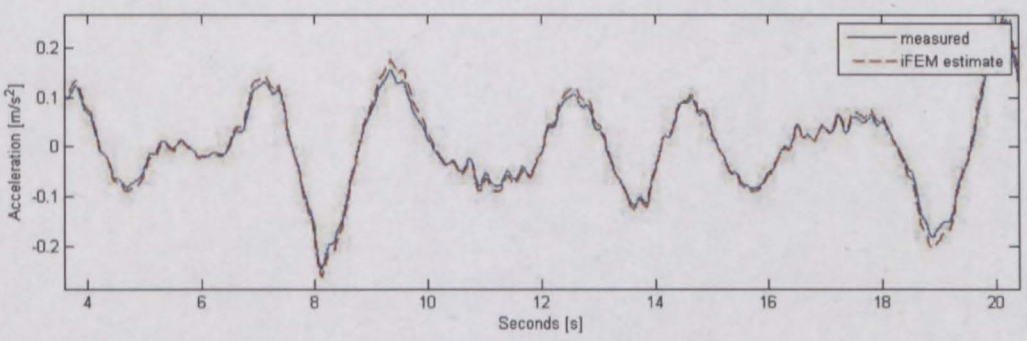


(c) iFEM estimated acceleration compared to measured acceleration

**Figure 11.2:** *Example of iFEM estimates for a test with external excitation*

### 11.3.3 Direct FEM analyses

When the measured forces (Figure 11.3) are used in a direct FEM analysis to estimate the acceleration- and displacement response, the estimated and measured response differ significantly: Because the excitation is close to a structural eigenfrequency, the structural damping values used have a strong influence on the FE results. The same is not true for the iFEM estimates, which gave good results also when damping was simply assumed to be zero. This is possible, because the damping forces were included into the external estimated forces. Close to resonance, these small forces have a significant influence on the response. Figures 11.4(a) and 11.4(b) compare the FEM estimated response to the measured response when the structural damping is assumed zero, while Figures 11.5(a) and 11.5(b) show the estimation when structural damping is modeled as Rayleigh damping, using decay test data.

The force found by an iFEM analysis is an equilibrium solution and to validate the iFEM software, the iFEM force estimate was used in a direct FEM analysis and the response values agree with what iFEM calculated previously (Figures 11.2(a) to 11.2(c)).

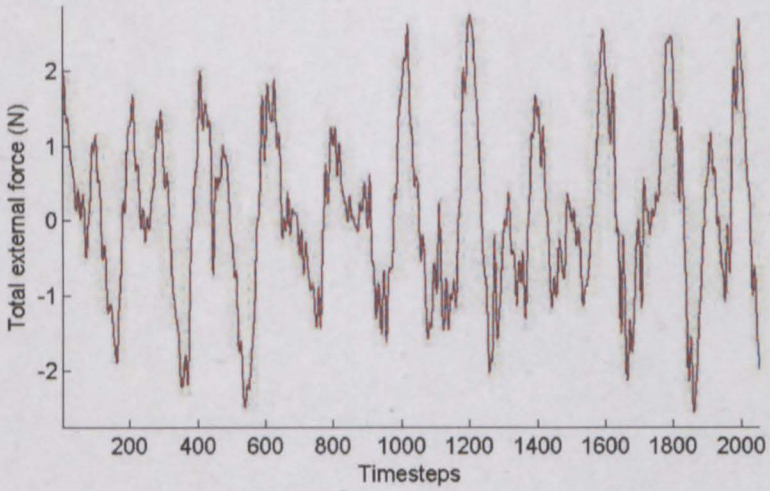


**Figure 11.3:** *FEM applied force (equal to measured force)*

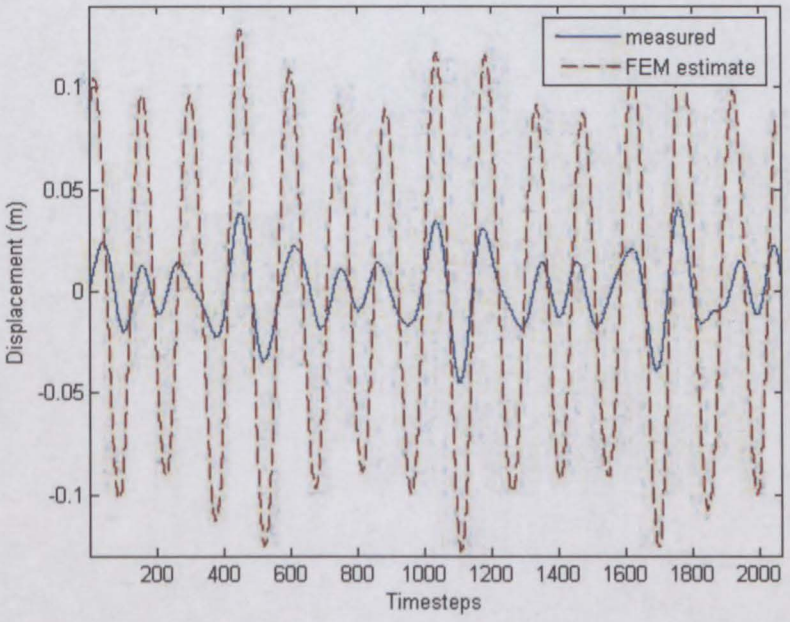


(a) FEM displacement prediction compared to measured displacement

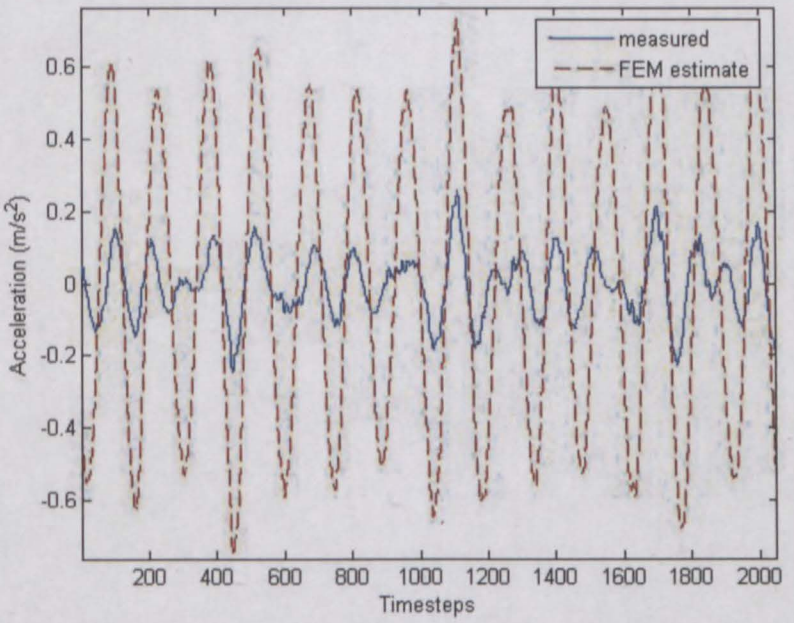


(b) FEM acceleration prediction compared to measured acceleration

**Figure 11.4:** *Example of direct FEM estimates with damping assumed zero*

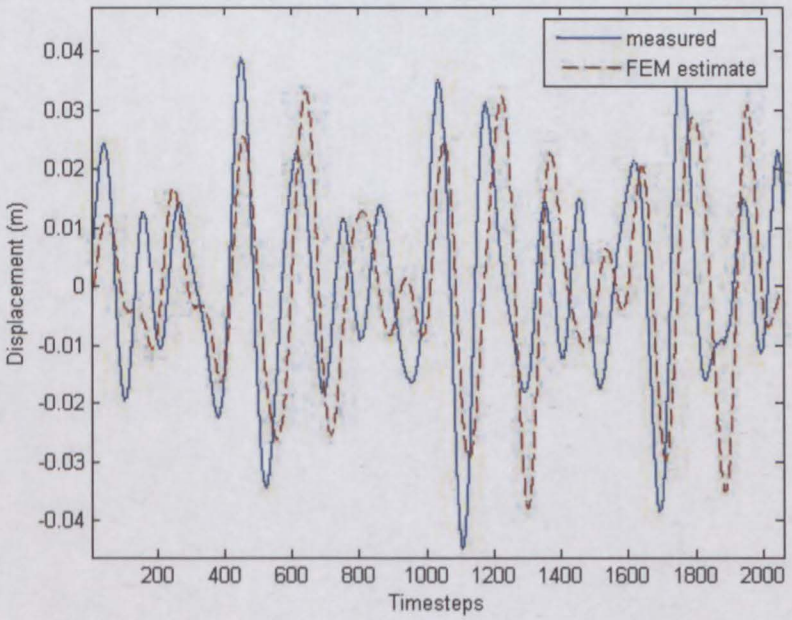


(a) FEM displacement prediction compared to measured displacement

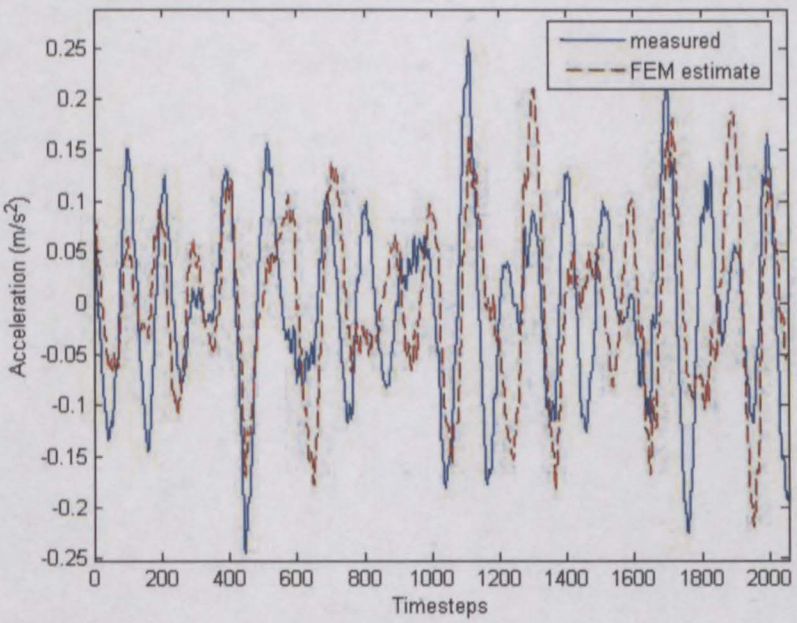


(b) FEM acceleration prediction compared to measured acceleration

**Figure 11.5:** *Example of direct FEM estimates with damping from decay test results*

### 11.3.4 Comments

The correspondence between measured forces and iFEM force estimates would also give an indication of how good the Finite Element model of the structure is. In this case the stiffness, damping and mass values were estimated with a high confidence, but normally these values will be more uncertain. The FE model would influence the result obtained (Refer to chapters 3 and 4) and if the iFEM force estimate does not agree with the measured value, a poor model is a probable reason. In this case the agreement was very good, as would be expected, given that the structural properties were well known.

## 11.4 iFEM parameter identification

In this section, the dynamic iFEM parameter identification algorithm is used to estimate time invariant parameters of the hydrodynamic force process.

### 11.4.1 The iFEM model

Consider Equations 10.5 to 10.9 from Chapter 10, where it is shown how the unknown hydrodynamic force can be parameterised by the added mass $C_{M_0}$ and lift coefficients $C_{LV_0}$. It is these parameters that we wish to estimate. Only pure towing tests are used in the parameter identification analysis. In these tests, the response is a lock-in behaviour, so that no energy is added to the system and since the structural damping for these tests are very low, the cross-flow lift coefficient $C_{LV_0}$ is assumed to be zero (cf. Chapter 10, Section 10.6). This leaves only the added mass $M_{A_0}$ to be estimated. The added mass coefficient $C_{M_0}$ can then be calculated and compared to values obtained by Vikestad [72].

Equation 10.7 from the previous chapter is repeated here (Equation 11.3). This equation was obtained in Chapter 10, by writing the total hydrodynamic force acting on a cylinder as the sum of two components. The first component is in phase with cylinder velocity and the second component in phase with cylinder acceleration. The amplitude of each component was then used to define a force coefficient, the lift coefficient $C_{LV_0}$ and

added mass coefficient $C_{M_0}$ respectively.

$$K.x_0 sin(\omega_s t) + \omega_s.C_{dry}.x_0 cos(\omega_s t) - \omega_s^2.x_0(M + M_{A_0}).sin(\omega_s t) = \hat{F}_{LV_0}.cos(\omega_s t) \tag{11.3}$$

This becomes

$$K.x(t) + C_{dry}.\dot{x}(t) + (M + M_{A_0}).\ddot{x}(t) = F_{LV_0}(t) \tag{11.4}$$

where $x(t) = x_0 sin(\omega_s t)$. Under lock-in conditions $F_{LV_0}(t) = C_{dry}.\dot{x}(t)$ so that no energy is added to the system. In these tests, lock-in conditions apply and the structural damping is very low $C_{dry} \approx 0$, therefore $F_{LV_0}(t) \approx 0$.

Using the result above and introducing the external excitation force that was present in Vikestad's experiments, the relevant iFEM equilibrium equation for the parameter identification analysis can be derived

$$\begin{aligned} k_1.x(t) + c_{dry}.\dot{x}(t) + m_{dry}.\ddot{x}(t) &= F_L(t) + F_e(t) \\ k_1.x(t) + (m_{dry} + M_{A_0}).\ddot{x}(t) &= F_e(t) \end{aligned} \tag{11.5}$$

where the external excitation force $F_e \approx k_2.x$ for the pure towing cases that will be considered here. (The stiffness $k_2$ being that of the spring used to apply the external excitation in experiments other than the pure towing tests.) In the iFEM model, $M_{A_0}$ is defined as an unknown mass parameter to be estimated.

In this case the measured external excitation force $F_{e_{meas}}$ was given as a force measurement in addition to the measured displacement $x_{meas}$ and acceleration $\ddot{x}_{meas}$.

The following values each follow a Gaussian distribution with zero mean: $(F_e - F_{e_{meas}})$, $(x - x_{meas})$, $(\ddot{x} - \ddot{x}_{meas})$ and $(M_{A_0} - 0)$. The standard deviation of the Gauss distribution for each of these is a user-defined input encoded by the cost matrices in the quadratic cost function minimised in the implementation. Minimising a quadratic cost function is equivalent to maximising a Gaussian probability function [44], see Chapter 2, Section 2.2.3. The cost function for this system, given in Equation 11.6, encodes that a probable

solution is one in which the response and external force follows the measured values and in which the estimated constant parameter $M_{A_0}$ are of reasonable magnitude.

$$\begin{aligned} J = \int_t (&\frac{1}{2}(x(t) - x(t)_{meas}).Q_{xx}.(x(t) - x(t)_{meas}) \\ &+\frac{1}{2}(\ddot{x}(t) - \ddot{x}(t)_{meas}).Q_{\ddot{x}\ddot{x}}.(\ddot{x}(t) - \ddot{x}(t)_{meas}) \\ &+\frac{1}{2}(F_e(t) - F_e(t)_{meas}).Q_{uu}.(F_e(t) - F_e(t)_{meas}) \\ &+M_{A_0}.Q_{\alpha\alpha}(t).M_{A_0})dt \end{aligned} \tag{11.6}$$

### 11.4.2 Limitation of the parameter identification algorithm

The parameter identification algorithm only allows the estimation of structural parameters that can be assumed to be constant over time, which also means that such parameters must have the same value at all frequency components involved in the vibration. Because of this, the tests that involve external excitation are not suited for treatment using iFEM parameter identification. In those cases we would have liked to estimate both a (non-zero) lift coefficient $C_{LV_0}$ (excitation) and an added mass coefficient $C_{M_0}$. However, looking at Figure 10.8, we see that for a pipe of given diameter $D$ in a cross-flow of velocity $U$, the added mass coefficient will differ as the frequency of vibration changes. The same holds for the lift coefficient $C_{LV_0}$, Figure 10.7. Vikestad's experiments with external excitation simulates the situation where a long riser is subject to VIV: While vortex shedding is taking place at one frequency, the riser motion from another location is transmitted along the riser, introducing another frequency. In these experiments, the forced excitation and the vortex shedding will not necessarily be at the same frequency and the coefficients will differ depending on the frequency under consideration. In other words, the lift coefficient may be positive (excitation) at the shedding frequency, but negative (damping) at the frequency of forced excitation. Unfortunately, the dynamic parameter identification algorithm cannot handle parameters that are frequency dependent, or not constant over time.

For this reason, only pure towing tests, where vibrations are taking place under lock-in at a single frequency, are analysed using the parameter identification algorithm. The results from these analyses will be discussed below.

### 11.4.3 Results and discussion

Figure 11.6 compares the iFEM estimate of the added mass coefficient $C_{M_0}$ with the values obtained by Vikestad [72]. The iFEM parameter identification algorithm also estimates the external force and response of the system, in addition to the estimated parameter. Figures 11.7 to 11.9 give estimated displacement, acceleration and excitation force compared to the measured values for one experiment.

iFEM estimates the added mass parameter by finding the change in the mass matrix that would give the most probable[2] solution given the measured external force and response and the initial FEM model. Three runs of the same experiment were done for each towing velocity and the iFEM parameter identification algorithm allows to combine the information from all three runs, giving the added mass value that is plotted on the graph. The added mass thus obtained is a constant, valid for all three runs of the same towing velocity.

Kyrre Vikestad calculated the added mass from the measured hydrodynamic force. The hydrodynamic force is the measured total external force minus the measured excitation force (in the case of pure towing tests the excitation force $F_e$ is approximately equal to $k_2.x$). Using the relation

$$lim_{T\to\infty}\frac{\int_t^{t+T} F_L(t).\ddot{x}(t)dt}{T} = -\frac{1}{2}\omega^2 x_0.\hat{F}_L.cos(\phi) \tag{11.7}$$

where $F_L(t)$ is the hydrodynamic force, as described in Equation 10.5 and 10.6, a formula for the calculation of the added mass coefficient can be derived as

$$C_{M_0} = -\frac{lim_{T\to\infty}\frac{1}{T}\int_t^{t+T} F_L(t).\ddot{x}(t)dt}{\rho\pi\frac{D^2}{8}L(\omega^2 x_0)^2} \tag{11.8}$$

which is the formula used by Vikestad in his calculations. For each towing velocity, the same experiment was repeated three times. Vikestad obtained separate added mass

[2]Probable, in terms of the cost function described in Equation 11.6. In this case, the cost function encodes that a probable solution is one in which the response and external force follows the measured values and in which the constant parameters estimated are of reasonable magnitude.

estimates for each of the three repetitions and averaged, giving the values plotted on the graph.

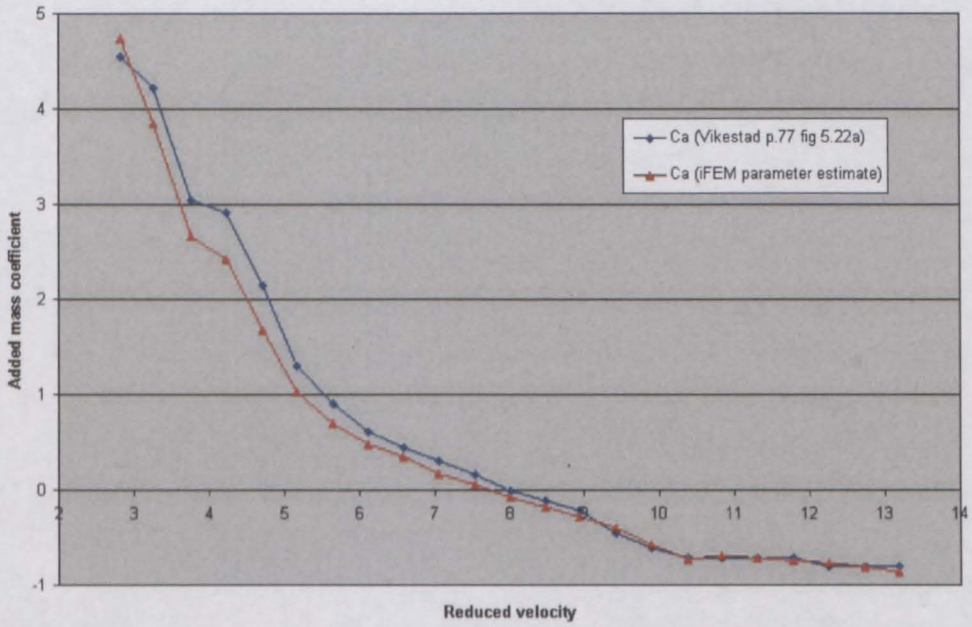


**Figure 11.6:** *iFEM estimated added mass coefficient compared to Vikestad added mass*

**Implications of the assigned probabilities or cost matrices** The most probable iFEM solution is one in which the estimated external force and response do not deviate from their measured values and in which the unknown parameter equals zero. However, at the same time, equilibrium is to be observed. Most of the time, equilibrium can only be achieved if one or all of the above deviates from their most probable values. In the Gaussian sense, it is quite unlikely that this will be achieved by having only one of the above deviate far from its most probable value. Instead, it is more likely that several of the above will deviate a little from their most probable values, in order to maximise the Gaussian probability function.

Minimising a quadratic cost function is equivalent to maximising a Gaussian probability function [44], see Chapter 2, Section 2.2.3. To cast the same argument in cost

function vocabulary: iFEM minimises a quadratic cost function that is a function of both the deviation of the estimated external force and response from their measured values and the deviation of the identified parameter from zero. It will thus be 'cheaper' to explain the response measurements by a combination of force and changed parameter, than by a changed parameter alone. The external excitation force will therefore deviate slightly from its measured value.

The total vortex induced hydrodynamic force can now be seen to be described by the identified added mass parameter plus the deviation of force from the measured external excitation. The cost, or equivalently, the Gaussian standard deviation of each component, is a user defined modeling choice. By assigning a high cost to deviating from the measured external excitation force compared to the cost associated to changed parameters, it is possible to have iFEM explain the displacement and acceleration measurements by mainly changing the added mass parameter (from a default value of zero). However, it was not possible to entirely remove this effect without causing numerical instability. This explains the slight deviation of the iFEM results from the results obtained by Vikestad.

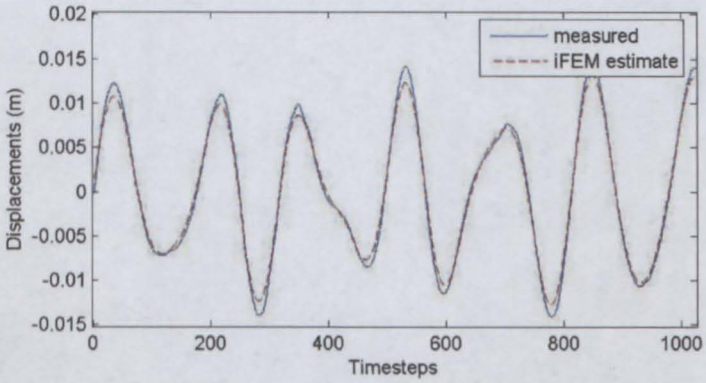


**Figure 11.7:** *Estimated displacement compared to measured displacement*

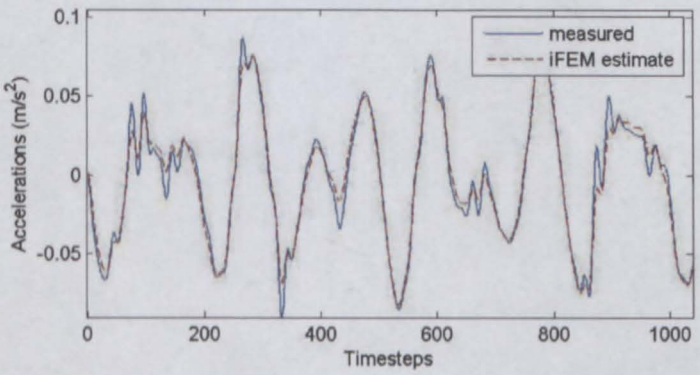


**Figure 11.8:** *Estimated acceleration compared to measured acceleration*

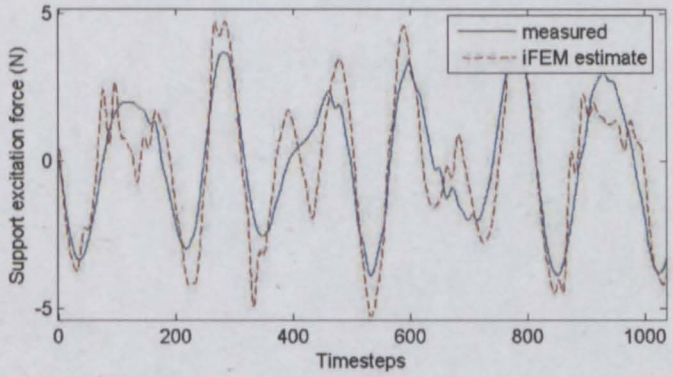


**Figure 11.9:** *Estimated excitation force compared to measured excitation force*

## 11.5 Conclusions

In this chapter iFEM was used to find and describe the forces acting on a vibrating cylinder subject to vortex induced forces. iFEM was also used to estimate the added mass parameters that characterise the hydrodynamic force in the case of lock-in behaviour. The performance of the algorithms could be tested by comparing the estimated forces and parameters to the known values from Vikestad's [72] work.

1. The iFEM XU force and response algorithm succeeded in correctly identifying the external force acting on the cylinder from measurements of its response.

2. The iFEM XUA parameter identification algorithm succeeded in correctly identifying the added mass parameters for towing tests in which the cylinder was responding with lock-in behaviour.

3. The response prediction from a direct FEM analysis (using the measured force) compared to the actual measured response of the cylinder, showed that direct FEM prediction is not particularly good due to high sensitivity to damping in the FE model.

# Chapter 12

# Cross-flow VIV on a riser - Rotating rig experiment

## 12.1 Introduction

In this chapter data obtained from a rotating test rig has been used to study the behaviour of VIV on a slender riser in uniform or sheared flow. The experiment was carried out in 1996 by MARINTEK (The Norwegian Marine Technology Research Institute) and the Department of Marine Technology of NTNU, Trondheim, Norway.

Using as input the measured response of the riser and applying the iFEM dynamic force and response estimation algorithm, give time series of the hydrodynamic VIV-induced force distribution over the riser. This force is further post-processed to derive the added mass and lift coefficients, which are then compared to results from previous experiments by Gopalkrishnan [23].

## 12.2 Description of the experiment

### 12.2.1 Test set-up

Figure 12.1 presents a schematic view of the test setup [37]. The test rig consists of a $12.6m$ long vertical cylinder. Two horizontal arms extend from the top and from the

bottom of the cylinder. The riser is connected between the upper and lower arms in pre-tension. At its lower end, the riser is fixed to the horizontal arm at a distance of $4.635m$ from the vertical cylinder axis. The horizontal position of the riser upper end may be varied from $4.635m$ away from the rotating axis (causing a vertical riser) to about $3.5m$ (causing a slightly inclined riser). The pretension system connects the upper riser end to a weight arrangement, to achieve approximately constant tension in the riser.

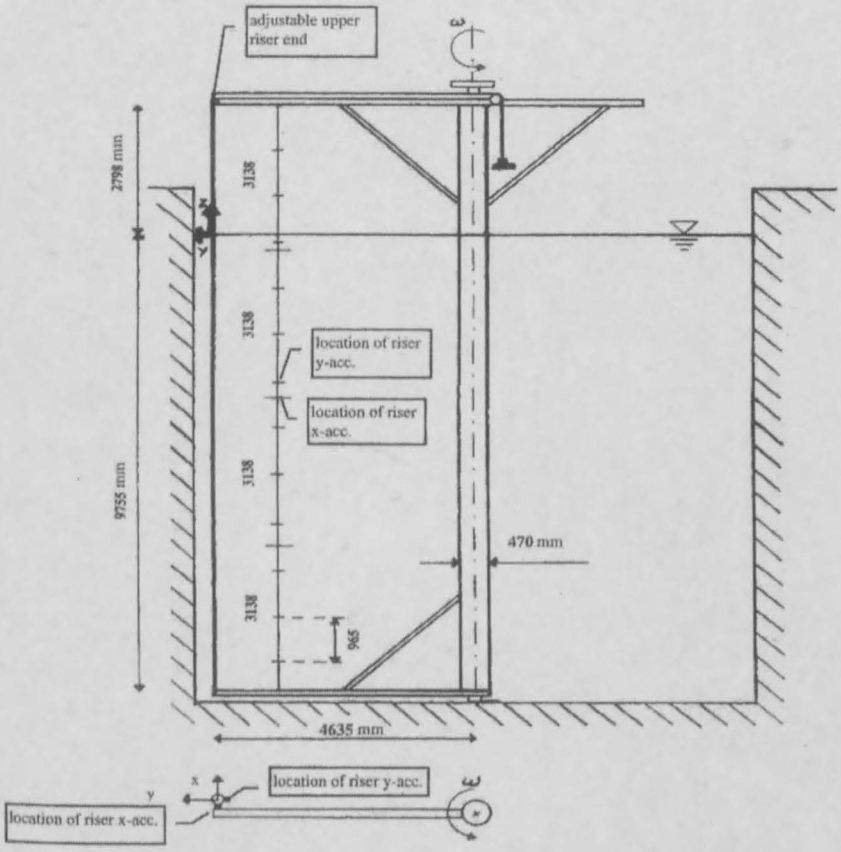


**Figure 12.1:** *Schematic drawing of the Rotating Rig test setup (Marintek, 1996)*

The test rig and riser are submerged in water to a height of about $9.8m$, which is the maximum depth of water in the tank in which the test is performed. In order to activate higher modes of the riser response, the riser was chosen to be as long as possible. Consequently about $2.8m$ of the riser extends above the water level into air.

### 12.2.2 Tests

The test rig is rotated around the vertical cylinder, setting up a flow around the riser. The flow profile is uniform along the depth when the riser is vertical. When the riser is inclined, the flow varies linearly (sheared current). The current is simulated by rotating the riser with a (nearly) constant velocity. The flow at any point on the riser is then given by $U = \omega.y$, where $\omega$ is the rotation velocity of the rig and $y$ is the horizontal radius from the vertical rotation axis to the riser at that point. When the riser is inclined, flow speed is maximum at the lower end of the riser. The velocity at the riser's lower end could be varied between 0.1 and $2.2m/s$. Since the lower riser end is fixed during the tests, the flow velocity at lower end, $U_l$, is used as a reference. The following flows were conducted: $U_l$ equal to 0.13, 0.18, 0.4, 0.6, 0.8, 1.0, 1.35, 1.5, 1.6, 1.8 and $2.0m/s$ respectively. The corresponding Reynolds numbers are between $2.2 \cdot 10^3$ and $3.3 \cdot 10^4$, meaning a sub-critical flow.

The horizontal position of the top of the riser was varied from test to test, to obtain different linear current profiles or different relative shear in the flow. A way to describe the shear is the ratio between higher and lower velocity (section 10.7). In the present test this becomes the ratio of the radius at bottom and still water level, between the vertical axis of the rig and the riser, i.e. $S = Yl/Yo$. Shear fractions that were used in tests were 1.0, 1.1, 1.2, 1.5, 2.0 and 3.3. The riser was tested with most of the combinations of $U_l$ and the shear fractions and at two different levels of tension ($450N$ and $750N$). Altogether 109 tests were conducted [37].

### 12.2.3 Measurements

**Measurements** Accelerations were measured by fifteen accelerometers placed along the riser at a sampling frequency of $200Hz$ [36]. Twelve of them measured accelerations in the cross-flow direction (sensors nr. 1-12), while the remaining three measured in the in-line direction (sensors nr. 13-15). Figure 12.2 shows the positions of the sensors on the riser. The tension in the riser was measured by a standard force transducer at the upper riser end. A tachometer located on the axis of the electrical motor driving the rotation was

used to measure the rotating speed of the test rig. This was used to calculate the velocity at riser terminations. Three accelerometers at the upper arm of the test rig, about 4.64m from the vertical rotation axis of the rig, measured vibrations (noise) transmitted from the test rig. Data from decay tests of the structure in water and in air were also available and were used to determine structural damping properties.

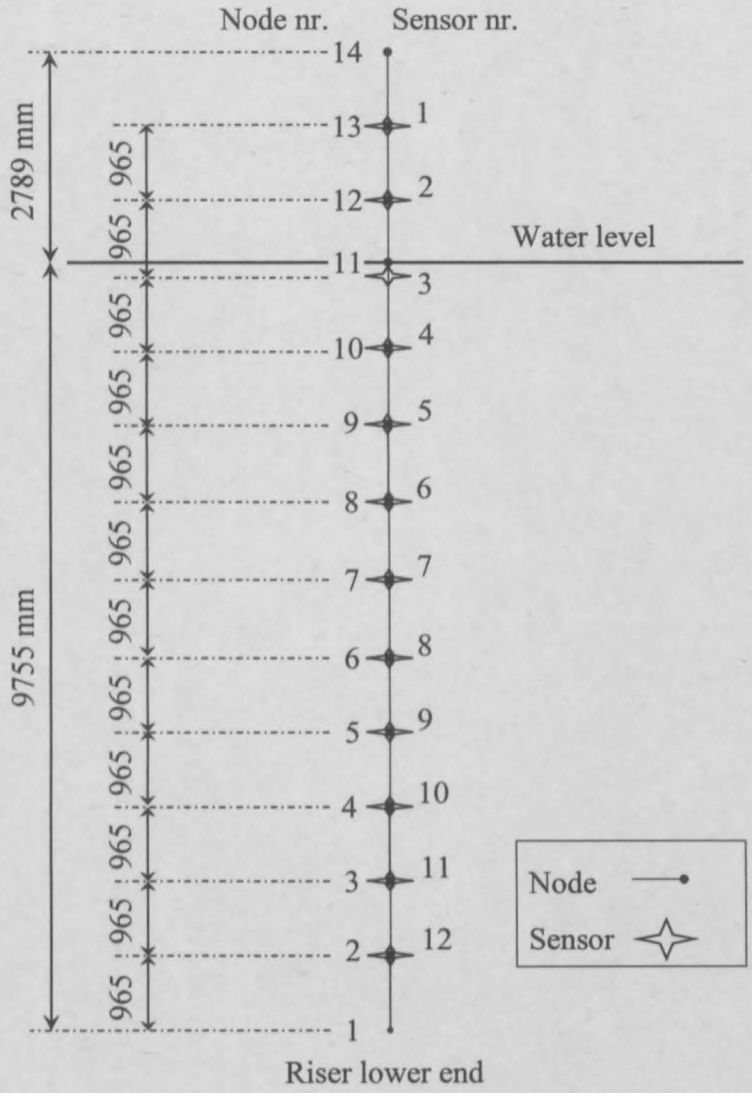


**Figure 12.2:** *Sensor placing on the riser and node numbers of the iFEM model*

**Broken accelerometers** Two accelerometer cables broke while conducting a test with the highest shear ratio. Consequently, no measurements from sensors nr. 11 and 12 (Refer to figure 12.2) are available in the tests with the highest shear ratio. Sensor nr. 9 broke before testing started and it was not logging during any of the tests.

**Filtering of measured channels** All channels were low-pass filtered at $80Hz$ in order to remove noise and the acceleration measurements were high-pass filtered to suppress non-zero mean values and drift. For the two lowest velocity tests ($0.13m/s$ and $0.18m/s$) the cut off frequency used was $0.5Hz$ and for all higher velocities $1Hz$ was used. The centrifugal acceleration component measured as a bias by the y-acceleration sensors is removed by the high-pass filtering.

## 12.3 iFEM model

A two-dimensional FEM model is chosen to represent the riser structure, mainly because the in-line response was measured by only three acceleration sensors, which is inadequate to get a good estimation of the forces acting in the in-line direction.

### 12.3.1 Stiffness, damping and mass properties

Structural stiffness and mass properties are available from the MARINTEK report [37] and used to set up the FEM stiffness and mass matrices.

#### Damping

Air decay test data is used to determine the structural damping properties. Proportional damping (Equation 12.1), also known as Rayleigh damping, is used in the FEM model to model structural damping.

$$\overline{\overline{\mathbf{C}}} = \overline{\overline{\mathbf{K}}}.\alpha + \overline{\overline{\mathbf{M}}}.\beta \tag{12.1}$$

$\overline{\overline{\mathbf{K}}}$, $\overline{\overline{\mathbf{C}}}$, and $\overline{\overline{\mathbf{M}}}$ are the stiffness, damping and mass matrices respectively. The damping

ratio $\zeta$ was calculated from decay tests, according to Equations 12.2 and 12.3.

$$\zeta = \frac{\delta}{\sqrt{4\pi^2 + \delta^2}} \tag{12.2}$$

with

$$\delta = \frac{1}{N} ln \frac{X_t}{X_{N+t}} \tag{12.3}$$

where $\delta$ describes how the amplitude of oscillation $X$ dampens out over the number of oscillation cycles $N$ between the two values of $X_t$ and $X_{N+t}$ used in the calculation.

The relationship between $\alpha$, $\beta$ and the damping ratio $\zeta$ at a frequency $\omega$ is given by Equation 12.4. The proportional damping parameters $\alpha$ and $\beta$ were subsequently calculated by solving Equation 12.4 simultaneously using the damping ratios at two different frequencies [11], yielding Equations 12.5 and 12.6.

$$\zeta = \frac{1}{2}(\alpha\omega + \frac{\beta}{\omega}) \tag{12.4}$$

$$\alpha = 2(\zeta_2\omega_2 - \zeta_1\omega_1)/(\omega_2^2 - \omega_1^2) \tag{12.5}$$

$$\beta = 2\omega_1\omega_2(\zeta_1\omega_2 - \zeta_2\omega_1)/(\omega_2^2 - \omega_1^2) \tag{12.6}$$

### Riser tension

A large part of the riser's stiffness is the geometric stiffness, derived from tension. It is therefor important to model the tension in the riser correctly. The riser tension was measured. In spite of effors by the experimentalists to keep riser tension constant, this was not achieved and the riser tension is varying over time. The variation is both an oscillation around a current mean value (due to the tensioning weight's inertia) and shifts in the mean value over time. Figure 12.3 shows a typical time series of measured tension. Tension variations as large as 30% were observed.

Care has been taken to choose tests and time-windows of measurements where the tension in the riser is fairly constant and use only these in analysis. Specifically, care has been taken to avoid time series in which the *mean value* of the tension shifts within the

analysed time series.

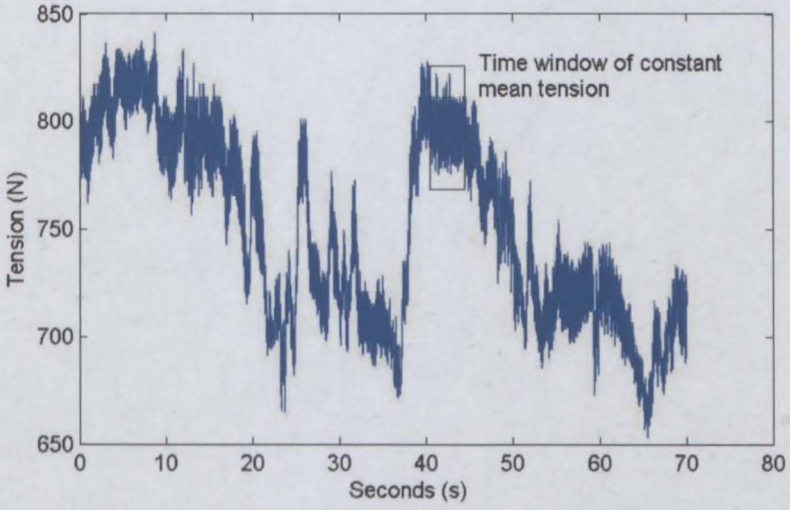


**Figure 12.3:** *Typical example of tension variation in the riser and choice of time-window for analyses*

**Effect of flow velocity on riser tension** In the tests with high flow velocities, the variation in tension was more pronounced and it was difficult to find long time windows of constant mean tension for analyses. However, in the case of high flow velocities, the frequency of vibration was also much higher than for low flow velocities (where longer time windows of constant mean tension were available) so that enough oscillation cycles were completed in a typical analyses to establish confidence in the results.

Haakonsen [27] studied the response of the rotating rig riser by investigating the participating modes and response frequencies for the different tests. He found that in the low velocity tests, long time windows of approximately constant tension were available, corresponding to a single mode lock-in response. In the high velocity tests it is likely that the vortex shedding process becomes stochastic in time and space. "In small time windows one or a few of these modes manage to synchronize the wake, but due to some mechanisms the process is very unstable and the synchronisation breaks up." Correspond-

ingly, constant tension is only found for short time periods and this corresponds to a time period during which one or a few modes managed to synchronize the wake. These time periods are therefor the moments during which the vortex shedding was periodic.

He also found that the response was usually at one dominating frequency, with one or more modes participating at this frequency. The response bandwidth increases with increasing velocity and more modes will participate in the response. There is strong communication of response along the riser, so that response at one position on the riser will influence the vortex shedding process at adjacent positions along the riser.

**Choice of tension level used in the iFEM model** As explained in Chapter 10 section 10.5 and in section 12.5 of this chapter, the identified force will be split into two components, the one component in phase with riser velocity and the other in phase with riser acceleration. To ensure the best estimates of these two force components, the oscillation of the tension around the mean value is handled as follows:

The tension is provided by a rope and weight. The weight would oscillate up and down as the riser is oscillating sideways. When the riser is moving sideways, away from its position of zero deflection, the weight will be pulled upwards. The weight will thus be in its lowest position when the riser is at the position of zero deflection and at its highest position when the riser has its maximum deflected shape.

The tension provided by the weight system reaches a maximum when it is moving through the lowest point of its oscillation and minimum when moving through its highest turning point. The riser again, will experience its maximum velocity (and therefor maximum force in phase with velocity) when moving through the point of zero deflection around which its oscillation is taking place. It will experience its maximum acceleration (and therefor maximum force in phase with acceleration) when the riser deflected shape is maximum.

In order to get the best estimates of the force in phase with velocity, the tension when the riser is moving through the point of zero deflection should be used, i.e. the tension when the weight is at its lowest position, i.e. the higher value of the values between which the tension oscillates. In order to get the best estimates of the force in phase with acceleration, the tension when the riser deflected shape is maximum should be used, i.e. the tension when the weight is at its highest position, i.e. the lower value of the values between which the tension oscillates.

Two iFEM analyses are done for each test, with the riser pretension at the higher and lower of the two values respectively to estimate the force in phase with velocity and acceleration respectively.

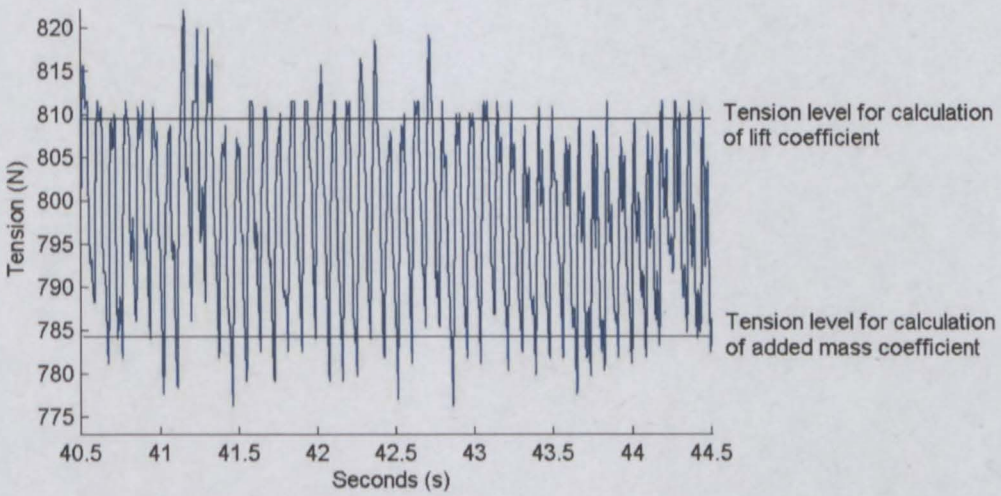


**Figure 12.4:** *Time window for analyses and tension levels for calculation of different force components*

### 12.3.2 Boundary conditions, measurements and costing

Figure 12.2 shows the iFEM model used, with node numbers indicated. Force degrees of freedom are introduced on all elements below the water level and will be used to estimate the distributed hydrodynamic force from the measured data. All vertical force degrees of

freedom are prescribed to be zero, so that only horizontal forces are allowed. No forces are allowed to act on elements above the water level. The top and bottom node of the riser are hinged. The cross-flow acceleration sensors are located at the nodes, except in the case of element nr. 10, where the second node is at water level and the sensor is located 0.965m along the length of the element. Measured accelerations as well as derived deflections are given as measurement input at the correct positions. This will be discussed in the following section.

Figures 12.5 and 12.6 show a typical example of the below water measured accelerations and derived displacements for a single test compared to the iFEM estimates of these values. In the figures, each sensor is represented by another colour, with the measured values given as a solid line and the iFEM estimates as a dotted line. These compare very well for all tests. Only a few timesteps are shown, for readability.

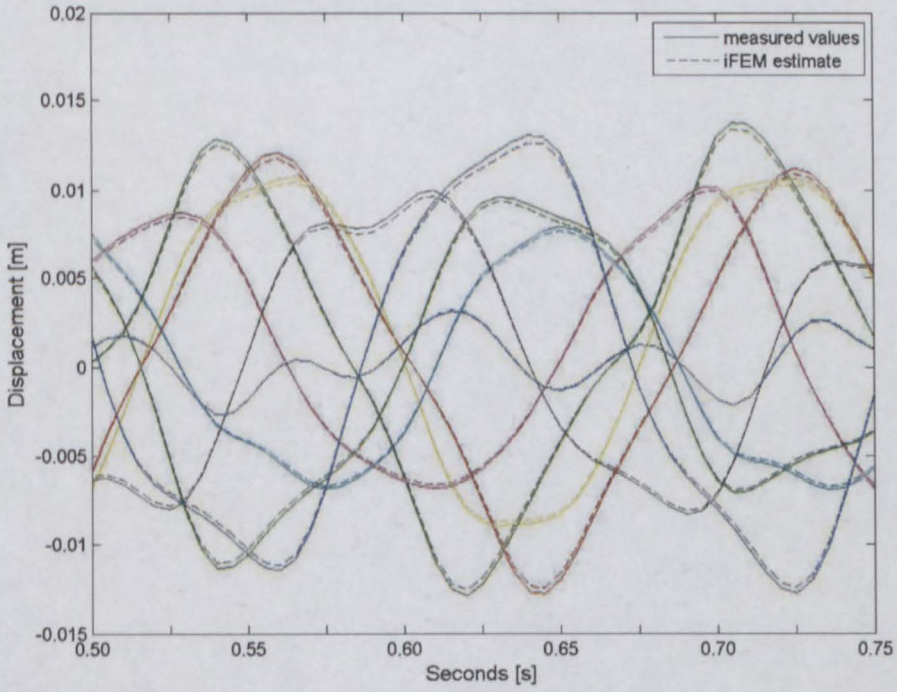


**Figure 12.5:** *Below water displacement estimates at sensor positions (9 sensors)*

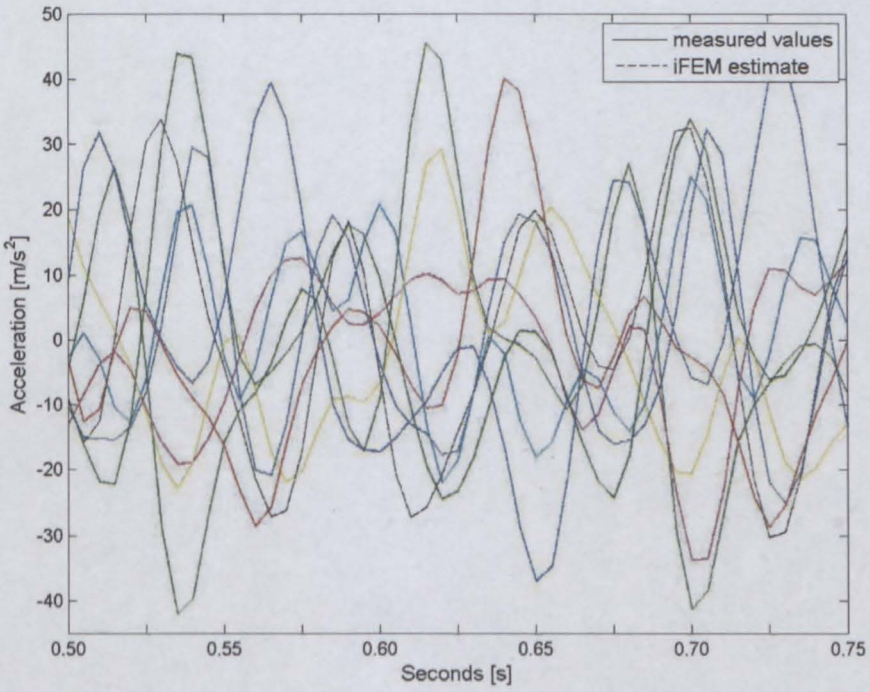


**Figure 12.6:** *Below water acceleration estimates*

### Effect of measurement input on response estimates

**Effect of types of measurements used** This section explains why it was necessary to include the derived displacement signal as a measurement input to the iFEM model, in addition to the acceleration measurements.

Assuming zero damping, the dynamic equilibrium equation for a single degree of freedom system is

$$F(t) = k.x(t) + m.\ddot{x}(t) \tag{12.7}$$

If the displacement is assumed to be periodic with amplitude $\hat{x}$ and pulsation $\omega$, then $x(t) = \hat{x}sin(\omega t)$ and $\ddot{x}(t) = -\omega^2\hat{x}sin(\omega t)$, leading to

$$F(\omega) = k.\hat{x}sin(\omega t) - \omega^2.m.\hat{x}sin(\omega t) \tag{12.8}$$

At high frequencies, the force $F(\omega)$ is well defined by the acceleration, while the term $k.x(t)$ becomes comparatively small: High frequency forces cause very little displacement.

On the other hand, for low frequencies, the inertia term $w^2.m.\hat{x}sin(\omega t)$, becomes negligible, so that $F(\omega) \approx k.\hat{x}sin(\omega t)$. A low frequency force causes very little acceleration, compared to displacement, with $\hat{\ddot{x}} = \omega^2\hat{x}$.

This property of the dynamic system is the reason why displacement measurements would be of little use when it comes to identifying high frequency forces. The high frequency force has no observable influence on the displacement and in turn, observing the displacements would give no indication as to what the high frequency force components were.

The same is true of acceleration measurements' ability to estimate low frequency forces. At low frequencies, a small error in the acceleration measurement will introduce a large error in the displacement estimate ($\hat{x} = \frac{1}{w^2}\hat{\ddot{x}}$) and hence in the force estimate. This was also observed when using iFEM to estimate the force and response history of the rotating rig using only acceleration measurements. The low frequency force and displacement estimates were very poor, in spite of the acceleration measurements being followed closely. Small low frequency errors in the acceleration measurement signal introduced an artificial drift in the displacement estimate and a corresponding error in the low frequency force estimates.

To address this problem, the derived displacement signal was added to the iFEM model as additional measurements. The derived displacement signal was obtained from the acceleration measurement signal by double integration. The signals were high pass filtered to remove the artificial drift that small errors in the acceleration measurement signal introduces into the displacement signal at low frequencies. Compared to the iFEM estimates obtained using only acceleration measurements, introducing these additional displacement "measurements" improved the force- and response estimates at low fre-

quencies, while making no difference at all to the higher frequency force- and response estimates.

Including displacement measurements obtained artificially from double integration of a high-pass filtered acceleration signal, means that the low frequency components in the displacement signal are assumed to be very small or negligible. It is possible that a low frequency drift could have been present in the actual displacement of the riser, but in the absence of displacement measurements, this cannot be known. Whatever is estimated at low frequencies is a guess based on very little evidence. Luckily, this assumption is not of great importance, since the estimates will be filtered during post-processing of the data (for reasons discussed in Section 12.5.3) around the main response frequency, which is usually well above the low frequency range. This filtering will remove both the low- and high frequency components of the signal, to keep only the main frequency range.

**Influence of the cost model on estimated forces** Increasing the cost $Q_{uu}$ associated to external forces will also decrease the large low frequency displacement- and force amplitudes. $Q_{uu}$ is constant, which means that the same value for $Q_{uu}$ is associated to all frequencies in the force signal. However, if only acceleration measurements are included in the iFEM model, increasing $Q_{uu}$ will filter out the low frequency forces more. This is so, because small deviations from low frequency acceleration data require larger forces than the high frequency forces needed to cause the same deviation from high frequency acceleration data. Increasing $Q_{uu}$ will reduce the low frequency drift, but the force estimate becomes over-regularised (cf. Section 2.2.4) before the low frequency drift is eliminated.

The algorithm requires that $Q_{uu}$ must be constant. This introduces a limitation in modeling prior knowledge on the frequency content of the force signal. It is known that the VIV mechanism is more likely to include forces of the frequency predicted by Equation 10.2, $f_v = St.\frac{U}{D}$. A lower cost, corresponding to a higher probability, should therefor be assigned to that range of frequencies in the force. Unfortunately, the present version of iFEM is not flexible enough to describe our knowledge of the real world situation. Thus,

while $Q_{uu}$ is tuned to give the best estimate of the VIV force around the expected vortex shedding frequency, $Q_{uu}$ for low- and high frequencies should have been higher.

$Q_{uu}$ is too low for low frequency forces, resulting in over-estimation of these forces. The high frequency force is saved from being over-estimated, because it is very well described by the acceleration measurements, so that small errors in the high frequency acceleration measurements does not result in a large error in high frequency force.

**Effect of omitting measurements from sensors located above water level** Only measurements from sensors located below water level were given as input to the analysis. Giving above-water measurements as input resulted in under-regularised force estimates[1] on the elements just below the water level, because these forces were used to coax the structure into mimicking the above-water measurements. As mentioned, no force degrees of freedom were introduced above water level.

In low velocity tests the above-water response estimate compared well to the measured response, in spite of the measurements not being given as input to the analysis. However, in high velocity cases, the below-water estimated forces failed to explain the above-water measurements. The reason for this is not fully understood. Figure 12.7 shows the above water response estimates compared to the measured values at the sensors for a low velocity test. Figure 12.8 gives the same for a high velocity test. Each colour in the graphs corresponds to a different sensor position on the riser.

---

[1]Refer to Chapter 2, Section 2.2.4. Under-regularised ("jittery") force estimates are unphysically large forces that appear as a result of a poor iFEM modeling choice. Usually, when the user defines measurement precision to be higher than it actually was, unphysically large forces will be estimated to make the structure follow these noisy measurements. In this case, unphysically large forces will be estimated to allow the structure to follow measurements at a location distant from the point of load application.

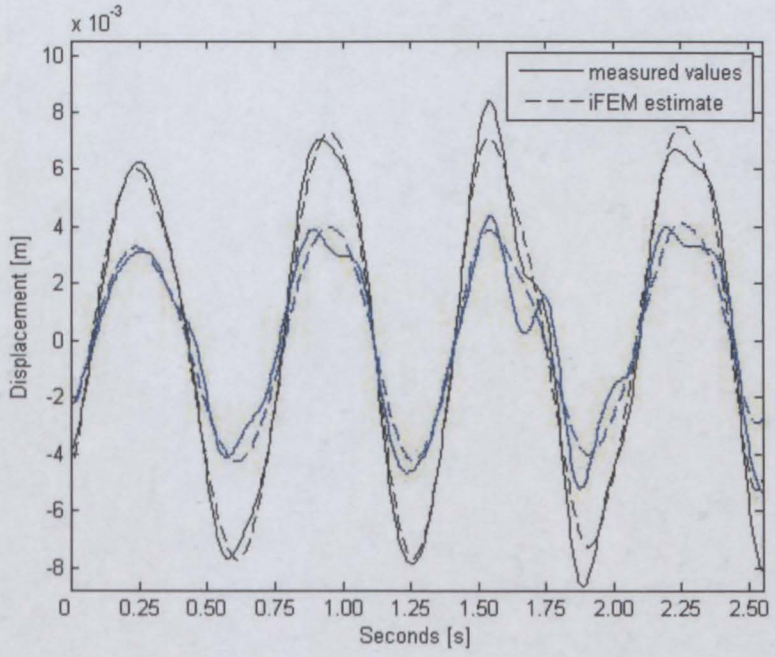


**Figure 12.7:** *Above water response estimate for low flow velocity test* ($U_l = 0.18m/s$)

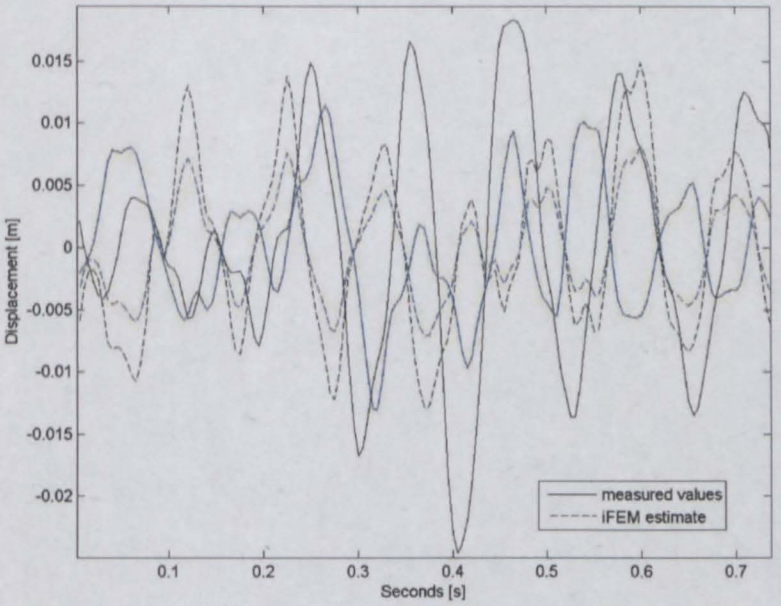


**Figure 12.8:** *Above water response estimate for high flow velocity test* ($U_l = 1.5m/s$)

One possible explanation could be that vibrations were transmitted from the test rig, which was not modeled. Even though rig vibrations were small in amplitude, it is possible that the frequency content of these vibrations corresponds to some natural frequencies of the piece of riser above water. If so, it could cause significant response of the above-water riser.

Another possible explanation could be that the response and force become more stochastic and more erratic in nature at high velocities. In such a case it might be that the actual distributed force cannot be adequately described by a fourth order polynomial over the length of an element. (The length of each element in the FEM model is equal to the distance between acceleration sensors, which is $0.965m$.) This would mean that the iFEM model and chosen shape functions is inadequate to describe the real situation. If this is the case, the result could be improved by using more elements. To investigate the possibility the number of elements used were doubled, so that it should have been possible to describe a much more complicated force distribution. The above water response estimate does not improve and the calculated below water force and related parameters are also not significantly changed. Therefor it is assumed that the number of elements used to describe the force distribution is adequate. However a related question is raised: Are there enough measurements to adequately describe such erratic forces?

### 12.3.3 Sensitivity studies

#### Sensitivity to measurement noise

A simple sensitivity study was conducted to evaluate the sensitivity of the estimated forces to measurement noise present in the data. Probably the largest source of measurement noise was vibrations transmitted from the test rig. It is assumed that the accelerations caused by these vibrations were significantly larger than random measurement error from the sensors.

A FEM model was used and imposing a identified force distribution on the structure yielded response estimates at the positions corresponding to the experimental sensor po-

sitions. These response estimates were purposefully corrupted by measurement noise of the order of magnitude, and with similar frequency content, of the vibrations transmitted from the test rig (known by measurement). The noise corrupted response was again used to identify the hydrodynamic forces and these were compared to the forces imposed on the original FEM model to evaluate their quality in the presence of measurement noise. The forces did not differ by much. In fact, the force estimate stayed stable for noise of up to ten times that of the expected noise levels. Assuming that the FEM model is an adequate representation of the structure, this proves that the iFEM solution is robust to measurement noise in the region of the solution. The FEM model used in the sensitivity study was the same one that was used to carry out all analyses and the iFEM model had measurement input at the same positions as for other analyses. It can not necessarily be assumed that the identified force distribution is a good estimation of the actual hydrodynamic forces that were acting on the riser, because factors such as a limited number of sensors (cf. page 215) and iFEM "artifacts" (cf. Section 8.3.5) may weaken the estimate.

**Unavailable sensors**

As mentioned in Section 12.2.3, three of the lower acceleration sensors were unavailable for tests with high shear current. When forces that were identified (for a test in which al sensors worked) using measurements from all sensors, are compared to forces (for that same test) that were identified using measurements from all sensors accept the lower three, the forces at the top nodes (where measurements were available in both cases) compare very well. The forces at the lower nodes, around the area where measurements were not available in the second analysis, do however not compare favourably. This means that the lack of measurement data produces a poor estimate of the forces in the area for which measurement data was unavailable. Lack of data in one area does not seem to corrupt the force estimate in an adjacent area. This is probably thanks to high hydrodynamic damping, so that forces act mostly locally, causing response only in their close vicinity.

### Sensor adequacy

The number of sensors on the riser was limited and it is unknown whether this was sufficient for iFEM to adequately estimate the distributed force over the riser. It is possible that the number of available sensors was to small to get a good force estimate. To investigate this, the force estimate if one sensor is omitted between two existing sensors, is compared with the force estimate if all sensors are used. When one sensor is omitted between two existing sensors, the quality of the result around that sensor decreases so that (in most cases) the amplitude of the force at that sensor is underestimated by about 40% compared to the estimate when the sensor was not omitted. In some cases however, the phase of the force is poorly estimated, in addition to the underestimation of the absolute value. This shows that fewer sensors would have resulted in poor estimates of the forces. Although this does not *prove* that more sensors were needed, it does raise the question whether the sensor density was in fact great enough to capture the force distribution adequately.

### Effect of gravity pollution

The potential of acceleration data corruption by gravity has been evaluated by Marintek, and judged to be of little consequence. The author also independently estimated the corruption to be between 2.5% and 6%, depending on which modes are active and the frequency of the response. The higher corruption will take place in the case where high modes (corresponding to higher out-of-vertical angles and higher gravity components) are participating at low frequency (corresponding to lower acceleration amplitudes).
The effect of Coriolis force from rig rotation was also previously investigated by Marintek and found to be negligible.

## 12.4 Identified forces

The distributed forces along the length of the riser over time were estimated for each of the 109 tests, for a length of time where the tension was approximately constant (Refer to Section 12.3.1, page 203). Figures 12.9 to 12.12 give representative examples from tests

with four combinations of low or high flow velocities and low or high shear fractions.

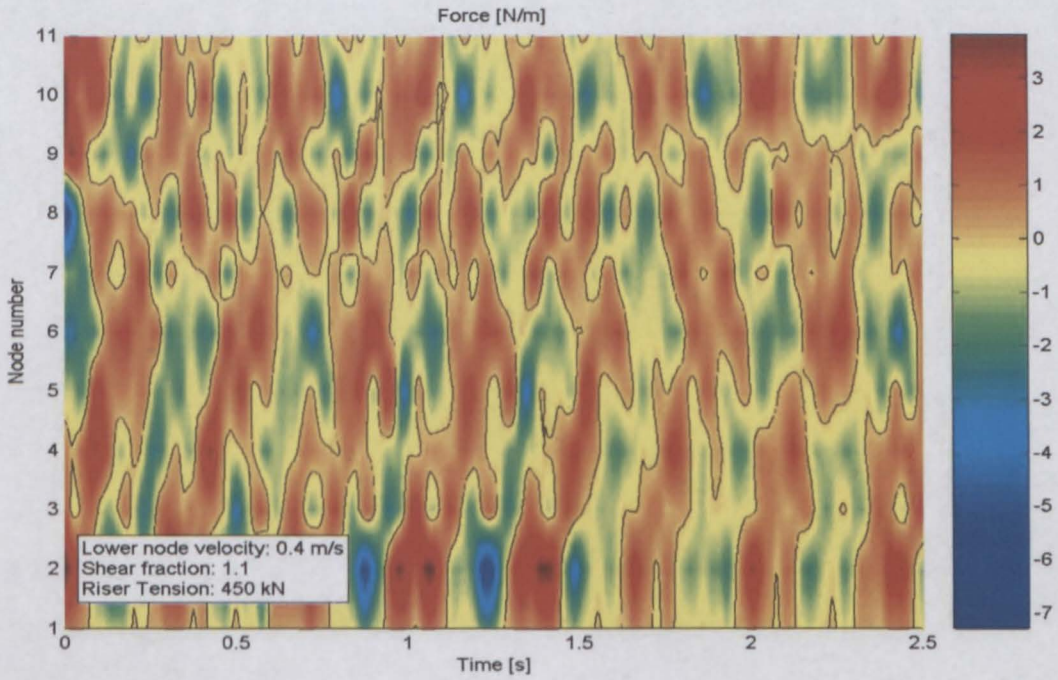


**Figure 12.9:** *Force contours for Test 4207: Low shear fraction and low flow velocity*

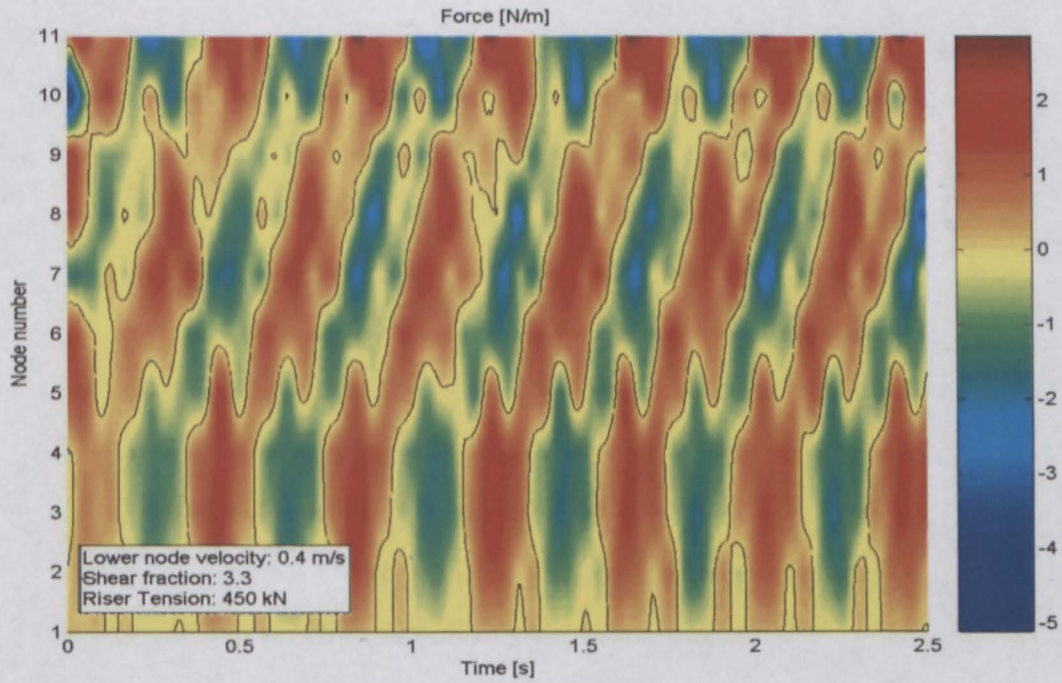


**Figure 12.10:** *Force contours for Test 4908: High shear fraction and low flow velocity*

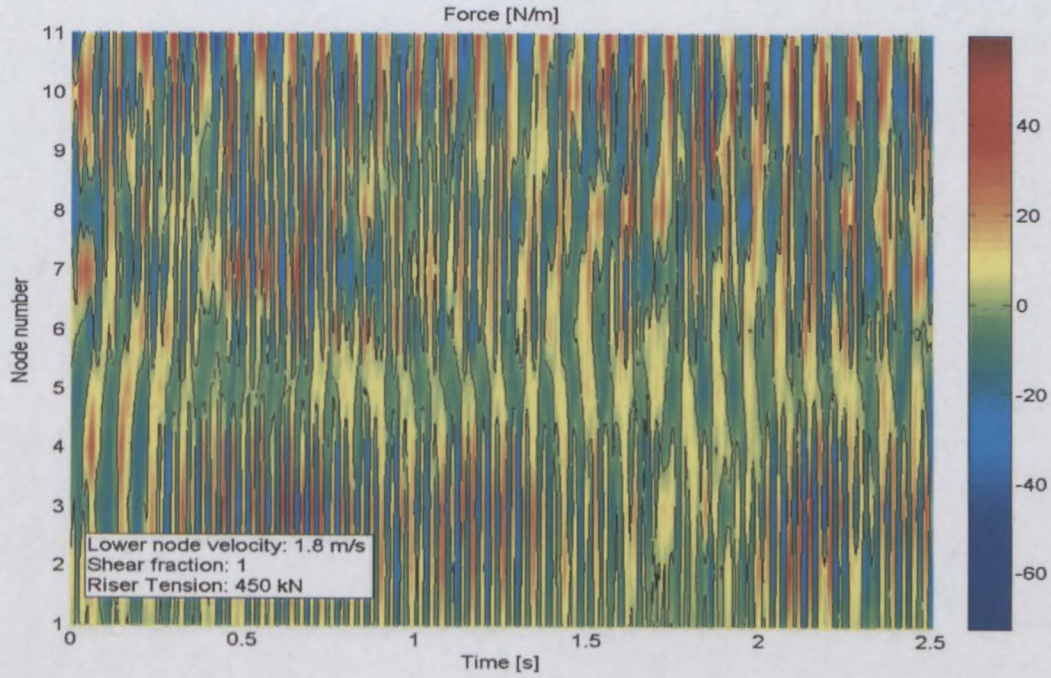


**Figure 12.11:** *Force contours for Test 4115: Low shear fraction and high flow velocity*

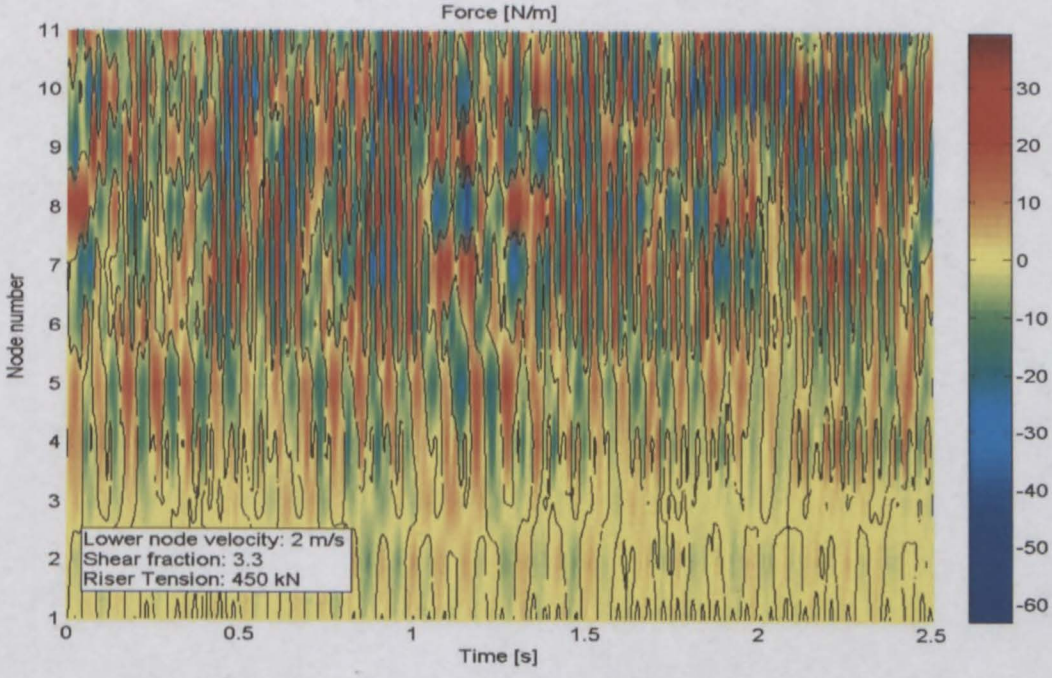


**Figure 12.12:** *Force contours for Test 4901: High shear fraction and high flow velocity*

The Figures show the value of the lift force (color coded) as a function of time (horizontal axis) and the position along the riser (vertical axis).

A striking feature is that the forces are quasi-cyclic. In the case of Figure 12.12, there seems to be transitions between periods of different quasi-cyclic behaviour, which is evident from the force distribution over time on the top halve of the riser. Incidentally, catastrophic transitions between periods of quasi-cyclic behaviour are characteristic of some chaotic systems, including the Lorenz oscillator (Figure 12.29), which was developed as a simple demonstrator of behaviour observed in turbulent weather systems.

Figure 12.13 shows the force distributions over time of tests nr 7114, 7115 and 7116. The three tests were done with identical experimental set-ups, i.e. the same shear fraction, flow velocity and riser tension were used. However, there are significant differences in the force patterns of the three tests. In Figure 12.13, the top and bottom test's force patterns are dramatically different, with the middle test pattern containing features that look like a combination of the patterns observed in the other two.

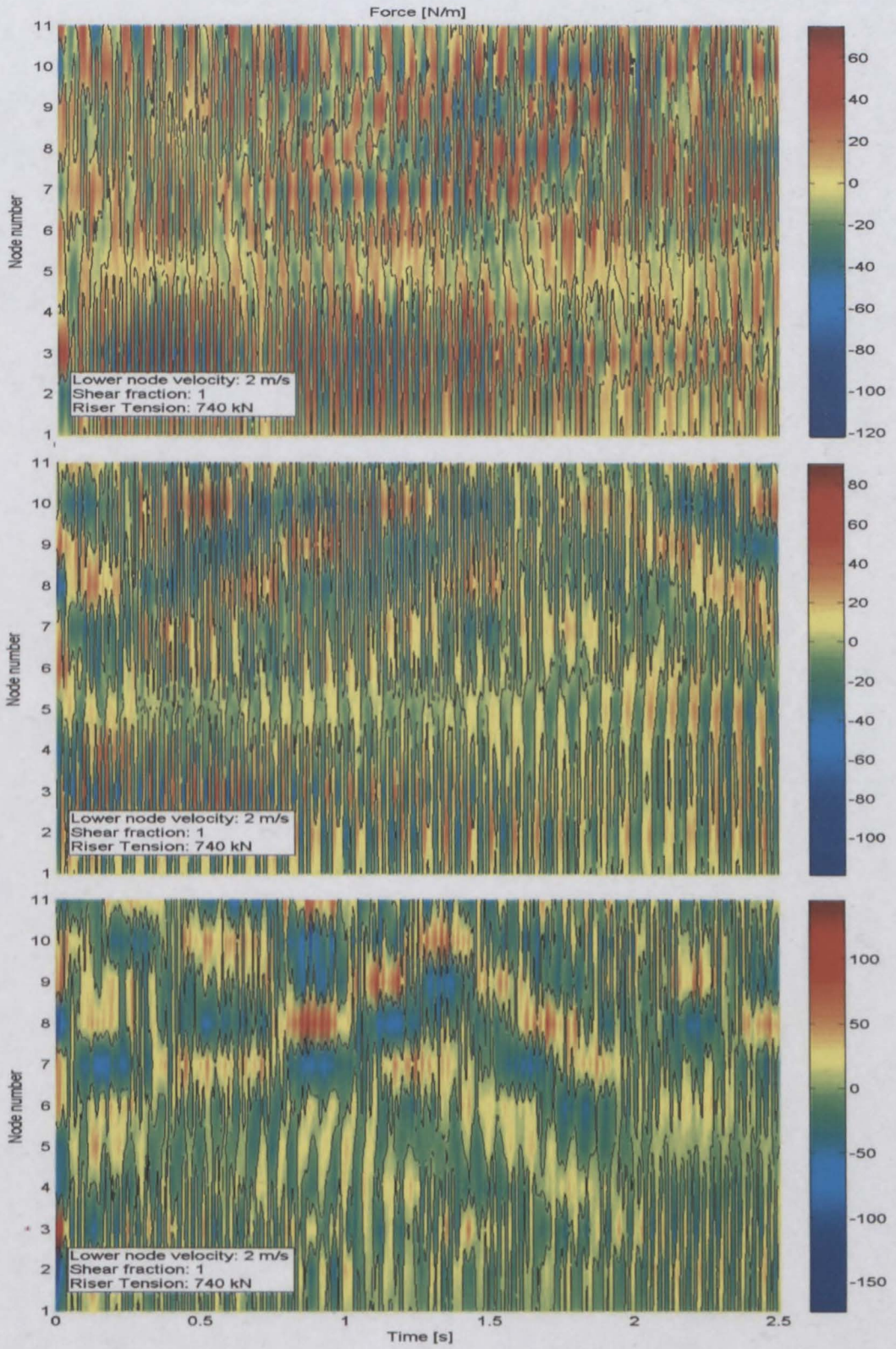


**Figure 12.13:** *Force contours for tests with the same shear fraction and flow velocity*

## 12.5 Post-processing the identified forces

### 12.5.1 Introduction

In Chapter 10 it was seen that the VIV-induced forces can be described by non-dimensional force coefficients that in turn allow the definition of empirical models, used to predict VIV on offshore structures. In Section 10.5, it was shown how a hydrodynamic force acting on a vibrating cylinder could be decomposed into two components. From these two force components respectively the added mass coefficient and cross-flow lift coefficient were obtained. Gopalkrishnan was able to draw a functional relation between each of these two coefficients and the amplitude ratio and non-dimensional frequency, as seen in Figure 10.7 and Figure 10.8 respectively. These functional relations of Gopalkrishnan are today widely used in the prediction of VIV. However, the experiments of Gopalkrishnan were comparatively simple, in the sense that they observed forced vibrations of a short cylinder at a single frequency. The rotating rig experiments studied in this chapter concerns a long cylinder, with a multiple frequency response.

The purpose of the next few Sections is to see if Gopalkrishnan's functional relations can be observed in the rotating rig data.

In this section the distributed forces identified by iFEM analyses are post-processed to obtain normalised consistent forces at each node. At each node, an added mass coefficient and cross-flow lift coefficient are calculated. Also at each node, representative values of the amplitude ratio and of the non-dimensional frequency are estimated. After taking into account some other matters, which will be discussed in subsequent sections, all of these are combined into contour plots. One contour plot will relate the added mass coefficient with the amplitude ratio and the non-dimensional frequency, while the other contour plot will relate the cross-flow lift coefficient with the amplitude ratio and the non-dimensional frequency. These can be compared to the contour plots of Gopalkrishnan.

### 12.5.2 Obtaining consistent nodal forces

The time series of distributed forces returned by the iFEM analyses often show erratic patterns along the length of the riser, with the value of the distributed force changing much over a short length of riser. Gopalkrishnan used a fixed cylinder in his experiments and thus used the force values measured at cylinder ends, normalised by the length of the cylinder, to calculate added mass coefficients and cross-flow lift coefficients. This means that, while erratic forces may have been acting on the cylinder, an averaged force value was used in further calculations.

Similarly, in this case, averaged force values are obtained at a limited number of points (equal to the number of nodes in the iFEM model), by using time series of normalised consistent forces in further calculations: The distributed force time series returned by the iFEM analyses are used to calculate the time series of horisontal consistent forces at each node of the iFEM model, which are then normalised by the length of the elements.
For each element in the riser, the nodal consistent forces are calculated as

$$\overline{\mathbf{R}} = \int \overline{\overline{\mathbf{N}}}(\overline{\xi}).\overline{\mathbf{f}}(\overline{\xi})d\xi \tag{12.9}$$

with $\overline{\mathbf{f}}(\overline{\xi})$ being the hydrodynamic force distribution over the element, $\overline{\overline{\mathbf{N}}}(\overline{\xi})$ the chosen shape functions that allows describing the displacement distribution as a function of the position $\overline{\xi}$ in the element.

### 12.5.3 Choosing a representative non-dimensional frequency and amplitude ratio

Figure 12.14 shows the time series for the total hydrodynamic lift force at a single node as estimated by the iFEM analyses, together with the displacement and acceleration signal at the same node. The time series of these nodal consistent forces are transferred to the frequency domain using the Fourier transformation [47]. This gives spectra of the total hydrodynamic lift force amplitude at different frequencies. The same is done for the time series of estimated riser response. Figure 12.15 shows the frequency spectra of these

signals. The response and excitation take place around a main frequency (in this case $10Hz$), but there are also significant response components at other frequencies.

When the response and excitation take place at a single frequency, it is straight-forward to present the results in contour plots of added mass $C_{M_0}$ and lift $C_{LV_0}$ coefficients as a function of the amplitude ratio $A/D$ and dimensionless frequency $\hat{f}$. A difficulty arises, however, when several frequencies are participating. It is not obvious which amplitude and frequency should be used in the calculation of $A/D$ and $\hat{f}$ when several frequencies are participating.

To address this problem, the signals are filtered to keep only the response and excitation force around the main frequency. The main frequency is used in the calculation of $\hat{f}$ and the amplitude of the filtered displacement signal is used to calculate $A/D$. The amplitude is thus an integrated value with contributions from each of the frequency components within the filtered range. The two black stars in Figure 12.15 indicates the filtering range for this node.

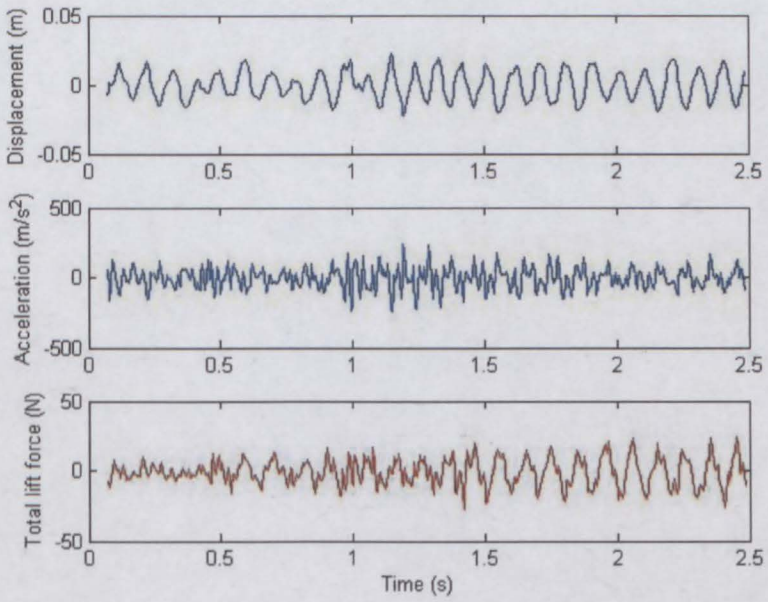


**Figure 12.14:** *Time series of estimated total lift force, displacement and acceleration at one node*

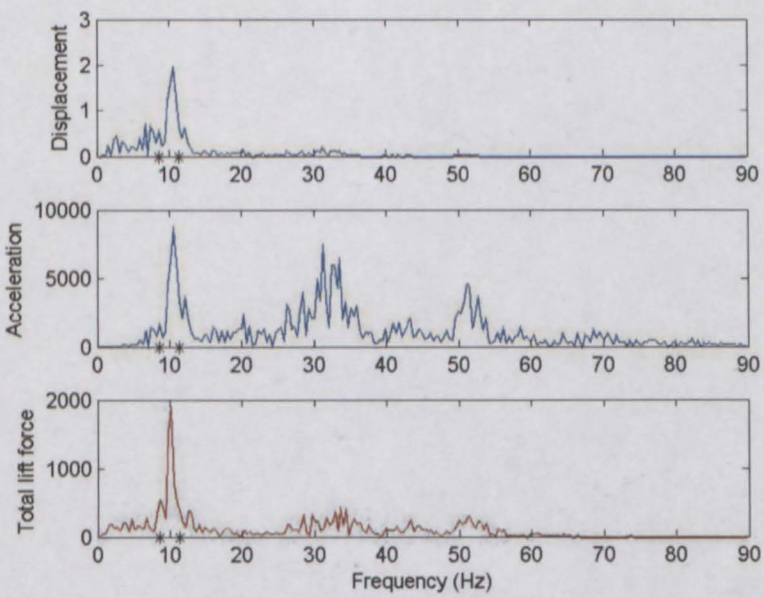


**Figure 12.15:** *Frequency spectre of estimated total lift force, displacement and acceleration at one node*

It is worth commenting on the transition of the total lift force (Figure 12.14(c)) from stochastic behaviour to a periodic load: Fourier decomposition is not fully adequate to describe such non-stationary processes, which explains the wide frequency peaks in Figure 12.15.

### 12.5.4 Calculation of added mass- and lift coefficients

The added mass and lift coefficients are calculated from the filtered force signal. The formulas derived in Chapter 10, Section 10.5, assume a single frequency of response, but Equation 11.7 from Chapter 11, allows to derive formulas for the added mass and lift coefficients that can handle signals with a broader frequency content. This leads to Equations 12.10 and 12.11, which were also used by Vikestad [72] in his calculations of the lift coefficient $C_{LV_0}$ and added mass coefficient $C_{M_0}$. Integration over a complete number of oscillation cycles will give good approximations of these limits.

$$C_{LV_0} = \frac{lim_{T\to\infty} \frac{\int_t^{t+T} F_L(t).\dot{x}(t)dt}{T}}{\frac{1}{4}\rho L D U^2 \omega x_0} \tag{12.10}$$

$$C_{M_0} = -\frac{lim_{T\to\infty} \frac{\int_t^{t+T} F_L(t).\ddot{x}(t)dt}{T}}{\rho\pi\frac{D^2}{8} L(\omega^2 x_0)^2} \tag{12.11}$$

$F_L(t)$ is the filtered hydrodynamic consistent force at each node, and $\omega$ is the main response frequency. The values obtained using Equations 12.10 and 12.11 are used in the contour plots.

If $F_L(t).\dot{x}(t)$ and $F_L(t).\ddot{x}(t)$ are non-stationary, so that the frequency content and amplitude of the signals change over time, the constants calculated by Equations 12.10 and 12.11 respectively are not really meaningful. For this reason, some data points will be discarded (Refer to Section 12.5.5).

#### Decomposition into force components

To better understand the meaning of the coefficients $C_{LV_0}$ and $C_{M_0}$, the total hydrodynamic lift force is decomposed into two components, which contributes to $C_{LV_0}$ and $C_{M_0}$

respectively. The development below refers to concepts defined in detail in Chapter 10, Section 10.5, and is only valid for single frequency response.

The equilibrium equation of a cylinder subject to VIV at a single frequency is given below. The total hydrodynamic force is $F_L(t) = \hat{F}_L.sin(\omega_s t + \phi)$, where $\phi$ is the phase angle between the hydrodynamic force and the body motion $x(t) = x_0 sin(\omega_s t)$.

$$\begin{aligned} K.x_0 sin(\omega_s t) + \omega_s.C.x_0 cos(\omega_s t) - \omega_s^2.M.x_0 sin(\omega_s t) &= \hat{F}_L.sin(\omega_s t + \phi) \\ &= \hat{F}_L.sin(\phi).cos(\omega_s t) + \hat{F}_L.cos(\phi).sin(\omega_s t) \\ &= \hat{F}_{LV_0}.cos(\omega_s t) - \hat{F}_{LM_0}.sin(\omega_s t) \end{aligned} \quad (12.12)$$

where $\hat{F}_{LV_0} = \hat{F}_L.sin(\phi)$ and $\hat{F}_{LM_0} = -\hat{F}_L.cos(\phi)$.

As shown in Equation 12.12, the total hydrodynamic force $\hat{F}_L(\omega)$ at each node can be split into one component $\hat{F}_{LV_0}(\omega)$ in phase with the riser's velocity and one component $\hat{F}_{LM_0}(\omega)$ in phase with the acceleration.

A positive amplitude for $\hat{F}_{LV_0}(\omega)$ indicates a positive power (excitation) at that frequency, while a negative amplitude means hydrodynamic damping. A positive amplitude for $\hat{F}_{LM_0}(\omega)$ will translate into a negative added mass coefficient at that frequency and vice versa, as seen from Equation 12.13. (Also refer to Equation 10.7.)

For a single frequency response, the added mass- and lift coefficients are defined as

$$\begin{aligned} C_{M_0} &= \frac{\hat{F}_L.cos(\phi)}{\omega_s^2.x_0 \rho \pi \frac{D^2}{4}} \\ &= \frac{-\hat{F}_{LM_0}}{\omega_s^2.x_0 \rho \pi \frac{D^2}{4}} \end{aligned} \quad (12.13)$$

$$C_{LV_0} = \frac{\hat{F}_{LV_0}}{\frac{1}{2}\rho D U^2} \quad (12.14)$$

This is done for each frequency separately, yielding the frequency spectre of the consistent force component in phase with acceleration, for each node. A similar force amplitude

spectre exists for the consistent force component in phase with velocity. These are shown for one node in Figure 12.16. The time signals for the same node can be found in Figure 12.17.

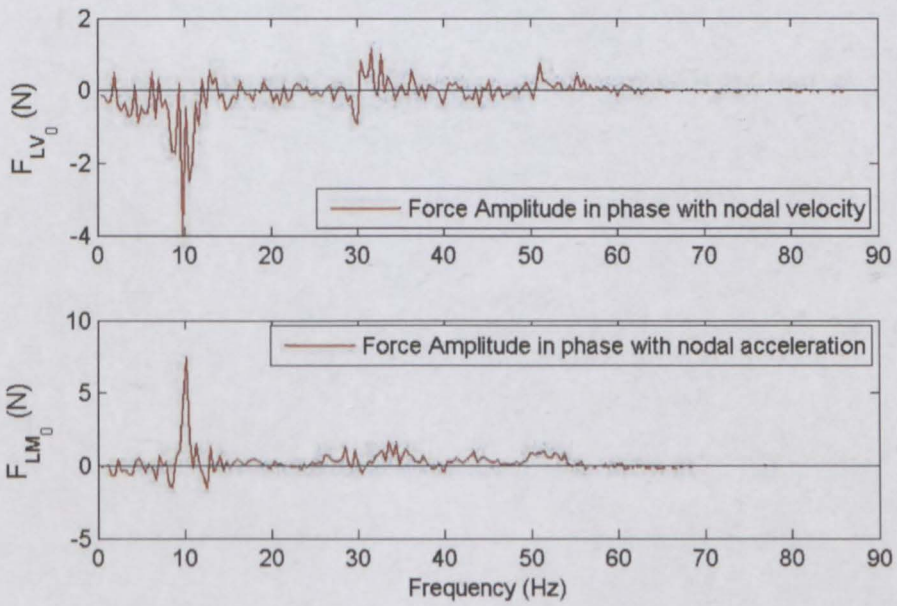


**Figure 12.16:** *Frequency spectra of* $\hat{F}_{LV_0}(\omega)$ *and* $\hat{F}_{LM_0}(\omega)$ *at one node*

Figure 12.17 shows, for one node, the filtered (refer to Section 12.5.3) and unfiltered signals for the displacement, with subplots containing the velocity and the force in phase with velocity and the acceleration and force in phase with the acceleration.

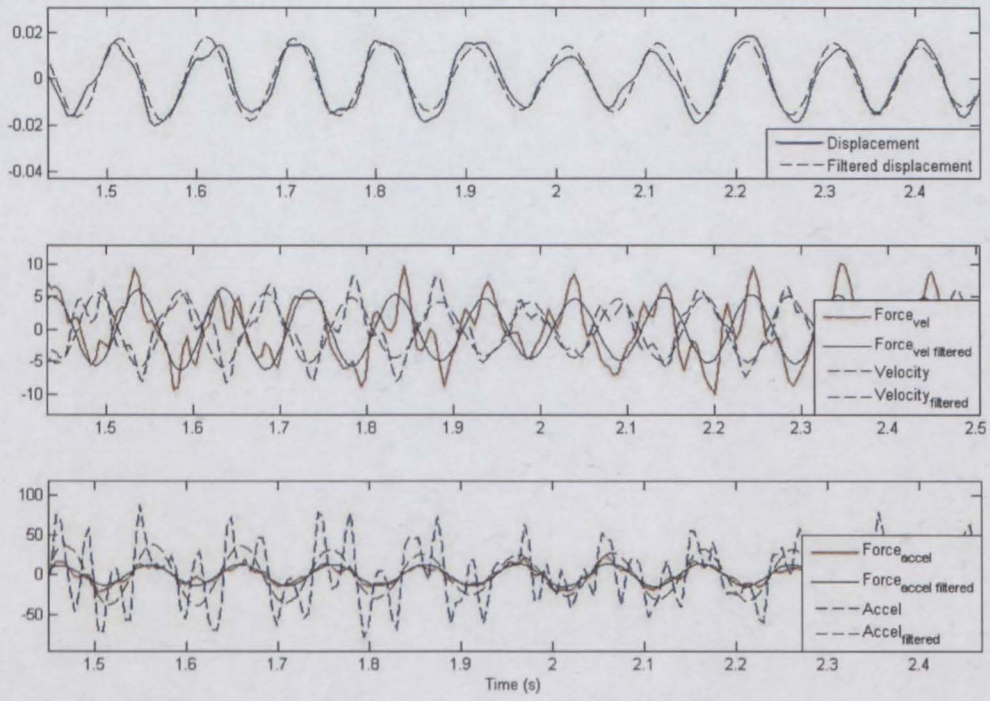


**Figure 12.17:** *Filtered and unfiltered response and force signals*

### 12.5.5 Usefulness of data points

A data point is defined by the value of an added mass- or lift coefficient, for a given combination of amplitude ratio and non-dimensional frequency. Two such data points (one for the added mass coefficient and one for the lift coefficient) can be estimated for every node of the riser in the iFEM model, although not all of them are useful, as will be explained below. By collecting all the useful data points from the many rotating rig tests, two contour plots are constructed.

If the force in phase with velocity is non-stationary, so that the frequency content and amplitude of the signal change over time, the lift coefficient $C_{LV_0}$ calculated by Equation 12.10 is not really meaningful. The same applies to $C_{M_0}$ when the force in phase with acceleration is non-stationary. Because of this, many data points had to be discarded. Data points were often not useful, because of the width of frequency components present, which made choosing a proper filtering window impossible. The criteria used to judge the

usefulness of a data point are explained below. In the following $F_v$ refers to the force in phase with velocity and $F_a$ refers to the force in phase with acceleration.

1. The frequency range is chosen to span the frequency at which $F_v(\omega)$ has its maximum amplitude and the frequency at which $F_a(\omega)$ is maximum by at least $1Hz$ to both sides. These frequencies are referred to as $f(F_{v_{max}})$ and $f(F_{a_{max}})$. This is done for each node and each node is filtered separately. For time-series that do not contain transient events $f(F_{v_{max}})$ and $f(F_{a_{max}})$ are close to each other and close to the main frequency of displacement response. However, in some cases this is not true, which makes it difficult to decide which frequency should be used to represent the data point. If $f(F_{v_{max}})$ and $f(F_{a_{max}})$ differs by more than $2Hz$ (making the total filtering range $= 4Hz$), or if the frequency at which the main response takes place falls outside of the frequency range chosen by considering $f(F_{v_{max}})$ and $f(F_{a_{max}})$, the data point is discarded.

2. When the frequency response spectrum is not narrow banded enough, it could happen that a significant amount of frequency components falls outside of the filtered range (as illustrated in Figure 12.18). If this is the case, the data point is discarded. Should the frequency components that falls outside of the filtered range be at frequencies far apart from the main response frequency, it is assumed that the responses at the different frequencies are well separated and can be viewed as independent superposed responses, so that filtering out these components will not introduce inaccuracies in the calculated values of $C_{LV_0}$ and $C_{M_0}$ around the main frequency. Then the data point is not discarded.

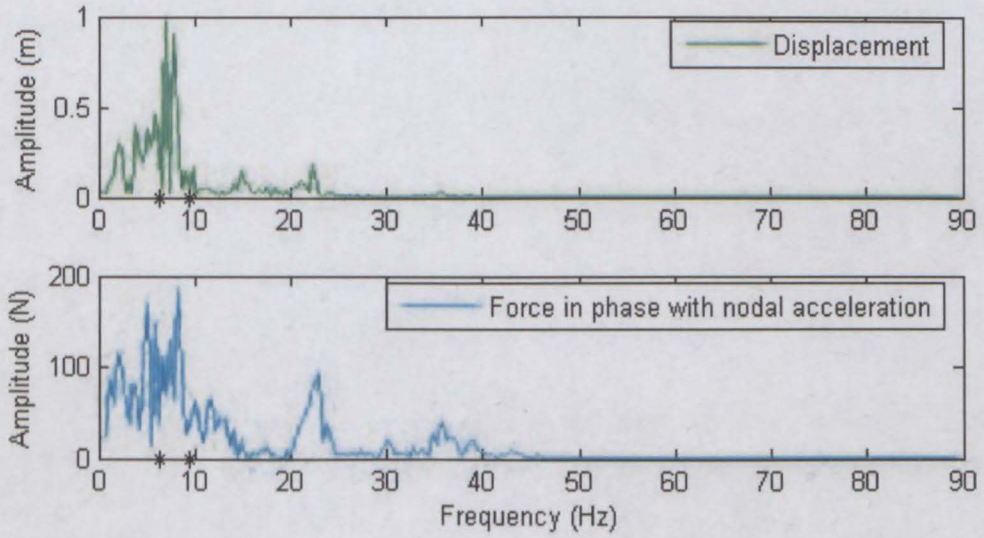


**Figure 12.18:** *Example of a response spectrum that is not narrow banded enough*

3. If, within the frequency range under consideration, the amplitude of $F_v(\omega)$ or $F_a(\omega)$ has significant values at opposite sign, it is an indication that $F_v$ or $F_a$ is non-stationary. Figure 12.19 shows an example of such a case. It is clear from the plot of $F_v(t)$ and velocity over time, that $F_v(t)$ is in phase with the velocity, then changes to being in phase opposition to the velocity and finally changes back to being in phase. The behaviour of $F_v$ is not well defined in this case and changes over time. Such data points are discarded.

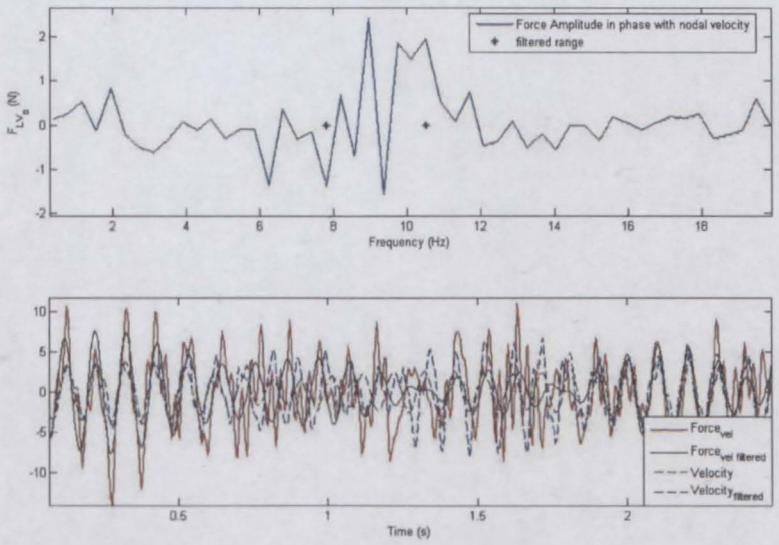


**Figure 12.19:** *Example of $F_v$ not well defined within the main frequency range*

4. In tests with high shear, the lower acceleration sensors were broken. It is assumed that the force estimate in that area is unreliable, because of lack of data, and therefor data points from the lower nodes are discarded. Also estimates from around node nr.5, corresponding to the position of sensor nr.9 (which was broken), are discarded for all tests.

## 12.6 Results

The contour plots of $C_{LV_0}$ and $C_{M_0}$ presented in this section collect data points from all tests, including a wide range of flow velocities and shear fractions.

### 12.6.1 Contour plot of the lift coefficient $C_{LV_0}$

Figure 12.20 shows the lift coefficient $C_{LV_0}$ as a function of the amplitude ratio $A/D$ and non-dimensional frequency $\hat{f}$. This figure can be compared to the contours of lift coefficient (Figure 12.21) found by Gopalkrishnan [23].

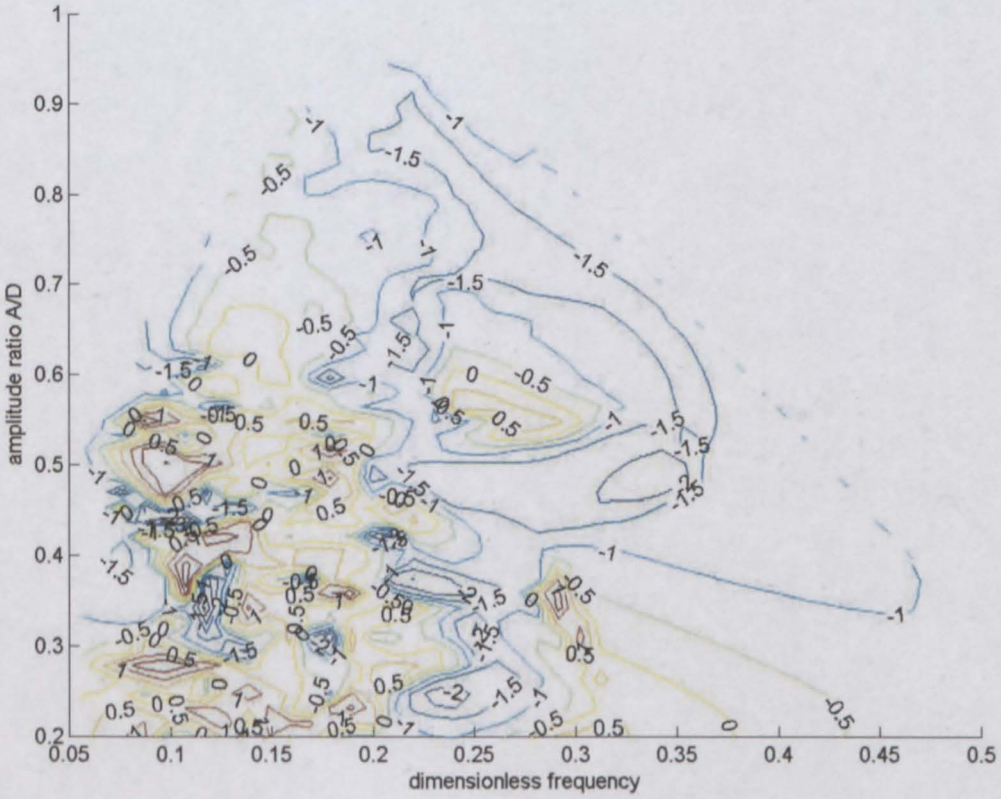


**Figure 12.20:** *Contour plot of the lift coefficient* $C_{LV_0}$

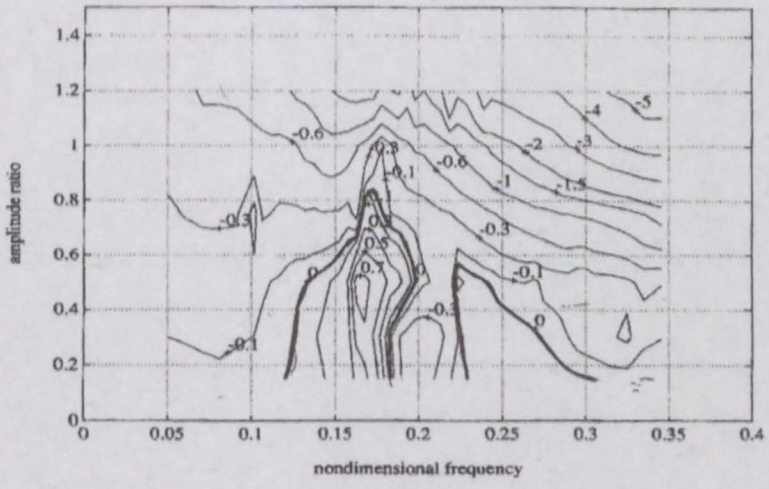


**Figure 12.21:** *Lift coefficient in phase with cylinder velocity (Gopalkrishnan, 1994)*

From the contour plot of the lift coefficient $C_{LV_0}$, it can be seen that $A/D = 0.7$ is the maximum value of the amplitude ratio for which positive lift coefficients are found. Most data points lie in the range $0.2 \leq A/D \leq 1.0$ and $0.1 \leq \hat{f} \leq 0.2$. Figure 12.22 shows the data points as small blue circles on the contour plot. It can be seen that there are very few data points to confirm the area of positive lift coefficients around $[0.2 \leq A/D \leq 0.4; \hat{f} = 0.3]$, while the area of positive lift coefficients around $[A/D = 0.56; \hat{f} = 0.26]$ is in fact defined by only one positive data point.

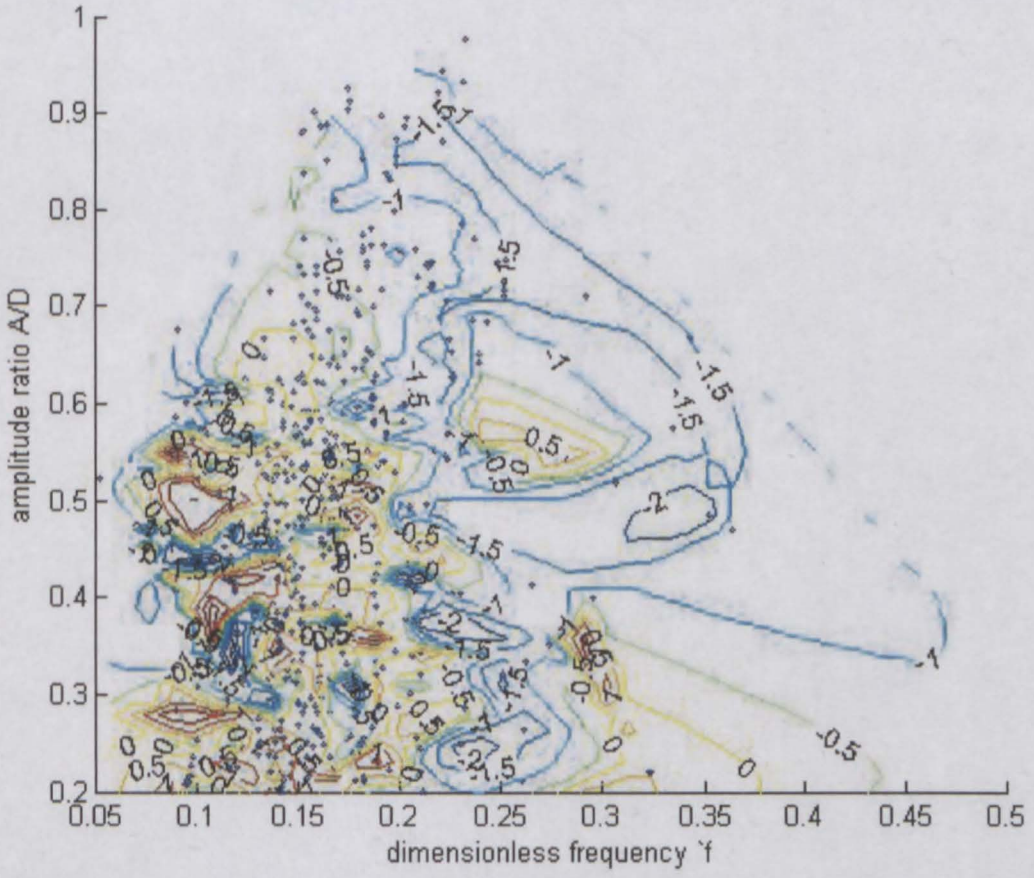


**Figure 12.22:** *Data points of the lift coefficient* $C_{LV_0}$

In the area of positive lift spanned by $[0.2 \leq A/D \leq 0.7; 0.1 \leq \hat{f} \leq 0.2]$ there are several islands of negative lift. To explain this one should look at the behaviour of a long

riser in multi-moded response (Refer to Section 10.5.2).

It seems that excitation can be taking place at one frequency in an excitation zone, while it is possible for damping to take place at another frequency in the same zone. Figure 12.19 indicates this kind of behaviour with a positive lift coefficient at $9Hz$ and a negative lift coefficient at $9.5Hz$. Such data points were discarded in the current investigation, but if this kind of mixed behaviour is possible at a single position on the riser, mixed behaviour should also be expected along the length of the riser.

It was observed in many of the tests that when the structure is excited (positive lift coefficient) at one position in the structure, the response at that frequency will be damped (negative lift coefficient) in another position along the riser. Table 12.1 contains an example. It is this interaction that produces the islands of negative lift in the midst of the area of positive lift. Similar islands are not present in the results of Gopalkrishnan, because a short cylinder was used in his experiments. This behaviour is demonstrated by looking at the data points from a single test and comparing the values at different nodes. Table 12.1 contains the values of $C_{LV_0}$, $\hat{f}$ and $A/D$ computed at the nodes of the riser for TEST4303, which had a lower node velocity of 0.8m/s and a flow shear fraction of 1.2. From these values it is clear that for a very similar combination of $\hat{f}$ and $A/D$, the lift coefficient $C_{LV_0}$ can vary from positive to negative on different parts of the riser. To see this, compare the values estimated at node 3 with those estimated at node 4, also compare node 8 and 10.

| Nodes | 2 | 3 | 4 | 5 | 6 | 7 | 8 | 9 | 10 | 11 |
|---|---|---|---|---|---|---|---|---|---|---|
| $C_{LV_0}$ | -0.729 | 1.027 | -0.273 | -0.307 | 0.161 | 0.447 | 0.194 | -0.186 | -0.961 | 0.150 |
| $\hat{f}$ | 0.146 | 0.148 | 0.150 | 0.152 | 0.154 | 0.156 | 0.158 | 0.171 | 0.162 | 0.165 |
| $A/D$ | 0.120 | 0.503 | 0.492 | 0.283 | 0.336 | 0.360 | 0.539 | 0.399 | 0.616 | 0.120 |

**Table 12.1:** *Values of $C_{LV_0}$, $\hat{f}$ and $A/D$ computed at the nodes of the riser for TEST4303*

While the contour plot of the lift coefficient shows some trends similar to what Gopalkrishnan found in his experiments, there is much more scatter of the results. Reasons for this are discussed in section 12.8. The question is raised whether the same simple functional relation between the lift coefficient, amplitude ratio and dimensionless frequency exists in this case, or if a more complicated relation is to be expected.

### 12.6.2 Contour plot of the added mass coefficient $C_{M_0}$

Figure 12.24 shows the added mass coefficient $C_{M_0}$ as a function of the amplitude ratio $A/D$ and non-dimensional frequency $\hat{f}$. This figure can be compared to the contours of lift coefficient (Figure 12.23) found by Gopalkrishnan [23]. A phase shift in the total lift force causes a change in sign of the added mass coefficient around $\hat{f} = 0.14$. Gopalkrishnan found this phase shift at $\hat{f} = 0.17$.

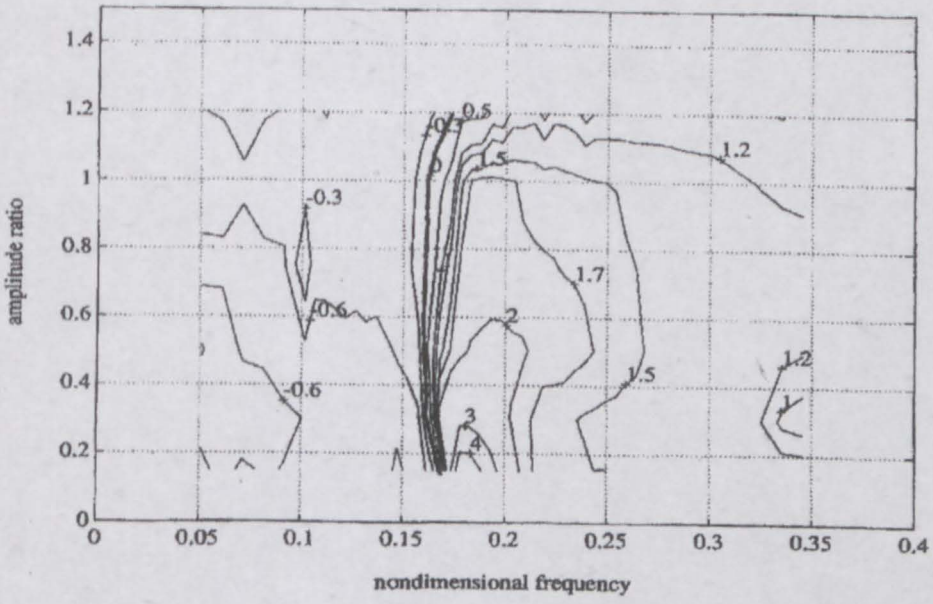


**Figure 12.23:** *Added mass coefficient (Gopalkrishnan, 1994)*

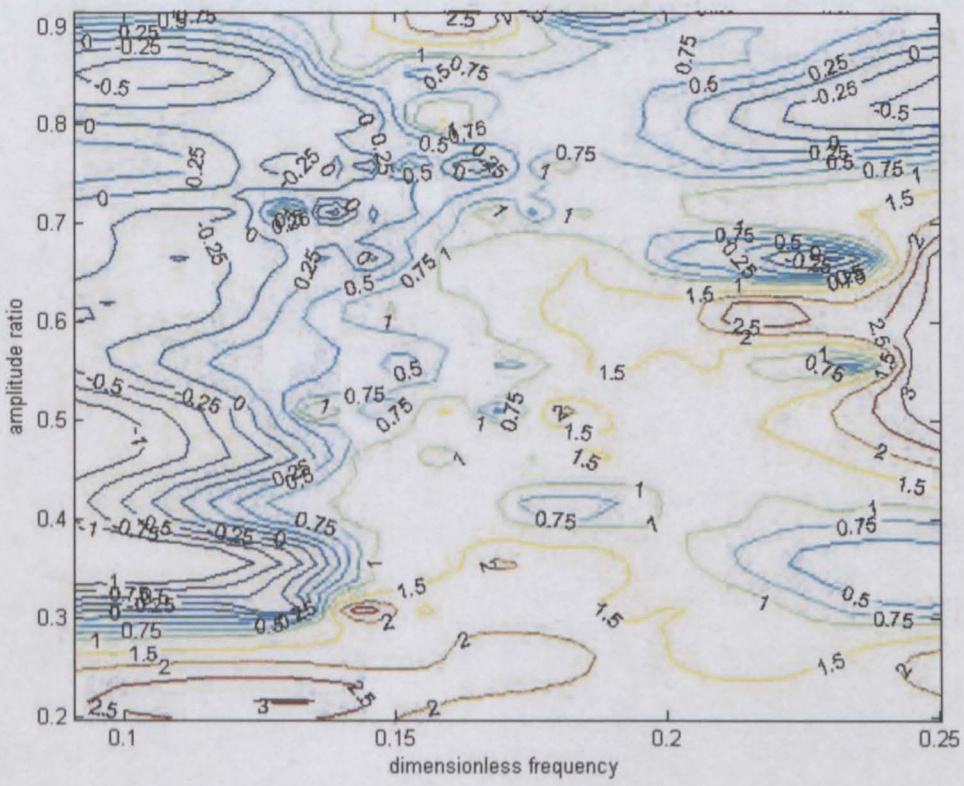


**Figure 12.24:** *Contour plot of the added mass coefficient* $C_{M_0}$

A lot of scatter is present in the values of the coefficients. To demonstrate this the data points of added mass coefficient is plotted for three ranges of $C_{M_0}$. Figure 12.25 shows all data points where $C_{M_0} \leq 0$, Figure 12.26 shows $0 \leq C_{M_0} \leq 1.0$ and Figure 12.27 shows $C_{M_0} \geq 1.0$. For $C_{M_0} \leq 0$, the mean value of $\hat{f}$ is 0.13, for $0 \leq C_{M_0} \leq 1.0$ the mean value of $\hat{f}$ is 0.145 and for $C_{M_0} \geq 1.0$ the mean value of $\hat{f}$ is 0.16. It is obvious from the figures that the mean value of $\hat{f}$ increases as $C_{M_0}$ increases, but with a wide scatter around the mean value. The contour plot figure 12.24 interpolates the averaged values of $C_{M_0}$.

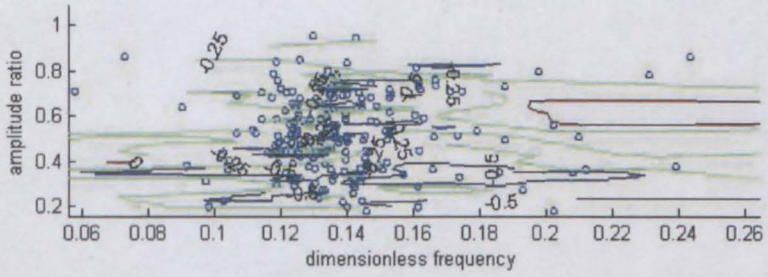


**Figure 12.25:** *Data points for added mass coefficient* $C_{M_0} \leq 0$

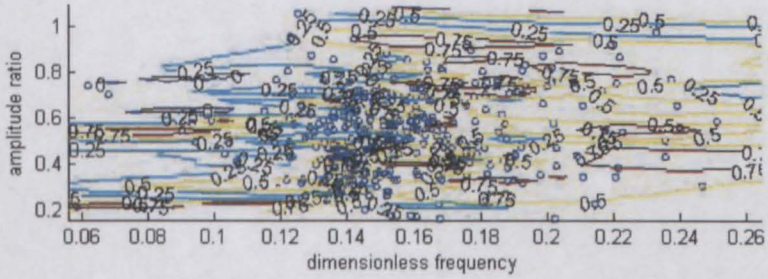


**Figure 12.26:** *Data points for added mass coefficient* $0 \leq C_{M_0} \leq 1.0$

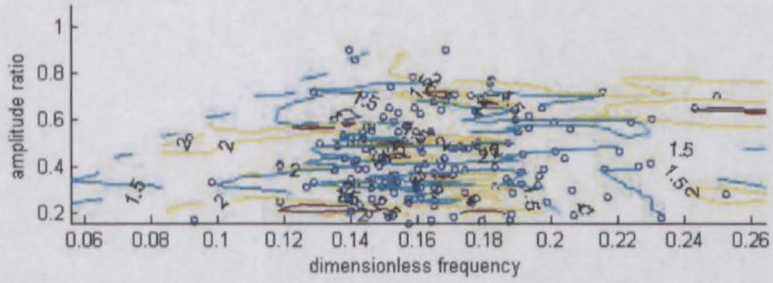


**Figure 12.27:** *Data points for added mass coefficient* $C_{M_0} \geq 1.0$

### 12.6.3 Excitation zones

The power input from the hydrodynamic force describes the rate at which the riser gains energy from hydrodynamic excitation, or loses it because of hydrodynamic damping. The

power input $P(t)$ from the hydrodynamic force is computed at each node as

$$P(t) = R(t).\dot{x}(t) \tag{12.15}$$

where $R(t)$ is the consistent force at the node and $\dot{x}(t)$ is the velocity of the node.

The calculated power values are plotted for each node at each time step, presenting as contours the excitation zones along the riser over time. Warm colours (red and yellow) presents a positive value of the power and can be seen as an energy input, while cold colours (green and blue) signify damping or energy dissipation (negative power). The black lines are zero power lines.

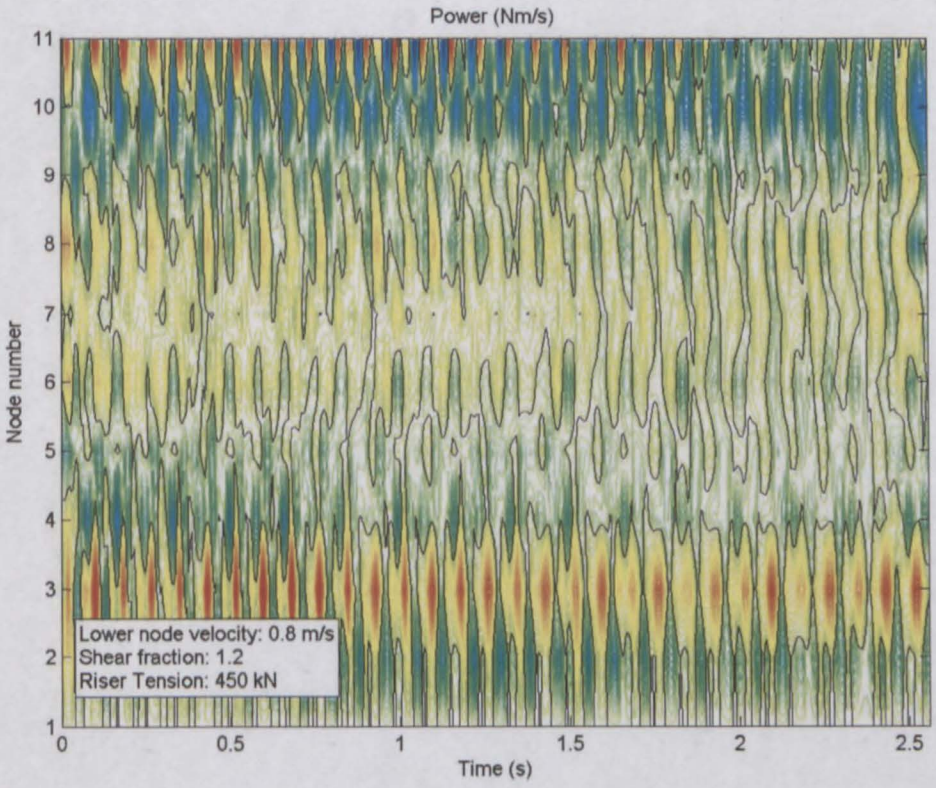


**Figure 12.28:** *Power contour plot for test nr. 4303*

For this same test, the values of $C_{LV_0}$ were given in Table 12.1. Nodes with a positive value of $C_{LV_0}$ in Table 12.1 corresponds to a positive power zone (excitation) over time

in Figure 12.28. Similarly, nodes in Table 12.1 with a negative value of $C_{LV_0}$ corresponds to a negative power zone in Figure 12.28. This is to be expected, since the lift coefficient $C_{LV_0}$ is used to express the excitation or damping experienced by a system subject to vortex induced vibration.

### 12.6.4 Quadratic drag mechanism

It is interesting to note in Figure 12.15 that significant frequency components appear at $3\omega$ and $5\omega$, where $\omega$ is the main response frequency. This suggests a quadratic drag mechanism comparable to what is described by Morison's equation. Morison calculates the drag force component of a wave load on a fixed cylinder as a quadratic function of $U$, the fluid velocity relative to the cylinder.

$$F_d = \frac{\rho}{2} C_D D L U \left|U\right| \tag{12.16}$$

When $U(t) = U_0 sin(\omega t)$ the drag force can be expressed as a Fourier series and becomes

$$F_d = \frac{\rho}{2} C_D D L (U_0)^2 \left[\frac{8}{3\pi} sin(\omega t) + \frac{8}{15\pi} sin(3\omega t) + \frac{8}{105\pi} sin(5\omega t) + ...\right] \tag{12.17}$$

## 12.7 Discussion

**Adequacy of the functional relation** In the previous section, contour plots of $C_{LV_0}$ and $C_{M_0}$ as a function of the amplitude ratio $A/D$ and non-dimensional frequency $\hat{f}$ were presented. These plots used data points from all tests, including a wide range of flow velocities and shear fractions. However, many data points were discarded (Refer to Section 12.5.5), because the estimated force histories often showed non-stationary or transient behaviour (Figure 12.14(c) shows an example). Such non-stationary forces cannot be adequately described by the constant added mass- and lift coefficients.

In addition, the full length of data for each test were not considered, because the riser tension varied over time (Refer to Section 12.3.1). Instead, only short lengths of data were analysed, corresponding to times where the riser tension remained fairly constant.

This was done, because the dynamic iFEM XU algorithm cannot handle stiffness matrices that vary over time. The jumps in riser tension might correspond to significant transient events in the response of the riser. If this is the case, an important part of the riser's behaviour were not captured.

Omitting data points that could not be adequately described and the fact that large parts of data (that might contain even larger transient events) were not analysed, means that the contour plots presented in the previous section contains a much simplified collection of data. The actual behaviour of a slender riser in multi-frequency response are more complicated.

While the contour plots presented in the previous section show some trends similar to what Gopalkrishnan observed in his study of short cylinders, there is a lot of scatter in the results. This scatter is present in spite of keeping only well-defined data points. The functional relation observed by Gopalkrishnan holds for short cylinders, but cannot adequately explain the force distributions observed on this slender riser with multi-frequency response.

**Adequacy of Fourier decomposition** Fourier decomposition was used to describe the estimated forces in the frequency domain. Fourier decomposition is not fully adequate to describe non-stationary processes, and will result in wide frequency peaks when transient behaviour is present. To describe non-stationary processes, a method is needed that can give the frequency content of the signal as a function of time. Methods such as wavelet theory might be used to describe such processes.

## 12.8 Uncertainties

The results obtained are promising and confirms some observations made previously concerning the VIV process. However, there are several uncertainties regarding this investigation that need to be mentioned.

### The VIV process

The largest source of uncertainty lies within the VIV process itself. The current experiment involved a long riser with several eigenfrequencies in the possibly excited range and correspondingly participation of several mode shapes. In previous work by Haakonsen [27] it was shown that, in most tests, the riser had a multi-modal response at a dominant frequency, but that the response were not stable in the high flow velocity cases. The fluid-structure interaction in the case of long risers in sheared flow is not yet fully understood. The mechanism behind excitation- and damping zones along such a riser needs further exploration.

Recent experiments show that the vortex shedding process are subject to 3D effect. The in-line motion has a significant effect on the vortex shedding process and therefor influences the cross-flow response. This interaction is also not yet understood. Gopalkrishnan's experiments considered cross-flow characteristics, with the in-line vibrations suppressed. In the current experiment in-line motion were present and would have influenced the vortex shedding and cross-flow response.

### The experiment

Haakonsen [27] showed that the tension in the riser had an influence on the riser response. The fact that riser tension were not constant introduces some uncertainty. A change in riser tension will cause a change in the stiffness, and the linear dynamic iFEM XU algorithm cannot handle a stiffness matrix that changes over time.

As with all experiments, limited sensors were available and in some tests up to four of the twelve sensors were broken. In section 12.3.3 the question was raised whether enough sensors were available for iFEM to adequately describe the force distribution, especially in the case of high flow velocity where the response often became stochastic in nature.

**The iFEM model**

The iFEM model introduces further uncertainties in the sense that it is impossible to provide a perfect model of the system. Several factors were left unmodeled, some because they were judged to be negligible and some because insufficient information were available to allow their modelling. Coriolis force from the rotating nature of the experiment, gravity pollution of the acceleration measurements, the unmodeled test rig and three dimensional effects on the riser are all examples of such factors. The most important concern however, is the failure in high flow velocity cases to explain above water measurements by only applying forces on below water elements.

## 12.9 Conclusions

1. The hydrodynamic forces acting on a long slender riser in sheared flow are identified from acceleration measurements using the inverse FEM force identification algorithm.

2. The forces found in this way are post-processed to obtain hydrodynamic force coefficients which are used to describe the vortex induced forces as a function of the dimensionless frequency and amplitude ratio. Such functional relations are often used in empirical models to predict the response of structures subject to vortex induced excitation.

3. The lift- and added mass coefficients obtained show some trends similar to the results of Gopalkrishnan, which were obtained for a short driven cylinder in cross flow. $A/D = 0.7$ is the maximum value of the amplitude ratio for which positive lift coefficients are found, compared to $A/D = 0.8$ from the results of Gopalkrishnan. The added mass coefficient displays the same change in sign, corresponding to a phase shift of the total lift force, around a value of $\hat{f} = 0.15$, while the results from Gopalkrishnan found this phase shift at $\hat{f} = 0.17$. However, the results show a lot more scatter, and it is concluded that the functional relation of Gopalkrishnan is not adequate to describe the multi-frequency slender riser behaviour. Reasons for

this and sources of uncertainty are discussed (Refer to Section 12.7 and 12.8).

4. Graphs that show the power input along the riser over time visually presents the excitation zones along the riser over time.

5. Frequency decomposition of the identified forces show significant frequency components at $3\omega$ and $5\omega$, where $\omega$ is the main response frequency. This suggests a quadratic drag mechanism comparable to what is described by Morison's equation.

6. The present investigation confirms the complex nature of the fluid-structure interaction in the case of vortex shedding on long risers in sheared current. It is the authors opinion that, while Gopalkrishnan's approach was adequate in presenting a functional relation between the force coefficients, the amplitude ratio and the dimensionless frequency in the case of short driven cylinders in cross flow, the same functional relation is poorly defined for long risers in sheared current. Long risers in sheared current exhibit behaviour that are more complex and can not be adequately described using such a simple relation. Instead, other ways of describing the general behaviour of long risers should be investigated.

## 12.10 Suggestions

### High speed camera imaging - a way to increase the number of sensors

Sensitivity studies in Section 12.3.3 raised the question whether or not the number of sensors used in the Rotating rig experiment were enough for iFEM to adequately describe the distributed hydrodynamic force acting on the riser over time. In future experiments, the possibility of using high speed camera imaging from which the riser deflections at a large number of points can be extracted, should be investigated.

### Other ways of presenting information

Since there is an interaction of excitation and damping zones along the riser, other ways of presenting the information from the identified force should be explored. The presentation

used by Gopalkrishnan is very suitable to represent information from short cylinder tests and also convenient to use in empirical models. However, this way of presenting results cannot capture all the information available in the hydrodynamic force histories for the long riser where complicated fluid-structure interaction is taking place.

**Vikestad's presentation** Vikestad [72] conducted forced excitation tests on an elastically mounted short cylinder and presents the hydrodynamic force coefficients as functions of the response amplitude ratio, reduced velocity, the frequency of the external excitation and the amplitude of external excitation. Tests done by Vikestad were specifically designed to provide some insight in the fluid-structure interaction of long risers. Information from these experiments are more difficult to incorporate in empirical models, but is valuable to understand the mechanisms that govern the VIV process in these cases. His experiments also allowed to control important aspects such as the external excitation's frequency and amplitude, making this a good way to investigate the process.

**Chaos theory** Chaos theory might proof useful in the search to understand the VIV process. The Lorenz chaotic attractor is a chaotic system first described by Edward Lorenz of the Massachusetts Institute of Technology. Figure 12.29 shows an animation of the integration of the three coupled nonlinear differential equations that define the "Lorenz Attractor". As the integration proceeds, a point moves around in a curious orbit in 3D space. The orbit is bounded, but not periodic and not convergent. It looks like the point is moving in a (seemingly) periodic pattern with a slow drift, but a sudden bifurcation takes place and the point starts to move in another pattern.

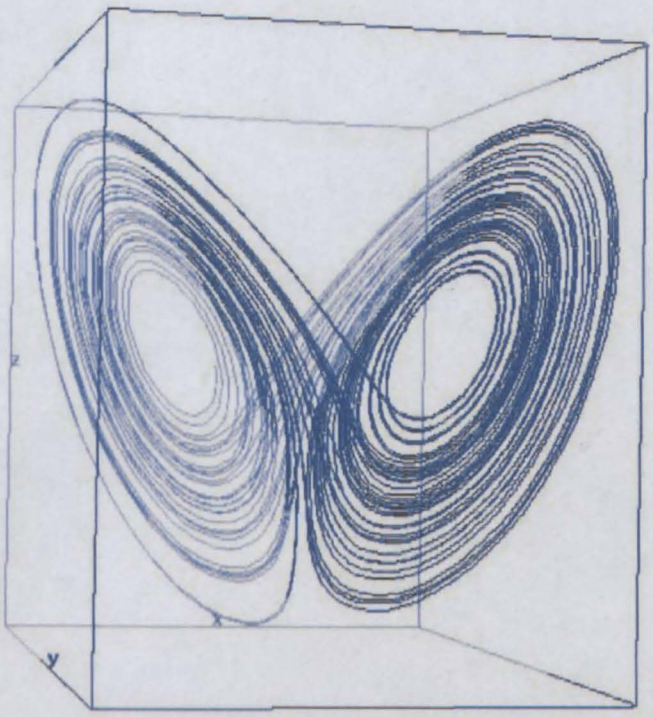


**Figure 12.29:** *Lorenz chaotic attractor (Elert, 2005)*

The author is no expert in chaos theory, but the above system seemed strangely familiar compared to what was observed in the response of the rotating rig experiments. As an example, refer to Section 12.4, Figure 12.12: There seemed to be transitions between periods of different quasi-cyclic behaviour, evident from the force distribution over time on the top halve of the riser. It is a pity that the jumps in tension prevented iFEM from treating the full length of data available. It might be that such a jump in tension corresponded to transient events or bifurcations similar to what is seen in the Lorenz attractor.

It is suggested that a fundamental approach should be followed in trying to explain the behaviour of the forces identified from the rotating rig data. This might require that the empirical approach used before be abandoned and even that the use of Fourier decomposition be reconsidered. Wavelets and chaos theory might provide a better way of explaining the behaviour of the hydrodynamic force histories for the long riser where

complicated fluid-structure interaction is taking place.

# Part V

# Conclusions

# Chapter 13

# Conclusions

This chapter draws conclusions based on the work presented in this dissertation and makes suggestions for future work.

## 13.1 Conclusions

The goal of the present work was first to understand how errors in the model affect the performance of iFEM in terms of assessed external loads or assessed stresses in the presence of localised and/or distributed model errors. This was investigated for both static and dynamic cases. The second goal was to investigate whether iFEM can be adapted to detect discrepancies between the model and the actual structure, then to develop algorithms for model parameter estimation for both static and dynamic systems and finally to implement these algorithms in a computer software that would allow us to treat inspection problems numerically. Thirdly, the iFEM algorithms were to be validated using numerical and, preferably, real world experimental examples.

All three of the above goals were reached and results are encouraging. Overall it can be concluded that the iFEM methods show promise to become a valuable tool in the field of structural monitoring, inspection and estimation.

### 13.1.1 Effect of model errors on the performance of iFEM

The performance of iFEM force and response estimation methods confirms that they are useful for real world applications. The dynamic XU algorithm was tested against several sets of real experimental data and performed satisfactorily.

It is further concluded that iFEM is stable with respect to model errors, meaning that the combination of inaccurate response measurements and an inaccurate structural model usually does not cause mathematical impossibilities, and iFEM gives usable results in spite of such inaccurate models. Thus, assuming that appropriate costs are associated to deviation from measurements and deviation from expected load values, iFEM can be used to process physical measurement data.

However, inaccurate modelling does have a significant influence on the output of iFEM. Specifically, it leads to the appearance of unphysical forces referred to as *ghost forces*. Distributed modelling errors cause distributed ghost forces that can easily go undetected. The behaviour of the structure does not appear unphysical and the estimated external forces look reasonable. The load is under- or overestimated depending on the nature of the modelling error. For example, if the error tends to weaken the modelled structure, compared to the actual, measured one, iFEM will tend to underestimate applied forces. In static cases, a linear relation exists between error in the stiffness matrix and the resulting error in the estimated force value. Local damage causes localised ghost forces in the area of the defect if measurements are adequate in precision, placement, type and number to describe the influence of the defect on the response of the structure.

In the dynamic analysis of a damaged beam, iFEM was able to make an assessment of the impact load that was applied to the beam, in spite of inaccurate modelling. This assessment was relatively accurate and, in some cases, easily distinguishable from the ghost forces that appeared as a result of the inaccurate model. It seems that iFEM gives the possibility of defect detection, at least in the present case, where alternating ghost

forces indicated the presence of defects. Here, the need for a post processing method to attribute ghost forces to stiffness-, damping-, or mass-related defects was identified. In the dynamic analysis of the damaged beam, error in the mass matrix of the system could be detected by noticing the strong correlation of the ghost force with the accelerations at that point.

During the course of work, it was observed that when continuity of the externally assessed load is not enforced, it is often achieved anyway. A general rule could be formulated, although this was only observed and not proven: Provided that the probability of externally applied load are the same for connected model elements, continuity of those $U$ degrees of freedom will be observed, of which the corresponding $X$ degrees of freedom have been required to be continuous. If continuity of $U$ need not be enforced in order to obtain continuity, the $U$ degrees of freedom can be eliminated from the iFEM system, thus reducing the number of unknown variables. However, doing this will take away our ability to later suppress or constrain $U$ degrees of freedom.

### 13.1.2 Algorithms for model parameter estimation

The author succeeded in developing algorithms that allow model parameters to be estimated in addition to force and response estimates. These XUA algorithms allow treatment of linear and non-linear static and linear dynamic problems. They further allow data from several load cases or experiments to be combined, accumulating information and providing a better basis for damage detection. An additional algorithm was developed that improves the computing time of both parameter identification algorithms significantly.

The appearance of localised ghost forces in the area of the damage when local modelling error was present, showed the potential of iFEM for damage detection. A theory was developed for static systems that allows the use of several experiments in order to accumulate information on the response, allowing a better basis for damage detection. The theory allows the updating of chosen structural parameters. The results obtained is encouraging and indicate that this theory can be used to detect damage in structures.

In complicated structures many experiments, or a large number of sensors, are needed to accurately point out the location of damage. Small damage is also hard to identify, and again a large number of experiments or sensors is needed to ensure that the damage is adequately described.

Many of the applications in structural monitoring are dynamic. Succeeding with the formulation of a static parameter identification algorithm encouraged the pursuit and completion of the development of the more challenging dynamic parameter identification theory. Similar to the static solution, this development also allows data from several experiments to be combined and in this way accumulate information for the identification purpose. Results obtained from numerical and actual experiments were encouraging and indicate that the algorithm can be used to detect damage in structures. In a cantilever bridge example small damages (2%) could be located and quantified. It is believed that the dynamic algorithm's ability to detect small defects is related to both the larger volume of measurement data accumulated in one experiment and the ability of higher frequency response to localise small defects that only affect response in a small area, thus providing better resolution than was the case for static experiments.

With regard to long-term health monitoring of large structures such as bridges and offshore platforms, the need to reduce the dependence upon measurable excitation forces is noted by many researchers. While a measured excitation force is an advantage, the parameter identification algorithms developed in this work do not require the excitation force to be measured. The dynamic algorithm can use vibrations induced by ambient environmental or operating loads for the assessment of structural integrity.

The parameter identification algorithms developed here initially required the inversion of matrices - a costly mathematical operation. An algorithm was formulated that succeeds in solving both the static and dynamic parameter identification problems without having to invert large matrices as was the case with their previous formulation. This results in algorithms with a lower order of complexity compared to the order of complexity of the

first solution. This formulation significantly reduced the computer time required to solve large systems.

The newly developed algorithms were implemented into the existing iFEM software SAFRAN and allow to treat inspection and defect detection problems numerically. The software was also restructured and improved to allow both the static and dynamic parameter identification algorithms to be properly utilised. SAFRAN is now, in spite of its limited element library and non-existent user interface, a well-structured computer implementation that includes all of the iFEM algorithms as well as capabilities for normal FEM analysis.

### 13.1.3 Experimental validations

Testing of the existing static and dynamic iFEM force and response estimation algorithms (iFEM XU) and the newly developed static and dynamic iFEM parameter identification algorithms (iFEM XUA) against numerical examples gave very encouraging results. The dynamic iFEM algorithms (both XU and XUA) were also tested against several sets of real experimental data and performed well.

#### Weimar Beam

Data from a vibrating damaged beam experiment [76] was used to validate the dynamic force and response algorithm (iFEM XU) and later also the dynamic parameter identification algorithm (iFEM XUA). The dynamic iFEM XU algorithm succeeded in correctly identifying the impact load that induced the vibrations, from acceleration measurements taken at seven positions along the beam. When a FEM model was used that did not account for the damage in the beam, the dynamic iFEM XUA algorithm succeeded in identifying the presence of damage and correctly located the two damaged areas.

#### Benchmark

The iFEM dynamic parameter estimation algorithm succeeded in locating the damage in the *Benchmark Experiment* for most of the damage scenarios and load configurations.

An important conclusion from this chapter is that iFEM models should explicitly allow for all model uncertainties by including appropriate model parameters. The presence of numerous false alarms could be explained by model uncertainty which were not properly accounted for due to a limited element library in the prototype software SAFRAN. Uncertainty related to the proper assignment of cost matrices in the iFEM theory also hampered performance. The existing iFEM theory for assigning costs proved to be of little value in practice and seems to be incorrect. It is urgently needed that this theory be revised to steer away from the trial and error approach that is currently followed. In addition to these problems, the full capacity of the iFEM theory could not be exploited due to computer memory problems, which were due to some parts of the computer code having been written in a memory inefficient way. At the time of going to print, the memory problems were solved by the writing of an "out of core" solver that reads and writes data to and from hard disk, instead of storing it all in the computer's limited Random Access Memory (RAM).

### VIV: Vikestad

Vikestad [72] conducted experiments to investigate the fluid-structure interaction of a short vibrating cylinder subject to vortex induced forces. iFEM was used to estimate, for numerous tests, the forces acting on this cylinder and also to estimate certain coefficients that can be used to describe the vortex induced force. The performance of the algorithms could be tested by comparing the iFEM estimated forces and parameters to the known values from Vikestad's work. The iFEM force and response algorithm succeeded in correctly identifying the hydrodynamic loads acting on the cylinder from measurements of its response. The iFEM parameter identification algorithm could accumulate data from three repetitions of each test, and succeeded in correctly identifying the added mass parameters for towing tests in which the cylinder was responding with lock-in behaviour.

### VIV: Rotating Rig

Vortex induced vibrations of a long slender riser in sheared flow were investigated by MARINTEK [37] in a *Rotating Rig* experimental setup. The hydrodynamic forces acting

on this structure were identified from measurements of its structural response using the iFEM force identification algorithm. The forces found in this way were post-processed to obtain hydrodynamic force coefficients. Functional relations between the force coefficients and other dimensionless parameters are often used in empirical models to predict the response of structures subject to vortex induced excitation. The results were compared to such a functional relation obtained in previous studies for short driven cylinders in cross flow. Although similar trends could be identified, the same functional relation is poorly defined for long risers in sheared current. Long risers in sheared current exhibit behaviour that are more complex and can not be adequately described using such a simple relation. Instead, other ways of describing the general behaviour of long risers should be investigated.

### 13.1.4 Other aspects

#### Sensitivity studies

The sensitivity with regard to several important aspects, including the number and placement of sensors, level of damage, position of physical excitation and appropriate costing was studied to varying degree in this work. The above sensitivity studies were not expressed goals of the present work. Where interesting results pertaining to the above aspects were observed, they were reported.

#### Seeding of damage

The familiar Finite Element Method (FEM) is widely used to discretise structures and analyse their response on known excitation forces. The user defined FEM model includes choices such as element type and meshing, which are made based on a good understanding of what kind of displacement fields are expected and what can be represented by the chosen element types. For example, a more refined element mesh will be placed around areas where stress concentrations are expected.

In a much similar way, the results obtained from an iFEM XUA analysis are not objective and will be influenced by modelling choices which encodes pre-knowledge on

the part of the user. The dynamic XUA algorithm has a high computing demand and is limited by CPU capacity, which increase linearly with the number of model parameters included in the iFEM model. For this reason, intelligent modelling choices are necessary to limit the amount of model parameters. In the analyses of numerical and physical experiments explored in this work, pre-knowledge on the location, severity or type of damage was exploited by the user to reduce the number of model parameters needed. Pre-knowledge on damage is introduced into the XUA analysis in two ways:

1. The choice of type and location of model parameters encodes prior knowledge on the type of damage and probable damage location.

2. The choice of cost associated to the model parameters encodes prior knowledge on the probability of damage or the level of damage.

To make good modelling choices requires that the user must have a proper understanding of what types of damage can be represented by different model parameters and what model discrepancies are likely to occur if poor choices are made. In Chapter 9, Section 9.5, the influence on the damage estimate of different choices of model parameters and of allowing unknown forces are discussed. When the types of model parameters that have been introduced in the iFEM model do not correspond to the types of model errors that are present, it is likely that iFEM will estimate external ghost forces to explain the effect of the model errors on the response of the structure. Alternatively, the model parameters that were allowed will be adjusted in a way that has little physical meaning, because the type of parameter that was allowed cannot adequately describe the model error that is present.

In addition to the modelling choices mentioned above, iFEM results will also be influenced by choices made in setting up the experiment, including the number and placement of sensors and the position of physical excitation. Further work is needed to understand how these factors will influence results.

## 13.2 Suggestions for future work

The current work's primary goal was to study the sensitivity of iFEM XU to modelling errors, develop static and dynamic parameter identification algorithms and test them using experimental data.

### 13.2.1 Development of non-linear dynamic estimation algorithms.

Almost all of the damage-identification methods found in literature rely on linear structural behaviour. Development of algorithms that have the ability to account for the effects of non-linear structural response has potential to enhance structural monitoring technology significantly.

An algorithm that allows for non-linear force- and response estimation based on measurement data, should be developed. A serious challenge in designing an algorithm for non-linear dynamic estimation is the computing time associated to numerically treat such problems. To be of practical interest, such an algorithm must be able to analyse large non-linear systems within an acceptable amount of time. Developing such an algorithm would in itself be a major accomplishment with many applications in the field of structural monitoring.

Once a non-linear force- and response estimation algorithm is in place, this should be adapted to also allow the identification of model parameters in non-linear dynamic systems. In chapter 7 a parameter identification theory for linear and non-linear static systems was developed. Chapter 8 developed a similar theory for linear dynamic systems. Both algorithms allow to combine data from several load cases to characterise damage in complicated structures. Ideally, the non-linear model parameter identification algorithm should also have this ability. The existing algorithms present a good example of how this can be achieved.

An algorithm that allows for damage detection or model parameter identification in

non-linear dynamic systems would be valuable. An example of a non-linear damage mechanism is the opening and closing of a fatigue crack during cyclic loading. Methods that are limited to linear models cannot account for the non-linear effects of such a damage scenario. Some other examples of non-linear behaviour is material plastification, buckling behaviour and systems in which the external load is response dependent.

Monitoring of structures has applications in civil, mining, mechanical, aerospace, offshore, and other branches of engineering. The market is fast expanding thanks to improved measurement and data-logging possibilities. Many of the applications are dynamic and a non-linear dynamic theory would open a vast market in structural monitoring.

### 13.2.2 The number and location of measurement sensors

A subject that merits further investigation is the effect of the number and placement of measurement sensors, and the precision and type of the measurement sensors. How many sensors are needed and where must they be placed to ensure that damage are detected? Obtaining an answer to this question was never a goal of this work and is left for future research.

Algorithms that can evaluate a given measurement setup or estimate optimal sensor placement for a given number of sensors will be extremely valuable. Techniques that are to be seriously considered for implementation in the field of structural monitoring and damage detection should demonstrate that they can perform well under the limitations of a small number of measurement locations, and under the constraint that these locations be selected a priori.

As part of the iFEM Research Project at the University of Stellenbosch, M.Sc. candidate Jacques Maree (under supervision of Dr. P Mainçon) [46] developed an algorithm that allows the user to estimate confidence intervals of any given static iFEM XU solution. This is valuable, because there are generally an infinite number of load configurations that could lead to the measurement data at hand. iFEM circumvents this problem by finding

the most probable of the above solutions, but this leaves open the possibility of other, almost as probable solutions. The results show probable behaviour of the structure that would not be captured by the sensors.

An important feature of the static sensitivity algorithm is that for linear structural behaviour and Gaussian uncertainties, its input does not include measured values. The uncertainty analysis is carried out on the basis of the description of the structure, the measurement setup and the order of magnitudes of external force only, and shows probable behavior of the structure that would not be captured by the sensors. This means that the algorithm can be applied before the sensors are installed and alternative sensor configurations can be rapidly evaluated in order to choose an appropriate measurement setup. It is envisioned that the dynamic development should have similar properties that would allow it to be used as a tool for design and planning of dynamic experiments.

A main objective of future research would be to develop a numerical method for systematic sensitivity study of iFEM estimates for dynamic (vibration) experiments, similar to the method developed by Jacques Maree for static experiments. The developed algorithm must then be implemented as computer software, in order for it to be a practical and useful engineering tool for the design of dynamic experiments. The computer implementation of the development would pave the way to proceed with numerical test cases to demonstrate the capabilities of the algorithm.

The success of Jacques Maree's research on the static algorithm is a strong encouragement to pursue with a more ambitious but also more important dynamic algorithm.

The above algorithm would supply structural experimentalists and experts in structural monitoring with a design tool for the instrumentation of the studied structure. It would allow predicting the adequacy of the measurement system, before the measurements are carried out.

### 13.2.3 Development of a better cost theory

When choosing Tikhonov parameters for a given analysis, the user is required to observe the character of the analysis output and adjust the Tikhonov parameters accordingly, so that a stable solution somewhere between under-regularised ("jittery") and over-regularised ("sluggish") behaviour is obtained. This way of choosing costs is subjective. A theory that would allow the objective choice of cost parameters would be valuable.

### 13.2.4 Further development of the software Safran

During the past four years, the SAFRAN computer software was under constant development. While a lot of work has gone into the implementation of new algorithms and creating a flexible and expandable software that allows to treat a wide variety of estimation problems, restructuring of the software meant that maintaining an extensive element library would have been costly. There is a need to improve SAFRAN's element library so that element types other than frame elements can be modelled.

Also, a user interface is at present non-existent. The user needs to know the code fairly well in order to write an input file, calling different functions in sequence and handing them the correct input, in order to set up a structural model, define constraints, add measurement data and execute an analysis.

### 13.2.5 Further experimental validation

In the current work, data from several experiments were used to validate the dynamic force- and response algorithm as well as the dynamic parameter identification algorithm. The static algorithms were tested using numerically simulated examples. There is much room for further experimental validation of all of the above algorithms. Further experimental testing of defect detection on large-scale and small-scale structures will be valuable to increase understanding of the capabilities and limitations of this theory. Numerical or experimental treatment of problems with a large number of degrees of freedom (i.e. degrees of freedom >10000; or damage parameters >1000) would test the algorithms

capability to handle large systems.

## 13.3 Future visions

In 2004 a company was started to develop the iFEM technology into a commercial product and take it to the market. First projects are underway, attracting interest from the offshore oil industry. Other potential clients would be the aviation- and mining industries. The proposed future work addresses needs identified by the industry.

# Bibliography

[1] BARNARDO, C., "Static and dynamic iFEM parameter identification algorithms - Confidential memo -." *Safran Engineering Algorithms*, 2006.

[2] BARUCH, M. and BAR ITZHACK, I., "Optimum weighted orthogonalization of measured modes." *AIAA Journal*, 1978, Vol. 16, No. 4, pp. 346–351.

[3] BECK, J. L., MAY, B. S., and POLIDORI, D. C., "Determination of modal parameters from ambient vibration data for structural health monitoring." *Proceedings of First World Conference on Structural Control*, 1994, p. TA3:3TA3:12.

[4] BERMAN, A., "System identification of structural dynamic models – theoretical and practical bounds." *AIAA conference*, 1984.

[5] BISHOP, C., "Neural networks and their applications." *Review of scientific instrumentation*, 1994, Vol. 65, No. 6, pp. 1803–1832.

[6] CAICEDO, J., DYKE, S., and JOHNSON, E., "NExT and ERA for Phase I of the IASCE-ASCE Benchmark Problem: Simulated Data." *Journal of Engineering Mechanics: Special Issue on the Structural Health Monitoring Analytical Benchmark Problem*, 2003.

[7] CHANCE, J., TOMLINSON, G., and WORDEN, K., "A simplified approach to the numerical and experimental modeling of the dynamics of a cracked beam." *Proceedings of the 12th IMAC*, 1994, pp. 778–785.

[8] CHING, J. and BECK, J., "Two-Stage Bayesian Structural Health Monitoring Approach for Phase II ASCE Experimental Benchmark Studies." *Proceedings of the 16th ASCE Engineering Mechanics Conference.*

[9] CHING, J. and BECK, J., "Bayesian Analysis of the Phase II IASC-ASCE Structural Health Monitoring Experimental Benchmark Data." *Journal of Engineering Mechanics*, 2004, Vol. 130, No. 10.

[10] COBB, R. and LIEBST, B., "Structural damage identification using assigned partial eigenstructure." *AIAA journal*, 1997, Vol. 35, No. 1, pp. 152–158.

[11] COOK, R., MALKUS, D., and PLESHA, M., *Concepts and applications of finite element analysis*. John Wiley Sons, 1989.

[12] DOEBLING, S., FARRAR, C., PRIME, M., and SHEVITZ, D., "Damage identification and health monitoring of structural and mechanical systems from changes in their vibration characteristics: a literature review." *Los Alamos National Laboratory*, 1996.

[13] DOHERTY, J., *Handbook on experimental Mechanics – Chapter 12*. Society for Experimental Mechanics, 1987.

[14] DYKE, S., BERNAL, D., BECK, J., and VENTURA, C., "Experimental Phase of the Structural Health Monitoring Benchmark Problem." *Proceedings of the 16th ASCE Engineering Mechanics Conference.*

[15] FARRAR, C., DOEBLING, S., CORNWELL, P., and STRASER, E., "Variability of modal parameters measured on the Alamosa Canyon bridge." *Proceedings of the 15th IMAC*, 1997, pp. 257–263.

[16] FENG, C., "The measurement of vortex induced effects in flow past stationary and oscillatin circular and d-section cylinders." Master's thesis, University of British Columbia, Canada, 2003.

[17] FISSETTE, E. and IBRAHIM, S., "Error location and updating of analytical dynamic models using a force balance method." *Proceedings of the 6th IMAC*, 1988, pp. 1063–1070.

[18] FOX, C., "The location of defects in structures: a comparison of the use of natural frequency and mode shape data." *Proceedings of the 10th IMAC*, 1992, pp. 522–528.

[19] FRISWELL, M., PENNY, J., and WILSON, D., "Using vibration data and statistical measures to locate damage in structures." *Proceedings of the 14th IMAC*, 1994, pp. 1278–1284.

[20] GIRALDO, D., CAICEDO, J., and DYKE, S., "Experimental Phase of the SHM Benchmark Studies. Damage Detection using NeXT and ERA." *Proceedings of the 16th ASCE Engineering Mechanics Conference.*

[21] GOGE, D., "Automatic updating of large aircraft models using experimental data from ground vibration testing." *Aerospace Science and Technology*, 2003, Vol. 7, pp. 47–61.

[22] GOGE, D. and LINK, M., "Assessment of computational model updating procedures with regard to model validation." *Aerospace Science and Technology*, 2003, Vol. 7, pp. 47–61.

[23] GOPALKRISHNAN, R., "Vortex induced forces on oscillating bluff cylinders." Ph.D thesis, MIT, USA, 1993.

[24] GRIFFIN, O. and KOOPMANN, G., "The vortex excited lift and reaction forces on resonantly vibrating cylinders." *Journal of Sound and Vibration*, 1977, Vol. 54, No. 3, pp. 435–448.

[25] GYSIN, H., "Comparison of expansion methods for FEM error localisation." *Proceedings of the 8th IMAC*, 1990, pp. 195–204.

[26] GYSIN, H., "Critical application of an error matrix method for location of finite element modeling inaccuracies." *Proceedings of the 4th IMAC*, 1986, pp. 1339–1351.

[27] HAAKONSEN, R., "Vorex induced vibration of long marine risers." Master's thesis, Norwegian Institute of Science and Technology, 1996.

[28] HE, J. and EWINS, D., "Analytical stiffness matrix correction using measured vibration modes." *The International Journal of Analytical and Experimental Modal Analysis.*, 1986, Vol. 1, No. 3, pp. 9–14.

[29] HEMEZ, F. and FARHAT, C., "Structural damage detection via a finite element model updating methodology." *The International Journal of Analytical and Experimental Modal Analysis.*, 1995, Vol. 10, No. 3, pp. 152–166.

[30] HUNTER, N., "Bilinear system characterization from nonlinear time series analysis." *Proceedings of the 17th IMAC.*, 1999.

[31] JAMES, G., CARNE, T., and LAUFFER, J., "The Natural Excitation Technique for Modal Parameter Extraction from Operating Wind Turbines." tech. rep., Sandia National Laboratories, 1993.

[32] JUNEJA, V., HAFTKA, R., and CUDNEY, H., "Damage detection and damage detectability: Analysis and experiments." *Journal of Aerospace Engineering*, 1997, Vol. 10, No. 4, pp. 135–142.

[33] KAOUK, M. and ZIMMERMAN, D., "Structural damage assessment using a generalized minimum rank perturbation theory." *AIAA Journal*, 1994, Vol. 32, No. 4, pp. 836–842.

[34] KIM, H. and BARTKOWICZ, T., "Damage detection and health monitoring of large space structures." *Journal of Sound and vibration.*, 1993, Vol. 27, No. 6, pp. 12–17.

[35] LARSEN, C. and HALSE, K., "Comparison of models for vortex induced vibrations of slender marine structures." *Proceedings of the sixth International Conference on flow-induced vibrations*, 1995, pp. 467–482.

[36] LIE, H., "Vortex induced vibrations in a riser - Model tests in a rotating rig - Data CD.." tech. rep., Marintek, Sintef Group, 1996.

[37] LIE, H., "Vortex induced vibrations in a riser - Model tests in a rotating rig data report.." tech. rep., Marintek, Sintef Group, 1996.

[38] LIM, T., "A submatrix approach to stiffness using modal test data." *AIAA Journal*, 1990, Vol. 28, No. 6, pp. 1123–1130.

[39] LIM, T., "Structural damage detection using constrained eigenstructure assignment." *Journal of Guidance, Control and Dynamics*, 1995, Vol. 18, No. 3, pp. 411–418.

[40] LIN, R. and EWINS, D., "On the location of structural non-linearity from modal testing – A feasibility study." *Proceedings of the 8th IMAC.*, 1990, pp. 358–364.

[41] LINK, M. and SANTIAGO, O., "Updating and localizing structural errors based on minimisation of equation errors." *International conference on spacecraft structures and mechanical testing*, 1991, pp. 503–510.

[42] LJUNG, L., *System Identification – Theory for the User*. Prentice Hall, Upper Saddle River, N.J., 1987.

[43] LOLAND, O. and DODDS, J., "Experience in developing and operating integrity monitoring system n the North Sea." *Proc. of the 8th Annual Offshore Technology Conference*, 1976, pp. 313–319.

[44] MAINÇON, P., "Inverse finite element methods – Part I: Estimating loads and structural response from measurements." *SEMC, A.Zingoni (Ed.)*, 2004.

[45] MAINÇON, P., "Inverse finite element methods – Part II: Dynamic and non-linear problems." *SEMC, A.Zingoni (Ed.)*, 2004.

[46] MAREE, J. and MAINÇON, P., "Inverse finite element methods – Part III: Influence of measurement data availability." *SEMC, A.Zingoni (Ed.)*, 2004.

[47] MEIROVITCH, L., *Fundamentals of Vibrations*. McGraw Hill, 2001.

[48] MOE, G. and WU, Z., "The lift force on a vibrating cylinder in a current." *Proceedings of the Fourth International Offshore and Polar Engineering Conference*, 1989, pp. 259–268.

[49] MORASSI, A. and ROVERE, N., "Localizing a notch in a steel frame from frequency measurements." *Journal of Engineering Mechanics*, 1997, Vol. 123, No. 5, pp. 422–432.

[50] MOTTERSHEAD, J. and FRISWELL, M., "Model updating in structural dynamics: a survey." *Journal of sound and vibration*, 1993, Vol. 167, No. 2, pp. 347–375.

[51] NARKIS, Y., "Identification of crack location in vibrating simply supported beams." *Journal of sound and vibration*, 1994, Vol. 172, No. 4, pp. 549–558.

[52] OSEGUEDA, R. and STUBBS, N., "Global non-destructive damage evaluation in solids." *Modal Analysis: The International Journal of Analytical and Experimental modal analysis*, 1990, Vol. 5, No. 2, pp. 67–79.

[53] PANDEY, A. and BISWAS, M., "Damage diagnosis of truss structures by estimation of flexibility change." *The International Journal of Analytical and Experimental Modal Analysis.*, 1995, Vol. 10, No. 2, pp. 104–117.

[54] PANDEY, A., BISWAS, M., and SAMMAN, M., "Damage detection from changes in curvature mode shapes." *Journal of Sound and Vibrasion*, 1991, Vol. 145, No. 2, pp. 321–332.

[55] RICLES, J. and KOSMATKA, J., "Damage detection in elastic structures using vibratory residual forces and weighted sensitivity." *AIAA journal*, 1992, Vol. 30, No. 9, pp. 2310–2315.

[56] SALAWU, O., "Detection of structural damage through changes in frequency: a review." *Engineering structures*, 1997, Vol. 19, No. 9, pp. 718–723.

[57] SAMPAIO, R., MAIA, N., and SILVA, J., "Damage detection using the frequency-response-function curvature method." *Journal of sound and vibration*, 1999, Vol. 226, No. 5, pp. 1029–1042.

[58] SARPKAYA, T., "Fluid forces on oscillating cylinders." *Journal of the Waterway Port Coastal and Ocean Division*, 1978, Vol. 104, pp. 275–290.

[59] SCHULZ, M., PAI, P., and ABDELNASER, A., "Frequency response function assignment technique for structural damage identification." *Proceedings of the 14th IMAC.*, 1996, pp. 105–111.

[60] SHYE, K. and RICHARDSON, M., "Mass, stiffness and damping matrix estimates from structural measurements." *Proceedings of the 5th IMAC*, 1987, pp. 756–761.

[61] SKJAERBAEK, P., NIELSEN, S., and CAKMAK, A., "Assessment of damage in seismically excited structures from a single measured response." *Proceedings of the 14th IMAC*, 1996, pp. 133–139.

[62] SMITH, S. and BEATTIE, C., "Model correlation and damage location for large space truss structures: Secant method development and evaluation." *NASA report*, 1991.

[63] SODERSTROM, T. and STOICA, P., *System Identification*. Prentice Hall International, Londen, 1989.

[64] SOHN, H., CZARNECKI, J., FARRAR, C., and MEMBER, P., "Structural health monitoring using statistical process control." *Journal of structural engineering*, 2000, pp. 1356–1363.

[65] STASZEWSKI, W., BOLLER, C., and TOMLINSON, G., *Health monitoring of Aerospace Structures*. John Wiley and Sons, Ltd., 2004.

[66] STAUBLI, T., "Calculation of the vibration of an elastically mounted cylinder using experimental data from forced oscillation." *Journal of Fluid Mechanics*, 1983, Vol. 105, pp. 225–229.

[67] STUBBS, N., KIM, T., and FARRAR, C., "Field verification of a non-destructive damage localization and severity estimation algorithm." *Proceedings of the 13th IMAC*, 1995, pp. 210–218.

[68] SURACE, C. and RUOTOLO, R., "Crack detection of a beam using the wavelet transform." *Proceedings of the 12th IMAC.*, 1994.

[69] THOREN, A., "Derivation of mass and stiffness matrices from dynamic test data." *AIAA conference paper*, 1972.

[70] VANIK, M., BECK, J., and AU, S., "Bayesian probabilistic approach to structural health monitoring." *Journal of engineering mechanics*, 2000, pp. 738–745.

[71] VENUGOPAL, M., "Damping and response prediction of a flexible cylinder in a current." Ph.D thesis, MIT, USA, 1996.

[72] VIKESTAD, K., "Multi-frequency response of a cylinder subjected vortex shedding and support motions." Ph.D thesis, Norwegian Institute of Science and Technology, 1998.

[73] WEST, W., "Illustration of the use of Modal Assurance Creterion to detect structural changes in an orbiter test specimen." *Proc. Air Force Conference on aircraft structural integrity*, 1984, pp. 1–6.

[74] WU, Z., "Current Induced Vibrations of a Flexible Cylinder." Ph.D thesis, Norwegian Institute of Science and Technology, 1989.

[75] YEUN, M., "A numerical study of the eigenparameters of a damaged cantilever." *Journal of sound and vibration*, 1985, Vol. 103, pp. 301–310.

[76] ZABEL, V., "Applications of wavelet analysis in system identification." Ph.D thesis, Bauhaus University, Weimar, Germany, 2003.

[77] ZHANG, Q. and LALLEMENT, G., "Dominant error localisation in a finite element model of a mechanical structure." *Mechanical systems and signal processing*, 1987, Vol. 1, No. 2, pp. 141 – 149.

[78] ZHANG, Z. and ATKAN, A., "The damage indices for constructed facilities." *Proceedings of the 13th IMAC*, 1995, pp. 1520–1529.

[79] ZIMMERMAN, D. and SMITH, S., "Model refinement and damage location for intelligent structures." *Intelligent structural systems*, 1992, pp. 403–452.

# Appendix A

# Attempt to derive an analytical sensitivity formula

## A.1 Introduction

An attempt was made to derive an analytical sensitivity formula to describe the influence of model error on the output of iFEM. This mathematical derivation result in expressions that are too complex to provide insight. It is easier to perform numerical sensitivity analyses (as was done in chapter 3), and they are also easier to interpret than the analytical result.

## A.2 Obtaining expressions for U and X

The three equations from iFEM theory for static systems are used,

$$\overline{\overline{\mathbf{K}}}.\overline{\mathbf{X}} = -\overline{\overline{\mathbf{H}}}.\overline{\mathbf{U}} - \overline{\mathbf{R}} \tag{A.1}$$

$$\overline{\overline{\mathbf{K}}}^{T}.\overline{\lambda} + \overline{\overline{\mathbf{Q}}}_{xx}.\overline{\mathbf{X}} + \overline{\mathbf{Q}}_{x} + \overline{\overline{\mathbf{Q}}}_{ux}^{T}.\overline{\mathbf{U}} = \overline{0} \tag{A.2}$$

$$\overline{\overline{\mathbf{H}}}^{T}.\overline{\lambda} + \overline{\overline{\mathbf{Q}}}_{uu}.\overline{\mathbf{U}} + \overline{\mathbf{Q}}_{u} + \overline{\overline{\mathbf{Q}}}_{ux}.\overline{\mathbf{X}} = \overline{0} \tag{A.3}$$

If $\overline{\lambda}$ is eliminated by extracting it from Equation A.2 and $\overline{\mathbf{X}}$ is eliminated by extracting it from Equation A.1, inserting these into Equation A.3, assuming $\overline{\overline{\mathbf{Q}}}_{ux} = 0$ and $\overline{\mathbf{Q}}_{u} = 0$, gives

$$\overline{\overline{\mathbf{U}}} = (\bar{\bar{\mathbf{I}}} + \overline{\overline{\mathbf{Q}}}_{uu}^{-1}.\overline{\overline{\mathbf{H}}}^{T}.\overline{\overline{\mathbf{K}}}^{-T}.\overline{\overline{\mathbf{Q}}}_{xx}.\overline{\overline{\mathbf{K}}}^{-1}.\overline{\overline{\mathbf{H}}})^{-1}.(-\overline{\overline{\mathbf{Q}}}_{uu}^{-1}.\overline{\overline{\mathbf{H}}}^{T}.\overline{\overline{\mathbf{K}}}^{-T}.\overline{\overline{\mathbf{Q}}}_{xx}.\overline{\overline{\mathbf{K}}}^{-1}.\overline{\mathbf{R}} + \overline{\overline{\mathbf{Q}}}_{uu}^{-1}.\overline{\overline{\mathbf{H}}}^{T}.\overline{\overline{\mathbf{K}}}^{-T}.\overline{\mathbf{Q}}_{x}) \tag{A.4}$$

Replacing back into A.1 will again give an expression for $\overline{\mathbf{X}}$.

These expressions assume $\overline{\overline{\mathbf{K}}}$ to be invertible. In iFEM $\overline{\overline{\mathbf{K}}}$ will not always be invertible, since the theory allows stiff body translations as long as the position/state of the structure are adequately described by measurements. For cases in which $\overline{\overline{\mathbf{K}}}$ is invertible, Equation A.4 can in theory be used to derive an analytical sensitivity formula.

## A.3 Deriving an expression for $\frac{dK^{-1}}{dK}$

Equation A.4 can be derived with respect to $\overline{\overline{\mathbf{K}}}$ to obtain an analytical formula that describes the influence of modelling error on the assessed external forces. In order to find this derivative, an expression for $\frac{dK^{-1}}{dK}$ is needed.[1]

$$\overline{\overline{\mathbf{I}}}_{ij} = \overline{\overline{\mathbf{K}}}_{ik}.\overline{\overline{\mathbf{K^{-1}}}}_{kj} \tag{A.5}$$

$$\frac{\partial \overline{\overline{\mathbf{I}}}_{ij}}{\partial \overline{\overline{\mathbf{K}}}_{lm}} = \frac{\partial}{\partial \overline{\overline{\mathbf{K}}}_{lm}}(\overline{\overline{\mathbf{K}}}_{ik}.\overline{\overline{\mathbf{K^{-1}}}}_{kj}) \tag{A.6}$$

$$\forall_{ijlm} \tag{A.7}$$

$$\begin{aligned} 0 &= \overline{\overline{\mathbf{K}}}_{ik}.\frac{\partial}{\partial \overline{\overline{\mathbf{K}}}_{lm}}(\overline{\overline{\mathbf{K^{-1}}}}_{kj}) + \frac{\partial \overline{\overline{\mathbf{K}}}_{ik}.}{\partial \overline{\overline{\mathbf{K}}}_{lm}}.\overline{\overline{\mathbf{K^{-1}}}}_{kj} \\ &= \overline{\overline{\mathbf{K}}}_{ik}.\frac{\partial}{\partial \overline{\overline{\mathbf{K}}}_{lm}}(\overline{\overline{\mathbf{K^{-1}}}}_{kj}) + \delta_{il}\delta_{mk}\overline{\overline{\mathbf{K^{-1}}}}_{kj} \\ &= \overline{\overline{\mathbf{K}}}_{ik}.\frac{\partial}{\partial \overline{\overline{\mathbf{K}}}_{lm}}(\overline{\overline{\mathbf{K^{-1}}}}_{kj}) + \delta_{il}\overline{\overline{\mathbf{K^{-1}}}}_{mj} \end{aligned} \tag{A.8}$$

Where $\delta_{il} = 1$, if $i = l$, else $\delta_{il} = 0$.

Rearranging Equation A.8 and multiplying both sides by $\overline{\overline{\mathbf{K^{-1}}}}_{ni}$

$$\underbrace{\overline{\overline{\mathbf{K^{-1}}}}_{ni}.\overline{\overline{\mathbf{K}}}_{ik}}_{\delta_{nk}}.\frac{\partial}{\partial \overline{\overline{\mathbf{K}}}_{lm}}(\overline{\overline{\mathbf{K^{-1}}}}_{kj}) = -\overline{\overline{\mathbf{K^{-1}}}}_{ni}.\delta_{il}\overline{\overline{\mathbf{K^{-1}}}}_{mj} \tag{A.9}$$

$$\frac{\partial}{\partial \overline{\overline{\mathbf{K}}}_{lm}}(\overline{\overline{\mathbf{K^{-1}}}}_{nj}) = -\overline{\overline{\mathbf{K^{-1}}}}_{nl}\overline{\overline{\mathbf{K^{-1}}}}_{mj} \tag{A.10}$$

$$\overline{\overline{\nabla}}_{\overline{\overline{\mathbf{K}}}}(\overline{\overline{\mathbf{K}}}^{-1}) = -\overline{\overline{\mathbf{K}}}^{-1}\overline{\overline{\mathbf{K}}}^{-1} \tag{A.11}$$

Note that, if $\overline{\overline{\mathbf{K}}}$ was a scalar, Equation A.11 would become $\frac{\partial}{\partial k}\frac{1}{k} = -\frac{1}{k^2}$

[1] In the notation "$\overline{\overline{\mathbf{M}}}_{ij}$", $i$ refers to the row-index of the matrix $\overline{\overline{\mathbf{M}}}$, and $j$ refers to the column-index

## A.4 Analytical sensitivity formula and related problems

Equation A.4 can be derived with respect to $\overline{\overline{\mathbf{K}}}$, using the proof from section A.3. The resulting analytical sensitivity formula is complex and difficult to interpret. A numerical approach to evaluate the sensitivity of a system to model error is much easier to implement and to interpret. The numerical approach was followed in chapter 3.

# Appendix B

# Alternative parameter identification approach

## B.1 Introduction

An alternative approach to determine $\overline{\alpha}$ for a set of experiments, using an unconstrained optimisation procedure, was investigated. To enforce constraints, an alternative to Lagrange multipliers is to use a contra-gradient transformation to make a change of variables. As in section 7.3, a combined cost function for all the experiments is compiled and derived with respect to $\overline{\alpha}$, to find the optimal $\overline{\alpha}$ for the set of experiments. When $\overline{\overline{\mathbf{K}}}$ is introduced as a function of the unknown $\overline{\alpha}$, the unconstrained optimisation approach fails, since it requires computing the null space of a matrix that is now a function of the unknown $\overline{\alpha}$.

## B.2 Unconstrained optimisation approach

For a known $\overline{\overline{\mathbf{K}}}$ and one set of experimental measurement data, an alternative to using Lagrange constrained optimisation, is to enforce $\overline{\overline{\mathbf{K}}}.\overline{\mathbf{X}} = \overline{\overline{\mathbf{H}}}.\overline{\mathbf{U}} + \overline{\mathbf{R}}$ by posing

$$\begin{bmatrix} \overline{\mathbf{X}} \\ \overline{\mathbf{U}} \end{bmatrix} = \overline{\overline{\mathbf{A}}}.\overline{\mathbf{V}} + \overline{\mathbf{B}} \tag{B.1}$$

with $\overline{\overline{\mathbf{A}}}$ and $\overline{\mathbf{B}}$ carefully chosen, as will be explained in section B.4

We now get a quadratic cost function Q, as a function of $\overline{\mathbf{V}}$ only, and we can do an unconstrained minimisation of $Q(\overline{\mathbf{V}})$.

Thus we obtain the optimum $\overline{\mathbf{V}}$ by requiring that

$$\overline{\nabla}_V Q = \overline{\mathbf{0}} \tag{B.2}$$

and we obtain $\overline{\mathbf{X}}$, $\overline{\mathbf{U}}$ by replacing $\overline{\mathbf{V}}$ back into Equation B.1.

## B.3 Introducing $\overline{\overline{\mathbf{K}}}$ as unknown

Consider a set of experiments and introduce $\overline{\overline{\mathbf{K}}} = \overline{\overline{\mathbf{K_o}}} + \overline{\overline{\mathbf{S}}}.\overline{\alpha}$.

For each experiment, this will result in

$$\begin{bmatrix} \overline{\mathbf{X}} \\ \overline{\mathbf{U}} \end{bmatrix} = \overline{\overline{\mathbf{A}}}(\overline{\alpha}).\overline{\mathbf{V}} + \overline{\mathbf{B}}(\overline{\alpha}) \tag{B.3}$$

Then, for a given experiment $i$, the residual cost of experiment $i$, will be a function of $\overline{\alpha}$. The residual cost of experiment $i$ is obtained by requiring that $\overline{\nabla}_V Q_i(\overline{\mathbf{V}}, \overline{\alpha}) = \overline{\mathbf{0}}$, thereby finding the optimum $\overline{\mathbf{V}}(\overline{\alpha})$ and substituting back into the cost function, to obtain $Q_i(\overline{\alpha})$. The sum for all experiments of the residual costs will thus also be a function of $\overline{\alpha}$, and hence, we can find the optimum $\overline{\alpha}$ by requiring that

$$\overline{\nabla}_\alpha(\sum_i(Q_i(\overline{\alpha}))) = \overline{\mathbf{0}} \tag{B.4}$$

Now $\overline{\mathbf{V}}$ and $\overline{\mathbf{X}}$, $\overline{\mathbf{U}}$ can also be computed for each experiment.

## B.4 Obtaining the matrix $\overline{\overline{\mathbf{A}}}$

Given a model, the system equilibrium equation is

$$\overline{\overline{\mathbf{K}}}.\overline{\mathbf{X}} = \overline{\overline{\mathbf{H}}}.\overline{\mathbf{U}} + \overline{\mathbf{R}} \tag{B.5}$$

A variation of this that also respects equilibrium, is

$$\overline{\overline{\mathbf{K}}}.(\overline{\mathbf{X}} + \overline{\mathbf{dX}}) = \overline{\overline{\mathbf{H}}}.(\overline{\mathbf{U}} + \overline{\mathbf{dU}}) + \overline{\mathbf{R}} \tag{B.6}$$

Subtracting Equation B.5 from Equation B.6 gives

$$\overline{\overline{\mathbf{K}}}.\overline{\mathbf{dX}} + \overline{\overline{\mathbf{H}}}.\overline{\mathbf{dU}} = \overline{\mathbf{0}} \tag{B.7}$$

or in matrix notation

$$\begin{bmatrix} \overline{\overline{\mathbf{K}}} & \overline{\overline{\mathbf{H}}} \end{bmatrix}.\begin{bmatrix} \overline{\mathbf{dX}} \\ \overline{\mathbf{dU}} \end{bmatrix} = \overline{\mathbf{0}} \tag{B.8}$$

Equation B.8 shows that $\begin{bmatrix} \overline{dX} \\ \overline{dU} \end{bmatrix}$ is in the null space of $\begin{bmatrix} \overline{\overline{K}} & \overline{\overline{H}} \end{bmatrix}$, thus

$$\overline{\overline{A}} = null(\begin{bmatrix} \overline{\overline{K}} & \overline{\overline{H}} \end{bmatrix}) \tag{B.9}$$

A problem now arises when $\overline{\overline{K}} = \overline{\overline{K_o}} + \overline{\overline{S}}.\overline{\alpha}$ is introduced,

$$\overline{\overline{A}}(\alpha) = null(\begin{bmatrix} \overline{\overline{K}}(\alpha) & \overline{\overline{H}} \end{bmatrix}) \tag{B.10}$$

Computing the null-space of a matrix that contains unknown variables is a complex mathematical problem, rendering this approach practically unusable.